Integration of innovative oxide materials in an IT-SOFC

Anne Morandi

N° d'ordre : 4775

THÈSE

PRÉSENTÉE A

L'UNIVERSITÉ BORDEAUX 1

ÉCOLE DOCTORALE DES SCIENCES CHIMIQUES

Par Anne MORANDI

POUR OBTENIR LE GRADE DE

DOCTEUR

SPÉCIALITÉ : Physico-Chimie de la Matière Condensée

Integration of innovative oxide materials in an IT-SOFC

Directeurs de thèse : M. J.-M. BASSAT et M. O. JOUBERT
Co-encadrants : M. Q. FU et M. M. MARRONY

Soutenue le : 04 Avril 2013

Après avis de :

M. BONANOS, Nikolaos	Senior research scientist, DTU, Roskilde	Rapporteur
M. VAN HERLE, Jan	Senior scientist, EPFL, Lausanne	Rapporteur

Devant la commission d'examen formée de :

M. MAGLIONE, Mario	Directeur de recherche, ICMCB, Bordeaux	Président
M. BONANOS, Nikolaos	Senior research scientist, DTU, Roskilde	Rapporteur
M. VAN HERLE, Jan	Senior scientist, EPFL, Lausanne	Rapporteur
M. FU, Qingxi	Chef de projet piles à combustible, EIFER, Karlsruhe	Examinateur
M. MARRONY, Mathieu	Chef de projet piles à combustible, EIFER, Karlsruhe	Examinateur
M. JOUBERT, Olivier	Professeur, IMN, Nantes	Examinateur
M. BASSAT, Jean Marc	Directeur de recherche, ICMCB, Bordeaux	Examinateur

Membres invités :

M. ANTOINE, Loic	Ingénieur, ADEME, Angers

EIFER - European Institute for Energy Research

Group Energy resources and decentralized production

Emmy-Noether Str. 11

76131 Karlsruhe, Germany

ICMCB - Institut de la Chimie de la Matière Condensées de Bordeaux (UPR9048)

Groupe 1 : Oxydes et intermétalliques pour la conversion de l'énergie et piles à combustibles

87 Avenue du Docteur Schweitzer

33608 Pessac Cedex, France

IMN - Institut des Matériaux de Nantes

Equipe ST2E : Stockage et Transformation Électrochimiques de l'Energie

2 rue de la Houssinière

BP32229

44322 Nantes Cedex 3, France

ADEME - Agence de l'Environnement et de la Maîtrise de l'Énergie

Centre d'Angers

20, avenue du Grésillé

BP 90406

49004 Angers Cedex 01, France

Remerciements

En tout premier lieu, je tiens à remercier l'ADEME et l'EIFER pour leur investissement dans ce travail de thèse, et plus généralement pour leur intérêt à l'égard de sujets tels que les technologies piles à combustibles.

Je remercie également monsieur Mohsine Zahid pour avoir initié ce projet et m'avoir intégrée dans l'aventure, ainsi que pour son encadrement de qualité durant la première année. Merci également à monsieur Norbert Menzler, chef de groupe au Forschungsszentrum Jülich, ainsi que messieurs Wolfgang Schafbauer et Ralf Kauert, pour leur apprentissage des techniques de coulage en bande et de vacuum slip casting.

J'aimerais également remercier vivement monsieur Mario Maglione pour avoir présidé mon jury, ainsi que messieurs Nikolaos Bonanos et Jan Van Herle, tous deux Senior Scientists à DTU et à l'EPFL, respectivement, pour m'avoir fait l'honneur d'accepter de rapporter ce travail. Merci également à monsieur Loic Antoine, ingénieur à l'ADEME, pour son suivi durant ces trois années.

Cette thèse s'est principalement déroulée à l'EIFER, sous la responsabilité de messieurs Mathieu Marrony et Qingxi Fu après le départ de Mohsine. Un immense merci à vous deux pour votre confiance et votre disponibilité, ainsi que pour l'investissement et l'intérêt que vous avez porté à mes travaux durant plus de deux années. Merci…

Mes remerciements les plus sincères vont à mes deux directeurs de thèse, messieurs Jean-Marc Bassat et Olivier Joubert, pour la confiance qu'ils m'ont portée ainsi que pour leur expertise scientifique et leur disponibilité tout au long de ce projet.
J'en profite pour remercier monsieur Jean-Claude Grenier pour m'avoir donné la chance de pouvoir intégrer l'équipe Piles à Combustible dès mon année de licence et pour ainsi dire m'avoir mis « le pied à l'étrier » dans le monde de la SOFC.

Cette thèse s'est déroulée sur quatre lieux différents, et j'aimerais donc remercier mes collègues (anciens et actuels) et amis des différents instituts dans / avec lesquels j'ai eu la chance de travailler, à savoir EIFER, l'ICT Fraunhofer, l'ICMCB et l'IMN. En particulier, merci à l'équipe de monsieur Vladislav Kolarik, ainsi qu'à Annelise Brüll, Sébastien Fourcade, Laetitia Etienne, Marika Letilly, Messaoud Benamira, Annie Le Gal La Salle et Maria-Teresa Caldes Ricos pour leurs contributions à cette thèse. Merci également à tous les partenaires du projet INNOSOFC pour les discussions et divers apports scientifiques.

Finalement, d'un point de vue plus personnel, cette thèse n'aurait abouti sans le soutien inestimable de mes amis proches et de ma famille. Maman, papa, Claire, Jérôme, Vincent, Silvia, Marc, Raquel, Nadia, Anja, Fran… un grand merci !

Summary

This thesis aimed at assessing the potential of a novel cathode / electrolyte couple for IT-SOFC applications (700°C), through the elaboration and testing of planar anode-supported cells. The materials involved were the perovskite-structured $BaIn_{0.3}Ti_{0.7}O_{2.85}$ (BIT07) electrolyte and the rare earth nickelate $Ln_{2-x}NiO_{4+\delta}$ (LnN, Ln = La, Nd, Pr) cathodes, both materials having shown promising properties in preliminary work done at the IMN and the ICMCB. The first part of this thesis concerned the implementation of a cell elaboration protocol using low-cost and scalable shaping techniques (cell size 3 x 3 cm^2); namely, the Ni / BIT07 anodes were elaborated by tape casting, the BIT07 electrolyte by vacuum slip casting and the cathodes by screen printing. Comparison of electrochemical results for a first and second generation of cells highlighted the usefulness of adding a GDC buffer layer in between the LnN cathodes and the BIT07 electrolyte. The best performance has been obtained for a cell BIT07 / Ni | BIT07 | GDC | PrN, with a power density at 700°C and 0.7 V of 176 mW cm^{-2} for a competitive polarisation resistance of 0.29 Ω cm^2. The main limitation of the performance has been determined to be related to the internal resistance of the test setup, giving anomalously high series resistances. This cell has been successfully operated beyond 500 hours under current, although with a fairly high extrapolated degradation rate of 27% / kh.

Key words: IT-SOFC, BIT07, $Ln_2NiO_{4+\delta}$, tape casting, vacuum slip casting, screen printing, cell testing, electrochemical impedance spectroscopy.

Résumé

Cette thèse vise à évaluer le potentiel d'un nouveau couple cathode / électrolyte pour une application en IT-SOFC (700°C), par le biais de l'élaboration et du test de cellules à anode support de configuration planaire. Les matériaux concernés sont l'électrolyte $BaIn_{0.3}Ti_{0.7}O_{2.85}$ (BIT07), de structure perovskite, et les nickelates de terres rares $Ln_{2-x}NiO_{4+\delta}$ (LnN, Ln = La, Nd, Pr) en tant que cathodes ; ces matériaux ont montré des propriétés prometteuses dans des travaux préliminaires effectués à l'IMN et l'ICMCB. La première partie de cette thèse porte sur la mise en place d'un protocole d'élaboration de cellules complètes utilisant des techniques bas coûts et industrialisables (cellules de taille 3 x 3 cm^2) : l'anode Ni / BIT07 a été élaborée par coulage en bande, l'électrolyte BIT07 par vacuum slip casting et les cathodes par sérigraphie. Les mesures électrochimiques réalisées sur une première génération de cellules ont mis en évidence la nécessité d'ajouter une couche barrière de GDC entre les cathodes LnN et l'électrolyte BIT07. Les meilleures performances ont été obtenues pour une cellule BIT07 / Ni | BIT07 | GDC | PrN, avec une densité de puissance à 700°C et 0.7 V de 176 mW cm^{-2} pour une faible résistance de polarisation de 0. 29 Ω cm^2. La principale limitation des performances a été identifiée comme étant la résistance interne du banc de test, donnant lieu à des valeurs de résistances séries anormalement élevées. Cette cellule a été opérée avec succès durant plus de 500 heures sous courant, avec néanmoins une vitesse de dégradation extrapolée élevée de l'ordre de 27% / kh.

Mots clés : IT-SOFC, BIT07, $Ln_{2-x}NiO_{4+\delta}$, coulage en bande, vacuum slip-casting, sérigraphie, test de cellules, spectroscopie d'impédance complexe.

Intégration de matériaux oxydes innovants dans une IT-SOFC

Les principaux obstacles au déploiement industriel de la technologie SOFC (Solid Oxide Fuel Cell) restent à ce jour des problèmes de fiabilité insuffisante, de longévité et de coûts. Bien qu'une diminution des températures de fonctionnement des SOFCs soit considéré comme une approche pertinente pour lever certains verrous liés aux hautes températures (technologie IT-SOFC pour Intermediate-Temperature SOFC), les performances des piles à combustible à base de matériaux céramiques classiques (zircone stabilisée à l'yttrium (YSZ) comme électrolyte, son cermet correspondant Ni / YSZ comme anode et $La_{1-x}Sr_xMnO_3$ (LSM) comme cathode) sont fortement réduites aux températures intermédiaires. Ainsi, cette dernière décennie a vu l'émergence de matériaux alternatifs, principalement d'électrodes, plus performants dans la gamme de températures intermédiaires.

En ce qui concerne la cathode, les matériaux à conduction mixte ions / électrons ont montré des performances accrues par rapport au matériau standard LSM. À cet égard, une cellule IT-SOFC typique implique l'association de l'électrolyte YSZ avec une cathode de type $La_{1-x}Sr_xCo_{1-y}Fe_yO_{3-\delta}$ (LSCF). Cependant, les contraintes thermomécaniques dues à une importante différence de coefficients de dilatation thermique entre les deux matériaux pourraient conduire à des problèmes tels que l'apparition de fissures ou la délamination de l'électrode lors de l'élaboration de cellules ou lors de cyclages thermiques. De plus, une réactivité chimique se produit entre YSZ et LSCF, conduisant à la formation d'une couche isolante de $SrZrO_3$ à l'interface électrolyte / électrode. Une couche barrière, généralement en GDC (cérine dopée au gadolinium), est donc souvent nécessaire entre les deux phases, ce qui augmente la complexité de l'élaboration des cellules.

En raison de ses bonnes propriétés intrinsèques telles qu'une conductivité ionique élevée (autour de 10^{-2} S cm^{-1} à 700°C) et une bonne stabilité chimique sur une large gamme de pressions partielles d'oxygène et sous CO_2, la phase $BaIn_{0.3}Ti_{0.7}O_{2.85}$ (BIT07) constitue une alternative potentielle à YSZ comme matériau d'électrolyte pour IT-SOFC. En outre, par comparaison avec YSZ qui est de structure fluorine, sa structure perovskite cubique peut offrir une meilleure compatibilité avec les matériaux de cathode usuels, également de structure perovskite (ou dérivée). Par exemple, une réactivité chimique bénéfique se produit entre BIT07 et LSCF, conduisant à la formation d'une solution solide conductrice.

Des matériaux de cathode qui pourraient être associés à BIT07 sont les nickelates de terres rares $Ln_{2-x}NiO_{4+\delta}$ (Ln = La, Nd, Pr), notés LnN, présentant une structure cristalline dérivée de la structure perovskite et des coefficients de dilatation thermique proches de celui de BIT07. Par ailleurs, cette famille de matériaux a montré ses qualités en tant que matériaux conducteurs mixtes, avec des coefficients de diffusion de l'oxygène plus élevés que pour LSCF.

L'objectif de ce travail a été d'associer ces deux matériaux oxydes innovants dans une SOFC à anode support de configuration planaire pour un fonctionnement dans la gamme de température intermédiaire, impliquant des techniques de mise en forme bas-coût et industrialisables. En outre, des poudres industrielles ont été volontairement utilisées dans ce projet.

Parmi les techniques existantes, le coulage en bande a été choisi pour l'élaboration du substrat anodique BIT07 (EMPA) / NiO (JT Baker®) (40 : 60% massique), étant peu onéreux et très répandu dans l'industrie.

Le principal enjeu de ce procédé réside dans la formulation des barbotines et nécessite une sélection rigoureuse et un contrôle précis des additifs utilisés. Dans notre cas, le mélange azéotropique bien connu MEK / éthanol a été utilisé comme solvant, associé à un système de liant standard à base de PVB (Butvar® B-98). Des plastifiants respectueux de l'environnement ont été sélectionnés, avec comme plastifiant de type I le Solusolv® S-2075 et comme plastifiant de type II le PEG400 ; le Nuosperse® FX-4086 a été utilisé comme dispersant.

Dans une première série de formulations, l'influence des conditions de séchage et de la teneur en liant sur le comportement en fissuration des bandes a été étudiée sur la base d'un ratio liant : plastifiants de 2 : 1. La teneur en liant optimale a été déterminée à 6% massique (pourcentage relatif à la masse de poudre). Toutefois, des problèmes de reproductibilité ont été rencontrés. Des essais avec une augmentation du contenu en plastifiants de type I et / ou II pour promouvoir la déformation plastique et le stress qui peut être stocké dans la matrice polymère du liant ont conduit à la détermination d'une recette impliquant un ratio liant : plastifiants proche de 1 : 1. Cette recette a été validée avec des poudres de BIT07 provenant de différents fournisseurs.

Les conditions de pré-frittage optimisées pour les substrats anodiques sont une température de 1150°C pour un temps de pallier de 6 heures, avec une vitesse de chauffage et de refroidissement de 1°C / min. La couche d'électrolyte BIT07 a été déposé par vacuum slip

casting (VSC®) et co-frittée à 1350°C pendant 9 heures (vitesse de montée et descente en température de 1°C / min), résultant en une couche d'électrolyte fine (8 - 10 um), dense, d'épaisseur homogène, et ce de manière reproductible.

Les trois cathodes $La_{1.95}NiO_{4+\delta}$ (LaN), $Nd_{1.97}NiO_{4+\delta}$ (NdN) et $Pr_{1.97}NiO_{4+\delta}$ (PrN) ont été déposées par sérigraphie sur les demi-cellules produites. Une bonne adhérence entre BIT07 et les cathodes LaN et NdN a été obtenue, tandis que PrN s'est facilement délaminée.

La première génération de cellules BIT07 / NiO | BIT07 | LnN (avec Ln = La, Nd, Pr) a été mesurée électro-chimiquement sous balayage d'hydrogène sec à l'anode et d'air à la cathode. La meilleure performance a été obtenue pour la cellule impliquant LaN comme cathode, avec une densité de puissance maximale à 700°C d'environ 80 mW cm^{-2}. Ces performances restent néanmoins bien en deçà des résultats reportés dans la littérature (sur pile bouton) pour le couple BIT07 / $La_{0.58}Sr_{0.4}Co_{0.2}Fe_{0.8}O_{3-\delta}$ (LSCF) (P_{max} = 336 mW cm^{-2}) ou pour le couple YSZ / NdN (P_{max}> 500 mW cm^{-2}) à la même température. Des valeurs de résistance série anormalement élevées (R_s) (> 1 Ω cm^2) ainsi que des résistances de polarisation (R_p) également élevées ont été mesurées. De telles valeurs de R_s ont été attribuées à la résistance interne du banc de test.

Par ailleurs, les valeurs d'OCV (Open Circuit Voltage) mesurées à 700°C apparaissent systématiquement faibles (< 0,9 V pour une valeur théorique au-dessus de 1,2 V). Les deux principales hypothèses formulées pour expliquer ce phénomène sont tout d'abord la présence de défauts microscopiques dans les couches d'électrolyte tels que des fissures, observées par microscopie électronique à balayage, et / ou une contribution électronique à la conductivité totale de BIT07. Des mesures d'impédance effectuées sur des pastilles denses de BIT07 pour trois lots différents de poudre ont montré une légère mais systématique diminution de la conductivité de la phase avec la p_{O_2}. Bien que les résultats semblent fortement dépendants des étapes de conditionnement de la poudre, ils semblent indiquer une faible conductivité électronique de type p de BIT07 sous atmosphère oxydante.

Les résultats obtenus pour cette série de tests ont mis en évidence des performances insuffisantes des assemblages BIT07 / LnN ; cette conclusion a conduit à la conception d'une deuxième génération de cellules impliquant des optimisations architecturales.

Pour améliorer la qualité de l'interface cathode / électrolyte, l'ajout d'une fine (2 - 3 um) couche barrière de $Ce_{0.9}Gd_{0.1}O_{2-\delta}$ (GDC) entre BIT07 et les trois nickelates a été étudié. Les

couches ont été déposées par sérigraphie sur demi-cellules et frittées à 1350°C pendant 2 heures. Les cathodes ont été ensuite sérigraphiées et frittées à 1170°C pendant 1 heure.

Pour les trois cathodes, une amélioration significative des performances a été observée avec l'ajout d'une couche barrière de GDC. Des valeurs plus élevées d'OCV ont été obtenues, ce qui peut s'expliquer soit par un remplissage (au moins partiel) des fissures présentes dans la couche d'électrolyte par la couche de GDC soit par un effet de blocage des électrons, GDC étant conducteur purement ionique sous air. Les meilleures performances ont été obtenues pour une cellule BIT07 / Ni | BIT07 | GDC | PrN, avec une densité de puissance maximale de 200 mW cm^{-2} à 700 ° C. Une faible résistance de polarisation (0,29 Ω cm^2) a été obtenue pour cette cellule, ce qui correspond à une amélioration d'un facteur 4 par rapport à la cellule sans couche barrière. Ces résultats sont prometteurs, en particulier comparés à ceux obtenus avec une cellule impliquant la cathode LSCF (R_p = 0,35 Ω cm^2). La majeure limitation des performances des cellules paraît être les valeurs anormalement élevées des résistances séries.

Ainsi, il apparaît que, comme pour le couple YSZ / LSCF, une couche barrière de GDC soit nécessaire, et ce contrairement à l'attente initiale qui était que l'ajout de cette couche pouvait être évité en associant des matériaux de structures cristallines analogues. Néanmoins, l'avantage de diminuer certaines contraintes thermomécaniques par l'association de matériaux aux coefficients de dilatation thermique proches persiste.

Cette deuxième génération de cellules à base de BIT07 a été mesurée en mode galvanostatique à 0,7 V (I = 248 mA cm^{-2}) pendant plus de 500 heures, avec un taux de dégradation moyen extrapolé assez élevé de 27% / kh. Bien que plusieurs hypothèses aient été avancées pour expliquer cette dégradation, d'autres expériences sont encore nécessaires pour une meilleure compréhension des phénomènes de vieillissement impliqués.

D'autres tentatives d'améliorations de l'architecture des cellules ont été réalisées côté anode via l'ajout de couches d'anodes fonctionnelles BIT07 (MT2) / NiO et BLITiMn (EMPA) / NiO (44: 66% massique), déposées par vacuum slip casting. Concernant BIT07 / NiO, une couche fonctionnelle fine (6 µm) et relativement dense a été obtenue, composée de grains plus fins. Les résultats électrochimiques préliminaires ne montrent cependant aucune amélioration, en raison d'une R_s élevée associée à une dégradation rapide des performances de la cellule. Des analyses post-test sur cette cellule n'ont pas révélé de défaillance expliquant ce phénomène, et la reproductibilité des résultats doit encore être évaluée avant de pouvoir conclure. La couche fonctionnelle BLITiMn / NiO s'est avérée plus épaisse (18 µm), assez poreuse (porosité supérieure à 45% après réduction), et l'interface entre l'anode et les couches d'électrolyte est

apparue détériorée. Les performances ont également été fortement réduites par l'ajout de cette couche, avec une augmentation importante de R_s et R_p.

Par ailleurs, un autre essai a consisté en l'augmentation de la porosité des substrats anodiques par l'ajout d'un agent porogène. Du gel d'amidon a été sélectionné et utilisé dans les formulations de barbotines. Des bandes sans cracks et de bonne qualité contenant 2 et 4% massique de gel d'amidon ont été obtenues (BIT07 lot MT1) en modifiant la recette standard (teneur en liant plus élevée). La porosité des substrats a augmenté de 8% à 25% (avant réduction) lors de l'ajout de 4% massique de porogène. Toutefois, aucune cellule complète n'a pu être obtenue avec des anodes contenant du porogène à cause de la déformation des substrats anodiques pendant l'étape de pré-frittage.

Enfin, une augmentation de taille a été réalisée avec succès à l'échelle du substrat anodique, avec une augmentation du volume des barbotines et l'obtention de substrats de taille 11,4 × 11,4 cm^2 après pré-frittage. Les substrats obtenus ont toutefois cassé lors de l'étape de dépôt de l'électrolyte par vacuum slip casting en raison d'une planéité non parfaite couplée à une tenue mécanique insuffisante. Des résultats préliminaires prometteurs ont été obtenus pour des demi-cellules de plus petite taille (4 × 4 cm^2) produites par sérigraphie de la couche d'électrolyte directement sur les bandes crues, évitant ainsi le problème de casse des substrats pré-frittés.

Table of contents

List of abbreviations

µ-CHP	Micro-Combined Heat and Power
AC	Alternative Current
ADEME	Agence du Développement et de le Maîtrise de l'Energie
AES	Auger Electron Spectroscopy
AFC	Alkaline Fuel Cell
APU	Auxiliary Power Unit
ASR	Area Specific Resistance
BIMEVOX	γ-bismuth vanadate γ-$Bi_4V_2O_{11}$
BIT07	$BaIn_{0.3}Ti_{0.7}O_{2.85}$
BLITiMn	$Ba_{0.5}La_{0.5}In_{0.3}Ti_{0.1}Mn_{0.6}O_{3-\delta}$
BSCF	$Ba_{1-x}Sr_xCo_{1-y}Fe_yO_{3-\delta}$
BSE	Backscattered electrons
CEA	Commissariat à l'Energie Atomique et aux énergies alternatives
CHIC	Clean Hydrogen In European Cities
CHP	Combined Heat and Power
CPE	Constant Phase Element
CVD / EVD	Chemical Vapour Deposition or Electrochemical Vapour Deposition
DC	Direct Current
DMFC	Direct Methanol Fuel Cell
EDF	Electricité de France
EDX / EDS	Energy Dispersive X-ray Spectroscopy
EIFER	European Institute for Energy Research
EIS	Electrochemical Impedance Spectroscopy
GDC	Gadolinia-Doped Ceria
ICMCB	Institut de la Chimie de la Matière Condensée de Bordeaux
IEA	International Energy Agency
IMN	Institut des Matériaux de Nantes
INNOSOFC	Intégration de matériaux d'électrolyte et d'électrodes innovants dans une cellule IT-SOFC
IT	Intermediate Temperature
LALLS	Low Angle Laser Light Scattering
LAMOX	Materials based on the $La_2Mo_2O_9$ parent compound
LaN	$La_{1.95}NiO_{4+\delta}$
LOM	Laminated Object Manufacturing
LSC	$La_{1-x}Sr_xCoO_{3-\delta}$
LSCF	$La_{1-x}Sr_xCo_{1-y}Fe_yO_{3-\delta}$
LSF	$La_{1-x}Sr_xFeO_3$

LSGM	Lanthanum gallate materials $La_{1-x}Sr_xGa_{1-y}Mg_yO_{3-\delta}$
LSM	$La_{1-x}Sr_xMnO_3$
MCFC	Molten Carbonate Fuel Cell
MEK	Methyl ethyl ketone
MFC	Mass Flow Controller
MIEC	Mixed Ionic Electronic Conductor
MTx	Different batches of BIT07 supplied by Marion Technologies
NdN	$Nd_{1.97}NiO_{4+\delta}$
OCV	Open Circuit Voltage
$P_{(0.7V)}$	Power density at 0.7 V
PA-CVD	Pressure-Assisted Chemical Vapour Deposition
PAFC	Phosphoric Acid Fuel Cell
PCFC	Proton Conducting Fuel Cell
PEG	Poly (ethylene glycol)
PEMFC	Proton Exchange Membrane Fuel Cell
P_{max}	Maximal power density
PrN	$Pr_{1.97}NiO_{4+\delta}$
PVB	Polyvinylbutyral
PVD	Physical Vapour Deposition
RP	Ruddlesden-Popper
RT	Room Temperature
ScSZ	Scandia Stabilised Zirconia
SDC	Samaria-Doped Ceria
SE	Secondary Electron
SEM	Scanning Electron Microscopy
SOFC	Solid Oxide Fuel Cell
TEC	Thermal Expansion Coefficient
TGA	Thermogravimetric analysis
TPB	Triple Phase Boundary
VSC®	Vacuum Slip Casting
XPS	X-rays Photoelectron Spectroscopy
XRD	X-ray Diffraction
YSZ	Yttria Stabilised Zirconia

List of symbols

$\Delta G°$	Free energy change
a, b, c, α, β, χ	Lattice parameters
$ASR_{(I-V)}$	Area Specific Resistance determined from the slope of an I-V curve around the operating point 0.7 V
C	Capacity
C_{eq}	Equivalent capacity
D*	Oxygen diffusion coefficient
d_{50}	Medium value of particle diameter
d_{hkl}	Interplanar spacing
E / E_{th}	Nernst potential
E°	Electromotive force at standard pressure
E_{obs}	Measured Open Circuit Voltage
F	Faraday constant
f	Frequency
f_{summit}	Summit frequency
η**(i)**	Polarisation or overpotential
$h^{\bullet}$	Kröger-Vink notation for an electron hole
h, k, l	Miller indices
I	Current
L	Inductance
O_o^x	Kröger-Vink notation for an oxygen ion sitting on an oxygen lattice site, with neutral charge
$P_{(0.7V)}$	Power density at 0.7 V
p^a_{H2}	Partial pressure of H_2 in the anode gas
p^a_{H2O}	Partial pressures of H_2O in the anode gas
P^c_{O2}	Partial pressure of the oxygen in the cathode gas
P_{max}	Maximal power density
p_{O2}	Partial pressure of oxygen
R	Gas constant
R	resistance
R_p	Polarisation Resistance
R_s	Series Resistance
R_{tot}	Total Resistance
$\sigma_{electric}$	Electrical conductivity
σ_{ionic}	Ionic conductivity
σ_{tot}	Total conductivity

τ	Time constant
T_g	Glass transition temperature
V	Potential
$V_o^{\cdot\cdot}$	Kröger-Vink notation for a vacancy on the oxygen site
ω	Pulsation
Y_0	Admittance
Z	Impedance

Chapter I

General introduction

1. *Energetic context*

Nowadays, main conventional power generation technologies rely on fossil fuels. Population growth and increased standards of living led to an overall rise in the energy consumption in the last decades (as can be seen in *Fig. I-1*), being faced with problems of fossil resources depletion. For instance, according to the BP statistical review of world energy 2012 [1], lifetime of oil, gas and coal reserves are estimated to be around 55, 65 and several hundred years, respectively, in a "business-as-usual" scenario [2].

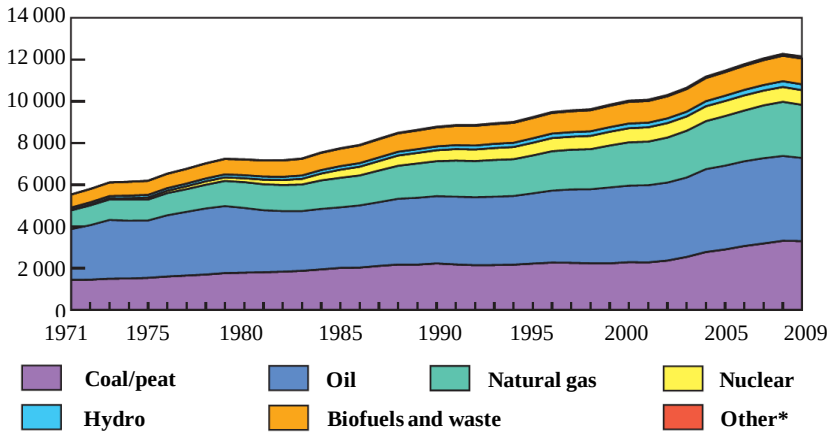

Figure I-1: World total primary energy supply from 1971 to 2009 by fuel (Mtoe) [3].
** Other includes geothermal, solar, wind, heat, etc.*

In most of the actual energy systems, based on internal combustion engines, more than 60% of the energy input is wasted. To conserve resources and increase the lifetime of the fossil fuels, efficiency improvements should be at the forefront of the efforts.

In addition, environmental issues stemming from the use of internal combustion engines have also been addressed. Indeed, combustion of fossil fuels is known to generate soot, sulphur compounds and other noxious emissions, well recognised as major contributors to the

global warming and local air pollution [4]. For instance, atmospheric concentration of CO_2 has grown from around 300 ppm in 1958 to above 390 ppm today [5], the main contribution coming from the electric power generation sector, relying extensively on coal, followed by transport and industry [2].

Major efforts are therefore needed towards a more efficient and environmentally benign use of the valuable fossil resources, but also towards alternative (renewable) energy sources.

Originating from the 1973 oil crisis, energy security concerns prompted investments for the development of alternative sources. Thus, both nuclear and renewable energies were developed, representing 5.8% and around 13.3% (0.8% from alternative energy sources as wind, solar or geothermal) of the global energy supply in 2009, respectively, according to the IEA (International Energy Agency) [3]. However, concerns about waste, safety and security have still to be addressed before a further increase of the proportion of nuclear in the energy mix, and renewables are usually characterised by their large intermittency or interruptability, making further expansion relying on substantial improvements in storage technologies. Problems of cost, if not of their environmental impact in some cases, are also limiting factors [2].

In this context, fuel cell systems are attracting a great interest worldwide for a rapid emerging "energy technology" for the efficient conversion of fossil resources, but also for playing a substantial role in the sustainability of the energy sources in association with hydrogen. Following efforts of several big industrial groups and automobile builders, fuel cells are now on the verge of a commercialisation [6].

In this chapter, the different technologies of fuel cells will be briefly described, with a concern on their potential / already existing applications. Solid Oxide Fuel Cells (SOFCs) will then be highlighted, with a description of their working principle, their different configurations, designs and fabrication processes. Finally, a state-of-the-art of the materials used for the different core cell components will be presented.

2. Generalities about fuel cells

2.1. Fuel cell as an efficient energy conversion technology

Fuel cells are devices that convert the chemical energy of a fuel directly into electrical energy. A cell consists of two electrodes (the anode and cathode) separated by an electrolyte. As can be seen in *Fig. I-2*, fuel (say hydrogen) is fed to the anode where it is oxidised and the

produced electrons are released to an external circuit. An oxidant (oxygen from air typically) is reduced at the cathode side. The electron flow (from the anode to the cathode) through the external circuit produces direct-current electricity. The electrolyte conducts ions between the two electrodes.

In practice, to build voltages, a fuel cell is constituted by a large number of these units to form stacks, electrically connected by interconnectors that allow the circulation of the current.

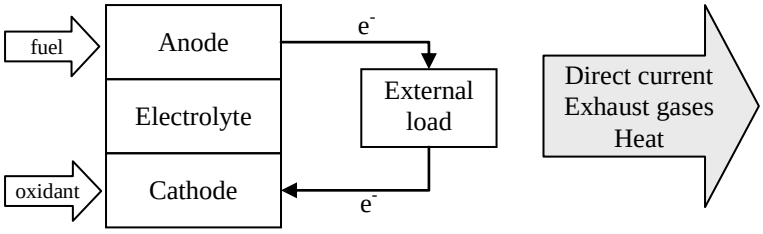

Figure I-2: Schematic diagram of fuel cell operation [7].

Fuel cells constitute a potential alternative energy conversion technology to the traditional power generation systems: they combine the advantages of both combustion engines and batteries. Indeed, they can operate continuously as long as fuel is available, with characteristics comparable to batteries under load conditions [8-9]. Fuel cell systems perform with the highest efficiencies compared to conventional distributed energy systems, and offer unique operational characteristics such as low emissions, low noise, off-grid capability, scalability and reliable power generation to almost any device requiring electrical power [6, 8, 10-12]. They compete to replace a range of power supplies in many portable, stationary and transport applications, from battery chargers to power plants or power-to-cars, making them unique in terms of the variety of their potential applications [11].

2.2. Types of fuel cells

In practice, fuel cells can operate in a wide range of temperatures (50 - 1000°C) depending on the nature of their electrolyte, and are usually classified regarding this component.

Five major fuel cell technologies can be differentiated: the Proton Exchange Membrane Fuel Cell (PEMFC), the Alkaline Fuel Cell (AFC), the Phosphoric Acid Fuel Cell (PAFC), the Molten Carbonate Fuel Cell (MCFC) and the Solid Oxide Fuel Cell (SOFC). All kind of fuel cells share the potential of high electrical efficiency and reduced emissions, having however

unique characteristics linked to their different constituting materials and operating temperatures.

A comparison of these major fuel cells in terms of components, fuels, capacities, costs, applications, advantages and drawbacks is shown in *Table I-1*.

Table I-1:
Comparison of the different types of fuel cells [8, 10, 13].

Type	PEMFC	AFC	PAFC	MCFC	SOFC
Electrolyte	Solid polymer membrane (Nafion)	Liquid solution of KOH	Phosphoric acid (H_3PO_4)	Liquid solution of lithium, sodium, and/or potassium carbonates, soaked in a matrix	Solid oxide electrolyte (ZrO_2 stabilised with Y_2O_3)
Operating temperature	50 - 100°C	50 - 200°C	~ 200°C	600 - 700°C	600 - 1000°C
Charge carrier	H^+	OH^-	H^+	CO_3^{2-}	O^{2-}
Fuel	Pure H_2	Pure H_2	Pure H_2	H_2, CO, hydrocarbons	H_2, CO, hydrocarbons
Efficiency	35 - 60%	~ 50%	40%	45 - 50%	> 50%
Power density (W cm^{-2})	1.1	1	1.1	0.7-1	0.8-1
Typical systems size	< 1 kW - 100 kW	10 - 100 kW	100 kW - 400 kW	300 kW - 3 MW	1 kW - 2 MW
Applications	Portable power backup power transportation distributed generation	Military; space; portable power	Transportation; commercial cogeneration; portable power	Transportation; utility power plants, distributed generation	Residential; utility power plants; commercial cogeneration; portable power
Advantages	High power density; quick start up; solid non-corrosive electrolyte	High power density; quick start up, low cost components	Heat waste; stable electrolyte characteristics	High efficiency; fuel and catalyst flexibility; heat waste	Solid electrolyte; high efficiency; fuel and catalyst flexibility; generate high grade waste heat
Drawbacks	Expensive Pt catalyst; sensitive to fuel impurities	Expensive platinum catalyst; sensitive to CO_2 in fuel and air; electrolyte management	Expensive Pt catalyst; Corrosive liquid electrolyte; sensitive to fuel impurities; long start up time	High cost; corrosive liquid electrolyte; high temperature corrosion; slow start up; intolerance to sulphur	High cost; high temperature corrosion; slow start up; intolerance to sulphur

One can also mention the Direct Methanol Fuel Cell (DMFC), belonging to the PEMFC technology, and the Proton Conducting Fuel Cell (PCFC), belonging to the SOFCs. In PCFCs however the charge carrier is a proton and the water is produced at the cathode.

Advantages and disadvantages provided are different depending on the kind of fuel cell and are related to their operating temperatures (linked with the nature of their electrolyte), having direct consequences on the trends for their respective commercial applications (*Fig. I-3*).

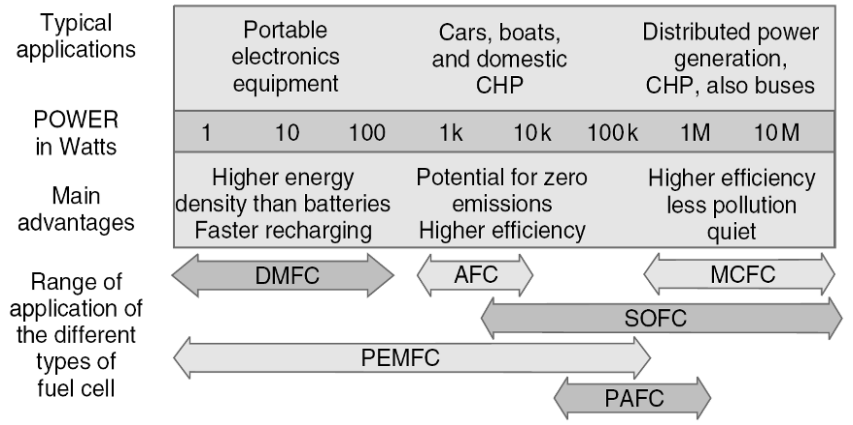

Figure I-3 : Chart for the foreseen applications of the different kinds of fuel cells (CHP = combined heat and power) [14]**.**

Low temperature fuel cells (PEMFC, AFC) can be characterised by their rapid start-up and are thus competitive in mobile applications. However, they need a good quality of hydrogen supply with a low CO content in the fuel. On the contrary, thanks to their high operating temperatures, fuel cells as SOFC and MCFC are able to operate on fuels containing large fractions of carbon monoxide, and can thus run either with an external or internal reformer without extensive gas cleaning. In addition, waste heat can be recycled to co-generate additional electricity, with systems reaching total efficiencies up to 85%.

2.3. Market applications: some examples

Fuel cells are commercially available today for power generation with sizes ranging from < 1 kW to several MW. These systems have achieved billions of kWh of successful operation at customer sites worldwide [12]: thousands of residential and commercial CHP (Combined Heat and Power) units installed in Japan, hundreds of PAFC and MCFC installed for large-scale CHP applications, and thousands of fuel cells providing back-up power for radio and telecom sites around the world [15].

Among all the fuel cell technologies, the PAFCs were the first to be commercialised [6, 14], with CHP systems up to 500 kW commercially available (suppliers as UTC Power with the PureCell® systems, with 300 units installed [14, 16-17], or the FP-100i modules from Fuji electric). Also, prototypes up to 11 MW are under test [10].

Regarding commercial success, the leader by far in terms of number of units is the PEMFC technology. For example, Ballard power systems Inc. is now commercialising the CLEARgen™, a 1 MW PEMFC-based system running with hydrogen, for distributed generation [18]. PEMs are also widely developed for automotive applications: for example the Clean Hydrogen In European Cities (CHIC) project, started in 2010, is the largest international trial of hybrid fuel cell buses. This project is collecting data from over 60 buses deployment around the world and involves the implementation of 26 additional buses in five locations across Europe [19]. Automotive constructors such as Daimler, Honda, Toyota or Opel are already releasing fuel cell-powered vehicles, with tens of thousands units expected to be on the roads by 2015 [11]. So far, there are approximately 200 hydrogen refuelling stations worldwide (~ 70 being publically accessible, as the one in Frankfurt shown in *Fig. I-4*). The objective in this area is to hit the market by 2015 and to penetrate it significantly by 2020, with 500 000 fuel cells powered electric vehicles and more than 1000 hydrogen filling stations available in Europe forecasted [20].

Figure I-4: Frankfurt hydrogen filling station, available as a bi-product from a chlorine electrolysis plant and transported via a high pressure 1.7 km long transport line to the fuelling service station [19].

The second most significant type of fuel cell is the DMFC, mainly found in the portable sector apart from some niche transport sectors (especially related to military applications). For

example, Toshiba launched in 2009 its Dynario fuel cell battery charger (*Fig. I-5*) with an initial production run of 3000 units, far outstripped by the demand [11, 21]. Other DMFC suppliers are Oorja in the U.S. or SFC Energy in Germany [15].

Figure I-5: Toshiba's DMFC as external power for mobile applications [21]**.**

FuelCell Energy is a MCFC manufacturer, with for example their 2.8 MW system DFC3000^{TM} running on natural gas, also commercially available [22]. POSCO Energy has also achieved the production of 100 MW MCFC units in 2011, with already 62 MW under operation since 2008 and 58.8 MW planned to be installed in Gyeongki, Korea, in 2012 [23].

SOFC technology is also attracting interest for a lot of industrial groups and R&D centres. Its lower maturity level compared to other fuel cell technologies due to several technical hurdles does not prevent SOFCs to be commercialised and demonstrated worldwide in different sectors. For residential applications, we can cite for example the 100 kW SOFC system running on natural gas or biogas, produced by Bloomenergy, with clients as Walmart, Google, eBay or Coca-Cola [24]. Panasonic started in May 2009 the commercialisation of the 700 W ENE-FARM systems running with natural gas, with 1000 units installed (from October 2011) [25]. Hexis is now demonstrating more than 100 natural gas-fuelled 1 kW Galileo 1000N systems (*Fig. I-6*) through the CALLUX project, and is planning to start commercialisation in 2013 [26-27].

Figure I-6: Galileo 1000N system [28]**.**

Note that the CALLUX project, started in 2008, achieved a million of hours of operation in june 2012, with 300 units (PEMFCs and SOFCs) installed in Germany at the end of the year 2012 [26, 29-30]. Delphi is also releasing 5 kW SOFC-based auxiliary power units (APUs) for a wide range of fuels (natural gas, diesel, bio-diesel, propane, gasoline, coal-derived fuel and military logistics fuel) and residential and transportation applications [31]. The BlueGen® 2 kW µ-CHP system running on natural gas is also released by Ceramic Fuel Cells Limited (CFCL), with over 150 Bluegen® and integrated systems installed to date [32-33].

3. Solid Oxide Fuel Cells (SOFC)

3.1. Working principle

An SOFC unit cell is composed of three parts: the solid electrolyte which separates oxygen and fuel to avoid direct combustion, the anode and the cathode where both electrochemical reactions are located. Oxygen (from air) is reduced at the cathode (equation 1); the O^{2-} anions are transported through the electrolyte and oxidise the fuel at the anode (Eq. 2 in the case of H_2 as a fuel), with water (steam) as a product of the overall reaction (Eq. 3 in the case of H_2 as a fuel).

$\frac{1}{2} O_2 + 2 e^- \rightarrow O^{2-}$	Cathode: reduction of the oxygen	**(1)**
$H_2 + O^{2-} \rightarrow H_2O + 2 e^-$	Anode: oxidation of the hydrogen	**(2)**
$H_2 + \frac{1}{2} O_2 \rightarrow H_2O$	Overall reaction	**(3)**

Under open circuit conditions, with electrochemical potential of oxide ions equilibrated across the oxide-ions conducting electrolyte, a voltage difference appears between the cathode and the anode. The Nernst potential, E, is the Open Circuit Voltage or OCV and is given in terms of the various partial pressures as follows (Eq. 4) [34]:

$$E = -\frac{\Delta G^\circ}{2F} - \frac{RT}{2F}\ln\frac{p_{H2O}^{a}}{p_{H_2}^{a}\,p_{O_2}^{c\,1/2}} = E^\circ + \frac{RT}{4F}\ln\frac{p_{O_2}^{c}\,p_{H_2}^{a\,2}}{p_{H2O}^{a\,2}} \qquad \textbf{(4)}$$

with ΔG° the net free energy change, the electromotive force at standard pressure and operating temperature E°, the gas constant R, the Faraday constant F, the absolute temperature T, the partial pressure of the oxygen in the cathode gas $p_{O_2}^{c}$, $p_{H_2}^{a}$ and p_{H2O}^{a} the partial pressures of H_2 and H_2O in the anode gas, respectively. As evidenced by the equation (4), the driving force of a SOFC is the difference of oxygen partial pressure between the anodic and the cathodic sides.

The Nernst potential gives the ideal open circuit cell potential. This potential sets the upper limit or maximum performance achievable by a fuel cell. In the case of an ideal cell (i.e. when the electrochemical processes are infinitely fast and for a 100% fuel utilisation), the potential of the electrodes would remain unchanged regardless of the current density. However, in practice, the fuel that is fed to a fuel cell is typically not completely converted, and a real cell exhibits large kinetic losses (overpotentials, polarisations or voltage losses) increasing with the current density, as can be seen *Fig. I-7* [34].

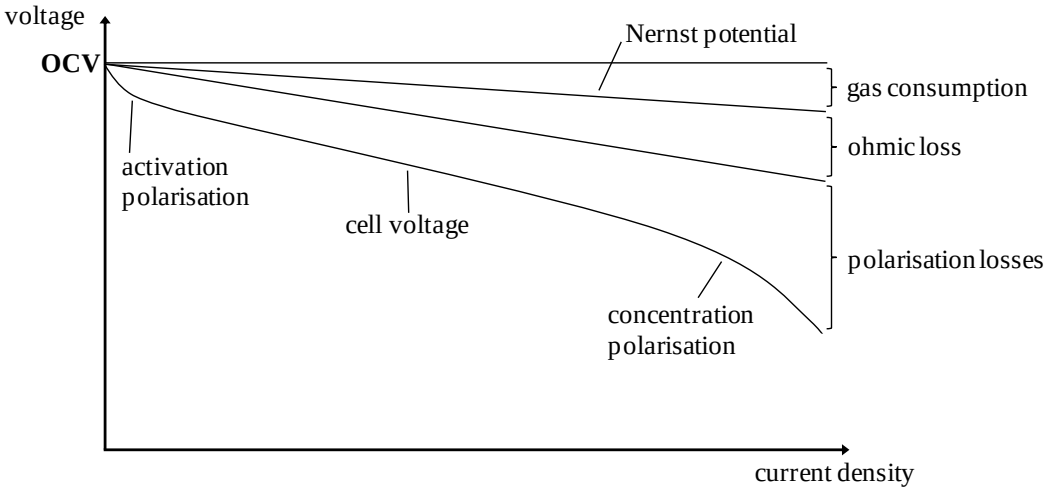

Figure I-7: Current-voltage characteristics of a cell [34].

The voltage loss term $\eta(i)$ includes ohmic loss and polarisation or overpotential and refers to a number of terms with origins related to different phenomena occurring in the cell. The ohmic loss originates from the resistance to electronic and ionic flows in a material, and is generally dominated by the electrolyte resistance considering its low ionic conductivity. Concentration polarisation stems from the resistance to mass transport through the electrodes and interfaces and activation polarisation is the voltage drop due to the slow kinetics of the charge transfer reactions occurring at the electrodes / electrolyte interfaces [34]. The overpotentials of the cathode and the anode η_c and η_a, respectively, depend on the material properties (composition), the microstructure and the temperature (though the contribution of the cathode to the overall losses is usually larger).

The aim of the fundamental and applied research is to decrease these overpotentials.

3.2. Configuration and fabrication of SOFCs

Because the electrolyte is solid, various shapes are available and thus many designs have been devised over the years [9, 35]. With pressed discs or thimbles starting in the 1930s, most development has focused on planar and tubular designs since the 1960s, and other geometries became less popular. Both designs with their advantages and disadvantages have been widely studied and discussed [35] and will be here briefly described, as well as industrial conventional cell fabrication processes.

3.2.1 *Tubular SOFC design*

Pioneered by US Westinghouse Electric Corporation (now Siemens Westinghouse Power Corporation or SWPC) in the late 1970s [14], the main advantages of tubular cells are higher mechanical and thermal stability and simpler sealing requirements [35]. Indeed, in the most common tubular design, the cell components are deposited in the form of thin layers on a cylindrical tube, sealed only at one end. Fuel flows along the outside of the tube, towards the open end, and air is fed through a thin alumina air supply tube located centrally inside each tubular cell, as can be seen in *Fig. I-8*.

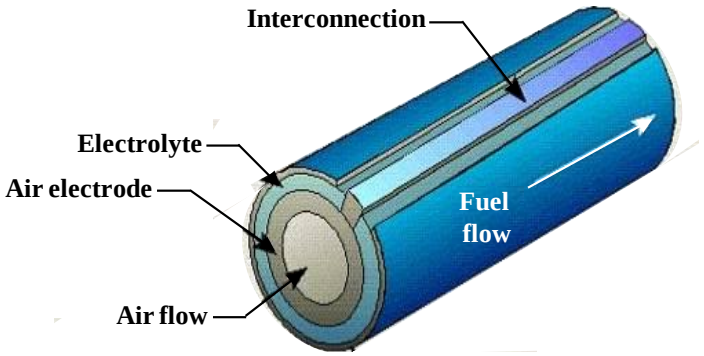

Figure I-8: Tubular design of Siemens Westinghouse [36].

In the latest design from Siemens Westinghouse, a cathode tube of 1 - 2 cm diameter is fabricated by extrusion (see section *2.2.3.*) and sintered; an electrolyte layer (ca. 40 µm thick) is usually deposited by Electrochemical Vapor Deposition (EVD, see section *2.2.3.*); an anode layer (ca. 100 µm thick) is deposited either by slurry application and / or EVD and the interconnect material is deposited by plasma spraying along the length of the cell [35, 37-38]. Cells with a length of 150 cm with an electrochemically active area of 1036 cm² can be thereby mass produced [35, 38]. Such tubular cells made with the state-of the art materials (lanthanum strontium manganese cathode, yttria stabilised zirconia electrolyte and nickel / yttria stabilised zirconia anode, see section *2.3*) are reaching power densities of about 0.20 - 0.30 W cm^{-2} at 1000°C [37-38].

These relatively low power densities are the result of the long path way for the current through each cell [14, 38]; the large voids within the stack structure (tubes) lead also to low volumetric power densities [14]. Thus, a decrease of the tube diameters down to 2 - 3 mm, so called microtubular SOFC, shortens the electrical paths, allowing higher power densities per volume unit as well as very high thermo-mechanical stability [38-39]. As alternative design, Siemens proposed the use of flat-tubes to decrease the costs, giving better compactness and increasing the contact areas between the cells [14]. Also, a tubular cell concept is pursued by Mitsubishi Heavy Industries, being an arrangement of multiple cells connected in series on one tube [38].

Another major disadvantage of the tubular design is the difficulty to reach competitive costs, caused by the design specific manufacturing technique: the EVD technique is complex, capital-cost intensive and requires vacuum equipment that hinders upscale to a cost effective and continuous manufacturing. Other techniques such as plasma spraying or slurry coating are investigated, and should lead to a substantial reduction of the costs [35].

3.2.2 *Planar SOFC design*

A planar SOFC enables simple series electrical connections of cell components configured as flat plates (*Fig. I-9*), avoiding the long current path occurring through tubular cells [14]. The cells are stacked between bipolar plates, decreasing ohmic losses and increasing the power densities of the cells (up to about 2 W cm^{-2} at 800°C [35, 37]) and thus the performance of the stacks. Besides, the planar configuration allows the use of cost-effective fabrication techniques, as tape casting or screen printing. Another important advantage of the planar configuration is the possibility of easily processing thin electrolyte layers, making the ohmic losses comparable with the other types of fuel cells [14].

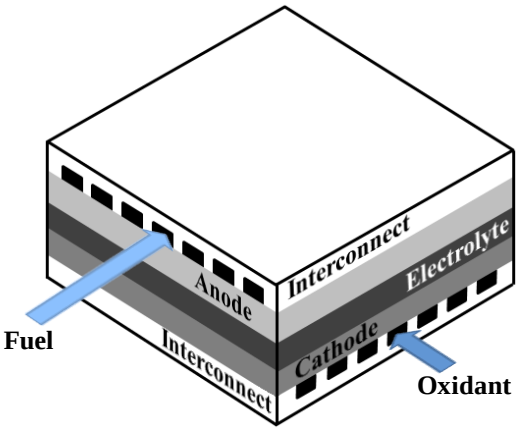

Figure I-9: Planar SOFC design [40].

Planar SOFCs can be classified into three main configurations: electrode-supported, electrolyte-supported or metal (interconnect)-supported. One can notice a better mechanical strength for electrolyte-supported configurations, whereas anode supported cells offer the potential to decrease electrolyte thicknesses below 10 µm, reducing ohmic losses and thus increasing the performance.

Advances in ceramic technology (tailoring of powder, fabrication processes...) have contributed to the increased interest for planar SOFCs starting from the 1980s [35]. However, in this configuration, gas-tight sealing materials are needed. The thermal stresses at the interfaces between the cells and the different stack components (interconnects and sealants) cause important mechanical degradation. Both issues of thermal stresses and wish to fabricate very thin components place a major constraint on the up-scaling [14].

3.2.3 *Industrial shaping techniques*

The fabrication processes for SOFCs can be distinguished in different ways. For instance, one can mention the following:

- the design (planar, tubular)
- the mechanical support (anode, electrolyte, cathode or metallic support)
- the thickness of the component or layer
- the elaboration of a substrate or a functional layer (coating).

In what follows, the separation will be made between substrate elaboration and coating technologies.

a) Substrate elaboration technologies

- Tape casting

In 1947, Glenn Howatt reported the process known today as tape casting (sometimes also called doctor-blading or knife-coating) and patented it in 1952. This technique is a basic fabrication process used for the elaboration of thin (down to 3 μm), two-dimensional films from any material that can be produced as a powder, with applications in many industries including food, electronic, paper, plastic and paint manufacturing [41]. This technique can also be used for manufacturing three-dimensional objects by the technique called LOM (laminated object manufacturing). Its application in the ceramic processing area gives the advantage to form large area, thin and flat ceramic or metallic parts.

Tape casting is a fluid forming process consisting in formulating a slip (named slurry) with powders (ceramic and / or metal), solvents and organic additives. The casting is industrially done by placing the slip into a reservoir open in the bottom side; a polymeric tape is transported bellow the reservoir and the slip covers the transport tape, as can be seen *Fig. I-10*. The thickness is being controlled by passing the transport tape and the coated slip through a doctor blade. The obtained layer (or tape) is dried to remove the solvents and the resulting green tape is then removed from the support and sintered to form a ceramic or metallic layer.

For SOFCs, it is used mainly for the fabrication of the mechanical support in planar design. For almost all the anode-supported cells and for the electrolyte-supported cells, the substrate is now manufactured by tape casting, due to the low-cost, easy to use and continuity of the process, allowing additionally the manufacture of large areas and flat sheets of desired thicknesses and microstructures [43].

A more detailed description of the process can be found in *Chapter II*.

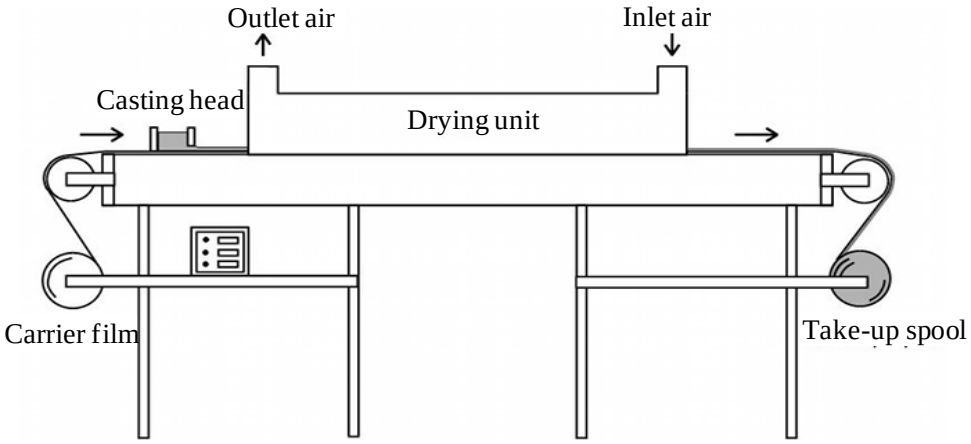

Figure I-10: Schematic of an industrial tape-caster [42].

- Pressing methods

Another technique to form two (three)-dimensional objects is to press the powders by cold, warm, hot, cold isostatic or hot isostatic pressing. For this, the powder is filled into a pressing unit or die and shaped by pressing (see *Fig. I-11*). This process can be done at different temperatures and pressures (uniaxial, isostatic…) and can eventually involve the use of additional polymeric resin.

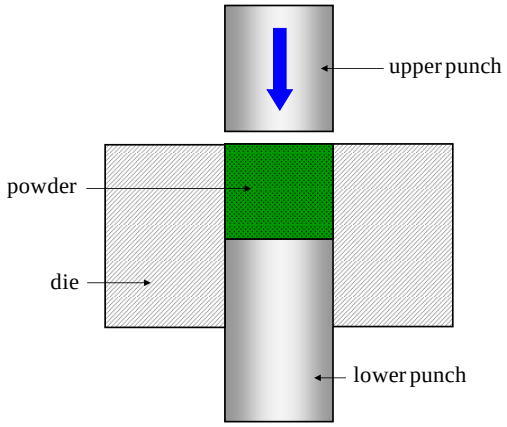

Figure I-11: Schematic illustration of the uni-axial die pressing process.

Uniaxial pressing in a die and isostatic pressing are commonly used for the compaction of dry powders in the ceramic industry, allowing the formation of simple shapes rapidly and

with accurate dimensions [44]. The main disadvantage of the pressing techniques, compared for example with tape casting, is that they operate discontinuously [45]. This is thus time-consuming and therefore less frequently used for SOFC substrate manufacturing but rather in the ceramic industry for the elaboration of smaller geometries with complex structures. However, pressing techniques (cold and warm pressing) are applied for SOFCs manufacturing in some cases for instance if thicker substrates (i.e. thicknesses > 800 µm) are needed.

- Extrusion

For extrusion, the powders are usually mixed with water-based plastics to form high viscosity slips, pushed or drawn through a die of desired cross-section [44]. This technique is low cost and continuous, allowing high production volumes from many types of raw materials. The process is illustrated in *Fig. I-12*.

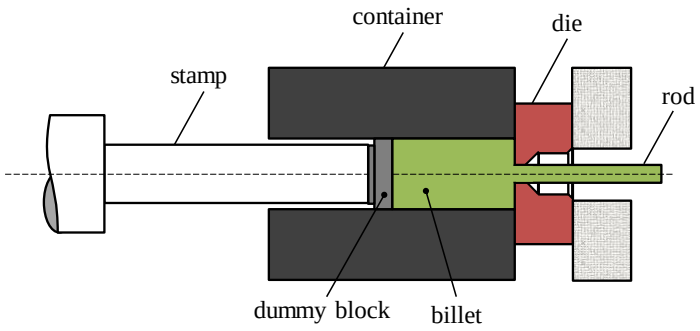

Figure I-12: Schematic illustration of direct extrusion [46].

Extrusion is used in the ceramic industry if a continuous structure with a one direction elongation is needed, as for example the cathode supported tubular SOFCs developed by Siemens mentioned earlier. While its use in planar design presents limited advantages due to limitations in the substrate width / thickness ratio, extrusion is the appropriate technique for tubular and quasi-tubular designs [47-48].

- Calendering

Calendering means the connection of more than one thin planar structure by pressing them together during rolling between two or more rollers. The process involves squeezing a softened thermo-plastic polymer / ceramic powder mixture between two rollers to produce a continuous sheet of material. Individual sheets can be calendered and joined to form the multilayer tapes required for SOFCs [49]. This technique is continuous and used to combine

the substrate with for instance one or two pre-fabricated functional layers. If the pre-fabricated layers are produced by tape casting, green tapes (e.g. without any sintering) are used, glued together by the remaining organics. Hence, calendering is a technique performed between substrate manufacturing and coating. The tape calendering process is illustrated in *Fig. I-13*.

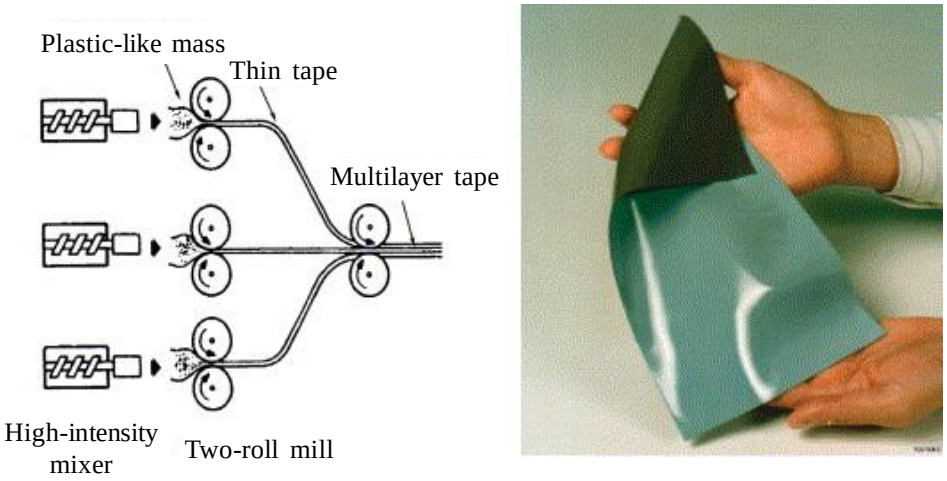

Figure I-13: Tape calendering process and green electrolyte / anode bilayer [50].

As SOFCs move closer to the market, substrate manufacturing techniques which are continuous and already well-established in other application fields are preferred. The trend is clearly moving to tape casting for planar designs and extrusion for tubular designs.

b) Coating technologies

- Screen printing

The method of screen printing is over 2000 years old. Since the middle of the twentieth century, the applications for screen printing have broadened from primarily decorative uses into a process to deposit electronic circuit materials onto a substrate [51]. It is one of just few methods which allow covering many different substrates (wood, metal, plastic, glass ceramic, paper etc.). Today, one of the principal applications for screen printing is the production of current collection wires on the top of solar cells. Screen printing is the most widely used coating technique for ceramic planar supports. This technology is industrially established, scalable and can be introduced in a production line, thus ideal for low cost fabrication.

The screen printing process involves the formulation of a paste containing powder and organic additives. The paste is rubbed with a squeegee, which moves across a screen with appropriate tension. The ink is pushed through the mesh onto the substrate placed under the

screen. A schematic illustration of the process is shown in *Fig. I-14*; a more detailed description can be found in *Chapter II*.

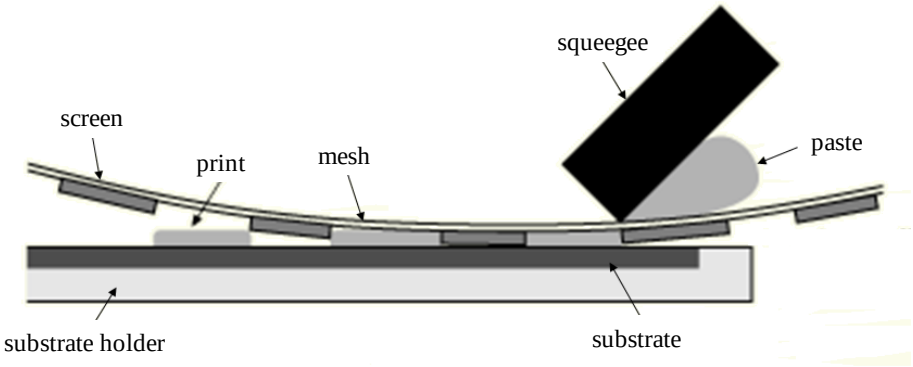

Figure I-14: Sketch of the screen printing process [52].

The screen printing process is used in planar SOFCs for the coating of the 2 electrodes in the case of an electrolyte support, or in the case of an electrode or a metal support for the functional electrodes and the electrolyte.

- Spraying methods

Spraying techniques involve the preparation of a suspension, sprayed on a substrate via a spray gun, either fixed with a moving piece or moving itself along the piece to coat, as illustrated in *Fig. I-15*. The main advantage of spraying techniques in comparison with for example screen printing is that non-planar and non-uniform substrates can also be coated. The spraying process is continuous, can be used with different geometry structures, is fast adaptable to variations of size and involves low equipment cost. However, in all the cases, spraying techniques suffer from overspray. The coating efficiency is thus reduced and the costs are consequently higher [43].

Spraying of liquid for coating planar, tubular or three-dimensional supports is widely used in various industries, as automobile or electronics. For SOFCs, spraying methods like wet powder spraying were formally used for coating the cathode and electrolyte layers in the old Siemens tubular design; wet powder spraying can also be applied for coatings of functional layers or metallic interconnects with protection or contact layers.

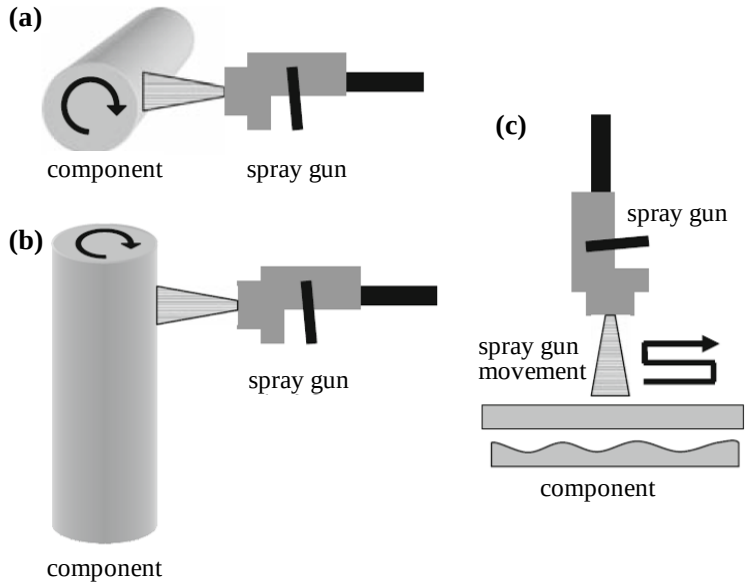

Figure I-15: Positions of spray gun and component to be coated; with a) horizontal / horizontal and b) horizontal / vertical configurations, both with tubular designs, and c) vertical / horizontal configuration with planar and planar-structured designs [43].

As part of the spraying techniques, plasma spraying should also be mentioned as an elaboration technique for SOFCs, used for coating metal supported cells as a sintering step at high temperature and in oxidising atmosphere (usually air), which would lead to the oxidation of the metallic support, is here not needed. In this technique, a high-temperature plasma jet, emanating from an anode nozzle, will heat and accelerate particles, injected into a high-temperature gas region by means of a cold carrier gas perpendicular to the axis of the plasma jet. The heated powders inside the jet region will impact and adhere to the substrate, forming a coating (*Fig. I-16*) [53].

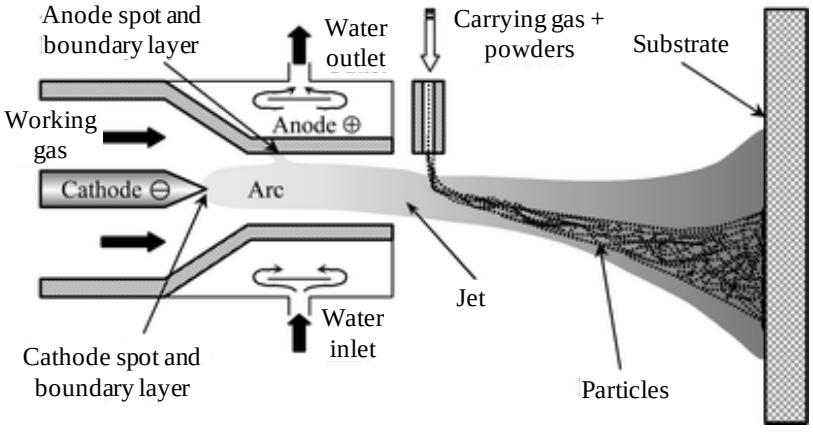

Figure I-16: Schematic diagram of atmospheric plasma spraying method [53].

Among the existing techniques, one can mention atmospheric, low pressure, suspension and vacuum plasma spraying.

However, such techniques are suffering several drawbacks such as remaining porosities in the electrolyte layers or difficulties to control the microstructure in case of electrodes coating. But due to the advantages of metal-supported cells (costs, low-temperature application etc.), coating with plasma spraying remains of great interest for many R&D groups worldwide [43].

- Slip casting

The slip casting process is used to manufacture three-dimensional ceramic components. The slurry is poured into a permeable mould; the microporous nature of the mould provides a capillary suction pressure which drives the liquid from the slurry into the mould. A solid layer called a cast forms on the walls of the mould. Both cast and mould are then dried, and the cast is sintered to produce the final product [44].

The vacuum slip casting process is directly derived from the well-known slip casting process and is used for coating planar or tubular porous substrates. The technique works as a filtration process in which a suspension (of powder typically in ethanol) is applied on top of a planar substrate, or for tubular designs the substrate is inserted into the suspension. The solvent is drawn through the porosity of the substrates by the help of a vacuum and a smooth and homogeneous film of powder remains, forming high quality layers after sintering. However, the major drawback of this technique is its difficulty to be introduced in an industrial line.

An illustration of the process in the case of a tubular substrate is shown *Fig. I-17*. A more detailed description of the process applied to planar substrates is given in *Chapter II*.

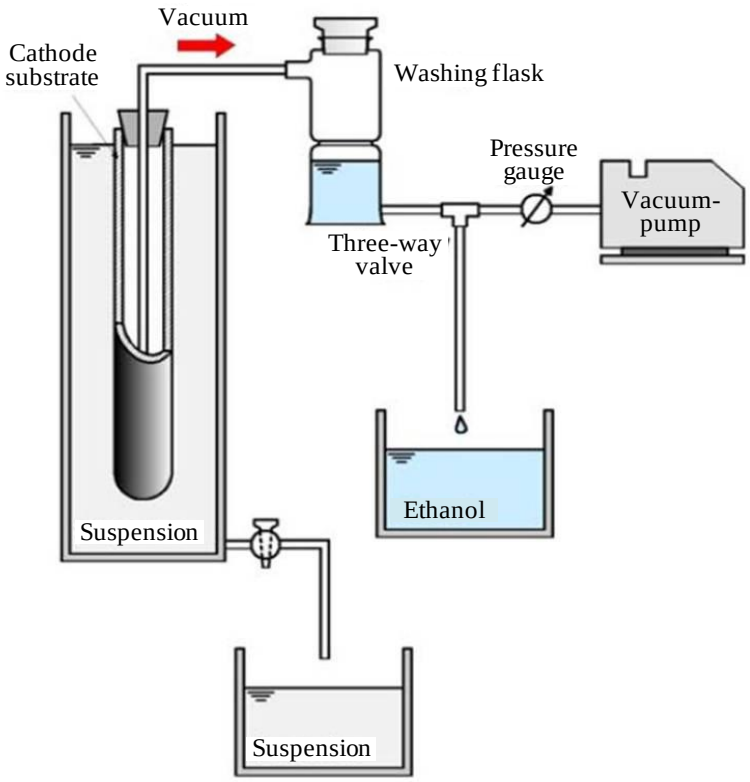

Figure I-17: Schematic illustration of the vacuum slip casting process in the case of a tubular cathode substrate [43].

- Roller / curtain coating

In roller coating, a suspension is moved from a reservoir via various intermediate rollers; the substrate is coated while passing through a coating roller, as illustrated in *Fig. I-18a*. Planar and even substrates are prerequisites for roller coating to achieve good homogeneous layer thickness. In curtain coating, the suspension is not applied by a coating roller but falls downwards a reservoir as a continuous curtain on the moving substrates, as can be seen *Fig. I-18b*.

In both techniques, the overlapping suspension can be easily collected by a basin under the rolling machine and reused. Both roller and curtain coating are in-line technologies, highly automated and suitable for continuous mass fabrication. While up to now only first attempts have been made using these techniques, such technologies will most likely be applied in the future for cell manufacturing if SOFCs enter the mass market [43].

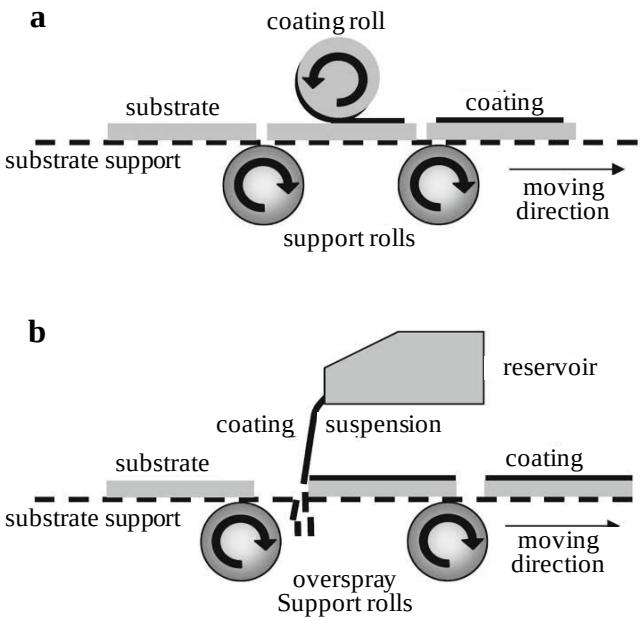

Figure I-18: a) Roller coating of functional layers and b) curtain coating of functional layers [43].

- Dip / Spin coating

Thin ceramic films can be prepared using a sol or solution by common methods such as dipping or spinning. For dip coating, the object to be coated is lowered into a solution and withdrawn at an appropriate speed, while for spin-coating the solution is dropped onto the object to be coated, which is spinning at high speed, spreading the suspension on its surface. Both processes are illustrated in *Fig. I-19*.

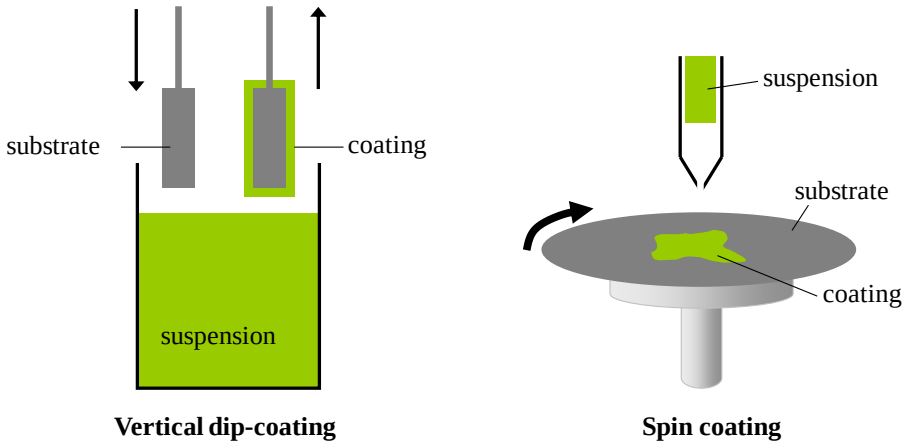

Figure I-19: Schematic of the dip and spin coating processes.

While the dip coating process is applicable to planar or three-dimensional objects, spin coating is restricted to planar supports.

Both spin and dip coating have been used at laboratory scale for SOFC applications, but both hold the potential of industrialisation if integrated in a production line.

- Gas phase deposition technologies

The first technique to be mentioned among the gas phase deposition technologies is the physical vapour deposition (PVD), which involves the transport via a gas phase of a material or target from a condensed matter phase to a "cold" substrate where the material condenses (*Fig. I-20*). Materials can be transferred into the gas phase by varying methods, including cathodic electrical arc evaporation, electron beam evaporation, laser ablation and sputtering (ions accelerated by an electric field). The PVD techniques enable casting high quality thin and dense layers but suffer several drawbacks as costs, non-continuity, slow deposition rates and difficulties to coat undercuts and similar surface features [43].

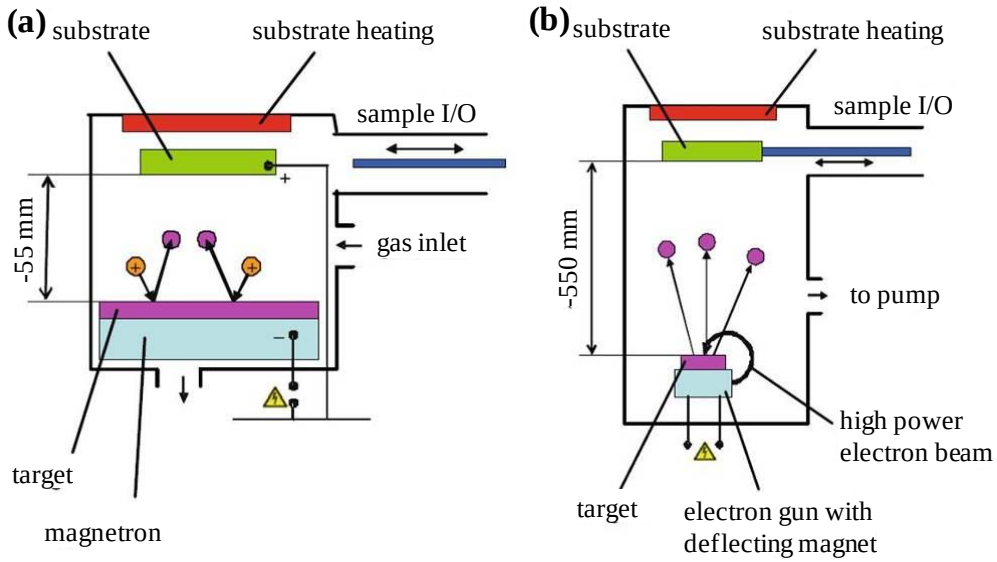

Figure I-20: Sketches of PVD methods with a) target materials brought into the gas phase by magnetron sputtered energetic argon ions and b) target materials melted with a focused electron beam [43].

The second gas phase deposition technique is the chemical vapour deposition (CVD), in which a chemical reaction takes place in the gas phase or on the surface of the substrate to be coated. Gaseous precursors diffuse to the sample and then react, thus creating the desired material. Some variants of the process exist, as for example plasma assisted CVD or PA-CVD, where a plasma near the surface to be coated helps controlling the position of the reaction, or

electrochemical CVD (EVD), a two-step process involving first a normal CVD deposition followed by a further growth of the layer, done in between ions moving from the substrate and the gas flow containing the precursors [43].

Chemical vapour deposition (CVD) constitutes an important technology for the manufacturing of thin solid films in semiconductors, microelectronics or solar cells [54]. For SOFCs application, EVD has been used by Siemens Westinghouse for coating tubular cathode-supported cells [55]. However, one major disadvantage concerns the precursor materials, difficult to purchase in certain processes and generally expensive [43].

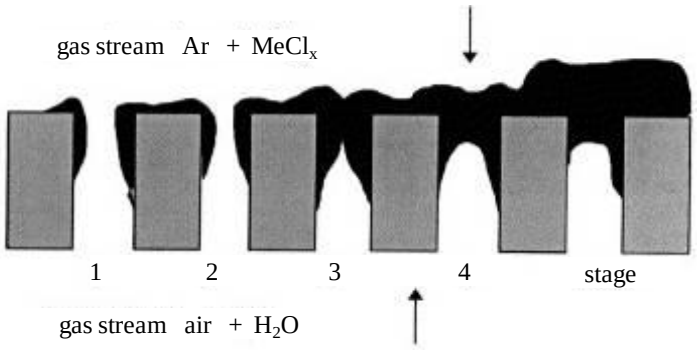

Figure I-21: Sketch of the different stages during the CVD / EVD [49].

3.3. State-of-the-art of SOFC materials

3.3.1 *Electrolyte materials*

For solid oxide fuel cells, the electrolyte membrane is, ideally, an ionic conductor and an electronic insulator. It performs three critical functions:

- separation of the oxygen from the fuel to avoid direct combustion. This implies that this membrane has to be gastight and chemically stable regarding the 2 atmospheres (oxygen partial pressure range $0.21 > p_{O_2} > 10^{-21}$ atm),
- electronic insulation,
- oxygen ion diffusion to feed the electrochemical reaction at the anode (ionic conductivity typically $\geq 10^{-2}$ S cm^{-1} at the operating temperature).

Additionally, good chemical and thermo-mechanical properties of the electrolyte are required (i.e. Thermal Expansion Coefficient or TEC, reactivity, adherence…).

The existing electrolyte materials are described below.

a) Zirconia-based

- Yttria stabilised zirconia (ZrO_2; 4 - 10% Y_2O_3) or YSZ

Oxide ion conductivity was first observed in ZrO_2 containing 15 Wt% Y_2O_3 by Nernst in the 1890s. Yttria is added to stabilise the conductive cubic fluorite phase, as well as to increase the concentration of oxygen vacancies and the conductivity [56-59].

The first solid oxide fuel cell using this electrolyte was manufactured in 1937 after the works of Baur and Preis [59].YSZ fulfils the electrical requirements for a high temperature SOFC (conductivity around 10^{-1} S cm^{-1} at 1000°C), and its good mechanical properties have been extensively covered in the literature [6, 56, 60-61]. For these reasons, YSZ is the standard state-of-the-art electrolyte material for SOFCs.

Nevertheless, the conductivity of this electrolyte decreases rapidly with the temperature, and problems of penalising chemical reactivity of this electrolyte with common cathode materials [56-57, 62-63] led to the need to find alternative materials.

- Other zirconia-based oxide ion conductors

The ionic conductivity of electrolytes can be maximised through composition modification by selecting an appropriate aliovalent dopant and its optimal concentration. Over the past 4 decades, solid solutions of ZrO_2-M_2O_3 (M = Sc^{3+} [56-59, 62, 64-70] Yb^{3+} [57, 59, 64-66, 68-69], Er^{3+} [57, 64-66, 68], Dy^{3+} [59, 64-66, 68], Gd^{3+} [59, 64-66, 68], Eu^{3+} [59, 64, 66, 68], La^{3+} [57, 68], Nd^{3+} [57, 68], Sm^{3+} [57, 68], Ho^{3+} [68], Pr^{3+} [68], Tb^{3+} [68], Lu^{3+} [68], Ce^{3+} [56, 64] In^{3+} and ZrO_2-MO (M'= Ca^{2+} [56-57, 68], Mg^{2+} [68]) have been studied. Doping of ZrO_2 with alkaline earth metal cations (A^+) is much less effective compared to rare earth dopants.

Fig. I-22 shows the influence of selected dopants on the total conductivity of the electrolyte at 1000°C, depending on the amount of dopant. Scandium doped ZrO_2 (ScSZ) exhibits a significantly higher conductivity than YSZ and is therefore a promising material for IT-SOFC. However, price and availability of scandium is uncertain [57, 60, 62] and may limit further use of this material. Some attempts have been made with ternary systems with the aim to increase the conductivity, enhance the stability of Sc-based materials or reduce the cost by mixing rare earths with cheaper alkaline earth dopants [65]. For instance, the company Kerafol (Keramische Folien GmbH) supplies two types of electrolyte substrates based on ScSZ; one ternary doped with ceria to stabilise the cubic phase or with yttria to improve the mechanical strength [71].

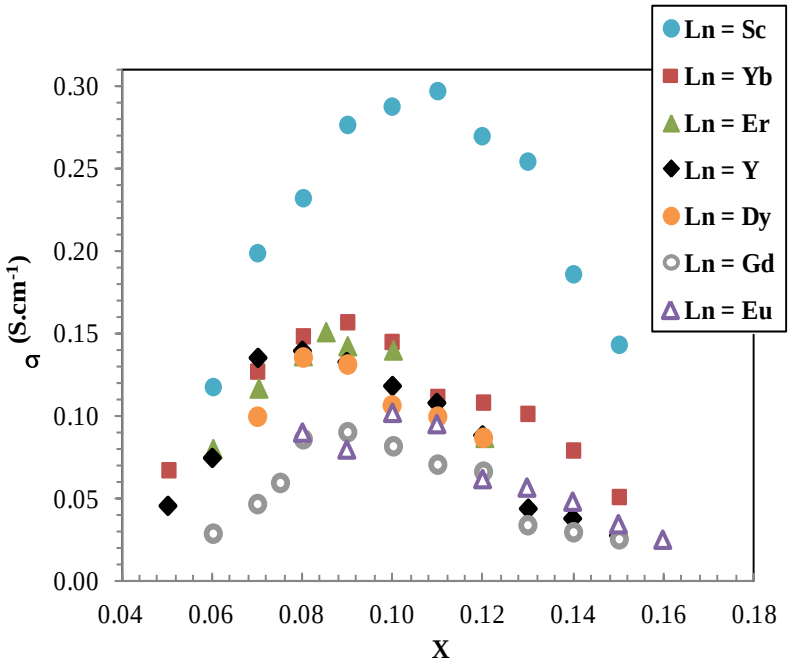

Figure I-22: Composition dependence of the electrical conductivity at 1000°C for ZrO_2 -Ln_2O_3 solid solutions (Ln = lanthanide) [64].

b) Ceria-based

The properties of electrolytes based on CeO_2 have been considered in many review and survey papers [58, 65]. Over the past three decades, many substitutions have been attempted on ceria in order to increase its anionic conductivity, mainly with alkaline earth or rare earth oxides. Systems based on CeO_2-M_2O_3 (M = Gd^{3+} [57, 59-60, 62, 64, 72-74], Sm^{3+} [59-60, 62, 72-73, 75], Y^{3+} [59, 62, 72-73], Dy^{3+} [72], Nd^{3+} [72], Eu^{3+} [72], Yb^{3+} [72], La^{3+} [62, 72-73], Sc^{3+} [73]) and CeO_2-M'O (M' = Mg^{2+} [72-73], Sr^{2+} [72-73], Ba^{2+} [72-73], Mg^{2+} [72-73], Ca^{2+} [59]) were reported.

Many co-doped ceria electrolytes have been as well investigated, as for example (Gr^{3+}, Pr^{3+}), (Sm^{3+}, Ca^{2+}), (La^{3+}, Sr^{2+}) or (Gd^{3+}, Mg^{2+}) [75]. The compositions CeO_2-Gd_2O_3 (GDC) and CeO_2-Sm_2O_3 (SDC) show conductivities significantly higher than those of zirconia-based electrolytes [59, 62, 64, 70, 74] (*Fig. I-23*) and therefore have been extensively examined for IT-SOFC applications.

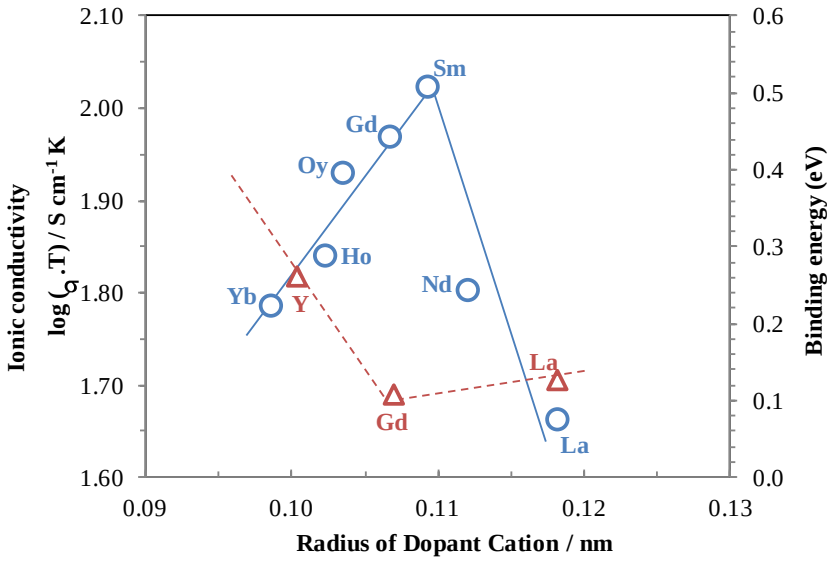

Figure I-23: Dependence of the ionic conductivity on ionic radius of M^{3+} for $(CeO_2)_{0.8}(M_2O_3)_{0.2}$ at 800°C [59].

However, at low oxygen partial pressures, ceria-based oxide ion conductors are partially reduced leading to a predominantly n-type electronic conductivity in a large fraction of the electrolyte on the anodic side, decreasing the efficiency of the cells [57, 59-60, 64, 70, 74]. To minimise such efficiency losses, these electrolytes are used in the low temperature range (e.g. 550°C) [59-60, 64], and the electronic leakage can be prevented by protecting the ceria electrolyte with a thin YSZ barrier layer on the anodic side [59]. However, the performance of multilayer cells is decreased due to the formation of a resistive phase at the YSZ / ceria interface [65]. Nevertheless, for low temperature operation, doped-ceria electrolytes remain to date one of the best candidate materials [60].

c) <u>$(La,Sr)(Ga,Mg)O_3$ and other oxygen-deficient perovskite structures</u>

The perovskite structure, with general formula ABX_3, where A is a large metal cation, B a transition metal and X a halogen or oxygen, comprises a large family of compounds with a wide variety of applications such as SOFC, ferroelectrics, superconducting materials and oxidation catalysts [59]. The possible combinations fulfilling the total charge (+6) on A and B are (1 + 5), (2 + 4), (3 + 3) and also in more complex ways on co-doping on both A- and B-sites, giving to perovskite-type compounds a wide variety of properties. But only a few perovskite phases are purely ionic in their behaviour.

High oxygen ion conductivity can be achieved in $LaGaO_3$ by substituting lanthanum with alkaline earth elements and incorporating divalent metal cations into the gallium sublattice [65]. Lanthanum gallate materials $La_{1-x}Sr_xGa_{1-y}Mg_yO_{3-\delta}$ (LSGM) were reported as superior

oxide ion conductors, with good chemical stability and negligible electronic conductivity over a broad range of oxygen partial pressures [57, 64-65]. Further improvement of the LSGM composition properties can be obtained by introducing a small amount of Co on B-site, without introducing electronic conductivity [65, 76]. Disadvantages of $LaGaO_3$-based materials include possible reduction and volatilisation of gallium oxide, relatively high cost of gallium and a significant reactivity with perovskite-type electrodes under oxidising atmospheres and with nickel metal constituting the anode in reducing atmospheres [57, 65, 70, 74, 76].

Other lanthanum-based perovskites, including $LaAlO_3$, $LaScO_3$, $LaInO_3$, $LaLuO_3$ and $LaYO_3$ doped on A and B-site typically with Sr and Mg [77] are oxide ion conductors [56, 77-78]. Especially, starting from an initial work of Takahashi and Iwahara in 1971 [79], many researches have been made on Al-based materials. Thus, compounds as $Ln_{1-x}M_xAlO_3$ (Ln = Yb^{3+}, Y^{3+}, Gd^{3+}, Sm^{3+}, Nd^{3+}, Pr^{3+}, La^{3+} [59, 77], Ba^{3+} [56]; M = Ca^{2+} [80], Ba^{2+} [59, 81], Sr^{2+} [81]) and co-substitutions on the aluminium site with Mg^{2+}, Ga^{3+}, In^{3+}, Sc^{2+} [77] have been studied. But these phases exhibited mixed electronic and ionic conductivities at high partial pressures of oxygen, and instability in reducing atmospheres in the case of the indates. Also, aluminates are mainly mixed ionic / electronic conductors [77].

Titanate-based phases have also been investigated as potential electrolyte materials, with doped-$CaTiO_3$ the most conducting ones [79].

d) Others

- LAMOX

These materials based initially on the $La_2Mo_2O_9$ parent compound present a competitive high ionic conductivity, with a phase transition above 600°C to a structure with a 2 orders of magnitude higher conductivity. Unfortunately, the molybdenum can be reduced and therefore induce electronic conductivity. There have been numerous studies to overcome both the reducibility and the phase transition with appropriate doping, such as $La_2(Mo_{2-x}M_x)_2O_9$ with M = Al [82], Fe [82], Mn [82], V [65, 83-84], Nb [82, 85], Ta [82, 85], Cr [83-84], S [83-84], Re [83-84],W [65, 83-84, 86] or $La_{2-x}M'_xMo_2O_9$ with M' = Na [82], K [83], Rb [82], Ca [82], Sr [83], Ba [83], Pb [82], Y [84, 87], Ce [82], Nd [84, 87], Sm [82], Eu [82], Gd [84, 87], Dy [82], Er [82], Yb [82], Bi [65, 83] and also on the oxygen site with F [88]. In most of the cases, the simple cubic structure is stabilised at room temperature, the phase transition being suppressed.

The maximum conductivity was found for the compositions $La_{1.7}Bi_{0.3}Mo_2O_{9-\delta}$, $La_2Mo_{1.7}W_{0.3}O_{9-\delta}$ and $La_2Mo_{1.95}V_{0.05}O_{9-\delta}$ [65]. But the electronic contribution to the total conductivity of LAMOX in reducing atmospheres increases with the temperature [5]. Doping of molybdenum by tungsten limits the reducibility, but the stability of $La_2Mo_2O_9$-based materials has still to be explored, some of them exhibiting degradation at moderate oxygen partial pressures [65]. The properties of LAMOX seem, therefore, rather inappropriate for practical applications.

- Apatite-type

Another group of ionic-conductors, the apatite type $A_{10-x}(MO_4)_6O_{2\pm\delta}$ where M = Si, Ge [89] and A is a rare earth or alkaline earth cation (A = La, Pr, Nd, Sm, Gd, Dy [90-92]) have been widely studied over the past 3 decades [65]. Rare earth silicates with apatite-type structure are promising materials for IT-SOFC, the phases with germanium presenting drawbacks as high volatility, tendency to glass formation and cost of GeO_2 precursor [65]. Doping on A-site with Ba^{3+}, Sr^{2+} or Ca^{2+} or on B-site with Al^{3+}, Mg^{2+} or Ti^{3+} have also been studied, with particular interest on Al- and Mg-doped phases. The lanthanum-based compositions exhibited the highest ionic conductivities, especially for A-site deficiency and doping with Mg or Al on the silicium site [82, 93-94]. But the extremely high sintering temperature of this family of materials remains still a problem for the cell processing [82]; also, little is known about their compatibility and performance with current electrode materials [58]. An improvement of the sinterability can be achieved by doping with transition metal cations such as Fe, with observed enhancement of the total conductivity, the ionic transport remaining the main contribution [94-96].

- BIMEVOX Aurivillius phases

Among oxygen ion conducting materials, the bismuth oxide with a fluorite-related structure δ-Bi_2O_3 exhibits the highest conductivity (1 S cm^{-1} at 750°C [97]) due to its extremely open crystal structure. Unfortunately, this material possesses several disadvantages such as instability in reducing atmospheres, volatilisation of bismuth oxide at intermediate temperatures, high corrosion activity or low mechanical strength [65]. Compared to the fluorite-like Bi_2O_3-based oxides, the phase stability of doped γ-bismuth vanadate γ-$Bi_4V_2O_{11}$ (BIMEVOX) is substantially better. Partially doped phases on vanadium-site with transition metal cations such as Al [98], Cd [99], Ti [100], Co [65, 101], Ni [65, 102], Zn [102], Mo [102], Mg [58] or Cu [65, 101-103] exhibit some of the highest oxygen ion conductivity levels reported. For instance, the maximum conductivity (10^{-3} S cm^{-1} at 300°C) was observed for

$Bi_4Cu_{0.2}V_{1.8}O_{11-\delta}$ [101]. Doping with Y_2O_3 or Er_2O_3 [103] stabilises the high conducting phase. Nevertheless, these materials present a huge chemical reactivity as well as low mechanical strength [65], and at relatively low partial pressures of oxygen, Bi^{3+} ion is reduced to metallic Bi and the electrolyte is decomposed [59]. Similar decomposition is observed under applied DC voltage [65].

- Pyrochlore-type

Pyrochlore-structured materials of general formula $A_2B_2O_7$ (A = lanthanides and B = transition metals) have been studied since the 1960s for their properties in ionic conductivity [65]. Usually, the maximum conductivity occurs for cation stoichiometry, e.g. compounds $Gd_2Zr_2O_7$ and $Gd_2Ti_2O_7$, but remains still low [65]. A value around 10^{-4} S cm^{-1} at 1000°C in air was reported by Mori et al. in 2002, increasing to 10^{-2} S cm^{-1} at $P_{O_2} = 10^{-18}$ atm [104]. The most highly conductive materials among this structural type are the titanates [56]. Samples of the series $Sm_{2-x}M_xTi_2O_{7-x/2}$ (M = Mg, Co, Ni) were also studied, with a conductivity increasing with the dopant content up to x = 0.4, with for Mg doping a corresponding conductivity value around 1.077×10^{-3} S cm^{-1} at 600°C [105].

e) <u>$Ba_2In_2O_5$-based</u>

- The brownmillerite $Ba_2In_2O_5$

The existence of $Ba_2In_2O_5$ crystallising in a structure related to the cubic perovskite had first been reported by W. Kwestroo et al. in 1973. It was later shown that this compound crystallises in the brownmillerite structure, where In^{3+} ions are located in both tetrahedral and octahedral coordinations. This structure has been first described in 1897 by Törnebohm, but the real crystal structure has been determined only in 1971 by A.A. Colville et al [106].

The system crystallises in the space group Ima2 and is composed of sheets of distorted perovskite-like octahedra InO_6 joined by the corners in between which are intercalated layers described as parallel chains of InO_4 tetrahedra, as shown in *Fig. I-24*.

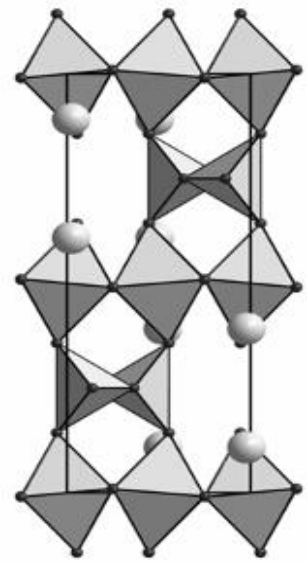

Figure I-24: The brownmillerite ($Ba_2In_2O_5$) structure with Ba in light grey, O in black forming octahedra and tetrahedra with In at the centre.

High oxygen ion conductivity abode 900°C was found in $Ba_2In_2O_5$ by Goodenough et al. in 1990 [107] and the compound has been studied in the 90s for applications as oxygen sensors, oxygen pumps, oxygen permeable membranes and electrolytes for high temperature fuel cells [107-111]. This compound exhibits a first-order transition to a disordered orthorhombic structure around 930°C and then to a perovskite-type cubic structure at temperatures above 1074°C. This order / disorder transition comes with a jump of more than one order of magnitude of the ionic conductivity, due to the fact that the perovskite structure exhibits a greater degree of disorder of the oxygen vacancies [112]. However, a structural transition at such temperature is unacceptable from a technical point of view, causing internal stresses during heating and cooling. Therefore, efforts have been made to stabilise the perovskite structure at room temperature by substitutions on either the barium or the indium site.

- The different substitutions

The easiest way to visualise the perovskite structure is in terms of BO_6 octahedra which share corners in all three dimensions. The A cations occupy every hole which is created by eight BO_6 octahedra, giving the A cation a twelve-fold oxygen coordination, and the B-cation a six-fold oxygen coordination, as shown in *Fig. I-25*. This structure offers a stable cation subarray within which O^{2-} ions may move. The disordered oxygen lattice in this structure offers very high oxygen ion conductivity.

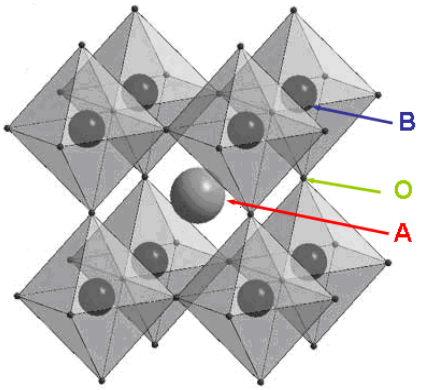

Figure I-25: The perovskite (ABO_3) structure.

Examples of the substitutions performed to stabilise the high conducting perovskite phase at room temperature are presented in *Table I-2*.

Table I-2:
Conductivities at 700°C of selected oxides derived from $Ba_2In_2O_5$.

Compound	Rate	Structure @ RT	$\sigma_{electric}$ at 700°C under oxidising atmosphere (S cm^{-1})	$\sigma_{electric}$ at 700°C under reducing atmosphere (S cm^{-1})	Relative densities	Ref
$Ba_3In_2CeO_8$		Brownmillerite	1.5×10^{-3} (400°C)		ND	[107]
$Ba_3In_2HfO_8$		Brownmillerite	1.1×10^{-3}		ND	[107]
$Ba_2In_2O_5$		Brownmillerite	2.0×10^{-4}		> 90%	[113]
$Ba_2In_{2-x}Ce_xO_{5+x/2}$	x = 0	Brownmillerite	7.0×10^{-4}	3.2×10^{-4}	ND	[114]
	x = 0.1	Brownmillerite	1.2×10^{-3}	5.6×10^{-4}	ND	[114]
	x = 0.2	Brownmillerite	1.6×10^{-2}	1.5×10^{-2}	ND	[114]
	x = 0.3	Cubic	1.0×10^{-2}	7.0×10^{-3}	ND	[114]
	x = 0.5	Cubic			poor	[114]
	x = 1	Cubic	5.6×10^{-3}	3.1×10^{-3}	ND	[114]
$Ba_2In_{2-x}Cu_xO_5$	$0 \leq x \leq 1$	Brownmillertie			ND	[115]
$Ba_2In_{2-x}Ga_xO_5$	x = 0.2	Brownmillerite	6.5×10^{-4}		ND	[110]
	x = 0.4		8×10^{-3}		ND	[116]
	x = 0.45	Brownmillerite	1.45×10^{-2}		ND	[110]
	x = 0.5	Cubic	6.3×10^{-3}		ND	[117]
	x = 0.6	Cubic	1.1×10^{-3}		ND	[117]
	x = 0.7	Cubic	1.1×10^{-3}		ND	[117]
	x = 0.8	Cubic	8.3×10^{-4}		ND	[117]
	x = 0.9	Cubic	8.3×10^{-4}		ND	[117]
$Ba_2In_{1.5}Mo_{O.5}O_{5.75}$		Brownmillerite	$\sim 10^{-3}$		61%	[118]
$Ba_2In_{1.8}Sc_{0.2}O_5$		Brownmillerite	5.0×10^{-4}		ND	[111]
$Ba_2In_{1.8}Sm_{0.2}O_8$		Brownmillerite	5.6×10^{-4}		ND	[111]
$Ba_2In_{2-x}Ti_xO_{5+x/2\square 1-x/2}$	x = 0	Brownmillerite	2×10^{-4}		ND	[119]
	x = 0.05	Brownmillerite	3.4×10^{-4}		ND	[119]
	x = 0.1	Brownmillerite	1.1×10^{-3}		ND	[119]
	x = 0.2	Tetragonal	4×10^{-3}		ND	[119]
	x = 0.3	Tetragonal	3.5×10^{-3}		ND	[119]
$Ba_2In_{2-x}Ti_xO_{5+x/2\square 1-x/2}$	x = 0.5	Cubic	4.0×10^{-3}		ND	[119]
	x = 0.66	Cubic	2.7×10^{-3}		ND	[119]

Compound	Rate	Structure @ RT	$\sigma_{electric}$ at 700°C under oxidising atmosphere (S cm^{-1})	$\sigma_{electric}$ at 700°C under reducing atmosphere (S cm^{-1})	Relative densities	Ref
$Ba_2In_{2-x}Ti_xO_{5+x/2}$□$_{1-x/2}$	x = 0.8	Cubic	1.6×10^{-3}		ND	[119]
	x = 1	Cubic	4.5×10^{-4}		ND	[119]
	x = 1.2	Cubic	6.3×10^{-4}		ND	[119]
	x = 1.4	Cubic	9×10^{-3}		92%	[120]
$Ba_2In_{1.3}V_{0.3}O_{5.3}$		Brownmillerite	~ 10^{-3}		62%	[118]
$Ba_2In_{1-x}W_xO_{5+3x/2}$	x = 0.1	Cubic	7.0×10^{-3}		> 90%	[113]
	x = 0.2	Cubic	1.0×10^{-2}		> 90%	[113]
	x = 0.5	Brownmillerite	~3×10^{-4}		65%	[118]
$Ba_2In_{1.8}Y_{0.2}O_7$		Brownmillerite	5.6×10^{-4}		ND	[111]
$Ba_2In_{1.8}Yb_{0.2}O_6$		Brownmillerite	5.0×10^{-4}		ND	[111]
$Ba_{2-x}La_xIn_2O_{5+x/2}$	x = 0	Brownmillerite	4.0×10^{-4}		> 90%	[95]
	x = 0.2	Brownmillerite	2.2×10^{-3}		> 90%	[95]
	x = 0.4	Brownmillerite	4.0×10^{-3}		> 90%	[95]
	x = 0.6	Tetragonal	6.3×10^{-4}		> 90%	[95]
	x = 0.8	Tetragonal	1.0×10^{-2}		> 90%	[95]
	x = 1	Cubic	1.2×10^{-2}		> 90%	[95]
	x = 1.2	Cubic	2.0×10^{-2}		> 90%	[95]
$BaZr_{1-x}In_xO_{3-0.5x}$	x = 0	Cubic			ND	[121]
	x = 0.1	Cubic	8.0×10^{-5}		ND	[121]
	x = 0.2	Cubic			ND	[121]
	x = 0.3	Cubic			ND	[121]
	x = 0.4	Cubic			ND	[121]
	x = 0.5	Cubic			ND	[121]
	x = 0.6	Cubic			ND	[121]
	x = 0.7	Cubic	1.8×10^{-3}		ND	[121]
	x = 0.8	Brownmillerite			ND	[121]
	x = 0.9	Brownmillerite			ND	[121]
	x = 1	Brownmillerite	3.5×10^{-3}		ND	[121]
$Ba_{1.6}Sr_{0.4}In_2O_5$		Brownmillerite			~ 86%	[122]
$Ba_{0.9}Sr_{0.1}In_2O_5$		Brownmillerite			~ 86%	[122]
$Ba_{2-x-y}Sr_xLa_yIn_2O_{5+y}$	**x = 0.1**				ND	
	y = 0.2	Cubic		4.0×10^{-3}	> 90%	[123]
	y = 0.3	Cubic		7.1×10^{-3}	> 90%	[123]
	y = 0.4	Cubic		0.20	> 90%	[123]
	y = 0.5	Cubic		0.40	> 90%	[123]
	x = 0.2				ND	
	y = 0.2	Cubic	1.2×10^{-2}	5.0×10^{-3}	> 90%	[123]
	y = 0.3	Cubic	2.8×10^{-2}	8.9×10^{-3}	> 90%	[123]
	y = 0.4	Cubic	5.0×10^{-2}	0.20	> 90%	[123]
	y = 0.5	Cubic	0.10	0.50	> 90%	[123]
$Ba_{0.3}Sr_{0.2}La_{0.5}InO_{2.75}$		Cubic	0.1 (800°C)	0.25 (800°C)	> 97%	[124]

This table illustrates the high interest in the literature for this family of oxides as electrolyte materials for IT-SOFC, because of their higher conductivities compared to the state of the art YSZ at 700°C. Notably, remarkable phases are $Ba_{0.5}La_{0.5}InO_{2.7}$ and some of Ba-site double-substituted La / Sr ones [95, 123-124]. However, for these phases, electronic

conductivity appears in the low and high partial pressures of oxygen, making them unsuitable for application as IT-SOFC electrolytes.

- The phases $BaIn_{1-x}Ti_xO_{2.5+x/2}\square_{0.5-x/2}$

In the frame of the PhD work of A. Magrez done in the Institut des Matériaux Jean Rouxel de Nantes (IMN), phases $BaIn_{1-x}Ti_xO_{2.5+x/2}\square_{0.5-x/2}$ have been extensively studied [125]. Indeed, substitution of In^{3+} with Ti^{4+} induces a disordering of the oxygen vacancies and therefore an expected enhanced conductivity in comparison with the parent $Ba_2In_2O_5$. Solid solutions with $0 < x < 0.7$ have been successfully synthesised and characterised, exhibiting promising performance. The disordered perovskite structure has been stabilised at room temperature for $x > 0.15$. Higher titanium content, typically for $x > 0.7$ led to difficulties in the synthesis of phase pure materials. The measured conductivities presented in *Table I-3* have been further enhanced during the PhD work of T. Delahaye by using samples with higher relative densities (*Fig. I-26*). All the phases in the range $0.2 < x < 0.7$ exhibited conductivities in the order of 10^{-2} S cm^{-1} at 700°C [126]. The best compounds are $BaIn_{0.8}Ti_{0.2}O_{2.6}$ (for $x = 0.2$) and $BaIn_{0.3}Ti_{0.7}O_{2.85}$ (for $x = 0.7$).

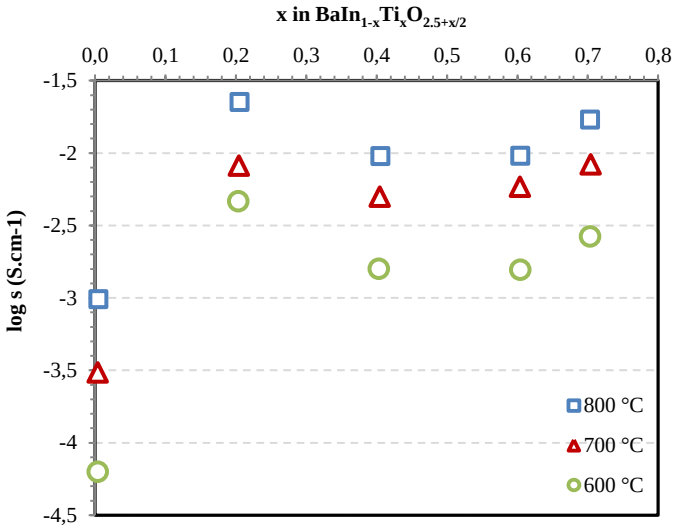

Figure I-26: Conductivities in air at different temperatures as a function of the composition x [126].

At low temperature, the conductivity of $BaIn_{1-x}Ti_xO_{2.5+x/2}$ compounds is mainly protonic due to a partial hydration of these phases. For high Ti content (e.g. $x > 0.25$), this hydration phenomenon occurs without huge volume variation of the structure, and therefore without introducing mechanical stresses [127]. The composition with $x = 0.2$ ($BaIn_{0.8}Ti_{0.2}O_{2.6}$) is

studied by our group for application in Proton Conducting Fuel Cells (PCFC) in the frame of the ANR-METPROCELL project.

The amount of incorporated protons decreases with increasing x in $BaIn_{1-x}Ti_xO_{2.5+x/2}\square_{0.5-x/2}$. Thus, the Arrhenius plot of the ionic conductivity for the phase with x = 0.7 ($Ba_{0.3}Ti_{0.7}O_{2.85}$ or BIT07) presents a quasi linear evolution, indicating a weak water absorption [126]. In addition, the phase BIT07 is stable over a wide range of oxygen partial pressures and under CO_2 gas up to 800°C, making it a material of interest for catalysis [126]. Indeed, the basicity of these compounds due to the high presence of barium can limit the formation of carbon deposit occurring under natural gas when BIT07 is used in an anode cermet (Ni / BIT07) [128-130], since CO_2 and H_2O sensibility could be actually an advantage to avoid anode coking, as recently shown in the case of Ba-modified cermets [131]. A basic support presents an affinity with the CO_2 molecules and can adsorb them; these molecules can then oxidise the deposited carbon to form CO molecules [132].

3.3.2 *Anode materials*

The main function of the SOFC anode is to provide reaction sites for the electrochemical oxidation of the fuel. Thus, the anode material must be stable in the fuel reducing environment and have sufficient electronic conductivity and catalytic activity for the fuel gas reaction at the operating conditions. The anode must be chemically compatible with adjacent components like electrolyte and interconnect at all temperatures (from the fabrication through assembling in a stack until operation). Several types of materials can be distinguished and are described in the following paragraphs.

a) <u>Ni-based cermet anode</u>

In principle, pure porous metallic electrodes (e.g. Ni, Pt, Ru etc.) can be used as anode materials [133]. Setoguchi et al. studied the electrochemical activity of Ni, Co, Fe, Pt, Mn and Ru and found that nickel exhibited the highest electrochemical activity for the oxidation of H_2 [133-134].

To improve the matching of the thermal expansion coefficient between the Nickel and the state-of-the art electrolyte YSZ, composites Ni / YSZ, called cermets, were investigated. Moreover, introducing YSZ phase in the metallic electrode expands the number of reaction sites by increasing the triple phase boundary (TPB, where fuel, Ni and YSZ meet) length, as shown in *Fig. I-27*. Thus, a reduction of the electrode polarisation resistance by using a cermet was observed, making this composite the most common anode for SOFC [135].

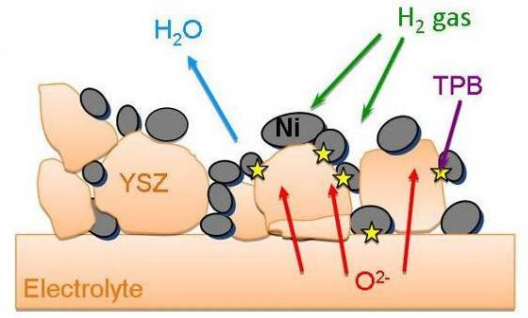

Figure I-27: Reaction zones in the case of a Ni / YSZ cermet.

Despite the excellent electrocatalytic properties of these cermets for operation with H_2 fuel, Ni / YSZ based anodes suffer a number of drawbacks when using direct methane fuel, such as carbon deposition caused by cracking of methane or sulphur poisoning. Also, operating in the intermediate temperature range (typically below 700°C) increases the possibility for the nickel to be oxidised as the result of the increased partial pressure of oxygen under typical operating conditions [133].

Successful modifications have been made on these cermets, for example by adding Mo, Ce, Mb, Co, Cu, Ru, Pt, Fe, Ti or alkaline earths (MgO, CaO, SrO, CeO_2) [133]. Tests have also been made to introduce electronic conductivity in the oxide phase by doping with cations forming a redox couple under anodic conditions, resulting in a decrease of the ionic conductivity in these phases.

Cermets using other transition metal components have also been investigated [136]. The copper, iron and cobalt-based anodes exhibit poor electrochemical properties. Ternary component anodes such as Cu / CeO_2 / YSZ showed encouraging results [137], Cu having no catalytic activity for the formation of C - C bonds. The effect of lanthanum additives on Cu / YSZ based anodes has also been studied, but the resulting cermets presented lower performance than the Cu / YSZ / CeO_2 cermet anodes.

Ceria-based compounds exhibit mixed electronic-ionic conductivity in reducing atmospheres. Similar to Ni / YSZ anodes, Ni / doped ceria has also been formulated and tested by several groups indicating a high activity towards methane reforming and improved performance [138-140], as it was shown that CeO_2 anodes can electrochemically oxidise dry methane and reduce the rate of carbon deposition [141]. Cermets such as Ni / CeO_2-ZrO_2, Ca-CeO_2 and Y-CeO_2 were studied by Kawada et al without showing any improvement in comparison with Ni / YSZ [133]. On the other hand, better performance was reported for Ni /

samarium doped ceria cermets [142-143], performance further improved by doping with Pd as reported in the work of Hibino et al. [144]. Significant improvement of the electrocatalytic activity of these compounds by adding small amounts of Ni (or Ru) can be achieved, also improving the performance of these cermets under methane [145-147].

b) Ceramic-based anode material

The main attraction of such mixed ionic electronic conducting oxides (called MIEC) is the possibility of an extended triple phase boundary length (meeting point of gas, electrons and ions) over the complete surface of the ceramic particle due to the electronic conductivity of these oxides, as illustrated in *Fig. I-28*. Furthermore, mobile lattice oxygen ions could reduce the rate of carbon deposition while using dry methane [148].

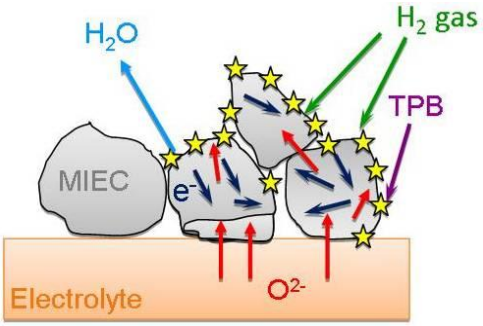

Figure I-28: Reaction zones in the case of a mixed ionic electronic conducting anode.

- Titanate-based oxides

Perovskite oxide materials are attracting increasing interest in application as SOFC fuel electrodes as alternatives to the traditional Ni / YSZ cermet [149]. Strontium titanate-based perovskite type compounds are relatively stable in fuel reducing atmospheres and present an ionic conductivity at low partial pressures of oxygen associated with electronic conductivity [150-151]. A slightly higher conductivity among these oxides is found for the substitution with yttrium, and can be even further improved by doping with Nb on B-site [142]. These phases have also been studied as composites with YSZ or ceria electrolytes.

Lanthanum strontium titanates as well as transition metal-doped lanthanum strontium titanates were fully studied for their resistance to sulphur poisoning (occurring while using natural gas as a fuel) [142, 149]. They show good total conductivities but a rapid degradation of the performance and a poor activity towards hydrogen oxidation [133]. $(La,Sr)TiO_3$ systems

have been doped with several transition metals (Ni, Co, Cu, Cr, Fe and Ce), the most effective among these dopants being the cerium [142].

Other titanates investigated for SOFC anode applications include other A-site deficient lanthanides [152-153], (La,Ca)$TiO_{3+\delta}$ [154] systems and $BaTiO_3$ doped with iron [142]. Properties of titanium-doped YSZ were also studied, with the aim of adding electronic conductivity in the oxide with doping [142, 155], but showed a certain limit of solubility due to problems of reactivity [156].

Systems such as YSZ doped with terbia were as well investigated and showed effective electronic conductivity, but only in oxidising atmospheres [133]. Y_2O_3-ZrO_2-TiO_2 and Sc_2O_3-Y_2O_3-ZrO_2-TiO_2 were also examined by Tao and Irvine [157], with promising results for the second system. Other TiO_2-based oxides for methane conversion and oxidation as rutile-type, pseudobrookite-type, pyrochlore-type and V_3O_5-structure type showed some activities towards methane conversion in the intermediate temperature range [158]. Spinel solid solution series $Mg_{2-y}Ti_{1+y}O_4$, with $0 < y < 0.5$ were also examined, with thermal expansion coefficients matching the state-of-the-art YSZ electrolyte and high temperature conductivities in the range 0.2 - 2 S cm^{-1} [159].

- Lanthanum chromite

The perovskite $LaCrO_3$ is quite inert for the reactions associated with reforming and carbon deposition. As for many perovskite-type compounds, the dominant p-type conductivity and catalytic activity can be enhanced by doping on the A-site with alkaline earth elements, such as Ca or Sr. Sr-doping improves the stability in reducing environment and reduces the polarisation resistance [142]. $LaCrO_3$-based materials such as (La,Sr)CrO_3 do not catalyse the carbon deposition and are therefore potential anodes for the direct oxidation of methane [160-161]. Co-doping with Mg, Mn, Fe, Co, Cu and Ni on B-site have been also reported, with an improvement of the electrocatalytic activity in the case of Mn, Fe and Ni [162-163]. Other double substitutions were also widely studied, with compounds of formula $La_{1-x}A_xCr_{1-y}B_yO_{3-\delta}$ (A = Ca, Sr; B = Mg [133, 136, 161, 163-164], Ti [136, 142], Fe [133, 136, 142, 163], V [136, 142, 164], Nb [136], Mn [133, 163], Ru [133, 142], Ni [133, 142, 163]. The compounds of the series $La_{1-x}Sr_xCr_{1-y}Mn_yO_{3-\delta}$ ($x = 0.2 - 0.3$; $y \leq 0.5$) present promising properties [136, 142, 165], especially while using methane. Enhancing effect with the addition of a small amount of catalyst such as Ni and Ru was also studied [164, 166-167]. Vanadium addition has also been shown to improve the catalytic activity of lanthanum-strontium chromites [164, 168].

- Other perovskites

Strontium-doped lanthanum vanadates $La_{1-x}Sr_xVO_3$ showed good sulphur tolerance with high conductivity level [169], further enhanced with nickel doping [170-171]. However, these phases present problems of stability in both oxidising and reducing atmospheres. Ferrites have also been investigated as potential anode materials, with in particular the lanthanum strontium cobaltite ferrites $La_{1-x}Sr_xFe_{1-y}Co_yO_{3-\delta}$, but presented poor stability at low oxygen partial pressures [142, 172]. Chromium-doped lanthanum-strontium ferrites $La_{1-x}Sr_xFe_{1-y}Cr_yO_{3-\delta}$ have however shown promising results for catalysing the methane oxidation reaction [142]. Perovskite gallates and niobates have as well been studied, but presented low conductivities [142, 173-174]. Barium cerate doped with yttrium has also been investigated, with conductivities remaining relatively low [175-176].

- Tetragonal tungsten bronze

Materials with the composition $(Ba / Sr / Ca / La)_{0.6}M_xNb_{1-x}O_{3-\delta}$ (M = Mg, Ni, Mn, Cr, Fe, In, Sn, Ti) have also been investigated as anodes for SOFCs because of their quite high electronic conductivity level and potential ionic one and their stability in both oxidising and reducing atmospheres for the phases containing Mg, In and Ti. The best performance is obtained with the Ti-based phases [133, 177].

- Pyrochlore and bismuth oxide

Conductivity of pyrochlore phases as $Gd_2Ti_2O_7$ increases with doping with Mo or Mn on B-site. The same tendency is observed for $Pr_2Zr_2O_{7\pm\delta}$ doped with Mn or Ce or $Pr_2Sn_2O_{7\pm\delta}$ doped with In [142, 178]. However, they are not suitable for SOFC application due to redox stability problems and low conductivity levels [178-179]. Because of their mixed conductivity in reducing atmosphere, bismuth-based compounds were studied as anodes for direct hydrocarbon fuel cells, presenting good electrocatalytic activity towards hydrocarbon oxidation, but the question of the stability of Bi-containing phases still remains (vaporisation of metallic Bi) [180].

- The phase $Ba_{0.5}La_{0.5}In_{0.3}Ti_{0.1}Mn_{0.6}O_{3-\delta}$

In his PhD work, François Moser studied the compounds $BaIn_{0.3}Ti_{0.7-y}M_yO_{3-\delta}$, with M = V, Nb, Ni, Cr, Fe and Mn [181]. By doping with transition metals on B-site, the idea was to introduce electronic conductivity in BIT07 for application as anode material associated with BIT07 itself as an electrolyte. Thus, associating materials with close chemical compositions and with the same structure can lead to a good chemical and mechanical compatibility. Using a

mixed ionic / electronic conductor allows a decrease of the needed nickel content and therefore of the problem of coking under natural gas. Furthermore, it has been shown that oxygen vacancies associated with electronic conductivity facilitates the oxidation of the carbon deposit [182], as shown in *Fig. I-29*.

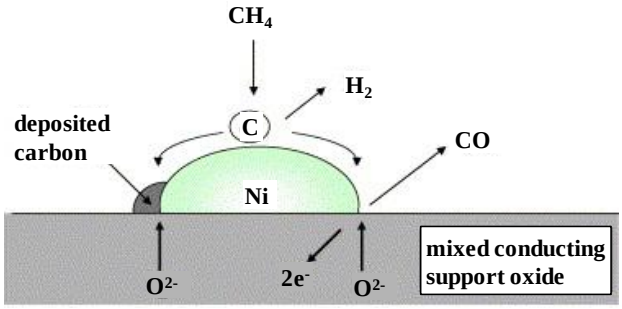

Figure I-29: Scheme proposed by Hamakawa et al. for the self-anti-coking performance of catalyst by lattice oxygen migration [182].

Among the studied compositions, monophasic compounds were obtained with substitutions with Fe and Mn. Substitutions on Ba-site with lanthanum successfully stabilised the cubic perovskite structure at room temperature. Under reducing atmospheres, the phase $Ba_{0.5}La_{0.5}In_{0.3}Ti_{0.1}Mn_{0.6}O_{3-\delta}$ (BLITiMn) presented a higher conductivity than the corresponding substitution with iron (cf. *Fig. I-30*), and a better mechanical compatibility with BIT07 is expected with regard to the thermal expansion coefficients (12.6×10^{-6} K^{-1} for BLITiMn vs. 22 $\times 10^{-6}$ K^{-1} for the phase with Fe).

However, despite the good performance of this material with low nickel content, its high sintering temperature induces difficulties in the shaping (problems of connexion between the ceramic grains). Optimisation of the anode microstructure has to be done before appreciating further the potential application of this MIEC (Mixed Ionic Electronic Conductor) as an anode for SOFC.

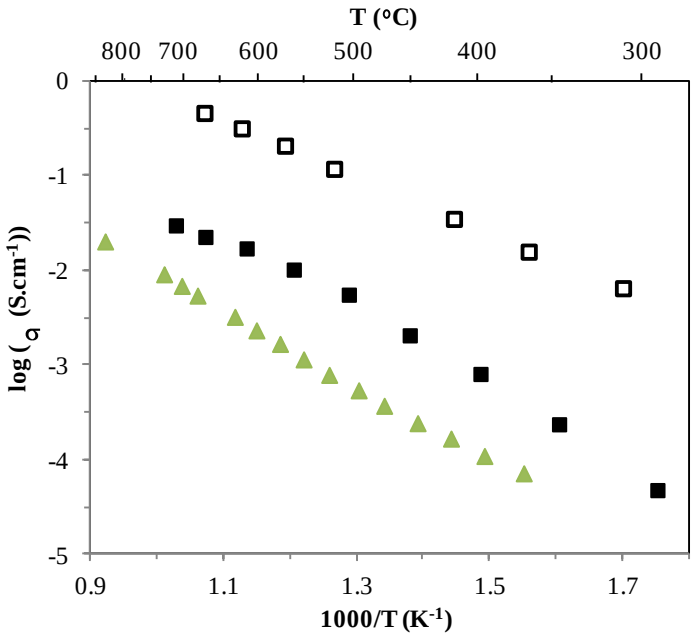

Figure I-30: Corrected Arrhenius plots of the total conductivities of BIT07 (triangles), $Ba_{0.5}La_{0.5}In_{0.3}Ti_{0.1}Fe_{0.6}O_{3-\delta}$ (full squares) and $Ba_{0.5}La_{0.5}In_{0.3}Ti_{0.1}Mn_{0.6}O_{3-\delta}$ (empty squares) under humidified Ar / H_2 (95% / 5%) [181].

3.3.3 *Cathode materials*

The main function of the cathode is to provide reaction sites for the electrochemical reduction of the oxidant. Thus, the cathode material must be stable in oxidising environments and have sufficient electronic conductivity (around 100 S cm^{-1}) and catalytic activity for the oxidant gas reaction at the operating conditions.

Since the SOFC operates at high temperatures (600 to 1000°C), the cathode must be chemically stable at different temperature ranges. The cathode in SOFCs is of particular concern for obtaining a high performing cell, especially at low operating temperature. In the 60s, doped-In_2O_3 was used, and in the 80s $LaMnO_3$ and $LaCoO_3$ were proposed [7].

Perovskite-type materials have been widely used as cathode materials in SOFCs [183]. For these ABO_3 structures, Sm, Pr, Ce, Tb [60] and mixtures of rare and alkaline earths, such as La, Nd, Gd and Sr, Ca or Ba have been considered for A-site [70, 74, 183]. The B-site cation is an oxidisable or reducible transition metal such as Mn, Co, Ni, Cr, Cu or Fe [60, 64, 70, 74, 183].

More recently, oxides from the Ruddlesden-Popper crystal structure were also proposed. Different materials that have been studied and used as cathode materials for (IT-) SOFC are presented hereafter.

a) $\underline{(La,Sr)MnO_3}$

The focus has been mainly done on lanthanum manganite materials due to their stability in oxidising atmospheres, their sufficient electrical conductivity at 1000°C and their thermal expansion coefficient matching with the state-of-the-art YSZ electrolyte. Doping with Sr on A-site (phases $La_{1-x}Sr_xMnO_3$ or LSM) increases the electronic conductivity of this kind of materials [6]. The absence of oxygen vacancies in LSM results in a conductivity that is almost purely electronic, the reduction of oxygen being then limited to the triple-phase boundaries. This is the main reason why LSM has no acceptable performance at lower temperatures.

Furthermore, a chemical reactivity of LSM (and more generally nearly all the lanthanum-based cathodes) at temperatures above 1200°C with YSZ is observed, forming the insulating $La_2Zr_2O_7$ phase at the cathode / electrolyte interface [60, 183]. This reactivity can be reduced by increasing Sr content (until 30% doping after which formation of $SrZrO_3$ is observed) or creating a slight A-site deficiency in the materials [183].

Two approaches have been studied to improve the performance of LSM:

- adding an ionic conducting phase to extend the surface area. Composite cathodes made with LSM-YSZ exhibited good performance [60].

- inducing ionic conductivity in LSM with appropriate doping of the structure. Indeed, replacing La by other rare earths elements as Pr, Nd, Sm, Gd, Yb or Y leads to performance improvement of the cathode and a decrease of the penalising reactivity with zirconia-based electrolytes [184].

The Sr-doped $PrMnO_3$ were reported to be suitable cathode materials for IT-SOFC, with electrical conductivity levels reaching 226 S cm^{-1} at 500°C [136, 185]. Further improved cathodes have been developed by replacing Sr with Ca, giving the phases $Pr_{1-x}Ca_xMnO_3$ [136, 186]. As concerns the doping on B-site, Al, Ga, Co, Fe, Sc or Ni have also been attempted [60, 183, 187]. The systems $Sr_{1-x}Ce_xMnO_{3-\delta}$ have also been reported as promising for IT-SOFC, especially when co-doping with Co on B-site [188].

b) $\underline{(La,Sr)(Co,Fe)O_3}$

Usually, cobalt-based materials display higher ionic and electronic conductivities than the other cathode materials. $La_{1-x}Sr_xCoO_{3-\delta}$ or LSC presents high activity for oxygen reduction. However, the presence of cobalt leads to thermal expansion coefficients significantly higher than the standard electrolyte materials, which can result in a delamination of the cathode or cracking of the electrolyte due to thermal stresses [70]. Furthermore, these perovskite-type

materials react widely with YSZ, resulting in the association of these cathodes preferentially with ceria-based electrolytes, or by using a diffusion barrier layer in between the cathode and the electrolyte [64].

To decrease the thermal expansion coefficient mismatch, different lanthanides (La, Pr, Nd, Sm, Dy and Gd) have been studied as A-site cations. Among these perovskites, those incorporating Pr exhibited the highest electrical conductivity levels (due to the additional Pr^{3+} / Pr^{4+} valence change). But the problem of high thermal expansion coefficients remains, as well as the huge reactivity with YSZ [189]. Doping with Cu or Mn on B-site can further enhance the ionic conductivity and catalytic activity of these cathodes [115-116], but without decreasing the thermal expansion coefficients.

Phases $Ln_{1-x}Sr_xFeO_3$ (Ln = La, Sr, Pr or Nd) have also been reported [183, 190]. Sr-doped $LaFeO_3$ (LSF) cathodes show promising electrochemical performance, stability, significantly reduced reactivity with YSZ and thermal expansion coefficients matching with YSZ and GDC [183, 191]. A complete anode-supported cell with YSZ electrolyte and LSF cathode doped on B-site by Cu exhibited power densities in the range of 1.35 - 1.75 W cm^{-2} at 750°C and 0.7 V [192].

More recently, phases $La_{1-x}Sr_xCo_{1-y}Fe_yO_{3-\delta}$ (LSCF) have been extensively examined and exhibited excellent performance associated with a GDC electrolyte (1.76 W cm^{-2} at 800°C and 0.7 V [193-194]. But these cathodes are generally incompatible with YSZ and the strontium tends to diffuse out of LSCF, leading to a degradation of the performance [183].

Phases with praseodymium on A-site showed also promising results for IT-SOFC applications, with a maximum total conductivity of 1040 S cm^{-1} at 300°C measured by Meng et al. for the phase $Pr_{0.6}Sr_{0.4}Co_{0.8}Fe_{0.2}O_{3-\delta}$ [195].

The compound family $Ba_{1-x}Sr_xCo_{1-y}Fe_yO_{3-\delta}$ (BSCF) shows excellent electrochemical performance. For example, a power density of 1.01 W cm^{-2} at 600°C was obtained with a BSCF cathode on a NiO / Samarium doped ceria (SDC) anode and SDC electrolyte [196]. Further doping on A-site with for example Sm or Nd to improve the electronic conductivity of these materials has also been reported [197-199]. The disadvantages of these materials are their high thermal expansion coefficients and their chemical reactivity with CO_2 from air at low operating temperatures (< 700°C) [198, 200].

c) $Ln_2NiO_{4+\delta}$

The rare earth nickelates $A_2NiO_{4+\delta}$ studied in the frame of this work (A = La, Nd, Pr) correspond to the first term (n = 1) of the so called Ruddlesden-Popper series of general formulation $A_{n+1}M_nO_{3n+1}$ (with n = 1,2,3, …∞), where A is a cation of high ionic radius (lanthanide or alkaline earth) and M a transition metal (M = Co, Ni, Cu, …). n = ∞ corresponds to the perovskite structure.

- Structural characteristics

The structure $A_2MO_{4+\delta}$ belonging to the structural model K_2NiF_4 can be simply described as a succession of perovskite-type MO_6 octahedra layers, shifted relative to each other by a vector (½, ½, ½) so that they appear linked together by a NaCl-type AO sheets (*Fig. I-31*). In reality, the octahedra are not regular and the apical oxygen atoms (in the summit of the octahedron) are far from the equatorial plan (elongated octahedron), for example due to the Jahn-Teller effect. In these conditions, a more precise description of the structure consists in a succession of square MO_2 plan sheets and A_2O_2 layers.

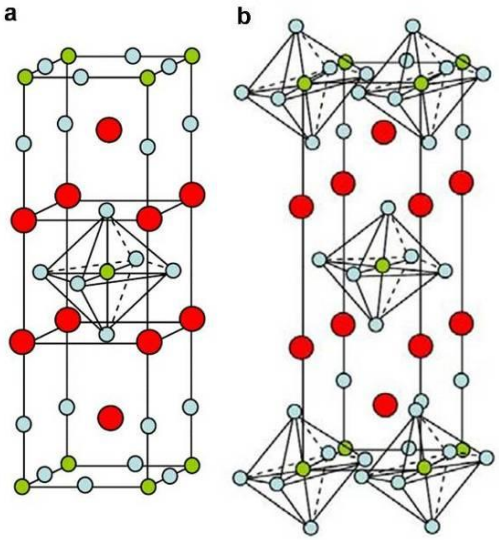

Figure I-31: a) the A_2MO_4 tetragonal structure and b) the A_2MO_4 orthorhombic structure [187]. A-site cations are in red, M-site in green and oxygens in light blue.

These materials, and more particularly the rare earth nickelates, present a tolerance or Goldschmidt factor close to the lower limit due to the small size of the rare earths and to the high ionic radius of the M^{2+} compared to the size of their respective sites. Thus, the A_2O_2 layer is in extension while the MO_2 sheet is in compression compared to the ideal quadratic structure

(space group I4/mmm). To release these structural constraints, several solutions are taken by the compounds:

i) The pleating of the MO_2 plan, the octahedra tilting around the a axis and giving to the structure an orthorhombic symmetry (space group Bmab), *Fig. I-31b*.

ii) The insertion of additional oxygen atoms in the A_2O_2 plans, leading to the elongation of the A-O bonds and thus to the release of the constraints. Simultaneously, the oxygen over-stoichiometry induces the partial oxidation of M^{2+} in M^{3+} in the MO_2 plans, which consequently decreases the constraints by releasing the MO_2 plans contraction. This is the reason why the rare earth nickelates prepared in air are over-stoichiometric in oxygen and formulated $A_2NiO_{4+\delta}$, the over-stoichiometry level δ being directly linked to the radius of the rare earth involved.

The rare earth nickelates are Mixed Electronic Ionic Conductors (MIECs), the electronic conductivity (relatively high at the working temperatures) being linked to the mixed M^{2+} / M^{3+} valence, whereas the ionic conductivity (high compared to most of the perovskite-type cathode compounds) is induced by the oxygen diffusion through the interstitial and apical oxygen networks of the structure.

It is worth noting that the structure of $La_2NiO_{4+\delta}$ is orthorhombic of space group Fmmm, therefore in between the "ideal" structure I4/mmm and the orthorhombic Bmab adopted by $Nd_2NiO_{4+\delta}$ and $Pr_2NiO_{4+\delta}$. For the two latter compounds, a crystallographic transition Bmab / I4/mmm occurs in air around 600-700°C, here illustrated in the case of $Nd_2NiO_{4+\delta}$ (*Fig. I-32*).

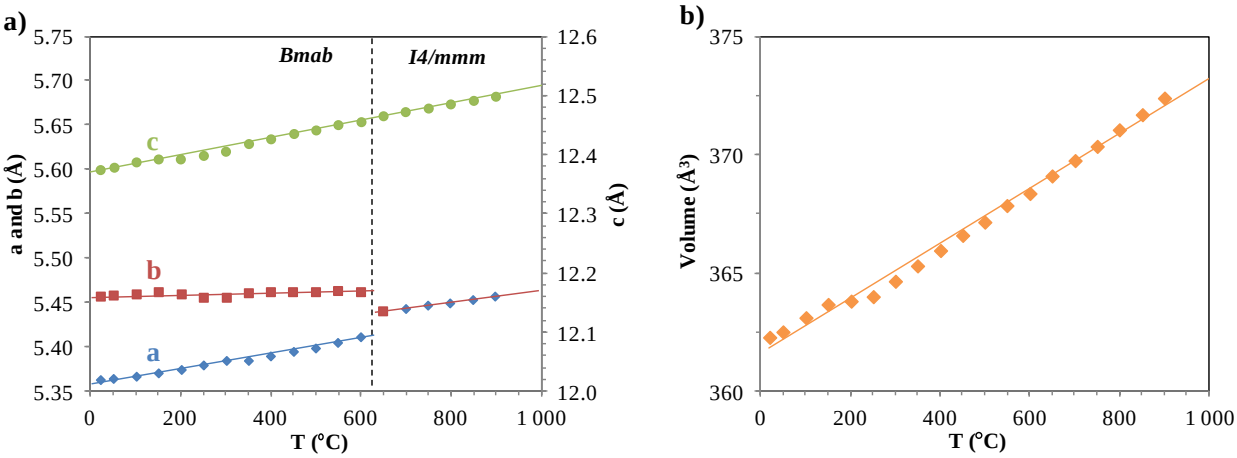

Figure I-32: Thermal evolution of a) the lattice parameters and b) the cell volume of $Nd_2NiO_{4+\delta}$ [187].

However, the evolution of the volume of the lattice with the temperature is linear, including during the transition, indicating no thermomechanical constraints, also confirmed by the linear evolution of the thermal expansion coefficients of the materials.

- Properties and performance

Total and ionic conductivities, diffusion coefficients and thermal expansion coefficients for selected A_2MO_4-type compounds are reported in *Table I-3*.

Table I-3:
Conductivities and oxygen diffusion coefficients (D*) at 700°C, and thermal expansion coefficients TEC) of selected $A_2MO_{4+\delta}$ oxides.

Compounds	σ_{tot} (S cm^{-1})	σ_{ionic} (S cm^{-1})	D* (10^{-8} cm^2 s^{-1})	TEC (10^{-6} K^{-1})	T (TEC)
$LaPrNi_{0.9}Fe_{0.1}O_{4+\delta}$				13.4 [201]	300-1100K
$La_2NiO_{4+\delta}$	50 [202-204]		3.38 [203]	12.6 [205]	300-1275K
$La_2Ni_{0.9}Fe_{0.1}O_{4+\delta}$				12.8 [201]	300-1100K
$La_2Ni_{0.9}Co_{0.1}O_{4+\delta}$	47.3 [187]			10.5 [201]	ND
$La_2Ni_{0.98}Fe_{0.02}O_{4+\delta}$	46.4 [201]			13.2 [201]	300-1100K
$La_2Ni_{0.8}Cu_{0.2}O_{4-\delta}$	52 [205]			13.9 [205]	300-1275K
$La_2Ni_{0.8}Co_{0.2}O_{4+\delta}$	72 [187]	7×10^{-3} [187]	2.2 [187]		
$La_2Ni_{0.88}Fe_{0.02}Cu_{0.1}O_{4+\delta}$	40 [201]			10.5 [201]	300-1100K
$La_2Ni_{0.75}Cu_{0.25}O_{4+\delta}$	50 [206]		3 [187]		
$La_2Ni_{0.6}Cu_{0.4}O_{4+\delta}$	70 [205]	4×10^{-3} [187]	1.5 [187]	13 [205]	300-1275K
$La_2Ni_{0.5}Cu_{0.5}O_{4+\delta}$	35 [206]	7×10^{-3} [187]	2.2 [187]	12.8 [206]	ND
$La_2Ni_{0.4}Cu_{0.6}O_{4+\delta}$	25 [205]		1.38 [203]	13.5 [205]	300-1275K
$La_2Ni_{0.25}Cu_{0.75}O_{4+\delta}$	25 [206]		1.8 [187]	12.7 [206]	ND
$La_2CuO_{4+\delta}$	5 [205]			10.6 [205]	300-1275K
$La_2CoO_{4+\delta}$	5 (750°C) [205]		2.5 (500°C) [205]		
$La_2Cu_{0.9}Co_{0.1}O_{4+\delta}$				13.3 [201]	300-1080K
$La_2Cu_{0.98}Co_{0.02}O_{4+\delta}$	15 [201]			12.2 [201]	470-1050K
$La_2Cu_{0.7}Co_{0.3}O_{4+\delta}$	3 [201]			12.6 [202]	300-1080K
$La_{1.9}Sr_{0.1}NiO_{4+\delta}$			1 [203]		
$La_{1.9}Sr_{0.1}Ni_{0.9}Fe_{0.1}O_{4+\delta}$	63 [202]			12.7 [202]	300-1100K
$La_{1.9}Sr_{0.1}Ni_{0.98}Fe_{0.02}O_{4+\delta}$	82.5 [202]			12.5 [202]	300-1100K
$La_{1.7}Sr_{0.3}NiO_{4+\delta}$	90 [207]			11.3 [207]	300-1275K
$La_{1.6}Sr_{0.4}NiO_{4+\delta}$				13.2 [207]	300-1275K
$La_{1.4}Sr_{0.6}NiO_{4+\delta}$	100 [207]			11 [207]	300-1275K
$La_{1.4}Sr_{0.6}CoO_{4+\delta}$	15 [207]			11 [207]	ND
$La_{1.3}Sr_{0.7}CoO_{4+\delta}$	65 [207]			9.6 [207]	300-1275K
$La_{1.2}Sr_{0.8}MnO_{4+\delta}$	0.6 [208]				
$LaSrNiO_{4+\delta}$	135 [187]				
$LaSrFeO_{4+\delta}$	3.2 [209]				
$LaSrCoO_{4+\delta}$	135 [207]			14.3 [207]	300-1275K
$LaSrAlO_4$	5.4×10^{-4} [187]	1.6×10^{-2} [187]			
$La_{0.9}Sr_{1.1}FeO_{4+\delta}$	1.7 [207]			12.7 [207]	300-1275K
$La_{0.8}Sr_{1.2}Mn_{0.4}O_{4+\delta}$	3 [208]				
$La_{0.8}Sr_{1.2}FeO_{4+\delta}$	25 [207]				
$La_{0.7}Sr_{1.3}FeO_{4+\delta}$	19 [209]				

Compounds	σ_{tot} (S cm^{-1})	σ_{ionic} (S cm^{-1})	D* (10^{-8} cm^2 s^{-1})	TEC (10^{-6} K^{-1})	T (TEC)
$La_{0.6}Sr_{1.4}MnO_{4+\delta}$	3.2 [208]			15.1 [208]	300-1075K
$La_{0.6}Sr_{1.4}FeO_{4+\delta}$	19 [209]		1 [187]		
$La_{0.5}Sr_{1.5}MnO_{4+\delta}$	7 [187]		2.5 [187]		
$La_{0.5}Sr_{1.5}Mn_{0.5}Fe_{0.5}O_{4+\delta}$	0.4 [187]		3.2 [187]		
$La_{0.5}Sr_{1.5}FeO_{4+\delta}$	22 [209]		4.8 [187]		
$La_{0.4}Sr_{1.6}MnO_{4+\delta}$	2 [208]			14 [208]	300-1075K
$La_{0.2}Sr_{1.8}MnO_{4+\delta}$	1.5 [208]			15.6 [208]	300-1075K
$NdSrCoO_{4+\delta}$	61 [210]			15 [210]	300-1075K
Nd_2NiO_4	27 [206]	5.73×10^{-3} [211]	1.5 [211]	12.7 [206]	1173K
$Nd_2CuO_{4+\delta}$				10.1 [202]	300-1050K
$Nd_{1.9}Ca_{0.1}NiO_{4+\delta}$	80 [187]	1.6×10^{-2} [187]	3.5 [206]		
$Nd_{1.95}NiO_{4+\delta}$	100 [206]	1.6×10^{-2} [187]	5 [187]		
$Nd_{1.90}NiO_{4+\delta}$	80 [206]		0.6 [206]		
$Nd_{1.8}Ca_{0.2}NiO_{4+\delta}$	80 [206]				
$Nd_{1.2}Sr_{0.8}CoO_{4+\delta}$	37 [210]			13.8 [210]	300-1075K
$Nd_{0.8}Sr_{1.2}CoO_{4+\delta}$	123 [210]			15.8 [210]	300-1075K
$Pr_2NiO_{4+\delta}$	100 [206]	2.6×10^{-2} [187]	5 [206]	13.6 [206]	1173K
$Pr_2Ni_{0.9}Fe_{0.1}O_{4+\delta}$	173 [212]			16.66 [212]	970-1300K
$Pr_2Ni_{0.8}Cu_{0.2}O_{4+\delta}$	190 [212]			13.24 [212]	300-1030K
$Pr_2CuO_{4+\delta}$	90			10.21 [202]	300-1070K
$Pr_{1.7}Sr_{0.3}NiO_{4+\delta}$	113.88 [211]			15.0 [211]	300-1275K
$Pr_{1.4}Sr_{0.6}NiO_{4+\delta}$	94.87 [211]			14.9 [211]	300-1275K
$Pr_{1.4}Sr_{0.6}MnO_{4+\delta}$	3.25 [211]			16.1 [211]	300-1275K
$Sr_2MnO_{4+\delta}$	0.3 [210]			16.5 [210]	300-1075K
$SrNdCoO_{4+\delta}$	0.19 (600°C) [213]				
$Sm_{1.4}Sr_{0.6}NiO_{4+\delta}$	80 [211]			11.8 [211]	300-1275K

$La_2NiO_{4+\delta}$ is the most widely studied compound among the nickelates [124-126]. However, this material reacts with YSZ, forming $LaNiO_3$, NiO or the pyrochlore phase $La_2Zr_2O_7$ [214]. Substituting the nickel by Fe or Cu did not improve substantially the conductivity level and the oxygen diffusion coefficients D* were found lower. Phases with neodymium, strontium, samarium or praseodymium on A-site have been investigated, with improved conductivity and oxygen diffusion coefficient noticed in the case of Pr. But it is known that phases based on praseodymium react strongly with the common YSZ electrolyte to form the insulating phase $PrZrO_3$. Mixes Pr / Sr, La / Sr, Sm / Sr and La / Pr were also attempted, with an improvement of the conductivity in the phase $LaPrNiO_{4+\delta}$ but a decrease of D* [201]. Substitution on B-site on the phase $Pr_2NiO_{4+\delta}$ with Fe and Cu improved significantly the total conductivity level [212], but in the case of substitution with iron the TEC is generally

too high. Poor performance is observed for the aluminates, the ferrites and the manganites, whereas promising properties are shown for the cobaltites [187]. Globally, the best performance is observed for the nickelates, with TEC matching with the state-of-the-art YSZ electrolyte.

The phases with a sub-stoichiometry in rare earth developed at the Institut de la Chimie de la Matière Condensée de Bordeaux (ICMCB - CNRS) showed increased conductivities and high oxygen diffusion coefficients, and exhibited good electrochemical performance. For instance, changing A-site deficiency x from 0 to 0.05 in $Nd_{2-x}NiO_{4+\delta}$ increased the conductivity by a factor 3, as illustrated in *Fig. I-33*. This may be due to an increase of the electron hole concentration to compensate Nd - vacancies [215].

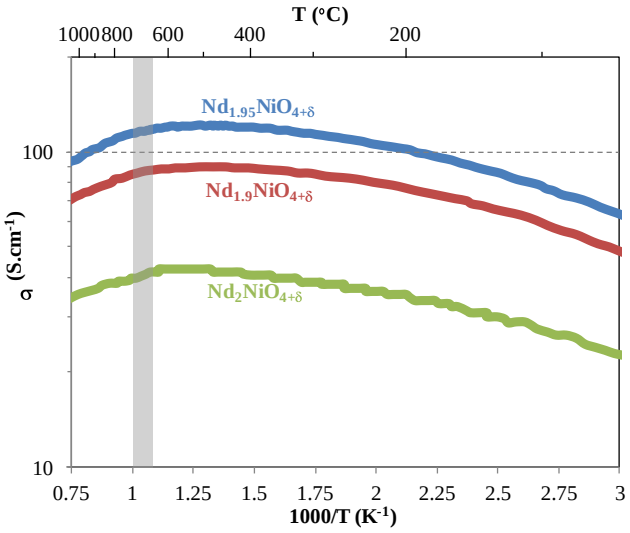

Figure I-33: Thermal variation of the total conductivity for the compounds $Nd_{2-x}NiO_{4+\delta}$ [187].

Finally, the phases $Nd_{2-x}NiO_{4+\delta}$ have been reported to be stable under both anodic and cathodic polarisation, and are therefore also studied for high temperature electrolysis [216].

3.3.4 *Interconnect materials*

Among all the cell components, interconnect material requirements are the most demanding. The role of interconnects is not only to make the electrical (current) connection in between the cells stacking, but also to ensure the separation of the different gases in the stack and a uniform distribution of heat and fuels in the cell.

Apart from cost and easy handling for mass-production requirements, interconnect materials must display [217-218]:

- high electronic conductivity (1 S cm^{-1}) with preferably no ionic contribution in SOFC operating environments,
- chemical stability in both fuel and air,
- thermal expansion coefficients comparable with the other cell components,
- high mechanical strength (especially in the planar configuration),
- fairly high thermal conductivity (5 W m^{-1} K^{-1}),
- chemical stability with the other components,
- low gas permeability.

Two classes of materials fulfilling these requirements are considered: ceramics and metals (or metallic alloys). Since this work focuses only on electrolyte and electrode materials, interconnects will be here only briefly reviewed. For more details, readers are invited to refer to literature reviews [217, 219-220].

a) Ceramic interconnects

Concerning ceramic interconnects, lanthanum chromite ($LaCrO_3$) is currently the most common candidate material for SOFCs. Indeed, this material exhibits a relatively high p-type electronic conductivity in oxidising atmosphere and n-type in reducing atmosphere, and a quite good compatibility with the other cell components (chemical, microstructural and thermo-mechanical).

In order to improve the electronic conductivity of $LaCrO_3$, doping is performed on La-site, Cr-site or both. The most common dopants for La-site are the alkaline metals $Sr^{2+}$and / or Ca^{2+} and Mg^{2+} for Cr-site [7, 217-218, 221-223]. Co^{2+} [220, 224] added on B-site also increases significantly the electrical conductivity but also the TEC, while doping with Fe^{2+} increases the electrical conductivity and lowers the TEC [217]. Some studies showed an improved ionic conductivity with Cu-doping [217] while Fu et al. showed a reduced value compared to the non-doped material [224]. Doping with Ni^{2+} on Cr-site has been shown in some studies to enhance drastically the electronic conductivity, with a transition to metallic conductor for the phase $LaNiO_{3-\delta}$. However, a limitation exists due to a resulting lower stability [217, 225]. In opposition, Fergus reported only a small increase of the conductivity with Ni^{2+}doping but with large improvement of the performance with co-doping, for instance with

Sr on A-site [220]. A good thermal expansion coefficient matching has been observed by Ding et al. by co-doping with both Ni and Co on $La_{0.85}Sr_{0.15}Cr_{0.95}Ni_{0.02}Co_{0.02}O_3$ [225]. More recently, Deng et al. showed that A-site excessive doping with Sm^{3+} enhances significantly the electronic conductivity while improving the sinterability of the samples [226].

Indeed, a big issue related to lanthanum chromite interconnects concerns their poor sinterability due to the evaporation of Cr, increasing manufacturing complexity and costs [60, 224, 227-228]. Thus, another role of the doping of lanthanum chromites is to improve their sinterability. V^{5+} [221, 227], Co^{2+} [221, 225, 227, 229], Ni^{2+} [225, 227], Cu^{2+} [225], Zn^{2+} [222, 230-231], Al^{2+} [7, 221, 229], Ca^{2+} [230] and Ti^{4+} [221, 232] doping or co-doping have been extensively studied over the past decades, with generally improved sinterabilities (especially with V, Ti and Al-doping) while TEC is maintained at acceptable values. Phases with a Cr-deficiency showed also improved sinterability [7, 223]. Finally, some studies revealed that A-site doping with Ca^{2+} is beneficial for the densification of lanthanum chromites [7, 224-225].

Despite all the attempts for improvement, several issues are still linked to the use of $LaCrO_3$-based compounds as interconnect materials. The first one concerns the strong dependence of the electronic conductivity on oxygen partial pressure due to the formation of oxygen vacancies in reducing atmospheres [7]. The first consequence is a conductivity gradient across the interconnect material and an increase of the oxygen permeability in reducing gases, leading to the reduction of the fuel cell performance [217]. Additionally, the formation of oxygen vacancies in the anode atmosphere side leads to different thermal expansion behaviours. Associated to the low thermal conductivity (< 5 W m^{-1} K^{-1}) giving thermal gradients within the cell stack, consequent internal stress is imposed to the material leading to warping and cracking of the material and thus failure of the stacks [228, 233]. Several studies related a diminution of this expansion by adding elements such as Al or Ti [234], but it is difficult to completely avoid this behaviour without losing properties of the materials such as electronic conductivity.

Other substitutions on A-site with Ba [220], Pr [235], Nd [235], Ce [235-236] and Nb [236] or Y [7, 237] on B-site have also been reported.

Finally, for most of the compounds, the electronic conductivity level remains too low at temperatures below 800°C in reducing atmospheres, making these materials not suitable for IT-SOFCs [217].

b) Metallic interconnects

Originally developed to overcome the difficulties encountered in the design of planar SOFCs, the metallic interconnectors are now the materials of reference for IT-SOFCs due to their electronic and thermal conductivities higher than the lanthanum chromites, their low cost, easy manufacture and good workability. However, serious issues such as thermal expansion coefficient mismatch with the other cell components, oxidation in cathode atmosphere or high temperature corrosion are limiting their long term stability [7]. The particularity linked to the use of metallic interconnects is the problem of high temperature corrosion, involving the formation under fuel cell atmospheres of an oxide layer at the surface of the interconnect, named scale. In the case of high temperature alloys, this scale is providing corrosion / oxidation resistance to the interconnect [238]; however, it has to present sufficiently low growing rates to prevent huge dimensional changes and enough electrical conductivity. Alumina or silica-containing alloys are presenting extremely good oxidation resistance, with a really slow growing rate of the alumina scale. However, the very low electrical conductivity of both alumina and silica makes them unsuitable for current-collection purposes [219].

Chromium-based alloys are favoured as interconnect materials mainly because the Cr_2O_3-forming scale has comparatively low electrical resistivity level [217, 238]. Additives such as Y_2O_3, La_2O_3, CeO_2, Fe_2O_3 or NiO are often used in the alloys to promote the electrical conductivity of the chromia scale. Concerning thermomechanical constraints, alloys as Cr-$0.4La_2O_3$ or Cr-5Fe-$1Y_2O_3$ have been reported as having TEC comparable to YSZ [217, 219, 238-239].

Problems of costs and fabrication difficulties of the chromium-based alloys made attractive the development of iron-chromium-based alloys, with Cr content usually ranking from 7 to 28 Wt% for commercially available products [219]. Ferritic steels are usually preferred because they present a body-centered cubic structure allowing a better TEC matching with the other components [238-240], and chromium content is usually set at a minimum of 17 Wt% to make the Cr_2O_3 scale continuous [217, 219, 238]. Refractory elements such as Mo or W are usually added to decrease the value of TEC [219].

The high diffusivity of Cr leads to high growing rates of the Cr_2O_3 oxide layer. A compromise between high electrical conductivity and oxidation resistance should thus be found. To promote adherence of this oxide layer and oxidation resistance, commercially available Cr-based alloys inevitably contain reactive species, in the form of oxides or metals, as Y, Ce, La or Zr [217, 219, 239]. Silica and alumina are thermodynamically far more stable than

chromia, and are often added to increase oxidation resistance of the interconnect, but at quantities low enough (< 1 Wt%) to not form a continuous electrically insulating scale [219]. Nickel-chromium alloys are also studied for their improved oxidation resistance and their high mechanical strength; however, they generally present high TECs [238, 240].

Another important weakness linked to the use of chromium in alloys is the high volatility of Cr under SOFC operating environments (typically at the cathode side), which is partly responsible for the rapid degradation of the SOFC cathode properties [217, 219, 241]. Mn or Ti can be added intending to form low electrically resistant protective spinel phases on the top of Cr_2O_3, expected to inhibit the formation of volatile Cr-species [217, 219]. Coatings with compounds as doped-$LaCrO_3$ [219, 238, 241], (La,Sr)CoO_3 [241], La(Ni,Fe)O_3 [241], (La,Sr/Ca)MnO_3 [219, 238, 241], (Y,Ca)MnO_3 [241], $CoCrO_4$ [238], $(Mn,Co)_3O_4$ [238], CeO_2 [241] or metallic layers [219] have also been reported to inhibit the Cr volatilisation, as well as to decrease the oxidation rate and improve the chemical compatibility with the cell components.

3.4. Advantages and limitations of SOFC

For decades, experts have agreed that Solid Oxide Fuel Cells hold a great potential among fuel cell technologies. SOFCs are complete solid-state devices using an ionically conducting ceramic electrolyte. It is therefore simpler in concept than all the other fuel cells, as only solid and gas phases are involved. The electrolyte management issues arising with PAFC or MCFC do not occur with SOFCs, and their high working temperatures (800°C - 1000°C) allow an operation without the need of precious metal catalysts and either H_2,CO or hydrocarbons as fuels [14]. Such temperatures are necessary to assure a sufficient ionic conductivity of the electrolyte, which has high activation energies (E_a) for the ionic transport (for example, for YSZ, $E_a \sim 1$ eV [242] compared to values around 0.1 eV for Nafion electrolytes in PEMFCs [243]). Furthermore, the high-temperature functioning allows the production of wasted heat, which can be transformed into electricity (co-generators, coupling gas turbines) [244]. The systems can thus reach efficiencies up to 85%.

The high working temperatures of the SOFCs are nonetheless presenting also drawbacks. There are thermal expansion mismatches among materials leading to thermomechanical constraints, and sealing is difficult in the flat plate configuration. The high operating temperature places severe constraints on material selection and results in difficult fabrication processes. Corrosion of metallic stack components (such as interconnects in some

designs) is also a challenge. These factors limit stack-level power density, thermal cycling and stack life.

Decreasing the operating temperature of the SOFC technology would provide some technological and economical advantages: decrease of the constraints on materials, cost reduction (by using less costly metal alloys for interconnect and external components and cheaper fabrication methods) and improvement of lifetime of the stacks, through slowing down thermally-activated degradation processes of components such as corrosion of metallic interconnect. Thus, research efforts are made nowadays on decreasing the operating temperature of this technology typically down to 600 - 800°C; these kinds of fuel cells are called Intermediate Temperature Solid Oxide Fuel Cells (IT-SOFCs).

However, the decrease of the operating temperatures to the intermediate range sharply affects the performance of the cells [136, 234, 244]. Indeed, if the working temperature decreases, the ionic conductivity of the electrolyte decreases in an exponential way. Furthermore, this decline involves a fall of the kinetics of the redox reactions, and thus the decrease of the transfer of charged species (reduction of the electro-catalytic activity of the electrodes).

Also, as mentioned previously, SOFCs are attractive for their flexibility in the choice of the fuel and their reduced sensitivity to fuel contaminants (as for example H_2S in natural gas or biogas). However, in the case of hydrocarbon fuels, the anode is vulnerable to deactivation by carbon coking, stemming from the cracking of methane (Eq. 5) or the Boudouard reaction (Eq. 6). In addition, it has been shown that both the poisoning effect from contaminants and carbon coking are strongly dependant on the temperature ([245] and [246], respectively), thus being more significant in the intermediate temperature range.

$$CH_4 \rightarrow C + 2H_2 \quad \textbf{(5)}$$

$$2CO \rightarrow C + CO_2 \quad \textbf{(6)}$$

To compensate these losses, two solutions are proposed at the moment:

- decrease the thickness of the electrolyte (< 15 µm),
- find higher performing materials.

4. Motivation and aim of the present work

Major hurdles to the industrial deployment of the SOFC technology remain to date insufficient reliability and longevity and unacceptably high costs. Although the emerging IT-SOFC technology should release some of the issues regarding SOFCs, the performance of the fuel cells based on classical ceramic materials (i.e. yttria stabilised zirconia (YSZ) as electrolyte, its corresponding cermet (Ni / YSZ) as anode and $La_{1-x}Sr_xMnO_3$ (LSM) as cathode) are sharply lowered at intermediate temperatures. In this case, the requirements on the cell materials are even more stringent due to the fact that the materials should show the same performance but at lower temperatures.

Concerning the cathode side, mixed ionic electronic conducting materials (MIEC) have been shown as promising for operation at the intermediate temperature range. In this regard, a typical IT-SOFC cell involves the association of the standard YSZ electrolyte with LSCF cathode. However, thermomechanical constraints due to TEC mismatch first between YSZ and Ni (10.5 10^{-6} K^{-1} vs. ~17 10^{-6} K^{-1}, respectively [247]) and between YSZ and LSCF (17.5 10^{-6} K^{-1} [248]) could lead to problems as cracking or delamination during cell elaboration and thermal cycling. Also, a penalising chemical reactivity occurs between YSZ and LSCF, leading to the formation of an insulating $SrZrO_3$ layer at the electrolyte / electrode interface. A barrier layer, generally made of GDC, is therefore often needed in between the two phases, increasing the cell elaboration complexity.

Due to its intrinsic properties, such as high ionic conductivity around 10^{-2} S cm^{-1} at 700°C, and good chemical stability over a wide range of oxygen partial pressures and in CO_2 atmosphere [119-120, 125-126, 132, 249-254], the perovskite oxide $BaIn_{0.3}Ti_{0.7}O_{2.85}$, labelled BIT07 (patent IMN-CNRS / EIFER-EDF n°0350807 from 2003), constitutes a potential alternative to YSZ to be used as an IT-SOFC electrolyte. In addition, in comparison with fluorite-structured YSZ, its cubic perovskite structure may offer an improved compatibility with the usual perovskite-structured (or derivates) cathode materials. For instance, a beneficial reactivity has been found between BIT07 and LSCF leading to the formation of a conducting perovskite-structured solid-solution; promising performance at button cell level have been obtained at intermediate temperature (700°C) for this cathode / electrolyte association [249], making BIT07 a promising material for application as IT-SOFC electrolyte.

Cathode materials that could be associated to BIT07 are the MIECs $Ln_{2-x}NiO_{4+\delta}$ (Ln = La, Nd, Pr), labelled LnN, (patent ICMCB-CNRS / EIFER-EDF n° 0403036 from 2004),

presenting a crystal structure deriving from the perovskite structure, as a good thermal expansion matching is found with BIT07 (12.2 10^{-6} K^{-1} vs. 12.7 10^{-6} K^{-1} for BIT07 and LnN, respectively [126, 187]. Furthermore, this family of materials showed enhanced performance compared to the standard electrode material LSM [187, 207, 209, 255-260] as well as higher oxygen diffusivity compared to LSCF [204], and have been validated through French national projects (Semi-EHT (ANR2005), Tectonic (ANR2005), Condor (ANR2008), Armanasol (ADEME2004)) and international projects (RealSOFC FP6, SOFC600 FP6, METPROCELL JTI10).

The purpose of the present work is to investigate the potential of these alternative materials by coupling them in an anode-supported SOFC architecture which can operate at intermediate temperatures. The anode-support configuration has been selected for the expected higher performance compared to electrolyte-supported cells. Industrially well-established and low cost shaping techniques have been selected for their potential of easy up-scaling (especially for tape casting and screen printing), also giving high quality layers. The anode, a standard cermet Ni / BIT07, will be elaborated by tape casting; the BIT07 electrolyte layer by vacuum slip casting (VSC®) and the LnN cathodes by screen printing. Obtained cells will be electrochemically tested and the assemblies optimised for high performance at 700°C. This project takes place in a larger context in parallel to the French national project INNOSOFC (ANR2009) involving five partners: IMN, ICMCB, CEA, Marion Technologies and EIFER.

In this context, *Chapter II* will be devoted to the description of the shaping and characterisation techniques used in this project. *Chapter III* will present experimental processes for the elaboration of the cells as well as microstructural characterisations and *Chapter IV* will provide the results of the electrochemical tests performed on the assemblies.

Chapter II

Shaping and characterisation techniques

As already mentioned, the elaboration processes used in this study present the advantages of being easy, low cost, giving high quality layers (vacuum slip casting) and being industrially applicable (tape casting, screen printing). But even if their basic principles are in theory easy, in practice a large number of parameters have to be considered. It can be cited notably the raw powders, all the (organic) additives to be used, the sintering treatments or even the processes themselves. A wide variety of problems and defects can be encountered if not each parameter is well handled and controlled when manufacturing the cells. Each fabrication step and the required techniques entail specific difficulties and an appropriate knowledge of the process is needed to obtain an adequate final product with the required characteristics.

In this chapter, the techniques chosen are described: tape casting, vacuum slip casting and screen printing. The main difficulties and interrelated aspects inherent to each fabrication process in use are also approached. Finally, some examples of typical defects that can be found are also presented, the objective being to give the reader tools to understand the methods and the different challenges and implications exhibited by each technique.

Characterisations of the produced cells from the characteristics of the raw materials to the microstructures are also key features, first to validate and optimise the elaboration processes and second to estimate the quality of the final cells. Measurement of electrical and electrochemical performance is also mandatory to evaluate the feasibility of the produced assemblies. The second part of this chapter will be thus devoted to the description of the characterisation techniques involved in this work (powders, microstructural and electrochemical characterisations).

This chapter will serve as a basis for discussions in the following chapters.

1. Shaping techniques

1.1. Tape casting

1.1.1 *Basic principle*

As already mentioned in *Chapter I*, tape casting is a fluid forming process for manufacturing thin sheets of any powder material. While in industry the casting is done by a moving polymer carrier film under a reservoir containing the slip (suspension of powder in a liquid), it involves in our case the spreading of the slip on a surface, the casting being done by the action of a moving doctor blade as illustrated in *Fig. II-1*.

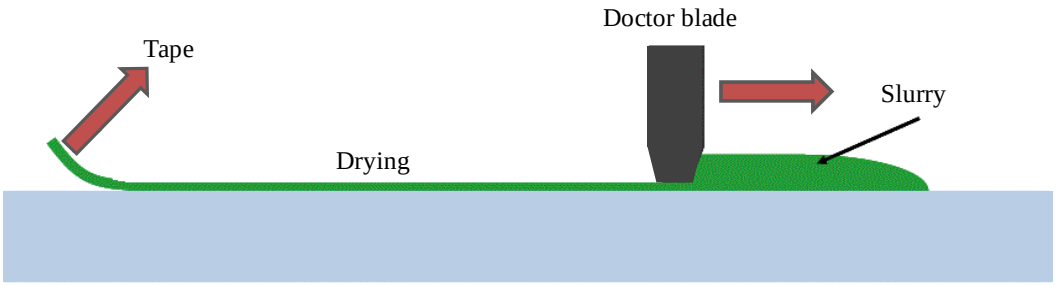

Figure II-1: Schematic of the tape casting process.

The device used in this work is a ZAA 2300 automatic film applicator coater from Zehntner GmbH, Switzerland, shown in *Fig. II-2*. The tapes are casted on a removable glass plate of 553 mm × 300 mm × 15 mm, with a silicon-coated polyethylene film as a carrier. The stop and start positions for the tapes are individually adjustable, and drawing speed can be settled between 0 and 99 mm / s (adjustable in 1 mm / s step). The doctor blade is 200 mm width and allows gaps between 0 and 3000 µm.

The arrangement and packing of the particles in the green tape determine the sintering behaviour and the final properties of the product. Thus, there is an interrelation between the slurry and the green tape and between the green tape and the sintered product. A uniform and homogeneous product can be obtained if the starting suspension has a high homogeneity and stability. Some organic additives are therefore necessary to assure the stability of the suspension (dispersants). Furthermore, to confer adequate strength and flexibility to the tape for its manipulation, binders and plasticisers are added. The slurry formulation is of crucial importance in the tape casting process and requires a careful selection and an accurate control on the processing additives.

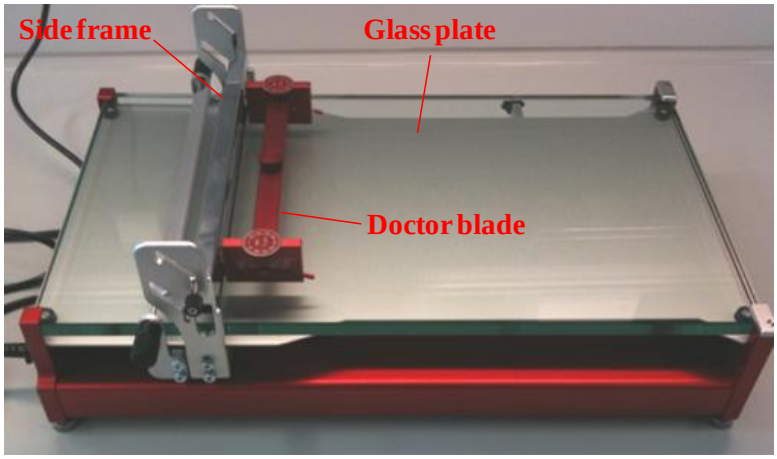

Figure II-2: Picture of the ZAA 2300 automatic film applicator coater from Zehntner GmbH.

1.1.2 *Slurry preparation*

In this section, a discussion about the different slurry components in terms of role and selection will be made, their role and their selection for the case of non-aqueous tape casting, i.e. using non-aqueous vehicle.

a) <u>The powders</u>

In all the material fabrication processes, the powder is the main ingredient for a batch formulation. In many cases, powder characteristics is the aspect on which the operator can have a minimum control since they are selected *ab-initio* for providing specific properties. Essentially, the additives in the tape casting process are used to obtain and hold the powder particles together in order to produce a sintered layer with appropriate size, shape and properties and are burnt during the sintering step. Therefore, it is essential to well characterise the starting powders in terms of average **particle size distribution**, **powder density**, **surface area** and **trace-impurity level**.

Numerous studies concerning the particles, their shape and size and their effect on ceramic processing have been reported in the literature [41, 44]. All these aspects play a strong role on the final microstructure of the tape and have therefore to be considered carefully.

The surface area is the most significant factor in its interaction with organics such as dispersants or binders since the total powder area is proportional to the amount of organics to be added to provide the proper dispersion or binding quantities. Concerning the particle size, small particles have a high surface energy and thus a high driving force for sintering. This

leads to higher shrinkage as well as the need of higher concentrations of additives, and therefore potential problems during drying, debinding (organic burnout) and sintering. The final microstructure depends also on the shape and size distribution of the particles since the packing structure is directly related to them [261]. However, small particles are needed to obtain a homogeneous and smooth surface in a thin tape. Particles with a wide range of sizes affect also strongly the homogenous sinterability of the tape by contributing to secondary grain growth. Furthermore, choice of the particle size is also related to the density of the powders. For example, high density powders may require the use of smaller particle size in order to keep the very heavy particles in suspension.

b) The solvents

The tape casting process is a "fluid forming" process where the powder has to behave as a fluid. To achieve this degree of flowability and formability, the powder is suspended in a solvent. The solvent must dissolve the organic additives added to the slurry as binders, plasticisers, dispersants or others, without reacting chemically with the powders. Moreover, the solvent has to evaporate quickly: the drying speed is the determining factor in the casting speed and therefore in the production capacity. However, too fast drying leads to the formation of a skin on the top of the tape and can also induce cracking [41]. Thus, a very efficient solvent will be a balance between the two extremes.

Most of the publications report the use of multiple solvents in slurry formulations, with major interest in increasing their ability to dissolve. Other important advantages of using a mixture of solvents are a better control of the drying speed, of the rheological properties, of the costs and of the safety issues. In order to avoid differential volatilisation when dealing with mixtures of solvents, azeotropic mixtures are used. The azeotropes combine the dissolving capabilities of each solvent while evaporating as a single liquid [41].

c) The dispersants

In the tape casting process, one of the most important steps is the dispersion milling procedure. The stability of a suspension depends on the sign and magnitude of the total energy of interaction between particles. As a result of high surface area, agglomerates and clusters are formed to decrease the solid-liquid surface area via interparticulate forces like van der Waals or hydrogen bonds. The agglomerates or clusters tend to trap air in the interstitial sites between particles that will cause trouble in deairing and form bubbles in the green tape. Furthermore, they cause inhomogeneities in the green tapes by introducing local high porosity

regions. When the polymeric binder is added, it will envelop the particle group instead of the individual particles, making the particle group permanent throughout the rest of the process [41].

A dispersant is an additive that works to keep particles apart, increasing the homogeneity of the slip / tape, and thus of the final product. The repulsion interaction can be provided by two general mechanisms: electrostatic repulsion, in which acids are adsorbed on the surface of the particles and are dissociated to leave a charge on the particle surface, and steric repulsion, in which a long-chain polymer is adsorbed onto the particle surface [262]. A third mechanism, referred as electrosteric stabilisation, is a combination of both steric and electrostatic repulsion. The stabilisation mechanisms are illustrated in *Fig. II-3*.

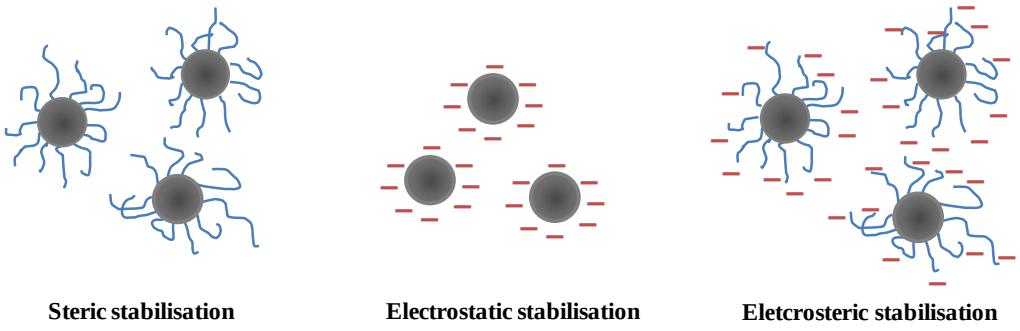

Figure II-3: Methods of stabilisation of particle suspensions.

Another interest of the dispersant is to decrease the viscosity of the slurry, allowing higher solid-loadings or a decrease of the amount of solvents and therefore of the drying speed, the costs and the shrinkage.

d) <u>The binders</u>

Typically, binders are precursors as monomers or emulsion of particles that become long-chain polymers during drying. Binders are probably the **most important processing additives** in the system because they supply the network that holds the entire chemical system together. For Mistler and Twiname [41], a green tape can be viewed as a polymer matrix that surrounds entrapped particles. A simile is presented by Moreno [263] in his laboratory report, describing the binding system as polymeric molecules adsorbed on the surface of the particles, forming organic bridges between them. There are much dispersions where the binder acts as a second dispersant and replaces some of it on the surface of the particles. The binder is the only continuous phase in the green tapes and provides properties as strength,

plasticity, toughness and flexibility. It must be chosen regarding its compatibility with the system, its solubility, viscosity, strength, cost, burnout temperature (with no residues) and glass transition temperature (T_g) [41, 263].

There are many types of binders used in ceramic processing such as the cellulose derivates, the polyvinyls and the polyacrylates. The main difference between them is the burn-off characteristics. For each category of polymers, various chain lengths are available, characterised by the molecular weight. Lower molecular weight polymers have shorter lengths resulting in lower viscosities and therefore higher solid loadings, but in counterpart offering weaker tapes.

e) The plasticisers

Plasticisers are added to the system to confer sufficient flexibility to the green tape for easy handling and storage. Plasticisers work either on or around the binder chains, allowing motion inside the tape matrix without breaking the matrix itself.

Two distinctly different mechanisms can be used to plasticise a green tape:

- Type I plasticisers, referred as T_g (glass transition temperature) modifiers or binder solvents [264], are chemicals that soften the polymer chains between the particles, allowing them to stretch more easily. They act either by shortening the polymer chain lengths or by partially dissolving them. Essentially, the only difference between the solvent and the type I plasticiser is the volatility [41], type I plasticiser being a slow-drying solvent.

- Type II plasticisers act as lubricants in the ceramic matrix [41], avoiding frictions in between the polymer chains. They allow a better mobility between the particles, and decrease also the strength by getting between the polymer chains and thus decreasing the van der Waals bonding between adjacent chains [44]. Type II plasticisers can help to prevent cracking during the drying step, decrease the yield stress, can act as release agents (to allow easy removal from the substrate) and increase the strain to failure of the green bodies.

The most common plasticisers are phtalate (type I) and glycol (type II) derivates.

Relationships between binders and plasticisers are strong, so that the binder / plasticisers system is called “binder system”. The optimum flexibility is obtained when the correct binder / plasticiser(s) system is selected and the relative concentrations adjusted properly.

Some other additives in the slurry formulations have been reported, as wetting agents (help the formation of a well defloculated suspension), homogenisers (as cyclohexanone) or antifoaming (mainly used when polymeric emulsions are used as binders) [263], and will not be described in this work.

f) Materials processing

The order in which the organics are added to the mill is critical. As already mentioned, dispersing agent is usually added first to provide efficient deagglomeration process. Thus, the binder will not encapsulate agglomerates and competitive adsorption on the particle surface can be prevented. Also, the binder is generally more soluble in the plasticisers than in the solvents, so adding first the plasticisers will help its dissolution [41, 265].

The first step in the preparation of a slurry is thus the dispersion milling of the powder(s) in the presence of dispersant in the solvent(s). As said previously, the purpose of this step is to break down the agglomerates and to coat the particles with the dispersing agent to keep them apart. Several milling equipments can be used, as ball-mills or planetary mills. Usually, a predetermined amount of dispersant is solved in the solvent(s) by milling with a grinding media and the powders are then added. The dispersion milling time can vary from 4 to 48 hours, depending on the "hardness" and the quantity of powder(s). The plasticisers are then added to help the dissolution process of the binder, followed by the binder itself. The slurry is mixed until the binder is completely solved.

Before casting, the air has to be removed from the slurry to avoid defects in the green tape (holes or spots). The most common technique for this process is to use a vacuum.

1.1.3 *Drying theory*

a) Introduction

In this section, important theoretical issues about the drying of casted tapes are presented. This discussion is mainly based on a book written by R. E. Mistler and E. R. Twiname, dedicated to tape casting, which gives a global overview of their experience on this elaboration process from fundamental aspects to experimental considerations [41].

With so many additives, and typically multiple solvents, the behaviour of the tape during drying can vary from slip to slip. In the tape casting process, the solvents are removed from a single side of the cast, due to the thin essentially two-dimensional shape and the impermeable carrier film on the bottom. The solvents take energy from the air and from the

rest of the tape to evaporate into the surrounding atmosphere at the surface of the tape. If evaporation occurs to expose the solid phase, a solid-liquid interface is replaced by a solid-vapour interface. The exposure of the solid phase would lead to an increase in the energy of the system; to prevent this, liquids tend to spread from the bottom part of the tape to cover the solid-vapour interface [44]. It implies that all the solvents must migrate to the surface of the tape to evaporate. The two major mechanisms for drying a tape-cast layer are, thus, the surface evaporation and the solvent transport trough the thickness of the tape to the drying surface. The transport of the solvent(s) during drying can occur either by flow if a pressure gradient exists in the liquid or by diffusion if a concentration gradient exists [44]. The solvent transport is consisting of two stages: the first one is controlled by capillary migration of the solvent and the second one is controlled by solvent diffusion through the solid layer [44, 266], the latest being the rate determining factor of the drying.

Fig. II-4 shows a schematic illustration of the drying process.

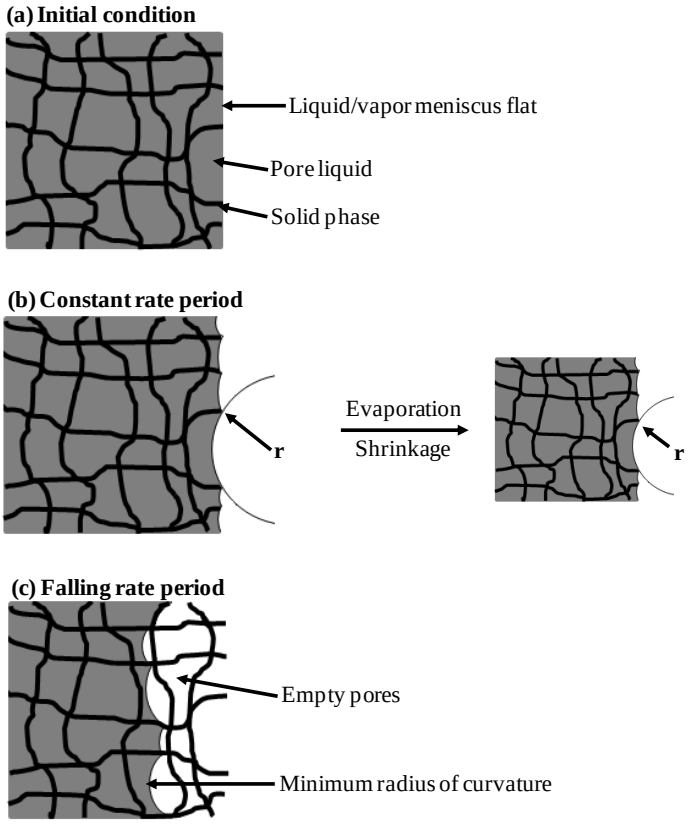

Figure II-4: Schematic illustration of the drying process [44].

Before evaporation starts, the surface is flat (*Fig. II-4a*). Then the liquid stretches to prevent exposure of the solid phase (*Fig. II-4b*) and capillary tension increases in liquid. The

solvent evaporates on the top surface, and the solvent inside the drying tape migrates to the surface by capillary action, process accompanied by the shrinkage of the tape (constant-rate period). When the surface gets critically dried (particles in contact with each other) and the solid phase stiffens, the migration of the vehicle to the top surface stops. The tension rises until the curvature radius equals the size of the pore (*Fig. II-4c*) and the liquid recedes into the matrix [267-268].

Ideally, the solvent concentration should be the same throughout the thickness of the tape for a homogeneous drying. In practice, the **drying conditions**, **tape structure**, **tape components**, and **solvent mixtures** are balanced to get as close as possible to the ideal conditions.

b) Drying rates

The rate of the surface evaporation is governed by the energy available for the solvents, the volatility of the solvent species and the vapour and saturation concentrations of the local atmosphere [41]. Different parameters can be settled to control the rate of the surface evaporation. The first one is the composition of the slurry itself, by using azeotropic mixtures of solvents. Raising the air temperature can also increase not only the evaporation rate, by giving an excess of energy for evaporation, but also the saturation concentration of the surrounding atmosphere. Many tape casting machines are equipped by an air heating system to speed the surface evaporation of the tape. Water vapour, and thus air humidity is also a part of the saturation concentration. Airflow plays a role since it allows to decrease the vapour concentration of the surrounding atmosphere and therefore to increase the speed.

However, the rate limiting factor in drying is the flow of the solvent(s) to the surface, and more particularly the diffusion through the solidified (surface) layer [266]. As concerns the diffusion of solvents, the rate is limited by the body itself, as the tape matrix is crowded by particles, binder, plasticisers, dispersant and the shrinkage of the tape occurring during drying limits the escape paths for the solvents. Large binder content fills the space between particles, limiting the diffusion rate. The particle size can be also considered, as small particles lead to better packing density and therefore slow diffusion [269-270].

To tend to an ideal case, the rates of diffusion and evaporation have to be as equal as possible. Since the surface evaporation rate is often much greater than the diffusion, inhomogeneities of the drying of the tape exist and, in the worst case, the formation of a "skin" (dry layer) on the surface of the tape is observed, while the solvent concentration does

not decrease substantially on the bottom part [41]. The skin formation remaining the most limiting factor of the diffusion through the matrix, precautions are often taken to slow the surface drying rate as much as possible, as adding skin retarders in the slurry formulation or placing containers of solvent in the drying chamber to saturate the local atmosphere. While effective, the last solution is problematic in terms of safety and fire concerns.

c) Stress during shrinkage

Since the solvents occupy a large volume of the slurry, the dimensions and structure of the tape change during their evaporation. Motion in the tape matrix is thus unavoidable as the particles are then settled under gravity, making the polymer chains of the binder shrinking and re-orientating. In most cases, the drying shrinkage is unidirectional along the z-direction (thickness): the carrier does not shrink and the tape is held in the lateral directions on the carrier surface.

In the first drying stage (capillary migration), the viscosity of the fluid phase is low enough to allow particle rearrangement, avoiding internal stresses. But when evaporation proceeds, the viscosity increases as well as internal stresses [41]. As liquid evaporates, capillary forces push the particles to approach each other until a network is formed, retaining liquid in the pores that empty as the evaporation takes place [271]. The liquid in the pores stretches to cover the dry region, and a tension develops in the liquid. This tension is balanced by compressive stresses on the solid phase, which induces the shrinkage of the tape [44, 270]. In the case of a thick tape (typically upon 50 μm depending on the particle size [269-270]), the top surface is subject to lateral tensile stresses (not constrained to shrink along the z-direction), the amount depending on factors such as solvent content or binder quantity, while the bottom part of the tape is bounded by the carrier. The top and bottom parts thus behave as different layers, leading sometimes to dramatic consequences on the quality of the green body. Some examples of defects in green bodies are presented hereafter.

d) Some examples

The response of the tape to lateral shrinkage can take several forms, depending on the energy the matrix can store, the yield, the adhesion of the tape to the carrier or the particle to particle adhesion forces [41]. For instance, if the stress is higher than what can be accommodated by the tape by storage of energy and plastic deformation, it can be released in three ways:

- if the adhesion to the carrier is less than the particle to particle adhesion, the bottom part of the tape will disengage to the carrier (effect called "self-release") to allow the bottom part to shrink.

- if both interparticulate and carrier adhesions are high, the tape curls. In this case, promoting plastic deformation by adding type II plasticiser, heating air to soften the polymer or slowing the surface evaporation rate can be solutions, but in most of the cases an appropriate conditioning of the green bodies allows their utilisation as-prepared.

- if the adhesion to the carrier is higher, then we will observe the formation of cracks. As example of solutions, increasing the type I plasticiser content can increase the stored stress of the matrix, but greater effect would be obtained by increasing the plastic deformation by adding type II plasticiser or increasing the binder content to increase the interparticulate adhesion (as well as the plastic deformation and the stress storage).

The presence of defects in the tape, as agglomerates, air bubbles, streaks or furrows on metering also promote cracking since the cracks have the tendency to nucleate at non-uniformities. Solutions as a proper slurry formulation, filtering before casting, or an appropriate de-airing step could decrease the number of defects, even if those are not completely avoidable. Increasing binder or type II plasticiser will also help the dissipation of the stress and thus the crack propagation. *Fig. II-5* gives some examples of defects that can be observed in green tapes.

The thickness of the layer plays also a role, since thick tapes need more time to dry (increased distance between the bottom and the top), therefore letting time to the polymer chains to shrink more before the tape gets solid. As a result, increased shrinkage and decreased particle mobility in the matrix (higher binder content needed to avoid lateral spreading after casting) increase lateral stress, resulting in the formation of cracks. If the bottom and the top layers dry at significantly different rates, effects as formation of wrinkles are observed. In this case, a skin is formed on the surface of the tape and solvent from the underlying slurry diffuses into the skin, making the polymer matrix of the skin layer swelling. The skin layer then wrinkles to provide additional surface area and accommodate matrix swelling. In this case, slowing the surface evaporation rate or decreasing the binder content would be solutions.

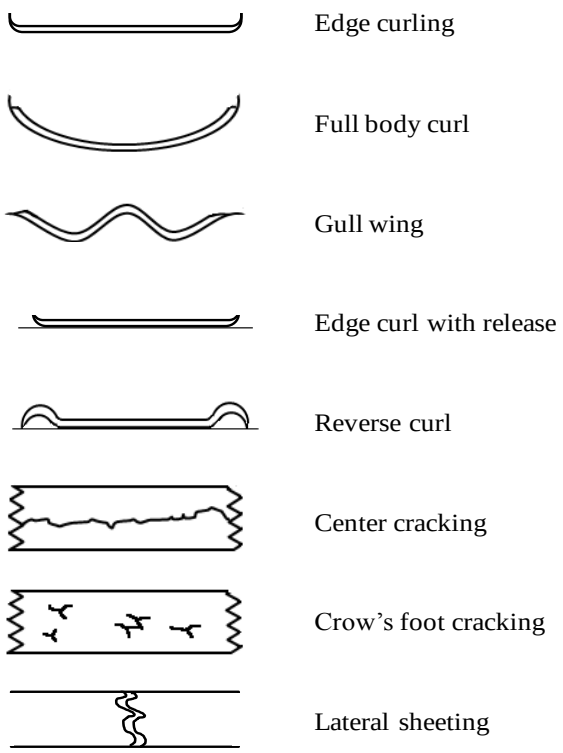

Figure II-5: Examples of observed curling or cracking behaviours of green tapes [41].

The last example that will be discussed here is the formation of non-depth cracks on the surface (cracks do not go through the entire thickness of the tape), referred as "mud flat" cracking. This is a consequence of the two layers drying: the bottom layer is drying slower, giving a higher density in comparison with the "solvent-depleted" dried surface layer. The higher shrinkage of the bottom creates tensile stress in the top layer, inducing ripping of the top layer. It results in superficial cracks or, in some cases, non-visible phenomenon as slight surface variations. Addition of type II plasticiser in this case would often solve the problem, as plastic deformation provides a tensile stress release mechanism.

1.2. Vacuum slip casting

For the production of thin electrolyte layers for planar SOFCs, a laboratory-made modified slip casting process has been used. It consists of a Plexiglas chamber, closed on the top by a stainless steel grid and connected to a vacuum pump (model V-700 from Büchi Labortechnik AG, Switzerland, ultimate vacuum < 10 mbar). The stainless steel grid serves as a support, and the samples are sealed at the edges by a silicon rubber. The tightness is ensured by closing the chamber with a Plexiglas cover fixed by a system of screws. A suspension

made of the ceramic powder, ethanol and a dispersant is applied on the samples, that are the planar and porous anode substrates, and the solvent is drawn through the pores. The vacuum accelerates the process flow. Remains then the layer of solid electrolyte particles, cast evenly on the surface [272]. Substrate sizes up to 150 × 150 mm can be used. The surface to be coated is adapted by changing the aperture size of the silicon rubber. The setup is shown in *Fig. II-6*.

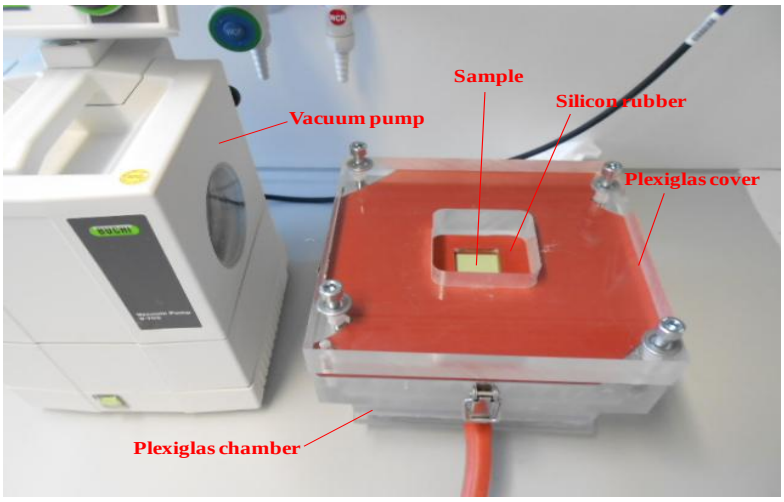

Figure II-6: Experimental setup for the vacuum slip casting process.

Using this process shows some advantages:

- easy and straightforward handling,
- excellent quality of the produced layers,
- reproducibility of the layer thickness, uniform thickness and structure,
- 2 to 50 µm layers realisable,
- little waste (the solvent can be re-used),
- long-term stable suspensions can be produced without effort.

The disadvantage of this process is the handling of large quantities of solvents and the limitation in the thickness of the layer. There is also a big influence of the structure of the substrate (surface topography, pore size, pore distribution…) on the quality of the layer.

1.3. Screen printing

1.3.1 *The screen printing process*

In the screen printing process, a paste is laid on top of a permeable screen in front of a rubber squeegee. The squeegee is moved forward, deforming the screen downwards until it makes contact with the substrate. The paste is pushed along in front of the squeegee and through the screen pattern onto the substrate. The screen just touches the substrate at the tip of the squeegee. The composition is deposited onto the substrate as the screen peels out of it [51, 273]. The process, illustrated in *Fig. II-7*, consists of the following steps:

(i) pre-printing: the open mesh area of the stencil is covered by scraping the paste,

(ii) real printing: the paste is squeezed through the mesh with the aid of a squeegee, generally in the opposite direction of the scraping movement, with a certain velocity, pressure and attack angle,

(iii) post-printing: process when the sieve snaps off from the substrate.

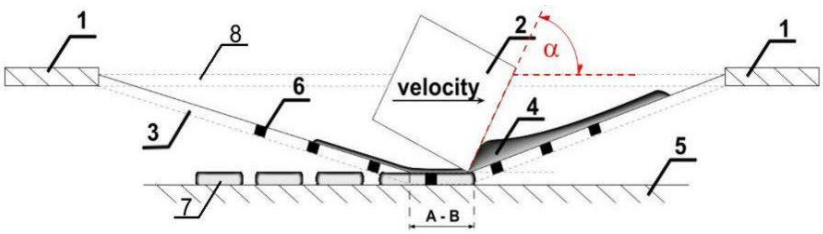

1. Frame
2. Squeegee
3. Sieve (or stencil)
4. Paste
5. Substrate
6.Mask (meshes covered with photopolymer to avoid the passage of the paste)
7. Printed layer
8. Normal stencil position
A-B Adherence distance
α attack angle

Figure II-7: Sketch of typical screen printing process [273].

In this work, screen printing has been performed with a XM semi-automatic screen printing device from EKRA (U.S), where the printing process is operated manually. This machine has been designed to print small series, in formats up to 450 × 450 mm. The pressure of the squeegee is adjustable and made using compressed air (P = 5 - 6 bar); samples are hold on the support using a vacuum. The device is shown in *Fig. II-8*.

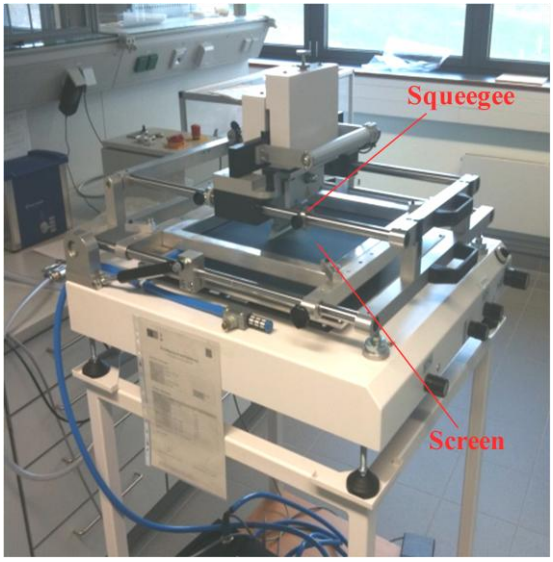

Figure II-8: Picture of the XM semi-automatic screen printing device from EKRA.

More than fifty variables are influencing the characteristics of the printed layers. Among them, we can cite:

- the screen parameters: type of screen, type of material, force of tension, warp thread diameter, weft thread diameter, type of weave (plain, twill), mesh orientation, mesh opening (width) or thickness of the sieve are having a direct influence on the printed layer. The most obvious is the direct relation between the thickness of the sieve and the one of the printed layer (usually the thickness of the sintered layer is about 25% of the wet thickness depending on the solid content in the paste). Also, the setting of the main threads of the frame with a certain angle (to the frame) will affect the edge properties of the printout. The distance between the screen and the substrate is also of great importance: it has been found in literature that a too short distance delays the snap-off of the screen, resulting diametrically in the low film uniformity, whereas a too high gap will cause an incomplete release of the paste on the substrate [274].

- the squeegee parameters: hardness, thickness, height, attack angle, force of pressure, velocity of movement or sharpness (profile / surface) are parameters to be considered. For example, a decrease in the hardness of the squeegee will increase the adherent distance, while too soft material causes deflection of the lower squeegee part, decreasing the attack angle [275]. Too low attack angles result in paste squeezing instead of scraping, while too high attack angle causes sliding of the squeegee. Low squeegee speed allows more time for the ink to flow, improving the print quality [275].

From these examples, it can be difficult to obtain good surface properties without a correct set-up of the equipment. Analogically, even with an optimum set of machine, it would be impossible to achieve high quality layer without a good paste rheology, as will be discussed hereafter.

1.3.2 *Paste formulation*

The screen printing process uses a paste as a vehicle to transport metal and / or inorganic powders onto a substrate. As it is desirable for a paste to give and maintain a crisp printing outline without spreading, yield point and thixotropic behaviour are considered. Note that the yield point corresponds to the stress threshold from which pastes would flow; thixotropy is the property of some non-Newtonian fluids to show a time-dependent change in the viscosity: the longer the fluid undergoes shear stress, the lower is its viscosity. Thixotropic fluids also revive the previous structure (determined by viscosity) within certain period of time [276]. Such behaviour is caused by the creation of a three-dimensional network structure, usually governed by hydrogen or ionic bonds that can break easily during application of a shear.

From the rheological point of view, the paste should manifest shear thinning behaviour, here elastic or viscoelastic. The "plastic" term has been introduced by Eugen C. Bingham to describe the behaviour of dispersions having a yield point. In his model, bodies under low shear stress behave like solids, while the body starts to flow and behave like a fluid after the critical threshold is exceeded. Terms "Viscoelastic liquid", "elasto-viscous liquid", "Elastic liquid" or even "memory liquid" are synonyms, and describe a body which possesses viscoelastic properties. Those fluids have a certain amount of energy stored in the fluid as strain energy. Thus, it shows partial elastic recovery (thixotropy) after the deformation stress is removed.

There is a wide range of studies on rheological properties of liquids, but only few of them involve screen printing application. Typically, as for tape casting slurries, a printing paste consists of powders and solvents with a binder, playing also the role of dispersant. It can also contain moderators, antistatic agents, adhesion promoters or even agents preventing sieves from drying up. A variety of pastes can be prepared depending on the printing needs, the suitability of the paste being determined by viscosity measurements as a function of the shear rate [277-278]. The behaviour of printing pastes will have a direct impact on the quality of the screen-printed layer (uniformity of the thickness, surface smoothness…). Special

concerns have also to be made on the de-agglomeration and the stabilisation of the pastes to avoid defects such as small points on the surface or holes if the agglomerates are bigger than the size of the mesh (typically, the size of particles / agglomerates should not excess one third of the size of a single mesh's orifice). Besides their direct influence on the viscosity of the paste, solid loadings have also to be adjusted properly: the solid-like behaviour of the paste is increasing with increased solid loadings, giving higher roughness of the layers [275]. Viscosities are also directly influencing the post-deposition flow that makes the films smoothen after printing.

1.4. Debinding and sintering

1.4.1 *Debinding*

The term binder removal or debinding refers to the removal of the binder and the other organic additives (plasticisers and dispersant) from the green body. By far, the most used method for debinding is the thermal decomposition, referred as thermal burnout or thermal debinding [279]. In this case, the organics are removed as vapour by heating, with emission of carbon and carbon monoxide, in our case in oxidising atmosphere (air) at ambient pressure.

The removal of the organics is physically controlled by heat transfer into the body and mass transport of the decomposition products out of the body. For a simple binder system, thermal debinding can be roughly divided into three steps:

- initial heating of the binder until it softens (at T_g, around 100°C),

- removal of the molten binder by evaporation (temperature range 200 - 400°C),

- further removal of the binder remaining in the tape at temperatures above 400°C, removal facilitated by the porous nature of the body.

The evaporation takes place at the surface of the tape, and for high molecular weight polymers a decomposition step (by oxidation or thermal degradation) to form lower molecular weighted chains is needed before they can diffuse through the molten polymer and evaporate from the surface [279-280]. Note that the decomposition of the binder in green bodies is more complex than for the binder alone, with for instance effects of the powders or the atmosphere on the chemistry of the binder burnout [44].

Practical binder systems consist of at least two components that differ in their volatility and decomposition behaviour. For an efficient debinding, the idea is to select materials that do not have a significant overlap in their removal temperature range: the

decomposition of the first component creates a porosity network, making easier the evaporation of the other component(s).

1.4.2 *Sintering*

The heat treatment step in which the dried, debinded green body is converted into the useful coherent solid with the required microstructure is called sintering. Sintering is one of the most important processes for the fabrication of ceramic materials, the properties of ceramic materials being modified through sintering to give the product its final characteristics [271]. Thus, the microstructure of a powder compact changes continuously and drastically during sintering.

The driving force for densification is the change in free energy by the decrease in surface area and lowering of the surface free energy by the replacement of solid-vapour interfaces. This can be accomplished by atom diffusion processes that lead to either densification of the body (by transport of matter from inside the grains into the pores), or coarsening of the microstructure (by rearrangement of matter between different parts of the pore surface). This diffusion is caused by a gradient of chemical potential. Atoms move from an area of higher chemical potential to an area of lower chemical potential. The different paths taken by the atoms to get from one spot to another are the sintering mechanisms. The six common mechanisms are (see *Fig. II-9*):

- surface diffusion: diffusion of atoms along the surface of a particle,

- lattice diffusion (from the surface): atoms from surface diffuse through lattice,

- vapour transport: evaporation of atoms that condense on a different surface,

- grain boundary diffusion: atoms diffuse along grain boundary,

- lattice diffusion (from the grain boundary): atoms from grain boundary diffuse through the lattice,

- plastic flow: dislocation motion causes flow of matter.

All of them lead to bonding and growth of necks between particles, increasing the strength of the body.

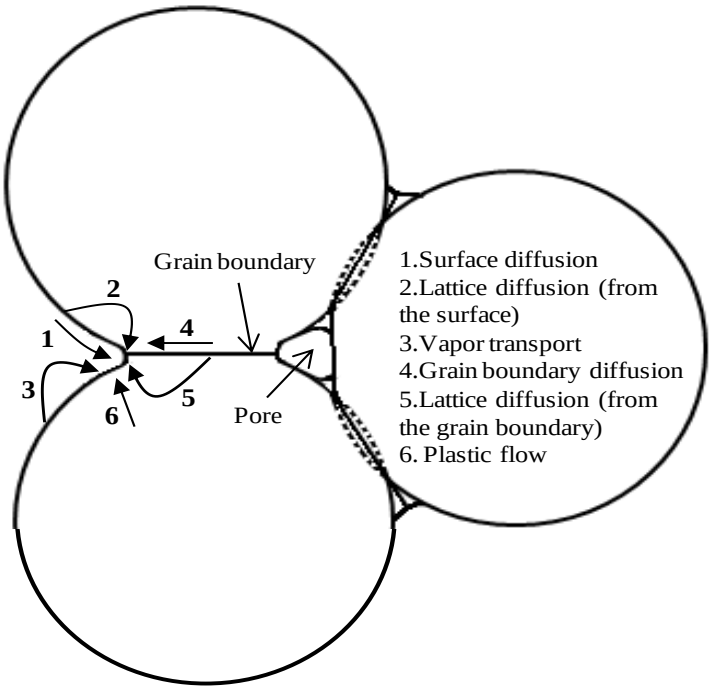

Figure II-9: Illustration of the six mechanisms that can contribute to sintering of a porous powder compact of crystalline particles [44].

One must distinguish between densifying and non-densifying mechanisms. The three first mechanisms above are non-densifying: they take atoms from the surface and rearrange them onto another surface or part of the same surface. These mechanisms simply rearrange matter inside of the porosities and do not cause pores to shrink. The term coarsening is frequently used to describe this process in porous ceramics in which the increase of the average grain size (grain growth) is accompanied by an increase of the average pore size. Grain growth happens due to motion of atoms across a grain boundary. Convex surfaces have a higher chemical potential than concave surfaces and therefore grain boundaries will move toward their centre of curvature. As smaller particles tend to have higher radii of curvature, atoms tend to move to larger grains. This is a process called Ostwald ripening; large grains grow at the expense of small grains. The three last mechanisms are densifying mechanisms: atoms are moved from the bulk to the surface of the pores thereby eliminating porosity and increasing the density of the sample.

The sintering involves a competition between these two processes, but their relative influences can be balanced by the processing parameters for a control of the final microstructure.

The domination of densifying diffusion processes will favour the production of a dense body, as required for the electrolyte, whereas coarsening diffusion processes favour highly porous microstructures, as required for the electrodes. Green bodies with large pores and small grains will lead to a porous microstructure, while higher temperatures or compact green bodies will promote the obtaining of a dense final product [44].

Other aids for densification can also be used, as applying an external pressure while heating or using an additive that will melt during the sintering, which will help the densification by promoting the packing arrangement and the Ostwald ripening (liquid phase sintering).

2. Characterisation techniques

2.1. Material characterisations

2.1.1 *X-Ray Powder Diffraction (XRPD)*

X-rays are electromagnetic radiations of exactly the same nature as light, but of very much shorter wavelength (typically 0.5 - 2.5 Å) [281]. When an X-ray beam hits an atom, the electrons around the atom start to oscillate with the same frequency as the incoming beam. In almost all directions, destructive interferences will be observed, that is, the combining waves are out of phase and there is no resultant energy leaving the sample. However, since the atoms in a crystal are arranged in a regular pattern, in very few directions we will have constructive interferences, in general when the wavelength of the wave motion is of the same order of magnitude as the repeat distance between scattering centres.

The diffraction of monochromatic X-rays has been demonstrated to take place only at particular angles of incidence satisfying the Bragg law [281]:

$$2d_{hkl} \sin\theta = n\lambda \quad \textbf{(7)}$$

with d_{hkl} the reticular distance between 2 consecutive plans of the crystal network, h, k and l the Miller indices, λ the wave length, θ the angle of the incident beam, and n the reflexion order. Note that the Miller indices are used to symbolically represent the orientation of reticular planes by giving the actual distances, measured from the origin, at which a plane intercepts the three crystallographic axes. The interplanar spacing d_{hkl} is a function of both

plane indices h, k, l and the lattice constants (a, b, c, α, β, χ). The exact relation between interparticular spacing and lattice parameters depends on the crystal system involved [281].

Thus, qualitatively, the technique allows:

- the determination of the crystallographic structure of a powder,
- the detection of impurities,
- the control of the crystallinity of a phase.

Quantitatively, we can:

- study the lattice parameters of a powder (a, b, c, α, β, χ) by structure refinement,
- find atomic positions and space groups,
- evidence the presence of eventual structural disorder.

An X-ray powder diffractometer consists of an X-ray source (usually an X-ray tube), a sample stage, a detector and a way to vary angle θ. The X-ray is focused on the sample at some angle θ. Once the radiation reaches the sample and is diffracted, the resulting signal is collected by a detector opposite to the source 2θ away from the source path. The incident angle is then increased over time while the detector angle always remains 2θ above the source path (see *Fig. II-10* for a schematic of the basic principle). Obtained XRPD diagram gives the intensities of the diffracted beam as a function of the 2θ angle. In absolute units, intensities are measured in ergs / cm² / sec but this measurement is a difficult one and is seldom carried out; most X-ray intensity measurements are made on a relative basis in arbitrary units.

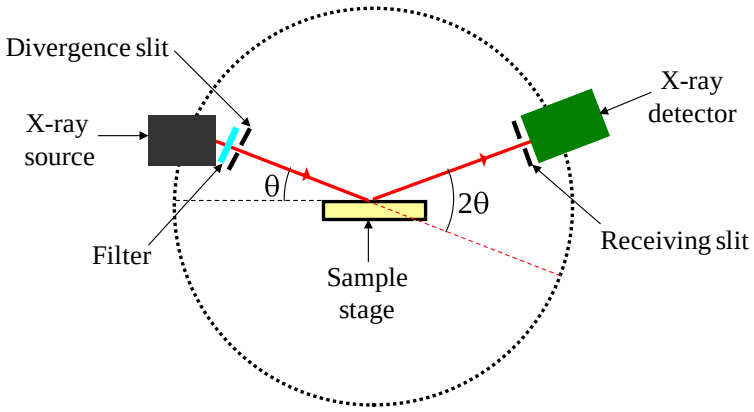

Figure II-10: Schematic of the principle of X-ray Diffraction.

The limit of detection of this technique is not a fixed parameter but depends on a number of variables. Crystalline samples with strong texture are difficult to assess since the preferred orientation of a large number of grains decreases the probability of finding planes oriented in other directions. The quality of the sample is also an important factor. For powders, the particle size strongly influences the process, smaller grains giving rise to broad peaks. Empirically, it can be said that in general in the case of samples with adequate preparation and favourable crystal orientations the limit of detection of a phase is around 4 - 5%.

Our measurements have been performed at room temperature using a diffractometer model D8 series 2 from Bruker Corporation, with 2θ varying between 10 and 100°.

The identification of crystalline phases in the samples has been done by a standard search / match procedure using the software DIFFRACplus EVA. Structural refinements have been performed based on the Rietveld method using the software TOPAS 4.

2.1.2 *Laser granulometry*

Relevant and reproducible particle size data are essential in many areas of manufacturing industry, and laser diffraction is a widely used technique. Laser diffraction, alternatively referred to as Low Angle Laser Light Scattering (LALLS), is a non-destructive technique used for the analysis of wet or dry samples, with particles in the size range 0.02 to 2000 µm [282]. Laser diffraction-based particle size analysis relies on the fact that particles passing through a laser beam will scatter light with angles inversely proportional to their size.

The first element of a typical laser granulometer is the laser, the most common being the He-Ne gas laser of wavelength 0.63 µm, to provide a source of coherent, intense light of fixed wavelength [44]. Note that the wavelength of light used for the measurements plays an important role in the measure, with for example smaller wavelengths (e.g. blue light sources) providing improved sensitivity to sub-micron particles.

The particles are suspended in a solvent that is routed and circulated by the action of a pump, in ethanol, to ensure that the material under test passes through the laser beam as a homogeneous stream of particles in a known and reproducible state of dispersion. The laser beam passing through the measurement chamber is deflected by the particles, at angles and intensities depending on the particle size. Indeed, as particle size decreases, the observed scattering angle increases logarithmically. Thus, large particles scatter light at narrow angles with higher intensity whereas small particles scatter at wider angles but with lower intensity.

A series of detectors (usually a slice of photosensitive silicon with a number of discrete detectors [283]) measures the light pattern produced over a wide range of angles. The working principle of the technique is illustrated in *Fig. II-11*.

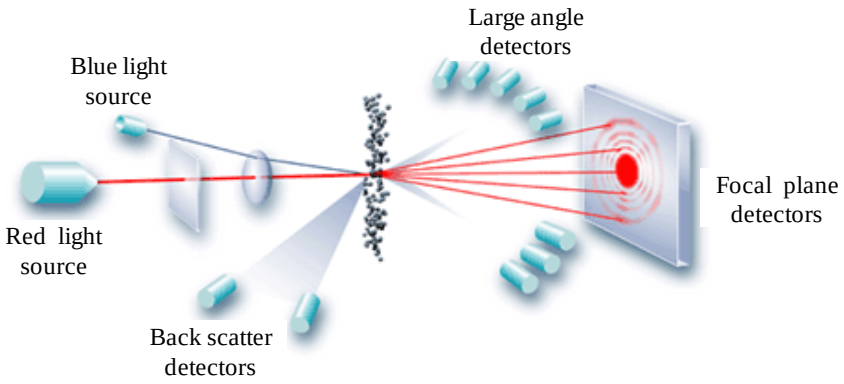

Figure II-11: Working principle of the laser diffraction particle sizing [284].

The analysis is performed simultaneously on all the particles flowing through the laser beam. Response analysis is obtained in the form of a histogram. Another important parameter representing the characteristics of the particles of a powder is the Median diameter or Medium value of particle diameter, d_{50}, which is the particle diameter value in case the cumulative distribution percentage reaches 50%. For instance, a d_{50} having a value of x µm means that 50% of the particles have a diameter below x µm (using a volume based calculation). Similarly, d_{10} and d_{90} means that 10 and 90% of the particles have a diameter below x µm, respectively.

Particles are three-dimensional objects for which three parameters (length, breadth and height) are required in order to provide a complete description. However, most sizing techniques, including laser granulometry, assume that the material being measured is spherical, as a sphere is the only shape that can be described by a single number (its diameter). This equivalent sphere approximation is useful in that it simplifies the way particle size distributions are represented. However, it does mean that different sizing techniques can produce different results when measuring non-spherical particles, and data have thus to be considered carefully. As an illustration, *Fig. II-12* shows some of the different possible answers for a single grain of sand. Other techniques to be mentioned are sieve, sedimentation, electrical sensing zone and microscopy; for more details please refer to [44, 283].

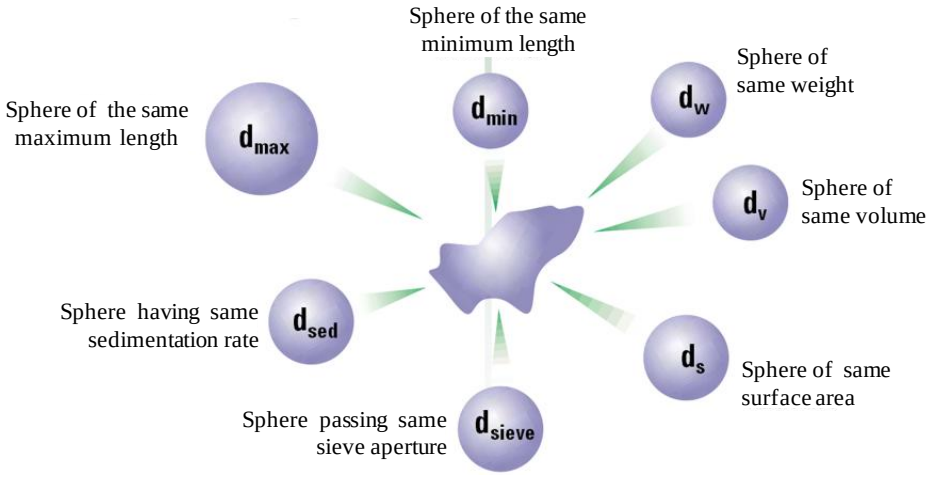

Figure II-12: Equivalent sphere representation for an irregularly shaped particle [283].

In laser diffraction, particle size distributions are calculated by comparing a sample's scattering pattern with an appropriate optical model. Traditionally, two different models are used: the Fraunhofer Approximation and the Mie Theory. The Fraunhofer approximation was used in early diffraction instruments. It assumes that the particles being measured are spherical, opaque and scatter light at narrow angles. As a result, it is only applicable to large particles and will give an incorrect assessment of the fine particle fraction, giving errors as high as 30% [283]. Mie Theory however provides a more rigorous solution for the calculation of particle size distributions from light scattering data, assuming the volume of a particle as opposed to the Fraunhofer theory [282-283]. It predicts scattering intensities for all particles, small or large, transparent or opaque. Mie Theory allows, for primary scattering from the surface of a particle, the prediction of the intensity by the refractive index difference between the particle and the dispersion medium. It also predicts the secondary scattering caused by light refraction within the particle, especially important for particles below 50 µm in diameter.

Measurements have been performed at the ICMCB using a laser diffractometer from Malvern Instruments Ltd. Prior to measurements, powders were accurately dispersed in ethanol by manual mixing in a mortar and kept in ultrasounds 15 to 30 min to break down the last agglomerates.

2.1.3 *Thermogravimetric analyses (TGA)*

Thermogravimetric analysis or TGA is an analytical quantitative technique commonly employed in research and testing to assess volatile content, thermal stability, absorbed moisture, degradation characteristics, sintering behaviour and reaction kinetics of materials by

monitoring the weight change that occurs as a specimen is heated. The measurement is usually carried out in air or in inert atmospheres like argon or helium and the weight is recorded as a function of the increasing temperature. A continuous graph of mass change against temperature is obtained when a substance is heated at a uniform rate or kept at constant temperature. TG curves are normally plotted with the mass change (Δm) expressed as a percentage on the vertical axis and temperature (T) or time (t) on the horizontal axis [285].

The instrument used in thermogravimetry (TG) is called a thermobalance. It consists of several basic components:

- a micro-balance: this high-precision balance is equipped with a pan (generally platinum or alumina), loaded with the sample. The most widely used balances are the null types, which incorporate a sensing element detecting a deviation of the balance beam from its null position [286]. The balance is deflected as the sample weight changes as a result of temperature change and the consequent movement of the pan is sensed. The output from the movement sensor applies a correction (often magnetic) that brings the balance pan back into its original position. The restoring force triggered to bring the balance back to the null position is directly proportional to the mass change. This procedure ensures that, as the weight of the sample changes, the pan is kept in the same position in the furnace and, thus, in the same thermal environment. The sensitivities and ranges of the microbalances depend on the model chosen, but typically the sensitivity is ± l μg with a maximum sample mass of 100 mg [285].

- a furnace and a temperature controller: the furnace should have a hot zone of uniform temperature, large enough to accommodate the sample and crucible. It is essential that the furnace in no way affects the microbalance mechanism [285].

- a data recording unit.

A basic illustration of a thermobalance is shown in *Fig. II-13*.

The first limitation of the TGA technique arises from the fact that the mass change characteristics of a material are strongly dependent on the experimental conditions employed. Thus, the recorded data are influenced by experimental parameters, such as sample dimensions, form and mass, heating / cooling rates, the nature and composition of the atmosphere in the region of the sample and the thermal and mechanical history of the sample.

Also, frequent calibration of the thermobalance is mandatory to guaranty the accuracy of the measures.

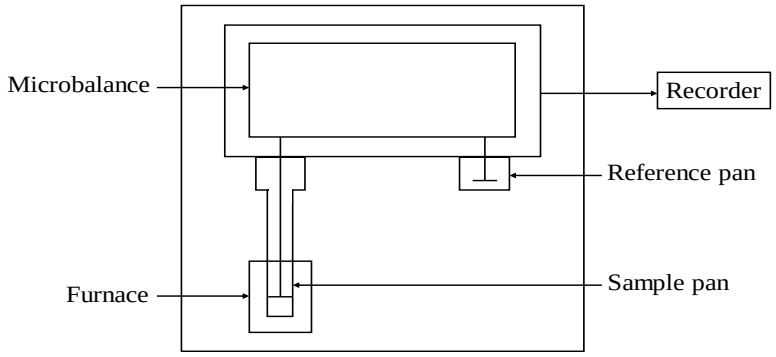

Figure II-13: Basic schematic of a typical balance and furnace assembly.

TGA measurements have been performed at the IMN using a thermobalance model TGS2 from Perkin-Elmer Corporation, from room temperature to 800°C, with heating and cooling rates of 2°C / min.

2.2. Microstructural characterisations by SEM / EDX

The scanning electron microscope (SEM) allows three-dimensional representations of an object contained in a two-dimensional image, with a wide range of possible magnifications. There are many advantages in using the SEM, including a large depth of field, which allows a large amount of the sample to be in focus at one time, the production of images of high magnification and resolution (around 2 nm) and a sample preparation relatively easy since SEM only requires the sample to be conductive. All the advantages have made the SEM one of the most used instruments in research areas today.

SEM uses electrons rather than light to form an image. The incident electrons interact with the atoms of a sample and are significantly scattered by them. When an incoming electron is sufficiently energetic, a wealth of phenomena can take place leading to different types of emitted particles. In SEM imaging, the emitted particles of interest are the secondary and the backscattered electrons, corresponding to the two strongest regions of the energy distribution of the electrons leaving an irradiated sample [287].

By convention, the secondary electrons (SE) are defined as being the ones emitted with energies less than 50 eV [288]. They are coming from the inelastic scattering of the incoming electrons with matter: the incident electrons interact with the orbital electrons of the

atoms in the specimen, exciting an electron in the sample and losing some of its energy in the process, while the trajectory of the incident electron is only slightly perturbed. After interacting with the matter, the excited electron moves towards the surface of the sample, undergoing elastic and inelastic collisions until it reaches the surface where it can escape if it still has sufficient energy. Although electrons are generated throughout the region excited by the incident beam, only the electrons that originate from less than approximately 100 nm deep in the sample can escape to be detected as secondary electrons [289]. Secondary electrons are thus very sensitive to topography.

Backscattered electrons (BSE) are coming from the elastic scattering of the electron beam. In elastic scattering, the electron trajectory changes, but its kinetic energy and velocity remain essentially constant (due to large differences between the mass of the electron and nucleus). The pronounced forward scattering of those reflected electrons results in the formation of shadows, making them sensitive to relief contrast. Also, if the specimen to be observed is relatively smooth, the material contrast can be highlighted, as the number of emitted backscattered electrons rises with the atomic number of the atom; heavier elements appear thus brighter [290].

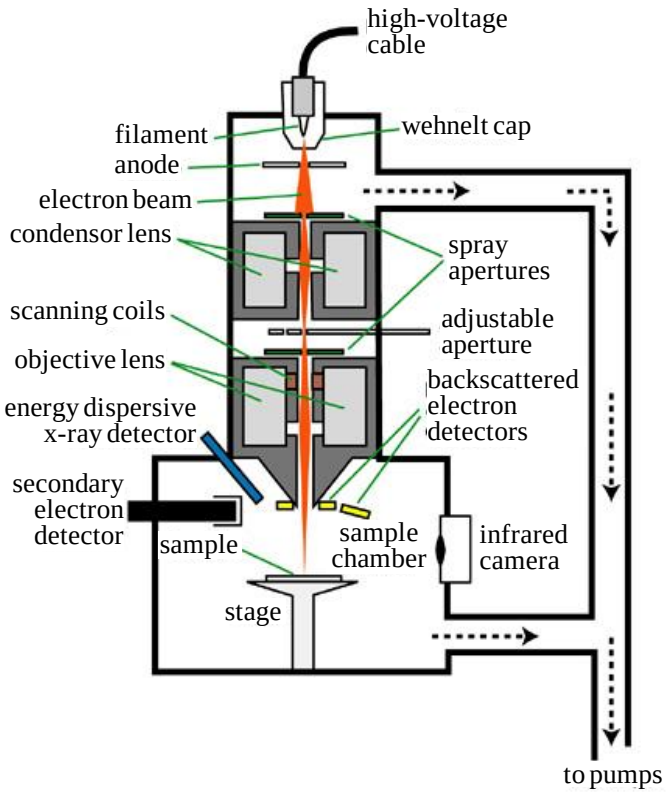

Figure II-14: Scanning electron microscope overview [291].

In practice, a SEM consists of an electron optical column (see *Fig. II-15*), linked to a control console. Within the column are an electron gun, electromagnetic lenses that accelerate and focus the electron beam, and deflection foils [287]. The electron beam is usually produced by field emission, a technique based on the quantum mechanical tunnel effect (discharge of electrons from the surface of a cathode material subjected to a strong electric field). At the base of the column are a specimen chamber, specimen stage and detector systems. The electron optical column with the specimen chamber has to be evacuated to at least 10^{-8} Pa, both to achieve long enough mean free pathways for the electrons and to prevent surface contamination of the electron gun [287].

Note that the use of the SEM is also not limited to imaging, but additionally it is possible to use the multiple interactions that electrons may have with matter to perform different types of analyses, such as topographic analysis or composition analysis at element level [287]. In the panel of emitted particles, one can mention the Auger electrons, used in so called Auger Electron Spectroscopy (AES), the photoelectrons, used in X-rays Photoelectron Spectroscopy (XPS), and continuum X-rays, used in Energy Dispersive X-ray Spectroscopy (EDX or EDS).

The Energy Dispersive X-rays analysis (EDX) is a method that can be easily applied in conjunction with the SEM for microanalysis. In this technique, a solid state detector converts the emitted X-rays to electrical pulses whose heights are proportional to their energy, thus allowing quantitative analyses. These pulses are amplified, providing after some counting time the energy spectrum of the characteristic X-rays of all elements present in the area hit by the electron beam [287].

This technique has advantages such as a high efficiency of detection, which allows simultaneous detection of all the elements of a material. In addition, as it can work in combination with the SEM, it allows the realisation of linear analyses and composition maps. However, this technique owns some detection limits, summarised below [287]:

- Only elements of atomic number $Z \geq 9$ can be resolved, the relaxation process for lighter elements producing Auger electrons rather than X-rays.

- The detection limit of an element of atomic number $Z \geq 9$ homogeneously dispersed in a material is 0.1%. Therefore, for the characterisation of certain materials such as alloys that have elements with lower percentages, other analysis techniques should be used.

It should be taken into account that this is a semi-quantitative analysis technique. Factors such as background noise of the signal, absorption coefficient of the material or the depth of penetration of the electron beam can cause some variations in the signal, thus percentages (atomic or weight) obtained for each element have to be taken carefully.

In this work, two different scanning electron microscopes have been used:

- Zeiss Supra 55 VP, with resolution of 1.7 nm at 1 kV, 2 nm at 30 kV, incorporating equipment for energy dispersive X-ray (EDX) analysis, brand EDAX.

- Zeiss Evo 60, incorporating equipment for energy dispersive X-ray (EDX) brand EDAX.

Analyses on images (as quantification of porosity, see *Chapter III*) have been performed using the software dhs-Bilddatenbank® from Dietermann & Heuser Solution GmbH.

2.3. Electrochemical characterisations

2.3.1 *Cell testing*

Such measurements have been performed in EIFER using the test bench shown in *Fig. II-15*. The cell is sealed between two alumina tubes using Thermiculite® gaskets in the cell housing, located in a vertical oven. The compression is made by a weight system. The upper compartment of the cell housing is dedicated to the anode and the lower part to the cathode. The gas flows are controlled using Mass Flow Controllers (MFCs) and transported to the cell through inner alumina tubes, as shown in *Fig. II-16*. In both sides, current collection is made by platinum grids of diameter Ø 16 mm, meaning an active surface of 2 cm^2, linked to the connectors by platinum wires. The pressure of the Pt grids on the cell is controlled by a system of springs. Both output gas lines (air and hydrogen) are equipped by condensers. Temperature is monitored using three thermocouples, one in each compartment and one in the oven. The electrochemical interface is a SOLARTRON 1286 from Schlumberger, the hardware control and data acquisition are realised using a DaisyLab interface and the electrochemical measurements carried out with the software CorrWare®.

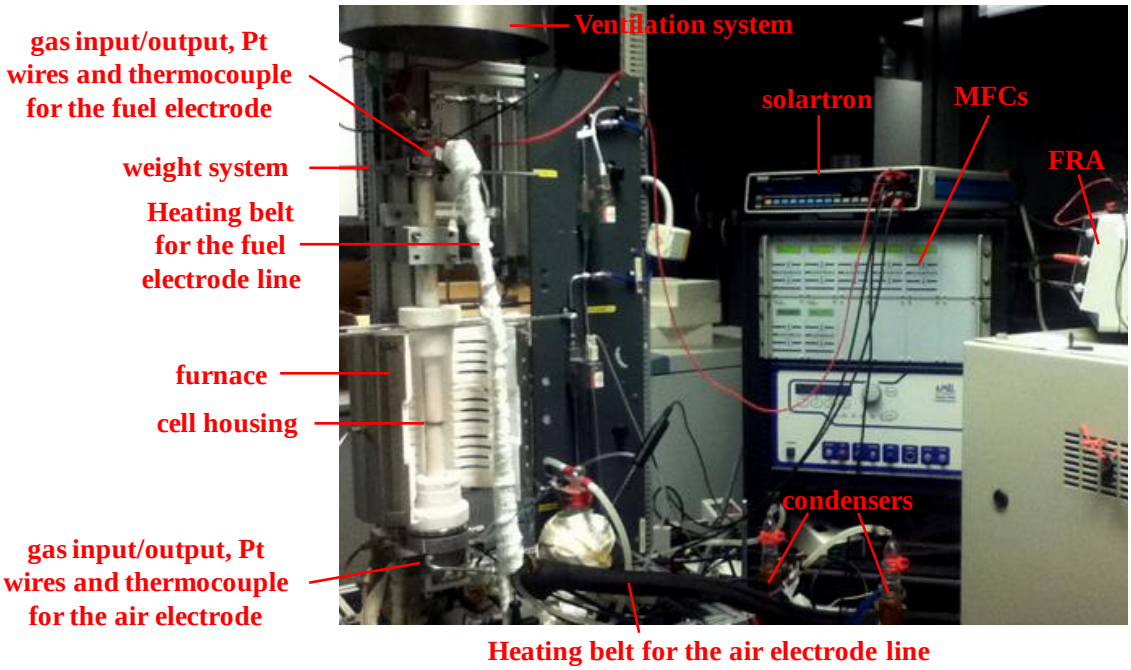

Figure II-15: Picture of the test bench used in this study.

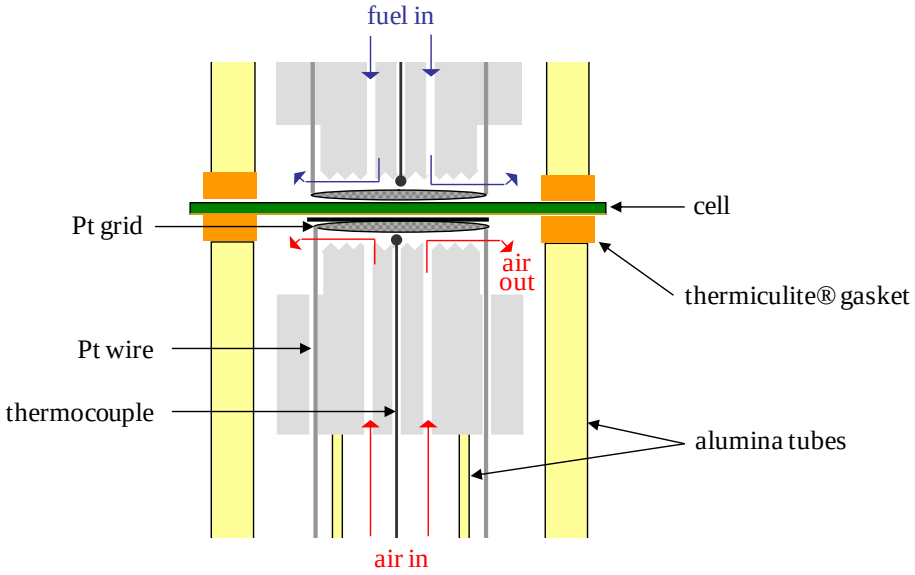

Figure II-16: Schematic illustration of the cell housing.

2.3.2 *Electrochemical impedance spectroscopy (EIS)*

In contrast to current voltage (I - V) characteristics, only giving a view of the overall losses of a cell, the technique of Electrochemical Impedance Spectroscopy (EIS) is one of the most effective methods for the unravelling of complex electrochemical systems [292]. The strength of EIS lies in the fact that by small signal perturbation, relaxation times and

amplitudes of the various processes of a system can be revealed over a wide range of frequencies. EIS is especially useful if the system performance is governed by a number of coupled processes, proceeding at different rates. The physical and chemical processes contributing to the internal resistance of a cell determine their dynamic behaviour over a wide range of frequencies: the various polarisations exhibit different time dependences, due to the different origins of the kinetic processes involved [292-293]. For instance, the response time for ohmic polarisation is essentially zero, for activation polarisation the time constant is related to details in the charge transfer process and the concentration polarisation is related to the relevant gas phase transport parameters such as diffusivity [293].

The method of EIS consists in superimposing a small sinusoidal current perturbation of variable frequency $I\ \omega$ around a stationary point of the polarisation curve (*Fig. II-17*).

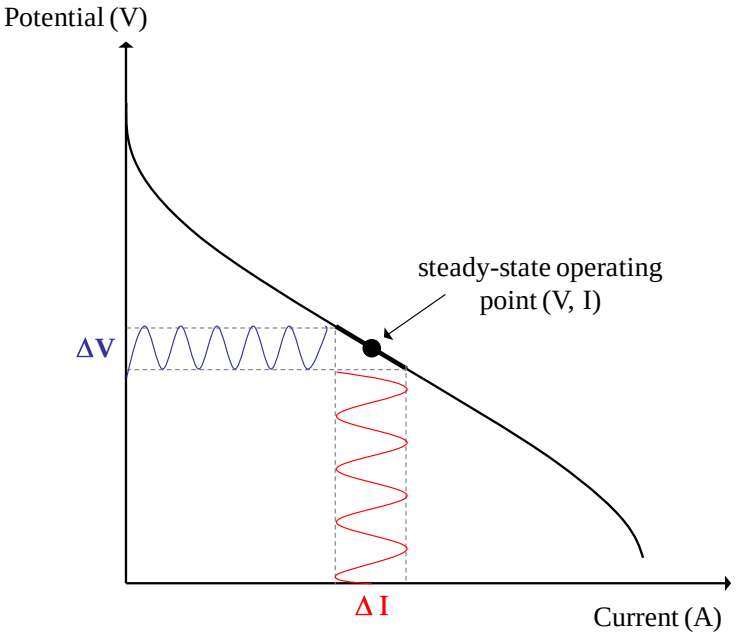

Figure II-17: Principle of the electrochemical impedance spectroscopy.

The response of the electrochemical system is a sinusoidal potential $V\ \omega$ and the ratio $V\ \omega\ \ I\ \omega\ = Z(\omega)$ defines the impedance of the material.

$$Z\ \omega\ = \frac{V(\omega)}{I(\omega)} = \frac{\Delta V \exp\ \omega t + \varphi}{\Delta I \exp\ j\omega t} = \ Z\ \exp\ j\varphi \qquad \textbf{(8)}$$

$Z(\omega)$ is a complex number that can be represented either by polar coordinates using its module Z and its phase φ or in cartesian coordinates by $Z\ \omega\ = Re\ Z\ + j\ Im\ Z\ = Z' + jZ''$, with $Re\ Z$ the real part and $Im\ Z$ the imaginary part. Impedance is generally represented in the complex plane of Nyquist $-\ Im\ Z\ = f\ Re(Z)$.

In first and very simplified approximation, an impedance spectrum can be interpreted in terms of "semi-circles" and electrical equivalent circuits made of capacitances, inductances and resistances, placed in parallel or in series. These three dipoles are represented in *Fig. II-18.*

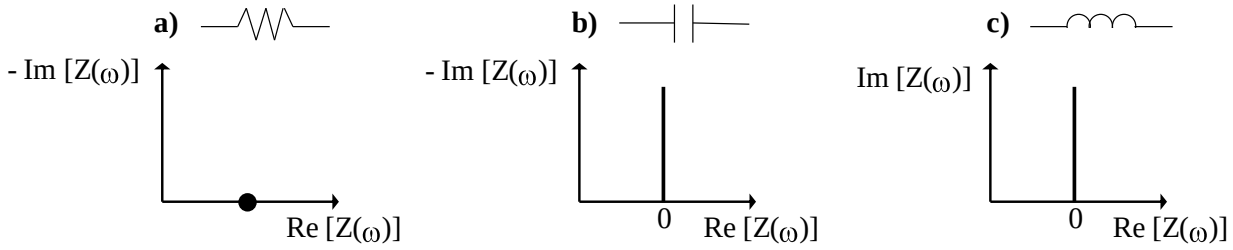

Figure II-18: Symbols and Nyquist representations for a) a resistance R, b) a capacitor C and c) an inductor L.

In an ideal case, the plots are a series of semi-circles, quarter-circles or distorted semi-circles and quarter-circles. The intercepts with the real axis are measures of resistive losses due to various physical processes, and positions on the arcs provide information on non-ohmic terms. For example, in the case of a monocrystalline material, the electrical behaviour can be modelled by a circuit with a resistance and a capacitance in parallel (*Fig. II-19a*). The impedance of such a circuit can be written as follows:

$$Z = \frac{R}{1 + j\omega\tau} = \underbrace{\frac{R}{1 + \tau^2\omega^2}}_{Re\ Z} - \underbrace{\frac{jR\tau\omega}{1 + \tau^2\omega^2}}_{Im\ Z} \qquad \textbf{(9)}$$

with $\tau = RC$ the time constant. This corresponds to the equation of a half-circle (*Fig. II-21b*); the intersection at low frequencies ($\omega\tau << 1$) of the half-circle with the real axis is the total resistance of the system. The value of the capacity is determined with the maximum value of the frequency on the imaginary axis by the relation $C_0 = 1\ \omega_0 R$. ω_0 is defined as the relaxation pulsation and is a characteristic of a given circuit, as for the relaxation frequency $f_0 = \omega_0 / 2\pi$.

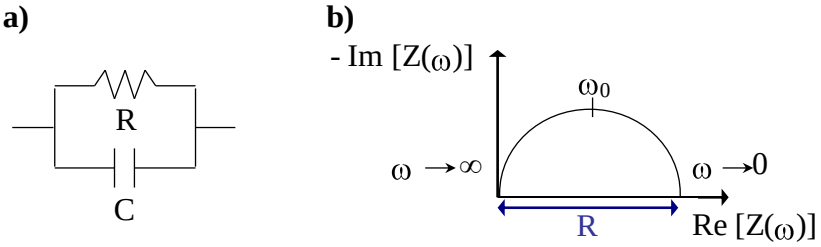

Figure II-19: For a monocrystal, a) equivalent circuit modelling the electrical behaviour of the material and b) theoretical impedance diagram.

Another element often found in electrochemistry is the Constant Phase Element or CPE. This element is defined by two parameters: an admittance, noted Y_0, and an exponent n. Y_0 is a pure imaginary element representing a capacity when n gets close to 1 and an inductance if n is negative. The impedance of this element is mathematically described by the following relation:

$$Z(\omega)_{CPE} = \frac{1}{Y_0(j\omega)^n} \quad \textbf{(10)}$$

The exponent n is linked to the decentering β of the circle arc by:

$$\beta = \frac{n\pi}{2} \quad \textbf{(11)}$$

The Nyquist representation of a CPE and the equivalent circuit R // CPE are shown in *Fig. II-20a* and *II-20b*, respectively. Also, the particular case n = 0.5 corresponds to the Warburg element, used to describe pure diffusion processes.

Equivalent circuits are used to model the impedance spectra, allowing some insight into the nature of the time constants involved in a process, although simple circuits made of R and R-C elements are rarely describing it accurately.

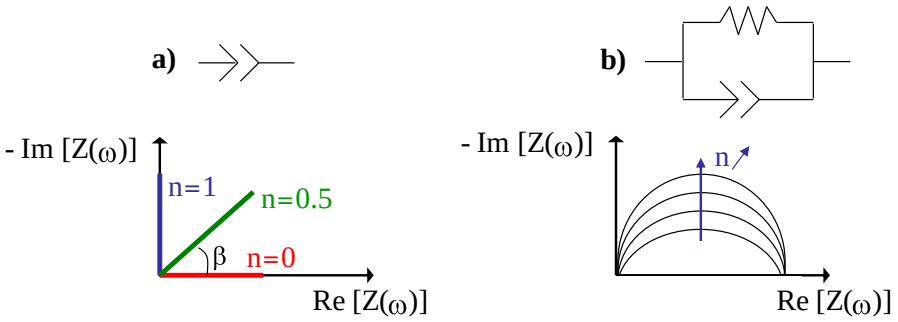

Figure II-20: a) symbol and Nyquist representation of a CPE for n = 0, 0.5 and 1 and b) symbol and Nyquist representation for the equivalent circuit R // CPE.

An additional difficulty in the comprehension of phenomena rises from the fact that different equivalent circuits can be used to describe an impedance spectrum, related to different physical phenomenon. Finally, experimental limits in separating relevant parameters are related to the overlapping of semi-circles, making the interpretation of spectra not straightforward.

EIS measurements on complete cells have been performed using a SOLARTRON SI 1255 HF Frequency Response Analyser (FRA) and the program Zplot®. The frequency range used was 50 kHz - 0.05 Hz (0.005 Hz), 7 points per decade, in galvanostatic mode. AC current modulation amplitudes were determined in order to be small enough to meet the linearity requirements of the transfer function, which reflects the relationship between the voltage and the current at different frequencies, but high enough to have a good signal / noise ratio [253, 294].

Chapter III

Fabrication and characterisation of cells

In the previous chapter, shaping and characterisation techniques used in this work have been described in terms of basic principle and difficulties and / or limitations.

Regarding the shaping techniques, the major concern is related to the tape casting process, since the quality of the final cell will be mainly governed by the mechanical and structural properties of the anode substrate. Although tape casting is a well-established industrial shaping technique, known for its easy handling and low cost, important upstream work has to be done for the development of a slurry formulation giving high quality tapes in a reproducible way. Thus, a proper selection of the raw powder characteristics (particle size, particle morphologies etc.) and the organic additives to be used is necessary. Besides, an accurate determination of the adequate relative proportions of the different components and additives appears mandatory.

Also, in order to avoid any mechanical stress and defects during the sintering steps of the cell elaboration, the thermal behaviour of each layer has to be studied and the heat treatment processes to be optimised.

In this chapter, the different optimisations performed at each processing step will be described, leading to the definition of a protocol for the elaboration of complete planar anode-supported cells. Thereby, a first part will concern the tape casting process, and more generally the fabrication of the anode substrate. The second part will present the vacuum slip casting process used for the elaboration of half-cells and the third part will describe the screen printing of the cathode layers. Finally, the fourth part of this chapter will be devoted to the attempts made during this work for microstructural improvements.

1. Fabrication of the anode substrate by tape casting and pre-sintering

1.1. Slurry formulation

1.1.1 *Powder characteristics*

The BIT07 powder has been produced by EMPA (Dübendorf, Switzerland) by solid state reaction. It appeared phase pure in the sense of X-rays, as can be seen in *Fig. III-1*. Rietveld refinement of the diffraction pattern in the space group Pm3m gave a lattice parameter a = 4.097 Å, in agreement with the value previously obtained by Jayaraman et al. at the IMN for BIT07 produced at lab scale (4.095 Å), also by solid state reaction [119].

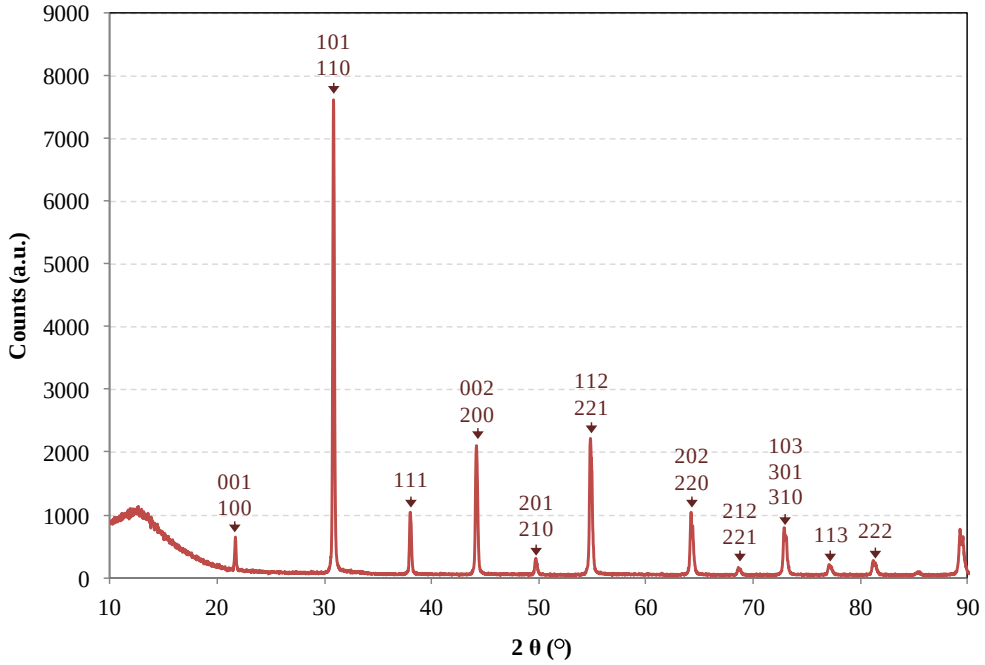

Figure III-1: Powder X-Ray Diffraction pattern for the BIT07 powder supplied by EMPA.

Particle size distribution of the BIT07 powder has been determined using laser granulometry measurements; the volumetric particle size distribution pattern is shown in *Fig. III-2a*. This powder presents a bimodal size distribution, with a d_{50} value of 0.84 µm and a d_{90} one of 2.84 µm. SEM analyses of the powder, shown in *Fig. III-3a*, confirmed the grain size.

The NiO powder has been supplied by J.T. Baker® (U.S.A), a supplier selected on the basis of a study performed by Tietz et al. at Forschungszentrum Jülich, comparing NiO commercial powders from different suppliers [295]. The volumetric particle size distribution pattern is shown in *Fig. III-2b*, the measured d_{50} and d_{90} values being 0.19 and 0.67 µm, respectively. These values were also confirmed by SEM, micrograph shown in *Fig. III-3b*.

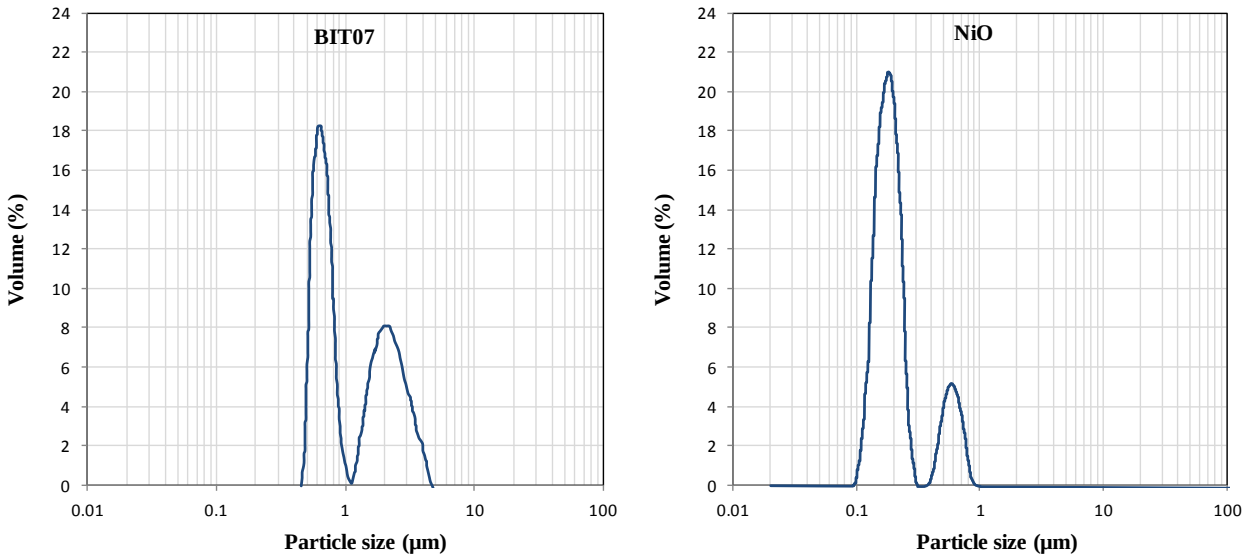

Figure III-2: Particle size distributions of the BIT07 powder from EMPA (left) and the NiO from J.T. Baker® (right).

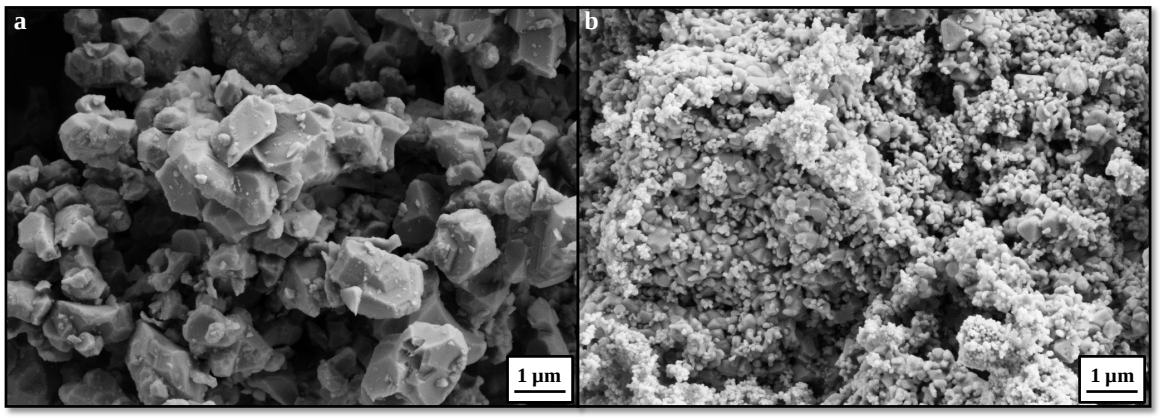

Figure III-3: SEM micrographs of a) BIT07 and b) NiO powders.

The tapes were prepared with a BIT07 / NiO weight ratio of 40 : 60, the high nickel content chosen to ensure a good path for electrons flux and thus a good current collection [265].

1.1.2 *Components in the slurry*

For the slurry formulation, the following additives have been selected on the basis of the work of Schafbauer et al. at Forschungzentrum Jülich [265, 296]:

- Dispersant: Nuosperse® FX-9086 (Elementis), a methoxy methylethylacetate (*Fig. III-4)*, showed the best dispersing activity regarding our powders (tests between Oleic Acid, Nuosperse® FX-9086, ethylcellulose, polyethyleneimine and Dolapix). It is a non-ionic

surfactant adsorbed physically on the surface of the particles by weak van der Waals forces, providing steric stabilisation [44].

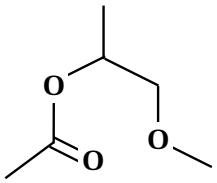

Figure III-4: Lewis representation of the 2 - methoxy - 1 - methyl ethyl acetate.

- Binder: for tape casting in organic solvents, the most frequently used polymer is the polyvinylbutyral (PVB) thanks to its flexibility (chain lengths from a few thousands g / mol to 10^5 g / mol available) and adaptability to many solvents and plasticiser systems [263, 297-298]. PVB is industrially produced from vinyl acetate and butyraldehyde, and is in practice a combination of vinylbutyral, vinyl alcohol and vinyl acetate monomers, as shown in *Fig. III-5* [263]. In our case, the PVB Butvar® B-98 (Sigma) with a molecular weight of 40 - 70 kg / mol was selected.

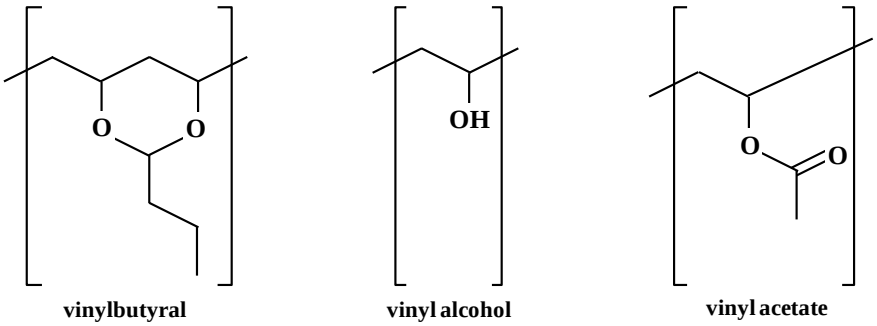

Figure III-5: Lewis representation of the monomers present in the PVB.

- Solvents: PVB and ethanol have similar molecular polarities, making ethanol a solvent of choice to be used with this binder. Also, 2-Butanone (methyl ethyl ketone, or MEK) is a fast drying solvent commonly used in tape casting. The mixture ethanol / MEK has been reported to be azeotropic for ethanol contents starting from 34 Wt% [299]; thus, a solvent system ethanol / MEK 34 : 66 Wt% has been selected for this study.

- Plasticiser I: in organic tape casting, phthalate plasticisers are commonly used and reported as being compatible with PVB binders. However, due to their toxicity (to environment

and humans), efforts were made in the last years to avoid the use of phthalates in industrial processes, expected to be included in the "dangerous substances" or "substances to be avoided" industry chemical lists [265, 300]. Since a few years, Solutia Inc. is releasing a phthalate-free type I plasticiser, the Solusolv® S-2075. This triethylene glycol di-2-ethylhexanoate (*Fig. III-6*) presents the advantages of being environmentally "friendly" and compatible with PVB binders [297, 300]. Comparative studies using benzyl butyl phthalate (98%, Aldrich), bis (2-ethylhexyl) phthalate and Solusolv® S-2075 plasticisers have been performed with different formulations using our powders, giving comparable qualities of the green tapes. Therefore, Solusolv® S-2075 has been preferred.

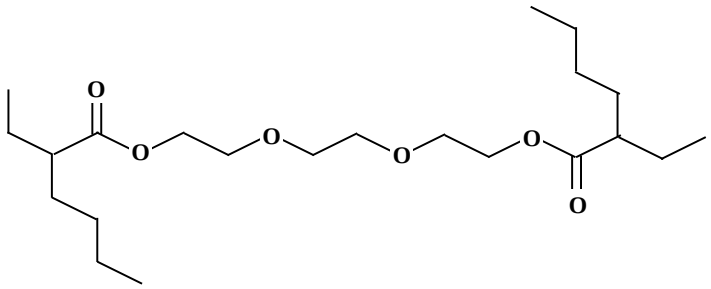

Figure III-6: Lewis representation of the triethylene glycol di - 2 - ethylhexanoate.

- Plasticiser II: poly (ethylene glycols) or PEGs are commonly used plasticisers in slurry formulations [263, 298, 301], being molecules chemically inert but compatible with PVB binders. The Lewis representation of a PEG molecule can be seen in *Fig. III*-7. Relatively low molecular weight PEG400 (Merck) has been here selected, considering that plasticisers with low molecular weight and small number of polar groups provide higher plasticisation and flexibility to the tapes [298].

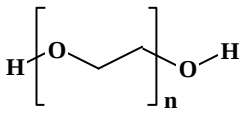

Figure III-7: Lewis representation of the PEG.

1.1.3 *Slurry elaboration process*

As previously mentioned in *Chapter II*, the order for adding the organics to the mill is critical [41]. Dispersing agent is added first to provide efficient de-agglomeration process, thus i) the binder will not encapsulate agglomerates and ii) the competitive adsorption on the particle surfaces is prevented. Note that usually the binder is more soluble in the plasticisers than in the solvents, so adding first plasticisers will help its dissolution. Taking these elements into account, the slurry elaboration process has been settled involving four steps:

(i) dispersion milling of the BIT07 and NiO powders in the presence of the dispersant and the solvents during 24 hours;

(ii) addition of the type I plasticiser, mixing during 1 hour;

(iii) addition of the binder, mixing until complete dissolution (usually 1 hour);

(iv) addition of the type II plasticiser, mixing during 1 hour.

All the mixing steps have been performed using a Turbula® shaker-mixer type T2F (W.A.B GmbH) with zirconia balls Ø5 mm as a grinding media. The slurry was then let to rest for 48 hours to allow the expansion of binder polymer chains.

1.2. Casting

Prior to casting, air is removed in a desiccator using a vacuum pump (500 mbars for 15 min) to prevent defects in the green tape caused by remaining air bubbles (holes or spots can be nuclei for the creation of cracks). A doctor blade gap of 1500 µm has been used and the casting speed controlled to 21 mm s^{-1}, speed selected on the basis of the work of Delahaye et al. [126]. The tapes are dried in ambient air under aspiration during 12 hours.

1.2.1 *Primary recipe*

a) <u>Dispersion of the powders</u>

The first parameter to be optimised in a slurry formulation is the dispersion of the particles. For this purpose, different amounts of dispersant ranking from 0 to 10% relative to the solid amount have been added to a suspension of BIT07 / NiO 40 : 60 Wt% powders in the MEK / Ethanol 66 : 34 Vol% solvent mixture. Suspensions containing 0, 0.5, 1, 1.5, 2 and 10% of dispersant have been mixed in a Turbula® for 4 hours and let to sediment during 12 hours. As expected, the suspension without any dispersant started to sediment right after stopping the shaking. After 1 hour of sedimentation (*Fig. III-8*), it was observed that the suspensions

containing 0.5 and 10 Wt% of dispersant were already sedimentating, while the suspensions containing 1, 1.5 and 2 Wt% remained stable.

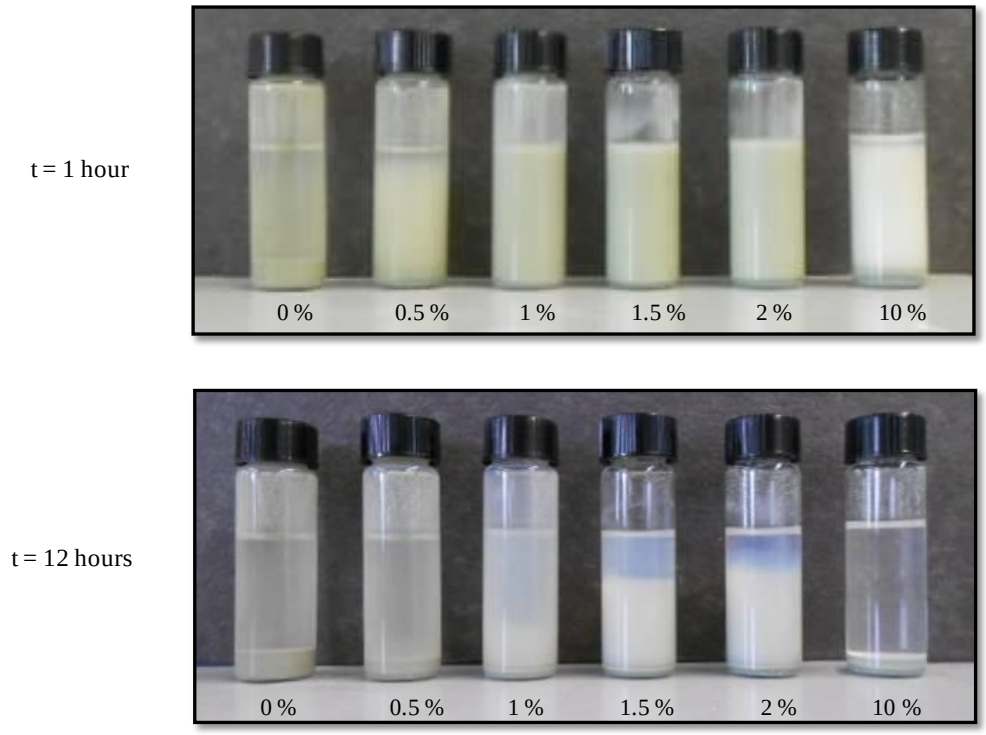

Figure III-8: Behaviour of a BIT07 / NiO 40 : 60 Wt% in a MEK/Ethanol suspension as a function of dispersant content and time.

In the case of a too low amount of dispersant (here 0.5 Wt%), the powders are not efficiently dispersed and re-agglomeration processes can occur, leading to an increase of the "particle" size and thus a higher sedimentation rate (though a delay was observed before the sedimentation started for a content of 0.5 Wt% in comparison with the suspension with no dispersant).

In the case of an important excess of dispersant (here 10%), a demixing of the BIT07 and NiO powders was observed. This could be explained by a higher affinity of the Nuosperse® with NiO than with BIT07. In this case, the excess of dispersant is adsorbed preferentially by the NiO particles, making the dispersion layer collapsing as illustrated in *Fig. III-9*.

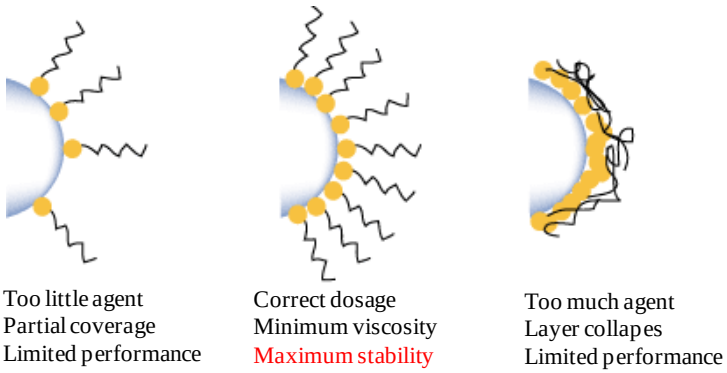

Figure III-9: Influence of the amount of dispersant on the stabilisation of particles [302].

After 12 hours of sedimentation (*Fig. III-8*), a green supernatant was observed for the suspension containing 0.5 Wt% of dispersant, indicating a better dispersion of the NiO compared to BIT07. As concerns the two extreme configurations (no dispersant versus 10 Wt%), for the system without Nuosperse® the supernatant is green (though lighter than with 0.5 Wt%), while for the system with a large excess of additive the supernatant is transparent. This indicates that the excess of dispersant does not only hinders its effect but also inhibits the dispersing action of the solvent system itself by preventing the formation of an electrostatic double layer around each particle, normally stabilising suspensions in the case of polar liquids. The dispersion containing 1 Wt% of Nuosperse® was the most homogeneous; a white / transparent supernatant is observed for contents of 1.5 and 2 Wt%, as explained previously by an excess of dispersant adsorbed preferentially by the NiO particles. Thus, an amount of 1 Wt% of dispersant was selected for the formulations.

b) <u>The other additives</u>

Once the proper amount of dispersant to be added is determined, the second parameter to consider is the solid loading, defined as the volumetric ratio of solids (here the BIT07 and NiO powders) to solids plus solvents. The amount of solvents was thereby empirically determined to give to the final slurry a sufficient viscosity without (excessive) spreading during casting. In our case, a solid loading of 34% has been selected. The amount of binder (relative to the solid amount) has been settled to 3.5 Wt% based on the empirical results obtained with $BaTiO_3$ powders. The ratio binder : plasticiser I (Solusolv® S-2075) has been fixed to 2 : 1 following the instructions of the supplier [297]; the ratio binder : plasticiser II (PEG400) was also taken as 2 : 1. This slurry formulation is summarised in *Table III-1*.

Table III-1:
Slurry formulation for the production of BIT07 / NiO 40 : 60 Wt% substrates with 3.5 Wt% of binder.

material	Wt% / solid amount	Wt%	Vol% slurry	Vol% green tape
NiO	60.00	45.70	17.21	38.84
BIT07	40.00	30.47	12.71	28.68
Ethyl Alcohol	7.92	6.03	55.69	
Methyl Ethyl Ketone	15.37	11.71		
Dispersant (Nuosperse® FX-9086)	1.00	0.76	1.89	4.25
Binder (Butvar® B-98)	3.50	2.67	6.09	13.74
Plasticiser I (Solusolv® S-2075)	1.75	1.33	3.46	7.80
Plasticiser II (PEG400)	1.75	1.33	2.96	6.69

c) Drying conditions

As said previously, the tapes are dried in air under aspiration. For this purpose, the tape caster is located in a Plexiglas chamber with a chimney on which an aspirating arm is positioned. The strength of the aspiration is here believed to have an important impact on the drying behaviour of the tapes due to its direct influence on the surface evaporation rate. For the optimisation of the drying conditions, 3 slurries from the previous recipe were dried at 3 aspiration levels, from low to high aspiration.

As presented in *Fig. III-10*, waves (wrinkles) appeared when fixing a too high aspiration level (*Fig. III-10c*), although this effect was already observed for the middle-high aspiration level even if less visible (*Fig. III-10b*).

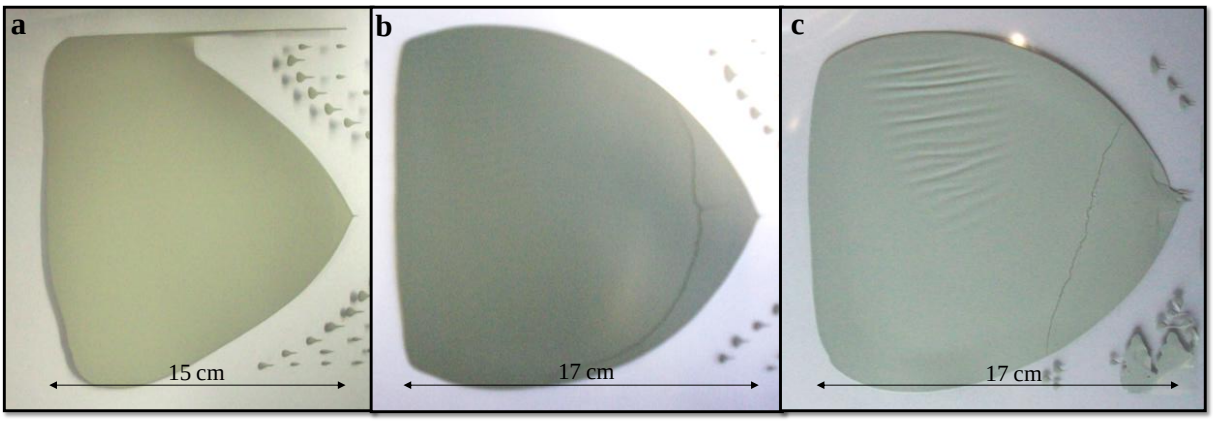

Figure III-10: Influence of the aspiration level on the drying behaviour of the tapes with a) low aspiration, b) medium aspiration and c) high aspiration.

This suggests a too fast evaporation of the solvents at the surface. This defect can be explained by the difference of drying speed between the bottom and the top layers. A solvent depleted zone forms at the top surface of the tape, which "freezes" into shape and size while the bottom of the tape is not dry. The solvents from the underlying layer diffuse to the top

surface at a rate too slow to "re-dissolve" the skin. As solvents migrate to the surface, the polymer matrix in the skin swells, leading to the wrinkling of the surface to provide additional surface area and accommodate the swelling [41].

A crack-free tape has been obtained in the case of a low aspiration (*Fig. III-10a*). This aspiration level has therefore been selected and kept constant along the thesis for comparison purpose. However, a problem of reproducibility has been encountered regarding this formulation. Attempts to further modify the drying behaviour of the tapes by modifying the ethanol : MEK ratio of the azeotropic mixture to 50 : 50, thus increasing the proportion of ethanol to decrease the surface evaporation rate, led to the same problem of reproducibility, as illustrated in *Fig. III-11* for tapes cast the same day. This might also be linked to the drying conditions: while in industrial tape casting machines the temperature of the air flow in the drying chamber is well controlled, in our case small temperature and humidity level variations in the laboratory atmosphere could play a role. This indicates however that improvements in the slurry formulation are needed.

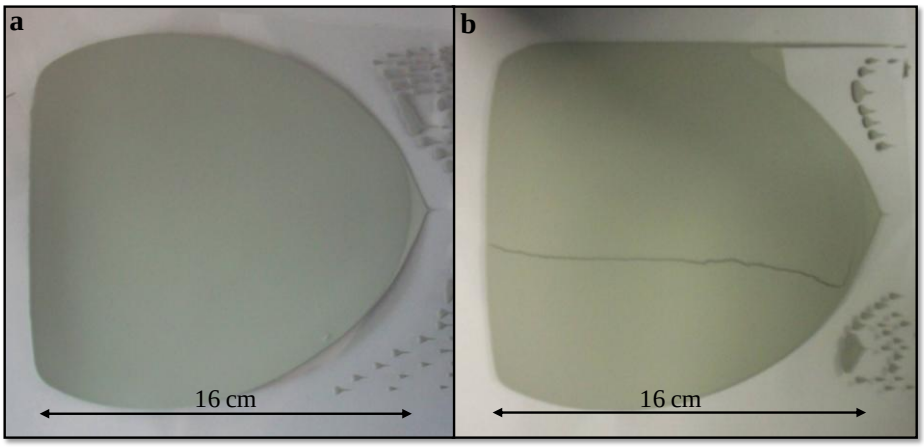

Figure III-11: Drying behaviour of green tapes BIT07 / NiO (40 : 60 Wt%) from identical slurries with solvent ratio 50 : 50 Wt%.

Maintaining the binder content at 3.5 Wt% while increasing type II plasticiser content to increase the plastic deformation or type I plasticiser content to increase the stored stress in the polymer matrix were not effective enough to avoid cracks. The problem of cracks seemed thus to stem from a too weak inter-particulate adhesion. This conclusion led to the formulation of slurries with increased binder content.

1.2.2 *Optimisation of the formulation*

a) Binder content

To increase the inter-particulate adhesion, plastic deformation and stress storage, formulations with increased binder content have been prepared. In all the formulations, the binder : plasticiser weight ratio has been kept to 2 : 1, and the solid loading decreased to 30% for slurries containing 5 and 6 Wt% of PVB to compensate for the important increase of the viscosity.

As can be seen in *Fig. III-12*, for slurries containing 4 Wt% and 5 Wt% of PVB, cracked tapes were obtained.

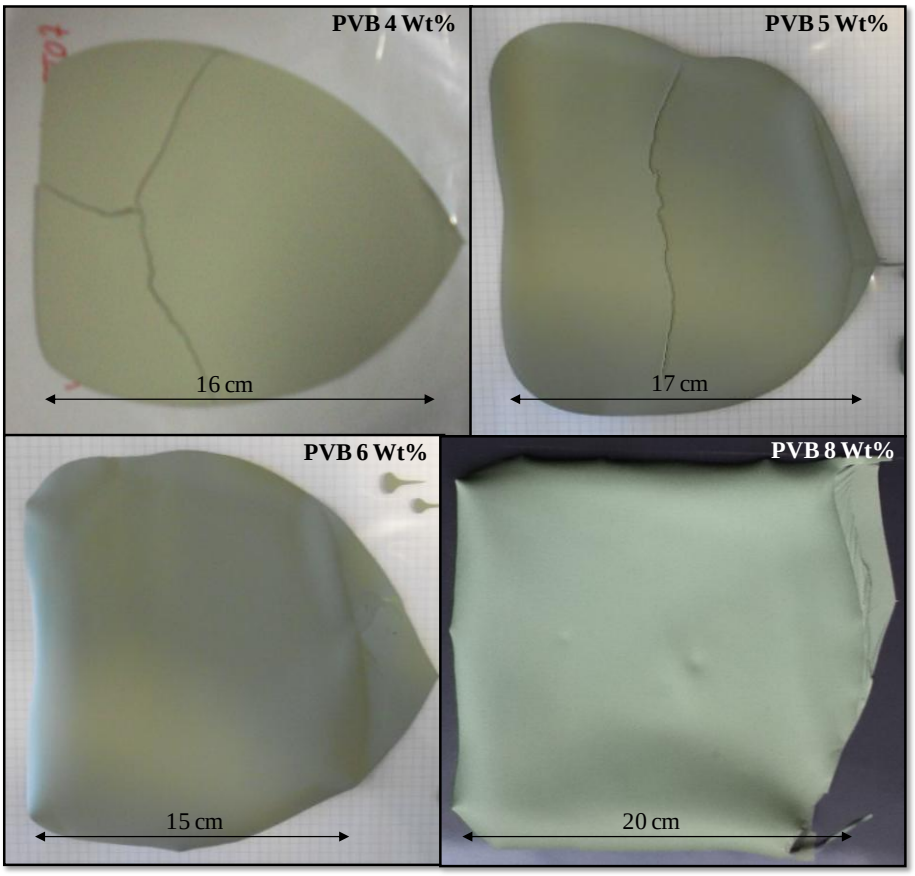

Figure III-12: Drying behaviour of green tapes BIT07 / NiO (40 : 60 Wt%) as a function of binder content.

Concerning the tape containing 5 Wt% of binder, an additional defect observed was a slight edge curling. This defect is often observed in tape casting of thick tapes when the carrier polyethylene film is not mechanically restrained. In this case, the higher shrinkage of the top layer compared to the bottom one is compensated by a lifting of the edges, lighter because

thinner. It can also be seen as an indication of an increased inter-particulate adhesion compared to the tape with 4 Wt% of PVB, at least high enough to lift the edges of the tape and the polymer carrier film as a stress-release mechanism.

For a **binder content of 6 Wt%,** a crack-free tape has been obtained. However, reverse curling of the tape is observed: as for the formation of wrinkles, a solvent-depleted zone forms on the top surface of the tape, forming a gel "frozen" in shape and size, while the bottom layer shrinks further due to a longer time for the polymer chains to re-organise, forcing the tape edges to curl downwards. This effect is here believed to be greater for larger binder contents, and thus plasticisers content, due to a corresponding increase in tight packing. This slows down the diffusion of the solvents and thereby creates a larger gradient of drying speed through the thickness of the tape. Nevertheless, even if not optimal, reverse curling is often tolerated in the industry since the flatness of the green tape can be recovered with a proper conditioning.

Nonetheless, problems of reproducibility have also been encountered in the case of a binder content of 6 Wt%. A further increase of the binder content to 8 Wt% gave also crack-free tapes, but problems of warping during de-binding of the substrates were experienced. Note that in this case the reverse curling effect is greater, confirming the strong influence of the organic content on the solvent diffusion rate.

b) Plasticisers content

From the previous series of experiments, solid loading, optimum dispersing agent and binder contents as well as drying conditions have been determined. However, problems of reproducibility led to a need in further modifications of the binder system, involving an increase of the plasticisers content to improve both plastic deformation and stress storage in the tapes.

Considering these last results and the recipe used at the IMN [126, 181, 303], a new slurry formulation has been developed on the basis of a binder content of 6 Wt%. A slightly higher binder : plasticisers ratio compared to the recipe of the IMN has been used in our study.

The type I plasticiser (Solusolv® S-2075) content has been increased compared to the recipe of the IMN, due to both a decreased effectiveness of this plasticiser with PVB binders compared to the phthalates (observed in our case by a better flexibility of the tapes prepared with phthalate-based slurries of equivalent formulations) and the increased length of the binder polymer chains used for our slurries (Butvar® B-98 vs. a mixture of Butvar® B-98 and B-90 for the IMN). Note that Solusolv® S-2075 has been kept because of its non-toxicity

and non-corrosivity compared to the phthalates, with no prejudicial difference in terms of tape quality evidenced in this study.

Lower type II plasticiser content has been selected, the tapes containing the same amount as the IMN appearing "oily" after drying.

The new recipe is presented in the *Table III-2*.

Table III-2:
Slurry formulation for the production of BIT07 / NiO 40 : 60 Wt% anode substrates.

material	Wt% / solid amount	Wt%	Vol% slurry	Vol% green tape
NiO	60	41.32	13.37	29.22
BIT07	40	25.55	9.88	21.58
Ethyl Alcohol	9.9	6.8	54.24	
Methyl Ethyl Ketone	19.3	13.3		
Dispersant (Nuosperse® FX-9086)	1	0.7	1.46	3.2
Binder (Butvar® B-98)	6	4.1	8.11	17.72
Plasticiser I (Solusolv® S-2075)	5.5	3.4	7.68	16.78
Plasticiser II (PEG400)	4.5	2.8	5.26	11.50

This new recipe gave good quality and reproducible green tapes (*Fig. III-13a*), despite slight wrinkling and reverse curling on the edges (*Fig. III-13b*).

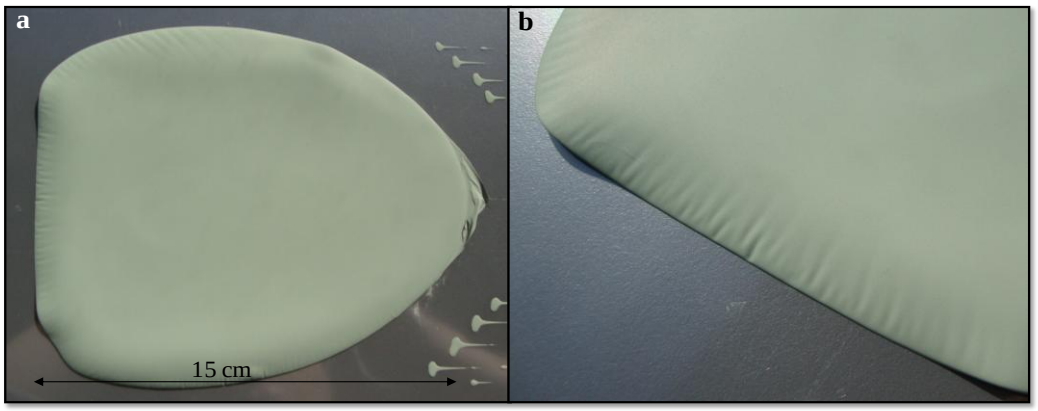

Figure III-13: Green tape BIT07 (EMPA) / NiO 40 : 60 Wt% out of the new recipe with a) full tape and b) zoom on the edges.

These physical phenomena could be attributed to the larger amount of additives, slowing the migration of the solvents to the surface. Decreasing the amount of additives could be a solution to minimise these effects; thus, formulations containing 5, 4 and 3 Wt% of binder have been prepared, keeping the ratio Solusolv® : PVB and PEG400 : PVB constant.

As can be seen in *Fig. III-14*, the obtained green tapes were all cracked with a binder content lower than 6 Wt%, their quality increasing with the binder content. Especially, in the case of a slurry containing 3 Wt% of binder, a complete demixing of the tape during drying was observed (*Fig. III-14*).

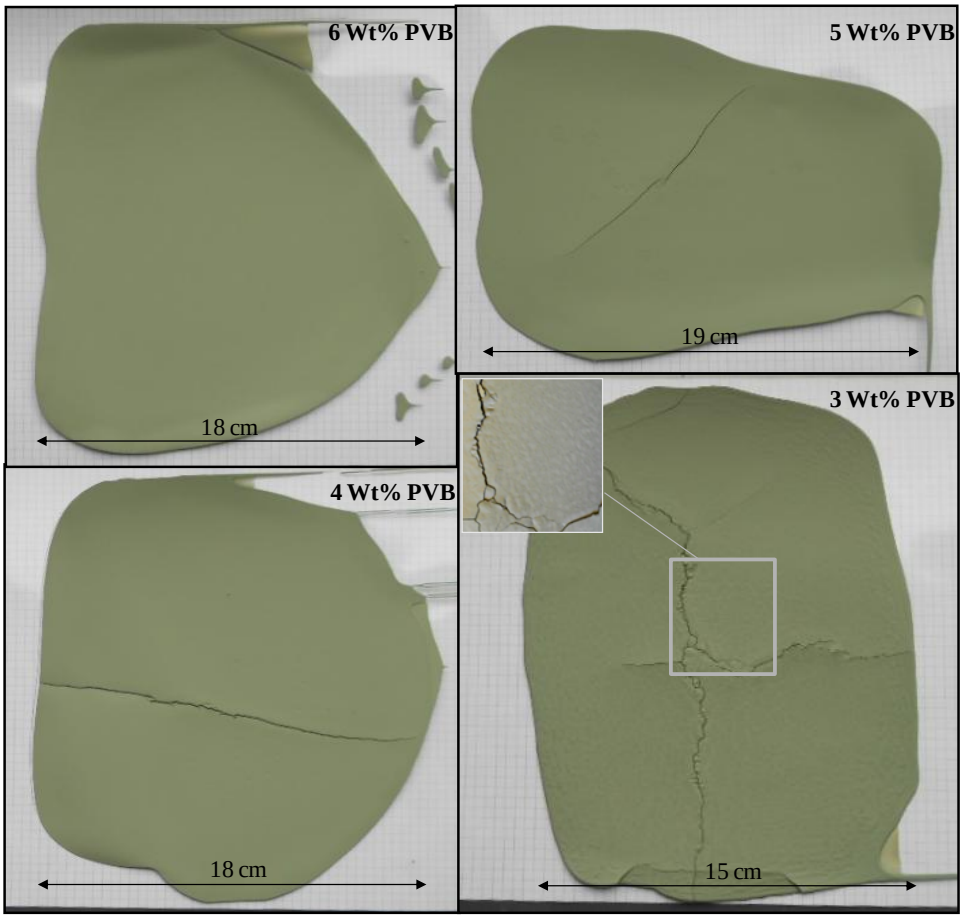

Figure III-14: Drying behaviour of green tapes BIT07 / NiO (40 : 60 Wt%) as a function of binder content, with increased plasticisers content.

A decrease in the binder content could not be done without directly impacting the quality of the tapes, even if being effective to solve the problem of wrinkling. Slurry formulations involving 6 Wt% of binder are thus further validated. Since the wrinkling concerns only the edges of the tapes, not used to prepare cells (see *Fig. III-15*), this defect has been neglected.

Finally, the difference of thicknesses between the tapes from the old recipe and this one has to be noticed. Indeed, the previous tapes were around 630 µm thick (300 µm in the edges), compared to an average of 540 µm in this case. It can be explained first by the lower solid

loadings and second by the lower drying speed of the tapes from the new recipe, which lets time to the polymer chains to reorganise, thus occupying less volume. A remark concerns here the secondary effect of the increased plasticisers content: besides slowing the migration of solvents to the surface by increasing tight packing, the type I plasticiser is a "binder solvent", thus similar to the solvent vehicle. This "binder solvent" is however much less volatile, and by remaining stable in the drying tape (the flash point of the Solusolv® S-2075 being 216°C) it allows even more motion and reorganisation of the polymer chains during drying.

An additional comment here concerns the non-homogeneity in the thickness of the tapes (thicknesses vary between 450 µm and 540 µm in the middle and beginning of the tape, and between 380 µm and 420 µm on the edges, the lowest thickness corresponding to the end of the tape). This effect, although normally observed in the tape casting industry due to some spreading of the slurries [41], could be an issue for the casting of homogeneous electrolyte layers in our case due to the relatively small size of the tapes. The thickness inhomogeneities might be reduced by using a reservoir for the slurry instead of pouring it manually on the front of the doctor blade. Casting larger tapes could also enable a decrease of these gaps by allowing less spreading in the border (slurries using the complete width of the doctor blade) and increase the relative proportion of the "middle" part of the tape.

The doctor blade gap has been increased from 1500 µm to 1750 µm to obtain workable thicknesses, giving comparable quality and crack-free tapes with dry thicknesses around 650 µm.

1.3. Pre-sintering

Apart from the de-binding, the pre-sintering step consists in heating the substrate to an intermediate shrinkage, which has to be high enough to ensure the mechanical strength needed for the vacuum slip casting process, but letting enough remaining porosity to facilitate the solvent migration. Also, additional shrinkage of the substrate during the sintering step of the electrolyte, performed at higher temperature, is believed to help its densification as well as to reduce thermal stresses by allowing the substrates to shrink along with the electrolyte layer.

The useful area of the tapes, i.e. the area where all the samples have been cut, is illustrated in *Fig. III-15*.

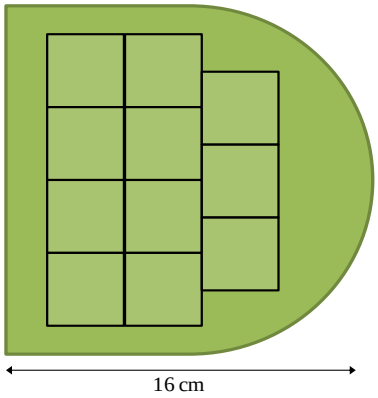

Figure III-15: Schematic illustration of the area of the green tapes where the substrates have been cut.

The thermal behaviour of the substrates during binder burnout has been characterised by TGA measurements, shown in *Fig. III-16*.

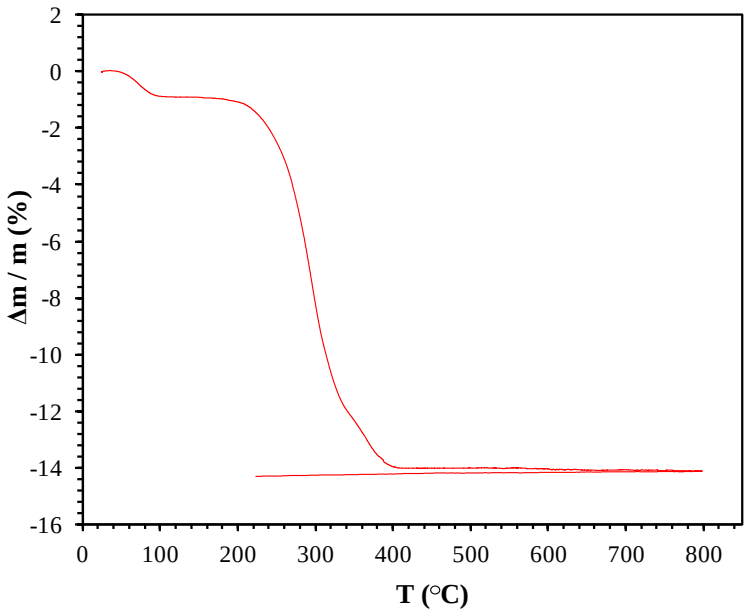

Figure III-16: Typical TGA measurement for a green tape BIT07 / NiO.

From the TGA results, three different phases can be identified. The first one from room temperature to 100°C corresponds to the dehydration of the tape and the evaporation of the last leftovers of solvents. The two other phases can be identified in between 100 and 400°C and correspond to the binder and plasticisers removal (lighter organics leaving the tape first). All the organics seem to be evacuated at around 400°C. First sintering programs involved heating and cooling rates controlled at 1°C / min, to prevent blistering or cracking caused by exiting gases during binder removal as well as to let enough time to the substrates to accommodate the

stresses occurring during sintering. All the obtained substrates remained flat (except for one sintering temperature as will be discussed hereafter) and crack free, so the heating and cooling rates have been kept at 1°C / min along this work

The optimal size for the pre-sintered substrates is empirically determined to be 10 to 15% larger than the expected size of the final cell; the pre-sintering program has thus to be selected accordingly. For this purpose, different temperatures (1100°C - 1250°C) and dwellings (6h - 9h) have been tested, taking into account a sintering temperature of 1350°C and a dwelling time of 9 hours for the densification of the electrolyte, optimised on the basis of the work of M. Letilly at IMN [303]. The shrinkages for the different sintering programs and the available additional shrinkage during the final sintering step to reach the final size of the half-cells are presented in *Table III-3*.

Table III-3:
Shrinkages after pre-sintering and shrinkages to the final size as a function of the sintering program for half-cells BIT07 / NiO 40 : 60 Wt% | BIT07.

(Pre-)sintering temperature / dwelling time	Shrinkage	Shrinkage to the final size
1350°C / 9h	18.0%	-
1250°C / 6h	13.0%	5.5%
1200°C / 12h	11.5%	7.3%
1200°C / 6h	9.3%	10.0%
1150°C / 9h	7.4%	12.2%
1150°C / 6h	6.0%	14.1%
1100°C / 6h	3.5%	17.0%

As can be seen from this table, three pre-sintering programs (1200°C / 6h, 1150°C / 9h and 1150°C / 6h) are giving tapes in the required size range, i.e. 10 to 15% larger than the final product. However, pre-sintering at 1200°C led to substrates not completely flat, thus breaking during the vacuum slip casting process. For pre-sintering at 1150°C, comparable quality of half-cells was obtained for both dwelling times; pre-sintering at 1100°C for 6 hours gave half-cells with comparable quality, but a lower mechanical strength of the pre-sintered substrates was noticed and led to handling difficulties regarding the casting of the electrolyte.

A pre-sintering program at **1150°C for 6 hours** was thus selected.

2. Deposition of electrolyte layer by vacuum slip casting and co-sintering

The produced green tapes were cut into 4 × 4 cm² pieces and pre-sintered at 1150°C during 6 hours. For the vacuum slip casting process, a suspension of electrolyte particles is prepared by ball-milling during 100 hours the BIT07 powder in ethanol with polyethylene imine (50 Wt% solution in water, Aldrich) as dispersant and Ø3 mm and Ø5 mm zirconia balls as a grinding media. The suspension is left to sediment for 6 hours, and the upper part is taken for casting, letting the biggest particles which have sediment faster in the bottle. The average particle size after milling and sedimentation is about 0.5 µm with a broad repartition of the size of the grains (*Fig. III-17*), believed to improve the packing density of the green layer and thereby the density of the sintered product.

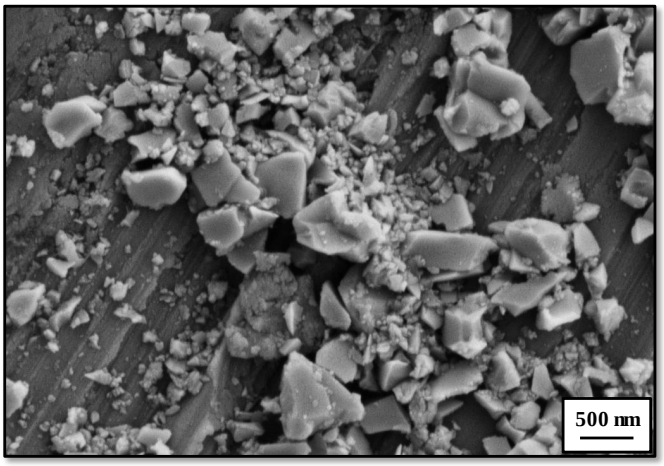

Figure III-17: SEM micrograph of the BIT07 powder after ball-milling during 100 hours.

The concentration of the suspension has been calculated by the determination of the difference of weight of a sample of the suspension before and after evaporation of the solvent; the given value is an average made from five samples. The concentration was thereby determined to be around 9g / L, with a deviation around 6%. After this grinding step, XRD measurements on the BIT07 powder showed the apparition of barium carbonate due to the presence of water during the ball-milling step, as can be seen in *Fig. III-18*. However, $BaCO_3$ decomposes at around 900°C i.e. will disappear during the sintering step of the half-cell.

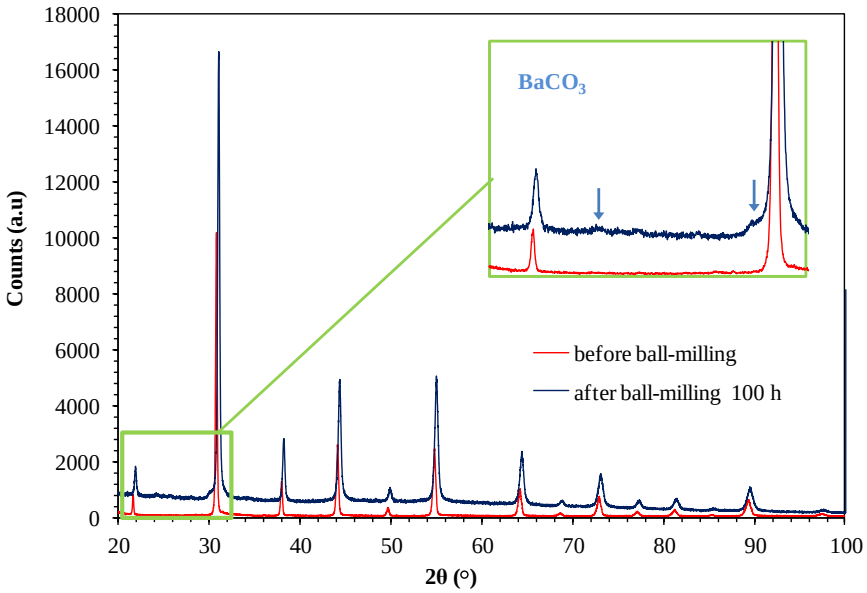

Figure III-18: X-Ray Powder Diffraction patterns for the BIT07 powder supplied by EMPA as received and after ball-milling during 100 hours.

The targeted thickness for the electrolyte is 10 µm, which corresponds to a volume of suspension of 4.7 mL, calculated from Eq. 12 for a green size of the electrolyte of 3 × 3 cm² and a final size of 2.64 × 2.64 cm².

$$\text{Volume (L)} = \frac{\text{desired thickness (cm)} \times \text{powder density (g / cm}^3\text{)} \times \text{surface (cm}^2\text{)}}{\text{concentration of the suspension (g / L)}} \qquad \textbf{(12)}$$

The suspension is poured on the surface of the sealed pre-sintered substrate and a pressure of typically 700 mbar is applied until complete aspiration of the solvent. The samples are then let to dry for 12 hours prior to sintering. *Fig. III-19* gives an illustration of the samples at the different elaboration steps, from the green tape to the sintered half-cell.

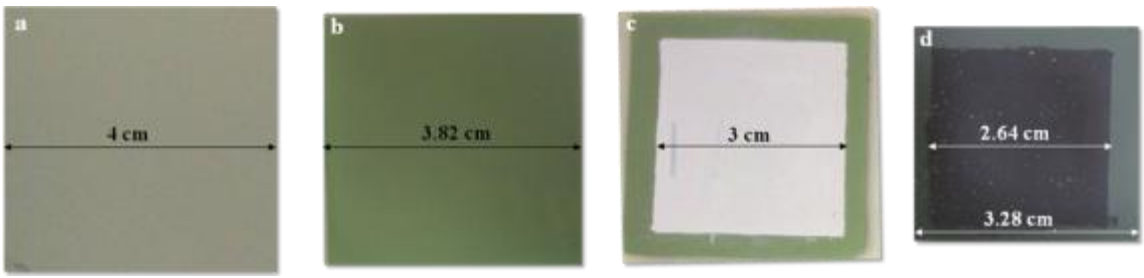

Figure III-19: Pictures of the half-cells produced with a) cut green tape, b) pre-sintered anode substrate, c) after vacuum slip casting of the BIT07 electrolyte layer and d) after final sintering.

Cross-section SEM characterisations on half-cells after sintering at 1350°C for 9 hours outlined **thin (around 10 µm) and dense** (density around 97% determined by image analyses) **electrolyte layers**, with a **good interface with the anode substrate** (*Fig. III-20a* and *Fig. III-20b*, respectively).

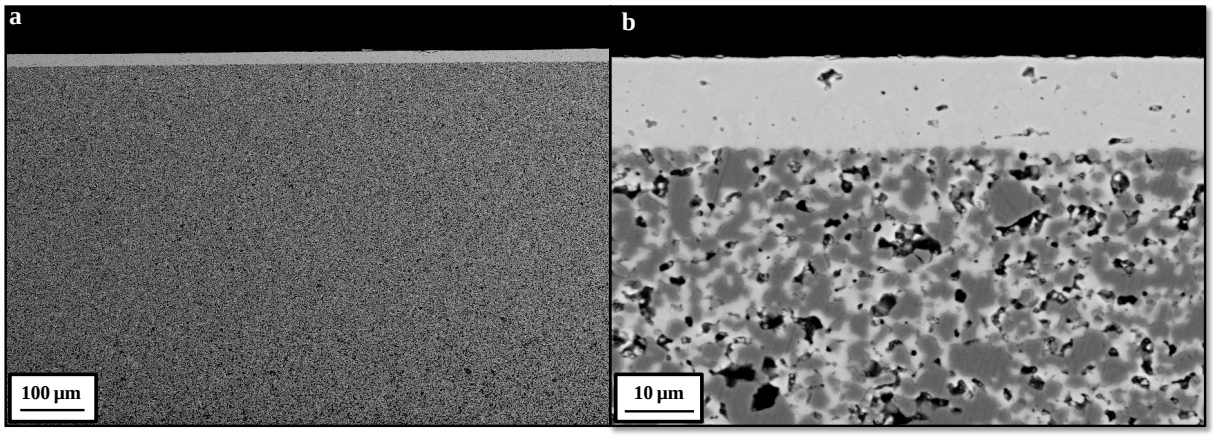

Figure III-20: BSE SEM micrographs of polished cross-section for a sintered half-cell BIT07 / NiO | BIT07 with a) overview and b) higher magnification.

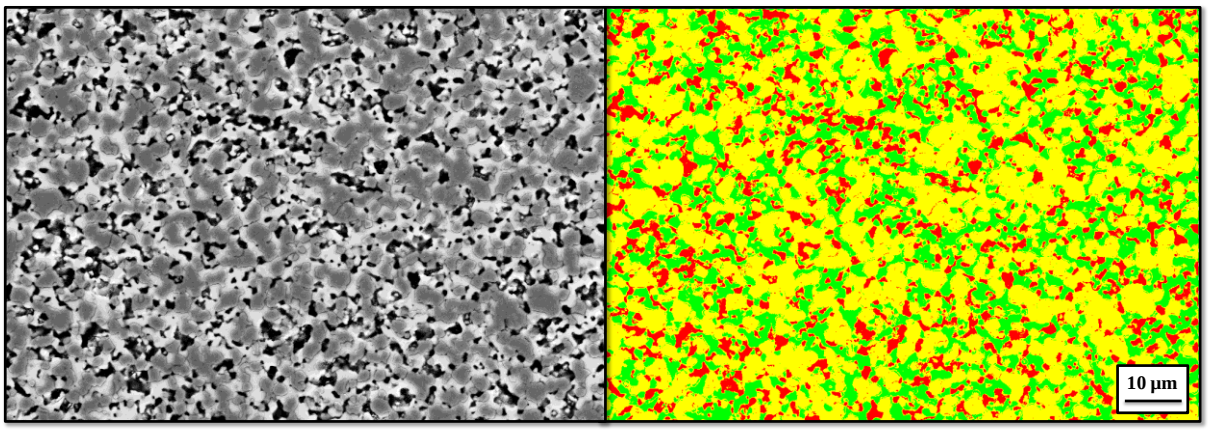

Figure III-21: BSE SEM micrograph before (left) and after (right) image treatment of polished cross-section for a BIT07 / NiO anode substrate. Pores are in red, BIT07 in green and NiO in yellow.

After sintering at 1350°C for 9 hours, the BIT07 / NiO anodes showed highly homogeneous repartition of BIT07 and NiO in the cermet (*Fig. III-21)*. Porosities of the anode substrates before reduction were found between **13 and 20%**, both by direct measure of the volume of the samples and by SEM micrograph analyses. Also, most of the half-cells appeared bended after sintering, and thus an ironing step was needed before coating the cathodes. This was made by heating the half-cells at 1300°C for 2 hours between 2 alumina plates.

Finally, a reactivity between the substrates and the alumina plates occurred during sintering, despite a protective layer of GDC powder in between, leading to the formation of a brown compound on the bottom of the half-cell. It was not possible to identify this compound by XRD, but if insulating it could hinder electrochemical performance by penalising the current collection on the anode side. This problem has been solved by sintering the half-cells on nickel foam.

3. Cathode layer deposition by screen printing

The three cathode powders $La_{1.95}NiO_{4+\delta}$ (LaN), $Nd_{1.97}NiO_{4+\delta}$ (NdN) and $Pr_{1.97}NiO_{4+\delta}$ (PrN) were supplied by Marion Technologies (Verniolles, France), with a d_{50} value of 1.25, 0.65 and 0.29 µm, respectively. The particles size distribution spectra for the three powders can be found in *Fig. III*-22. SEM micrographs on powders confirm the granulometry measurements, as can be seen in *Fig. III-23*.

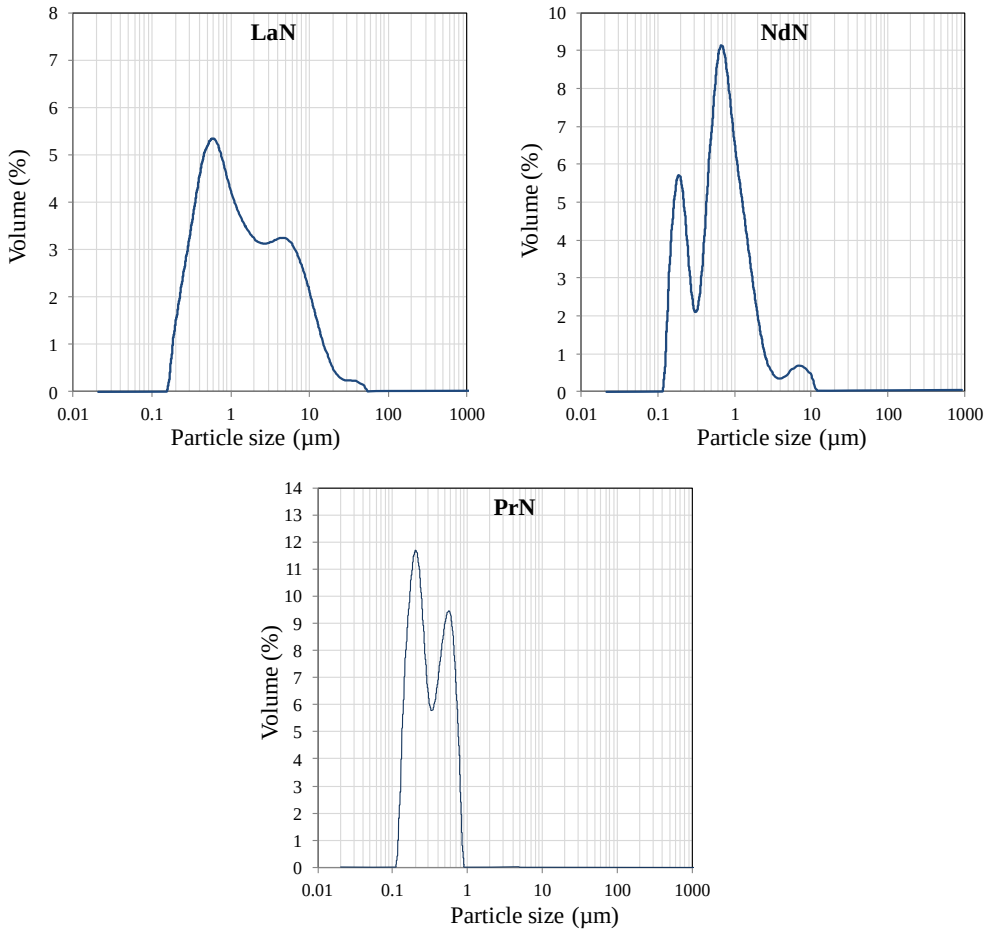

Figure III-22: Particle size distribution of LaN (left), NdN (middle) and PrN (right) powders from Marion Technologies.

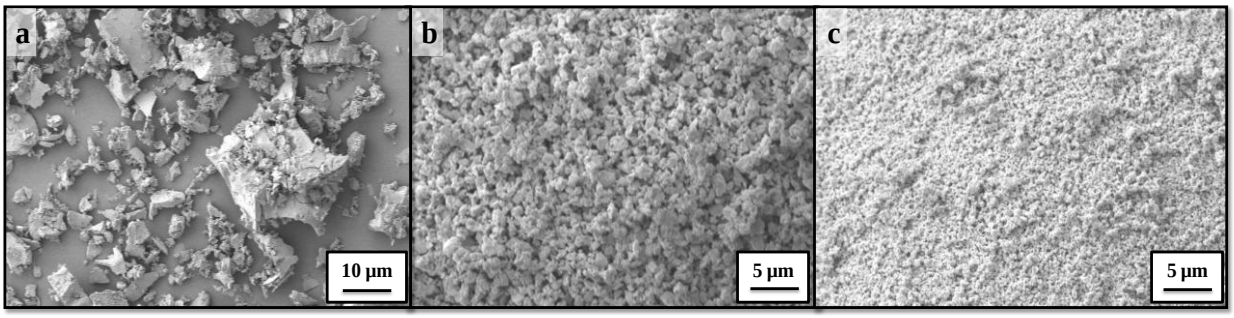

Figure III-23: SEM micrographs of a) LaN, b) NdN and c) PrN cathode powders.

The inks for the screen printing of the cathode layers have been prepared by mixing the cathode powders in a vehicle composed by terpineol (95% min, Alfa Aesar) and 6 Wt% of ethylcellulose (Aldrich) as a binder, first by manual grinding in a mortar and then using a three-roll mill. The three cathodes have been printed using a mesh for required wet thickness of 100 µm from Koenen GmbH, Germany, on the sintered BIT07 / NiO (40 : 60 Wt%) | BIT07 half-cells. The printing involved the deposit of 2 layers, with a drying step at 60°C for 1 hour in between. The diameter of the circular cathode layer was 16 mm. The three cathodes have been sintered using the sintering programs optimised by A. Brüll from ICMCB in the frame of INNOSFC project, at controlled heating and cooling rates. The sintering temperatures were thus 1050°C for NdN and PrN and 1100°C for LaN, dwelling times 1 hour.

By applying an adhesive tape on the sintered cathode layers, PrN delaminated completely when removing the tape, while NdN and LaN stayed fully attached. SEM characterisations on cross-sections of the complete cells with the three cathodes have been performed and are presented in *Fig. III-24*.

In the three cases, the layers obtained presented homogeneous thicknesses around 25 - 30 µm for LaN and PrN and 50 µm for NdN with homogeneous microstructures. The difference of thicknesses comes from the loading of the screen printing pastes.

Porosities seem also adapted for the three cathodes. However, while **NdN seems well bonded to the BIT07** electrolyte, the quality of the electrolyte / cathode interface is fairly **lower in the case of LaN and PrN**. In addition, the PrN layer appeared slightly cracked, which might be due to the relatively small size of the PrN particles leading to higher sintering activity and thus higher shrinkages. Using a PrN cathode powder with larger grains, for instance with a median size of 0.4 µm as optimised by Ferchaud et al. for a $Pr_2NiO_{4+\delta}$ cathode on YSZ electrolyte [260], may allow to reduce the cracks.

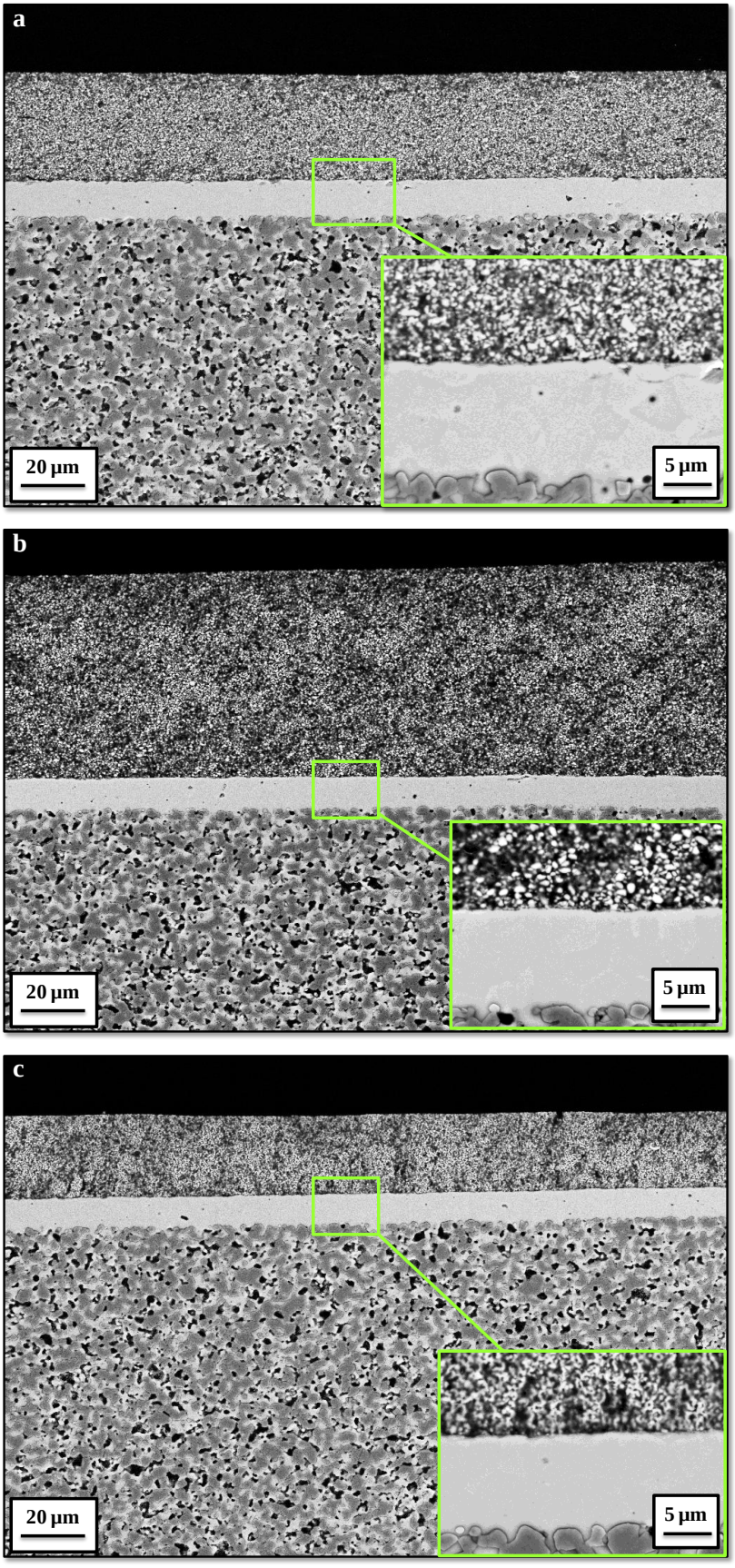

Fig. III-24: BSE SEM micrographs of polished cross-sections for the cells a) BIT07 / NiO | BIT07 | LaN, b) BIT07 / NiO | BIT07 | NdN and c) BIT07/NiO | BIT07 | PrN.

4. Towards a second generation of cells

4.1. Introduction of a cathode barrier layer

To improve the bonding between the cathode and the electrolyte, and more generally the quality of the cathode / electrolyte interface, the use of a thin (2-3 µm) $Ce_{0.9}Gd_{0.1}O_{2-\delta}$ (GDC for gadolinia doped ceria) barrier layer in between BIT07 and the three nickelates has been studied on the basis of the work of C. Ferchaud et al. [260] and the results obtained on symmetrical cells LnN (| GDC |) | BIT07 | (| GDC |) LnN by A. Brüll in the frame of the INNOSOFC project.

The GDC powder supplied by Marion Technologies (Verniolles, France) presents a particle size around 0.2 - 0.3 µm with a monomodal distribution, according to laser granulometry measurements.

The GDC layer has been deposited by screen printing on sintered half-cells using a 50 µm wet thickness mesh (one layer), and sintered at 1350°C for 2 hours. Note that in this case the ink has been prepared with lower solid content to obtain thin layers. The three different cathodes have been deposited by screen printing as well, as described in the previous section, and sintered at 1170°C for 1 hour as optimised by Ferchaud et al. for a GDC | PrN assembly [260].

Polished cross-section micrographs of the obtained cells are shown in *Fig. III-25*.

In the three cases, a **thin and homogeneous layer of GDC** can be observed. However, the adherence of the GDC layer on BIT07 seems fairly poor, and the layer appeared porous and cracked. Meanwhile, the **interface with the cathodes is substantially improved**, with a good adherence obtained for the three cathodes. In the case of PrN, the increased sintering temperature increased the number of cracks compared to what was observed in *Fig. III-24c*, although the cracks appeared mainly superficial (*Fig. III-25c*).

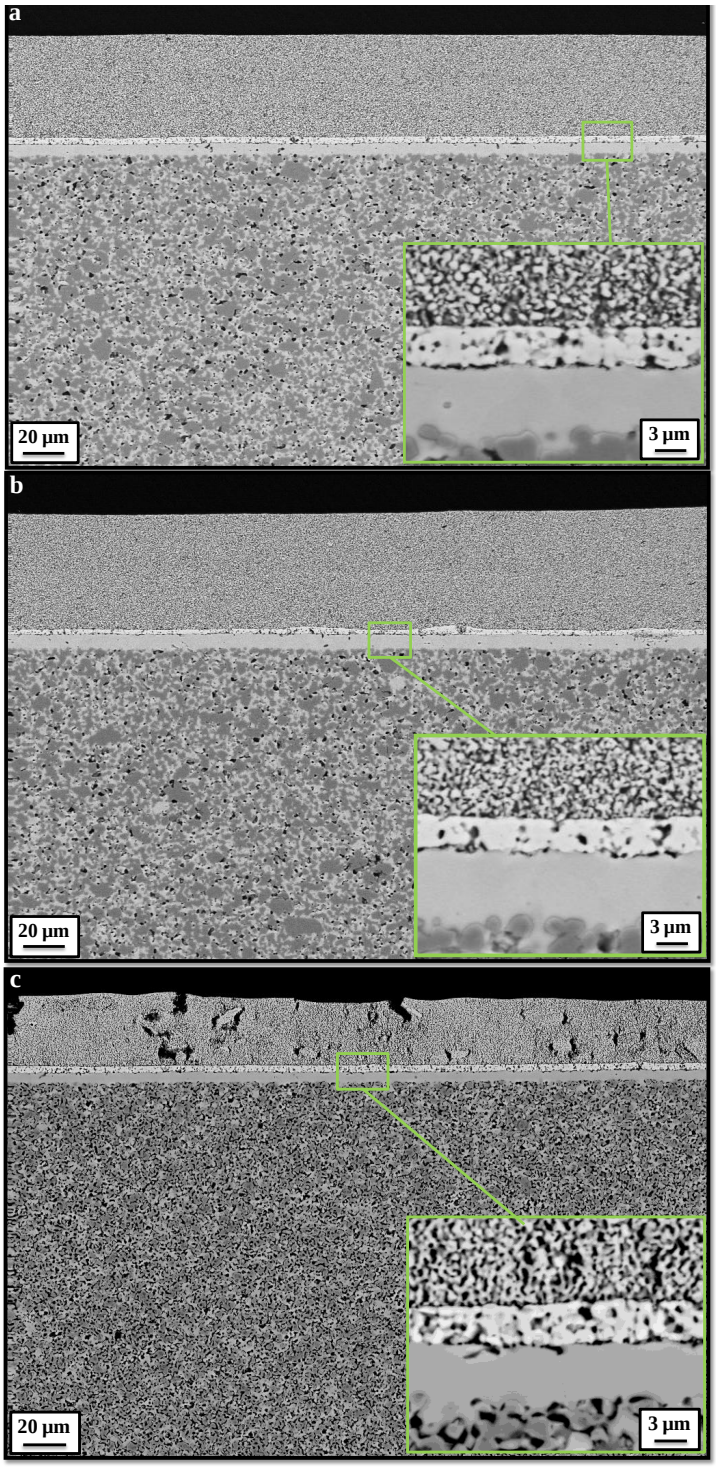

Figure III-25: BSE SEM micrographs of polished cross-sections for the cells a) BIT07 / NiO | BIT07 | GDC | LaN, b) BIT07 / NiO | BIT07 | GDC | NdN and c) BIT07/NiO | BIT07 | GDC | PrN.

In a wish to keep the number of sintering steps as low as possible and to improve both densification and adherence of the GDC layer, attempt has been made to co-sinter the BIT07 electrolyte layer with the thin layer of GDC. As concerns the coating of GDC by screen printing, no cell has been obtained due to the breaking of the substrates (at this step only pre-

sintered) during the printing process: increased mechanical cohesion would be thus needed for using screen printing.

Therefore, deposit of BIT07 and GDC layers by vacuum slip casting has been considered. The GDC slip has been prepared using the same protocol as for the BIT07 powder, with a concentration of the suspension around 10.5 g / L and a GDC particle size below 0.1 µm (SEM of the powder shown in *Fig III-26*).

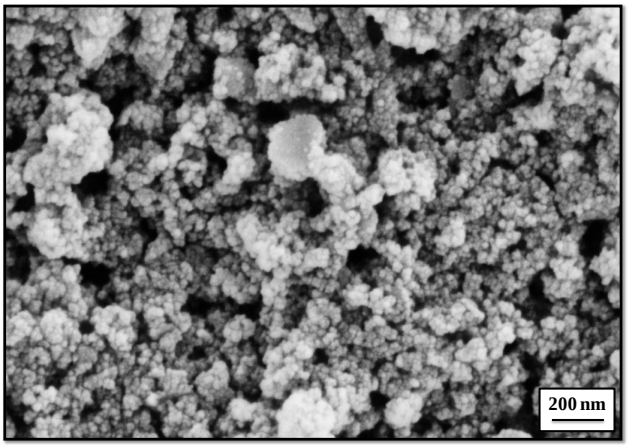

Figure III-26: SEM micrograph of the GDC powder after ball-milling during 100 hours.

From our observations, coating GDC by vacuum slip casting on a green layer of BIT07 gave limited available thicknesses. Indeed, when adding a too large amount of GDC suspension, both BIT07 and GDC green layers cracked and delaminated during drying, as shown in *Fig. III-27a*. Reducing the volume of GDC slip to 1 mL (corresponding to a targeted thickness around 2 µm) resulted in a crack-free GDC layer after drying (*Fig. III-27b)*.

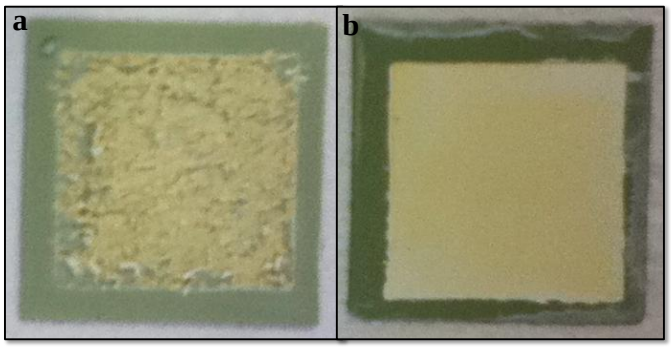

Figure III-27: Picture of half-cells BIT07 / NiO | BIT07 (green) | GDC (green) after drying with a) 3 mL of GDC suspension and b) 1 mL of GDC suspension.

After co-sintering, a homogeneous and thin layer (around 2 µm) of GDC has been obtained, as can be seen on the SEM micrograph in *Fig. III-28*. The BIT07 / GDC interface as well as the density of the GDC layer have been substantially improved; nonetheless, both layers appeared cracked due to the too high difference of sintering behaviour between the two layers. This could be improved by an increase of the particle size of the GDC powder in the slip (reduced ball-milling time) to decrease its sinterability, although dilatometry data would be needed to get relevant information on the respective sintering behaviours of the BIT07 and GDC powders.

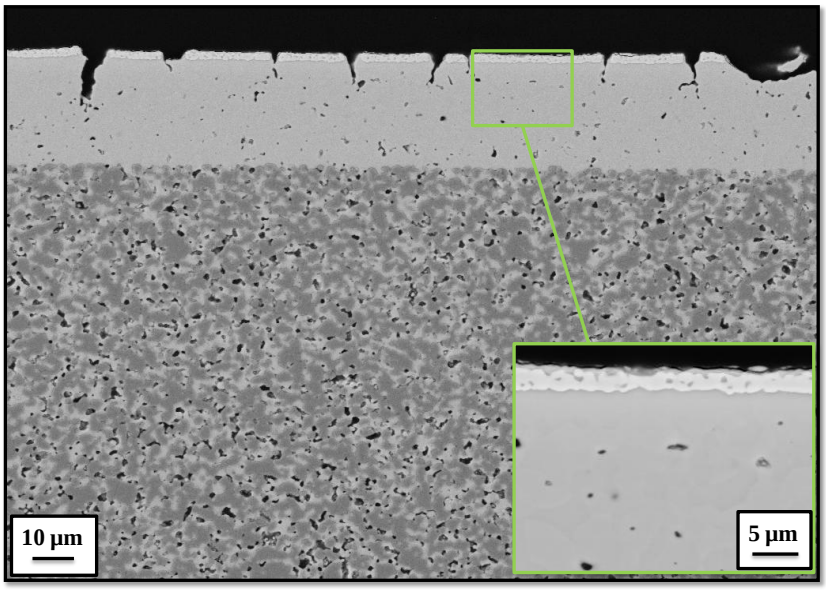

Figure III-28: BSE SEM micrograph of polished cross-section for the half-cell BIT07 / NiO | BIT07 | GDC, BIT07 electrolyte and GDC layers deposited by vacuum slip casting and co-sintered at 1350°C for 9 hours.

Tests with pre-sintering the BIT07 electrolyte layer at 1200°C for 6 hours prior to casting the GDC layer have been performed in order to try to create a bonding between the BIT07 grains and thus improve the thermal matching of the two layers.

As can be seen in *Fig. III-29* for a complete cell with PrN as cathode, densification of the GDC layer remains still better than for the layer deposited by screen printing on sintered half-cells; the cracks have been substantially reduced compared to the co-sintered samples but are nevertheless still present. We can also see from the SEM micrograph that a reactivity occurred in between the PrN cathode and the BIT07 electrolyte at the areas not covered by GDC, determined by EDX to be a diffusion of Pr. In this case as well, a small reduction of the ball-milling time of the GDC slip will increase the particle size of the powder and thus could

reduce its sinterability, improving the cracking behaviour. An increase of the GDC layer thickness could also help the covering of BIT07.

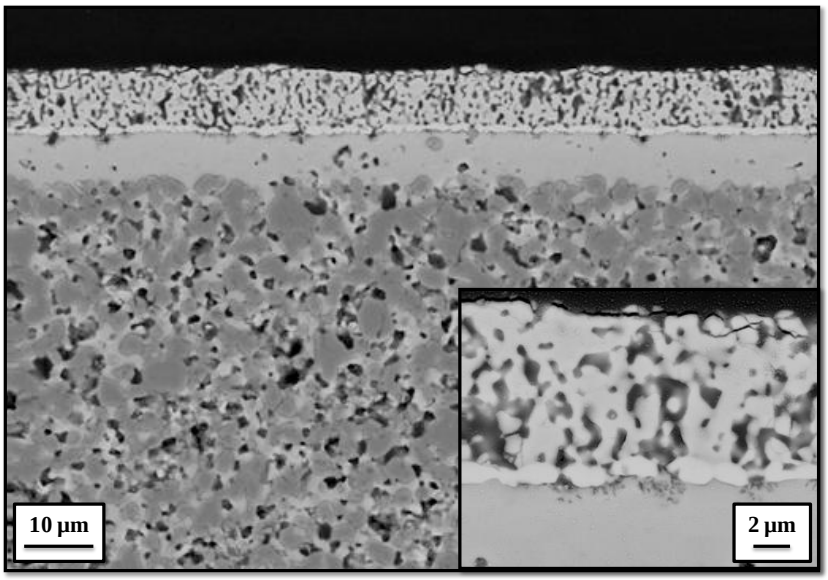

Figure III-29: BSE SEM micrograph of polished cross-section for the cell BIT07 / NiO | BIT07 | GDC | PrN, with BIT07 electrolyte sintered at 1200°C for 6 hours prior to GDC layer casting.

4.2. Transfer to powders from other suppliers

In the frame of the INNOSOFC project, a batch of BIT07 powder has been supplied by Marion Technologies, labelled MT1. This powder presents a particle size significantly lower than the powder from EMPA, as can been seen by SEM in *Fig. III-30*, with a d_{50} value around 0.22 µm (particle size distribution shown in *Fig. III-31*). The phase was pure in the sense of X-Ray diffraction.

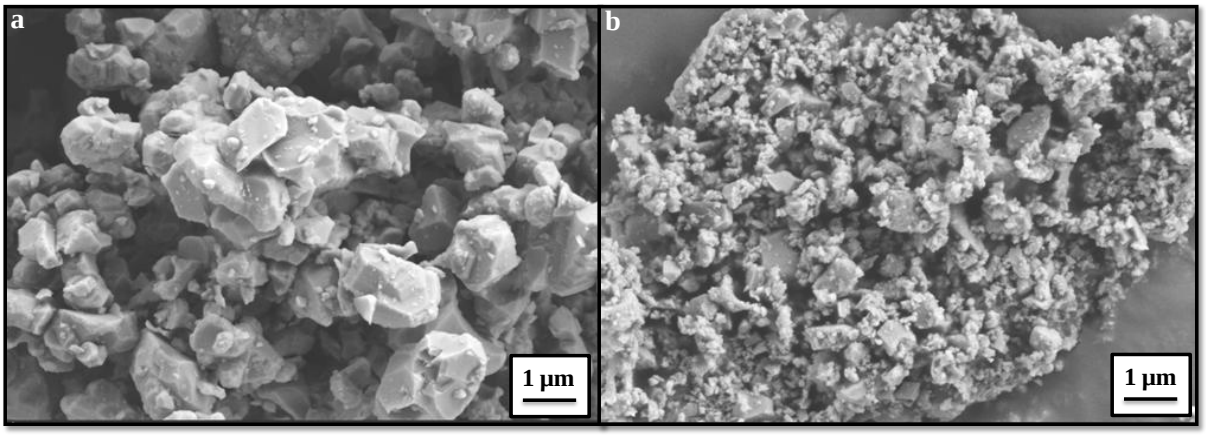

Figure III-30: SEM micrographs of the BIT07 powders supplied by a) EMPA and b) Marion Technologies.

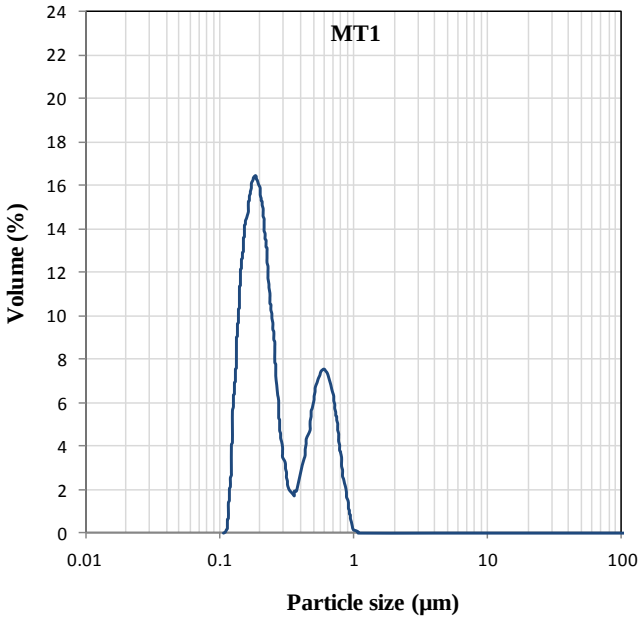

Figure III-31: Particle size distribution of the BIT07 powder supplied by Marion Technologies (batch MT1).

The **recipe** for tape casting developed with the BIT07 supplied by EMPA has been **successfully transferred** to the powder supplied by Marion Technologies (*Fig. III-32.*), with a decrease of the solid loading from 34% to 24.5% due to the lower particle size of the MT1 powder.

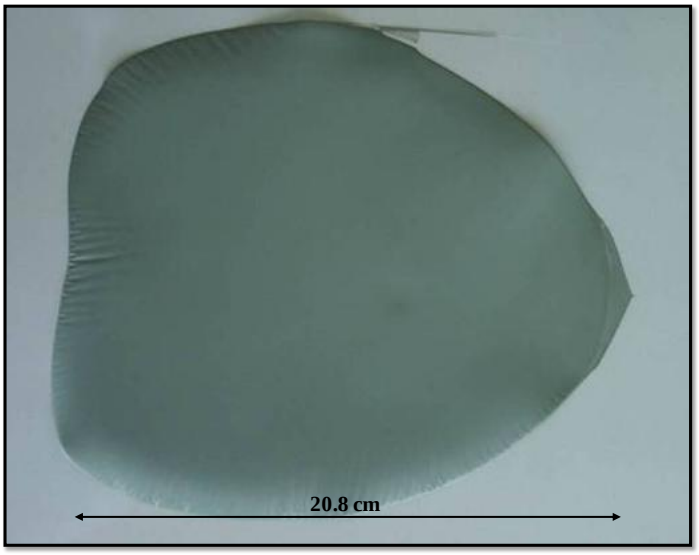

Figure III-32: Green tape BIT07 (MT1) / NiO 40 : 60 Wt%.

However, most of the substrates appeared **cracked after pre-sintering**, as illustrated in *Fig. III-3*3, making impossible the elaboration of complete cells. Following the TGA

measurements performed on standard green tapes, lowering the heating rate in the temperature range 25 - 500°C down to 0.2°C / min (instead of 1°C / min) to decrease thermal stresses during debinding was attempted, but appeared not effective to solve the problem.

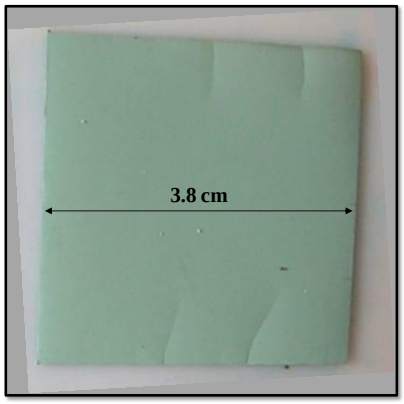

Figure III-33: Substrate BIT07 (MT1) / NiO 40 : 60 Wt% after pre-sintering at 1150°C for 6 hours.

Two more batches of BIT07 powder (labelled MT2 and MT3) with increased particle size (*Fig. III-34*), have been supplied by Marion Technologies and tapes BIT07 (MTx) / NiO were successfully tape-casted. Even if reduced (especially for MT3-based substrates), the cracking of the substrates during pre-sintering could however not be completely avoided.

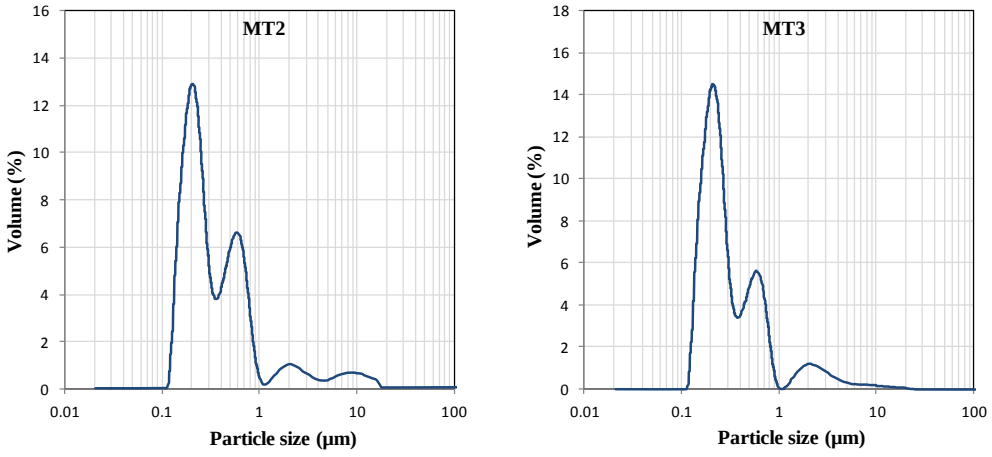

Figure III-34: Particle size distributions of the BIT07 powders supplied by Marion Technologies with on the right the batch MT2 and on the left the batch MT3.

Attempts to heat the BIT07 powders at different temperatures to increase their particle size (heating treatments between 1050°C and 1300°C during 6 hours) before using them have

been realised, without solving completely the above mentioned problem of cracks. The best results have been obtained with the MT3 batch heated at 1250°C for 6 hours. A ball-milling treatment of the powders after heating to remove the bigger grains and thus homogenise their particle size distribution is viewed for the future as a potential solution. As concerns the vacuum slip casting of the electrolyte, suitable layers have been obtained with MT1 and MT2 batches, with a slip ball-milled 24 h (compared to 100 h for the BIT07 from EMPA), both on standard BIT07 (EMPA) / NiO and BIT07 (MTx) / NiO (non-cracked) substrates, as illustrated in *Fig III-35* for an electrolyte made of MT2 on EMPA-based substrates.

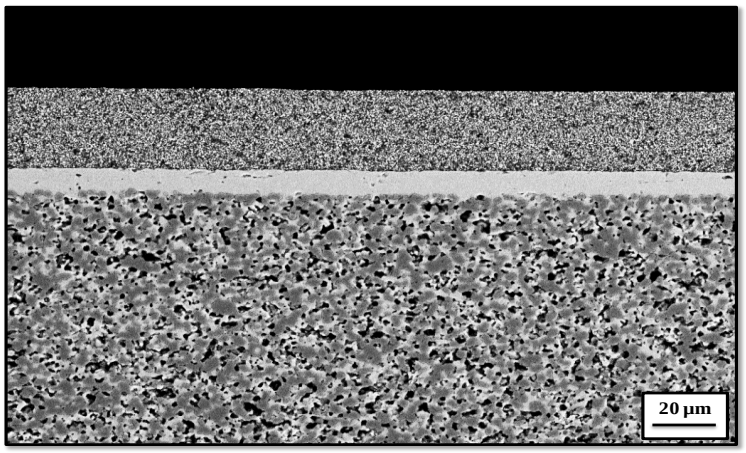

Figure III-35: BSE SEM micrograph of polished cross-section for the cell BIT07 (EMPA) / NiO | BIT07 (MT2) | LaN.

4.3. Introduction of an anode functional layer

In the anode-supported cell configuration, a coarse anodic microstructure of the anode substrate is beneficial for the rapid transport of the fuel gas throughout the whole thickness of the anode and the produced steam to / from the active reaction sites at the interface between the anode and electrolyte. However, triple phase boundaries (TPBs) are crucial for the electrochemical reactions, and the longer the TPB is, the higher the fuel cell performance becomes. Fine particles in an anode functional layer increase the length of the TPB, which results in faster kinetics of the charge transfer reactions and higher fuel cell performance.

In this study, both BIT07 and BLITiMn in association with NiO have been considered as anode functional layers. The BLITIMn powder was supplied by EMPA, with d_{50} = 1.16 µm. The chosen deposition technique was vacuum slip casting since pre-sintered substrates have, as already mentioned, insufficient mechanical cohesion for depositing by screen printing.

The preparation of the suspensions involved ball-milling separately the BIT07 or BLITiMn and NiO powders for 48 hours, based on the optimisations performed in Forschungszentrum Jülich; the sedimentation times for the BIT07 / BLITiMn and NiO ceramic powder slips were 6 hours and 10 min, respectively. Both NiO and ceramic suspensions were then mixed to obtain a weight ratio BIT07 or BLITiMn / NiO powders of 44 : 56, the ceramic content being increased compared to the anode substrate to improve the interface with the electrolyte [296].

Both anode functional layers have been deposited on standard BIT07 (EMPA) / NiO substrates, with a targeted thickness between 5 and 10 µm selected on the basis of the work of Schafbauer et al. [296]. The dried deposited layers have been then sintered at 1050°C for 6 hours, followed by the deposit of the electrolyte layer and the final sintering of the half-cell at 1350°C for 9 hours.

SEM micrographs of the polished cross-sections of the obtained half-cells are shown in *Fig. III-36*.

In both cases, a thin and homogeneous anode functional layer was obtained, well bounded with the anode substrate. For the BIT07 (MT2) / NiO layer, high shrinkage occurred during final sintering leading to a **thin** (around 5 µm) and **dense layer**, though with a good interface with the electrolyte (*Fig. III-36a*). The obtained BLITiMn (EMPA) / NiO layer was **thicker** (around 20 µm) **and more porous**, but the quality of its interface with the electrolyte layer appeared **lower** (see *Fig. III-36b*). This phenomenon might be explained by the lower sinterability of BLITiMn compared to BIT07 [181].

Concerning the anode functional layer involving BLITiMn, increasing both the BLITiMn content and its ball-milling time may allow an improvement of both the layer, by increasing the sinterability of BLITiMn, and its interface with BIT07. The porosity of the functional layer involving BIT07 might be increased by adding a pore forming agent to the slip.

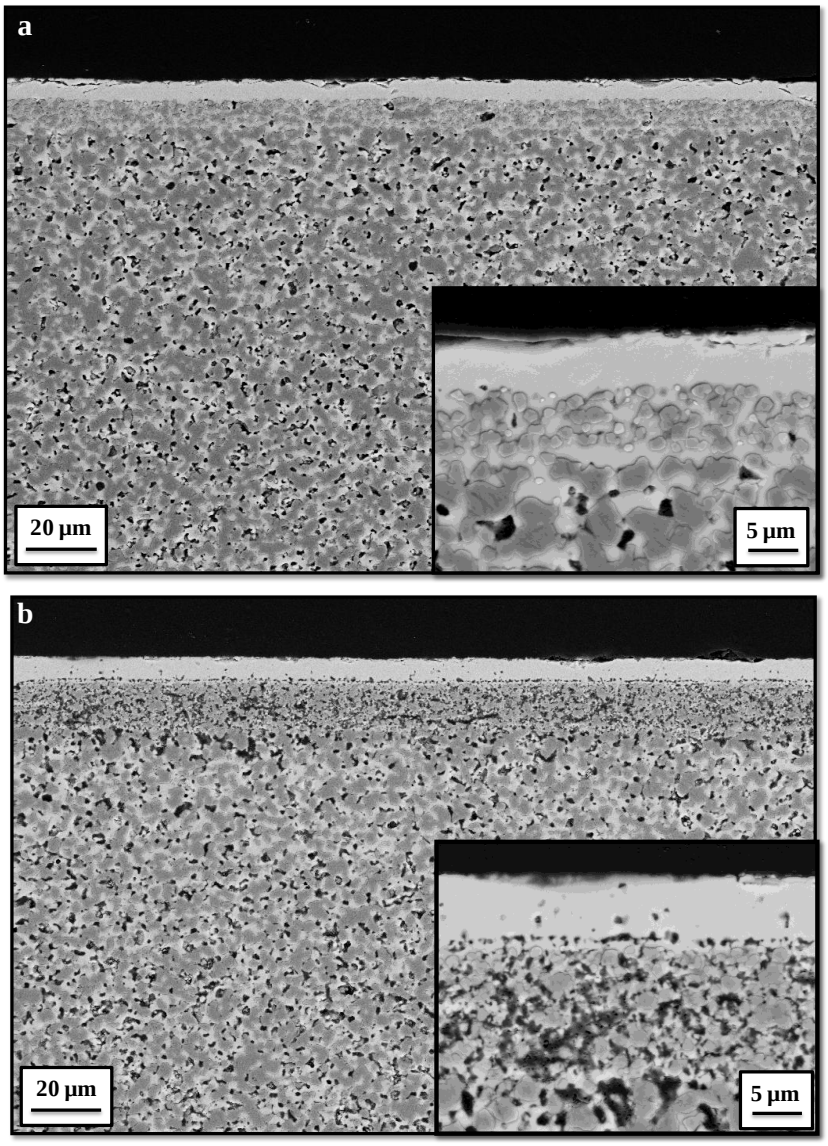

Figure III-36: BSE SEM micrographs of polished cross-sections for the half-cells a) BIT07 (EMPA) / NiO | BIT07 (MT2) / NiO | BIT07 (MT2) and b) BIT07 (EMPA) / NiO | BLITiMn (EMPA) / NiO | BIT07 (MT2).

4.4. Use of starch gel as a pore forming agent

After reduction, the porosities of the anode substrates were ranging from 18 to 35%, for a targeted minimum porosity of 30%. To ensure that all substrates are fulfilling the porosity requirements, gelled starch pore forming agent has been selected to process our cells, on the basis of the work of G. Taillades et al. [304].

The required amount of starch powder is added to water and heated to 80°C with stirring until pre-jellification occurs. The proper amount of BIT07 (in this study batch MT1) and NiO powders are mixed with the gel and the mixture is dried for 12 hours at 120°C. The resulting powder mixture is then manually grinded and used in the slurry.

The addition of jellified starch in the slurries led to **significant modifications** in the formulations. As suggested by Corbin and Apté [305], a first attempt was made by keeping the total weight ratio between solid content (thus powders + starch) and organic additives constant (the solid loading has been decreased). It resulted in an un-homogeneous slurry and consequently considerable heterogeneities appeared during and after drying, suggesting a complete demixing of the system as shown in *Fig. III-37*.

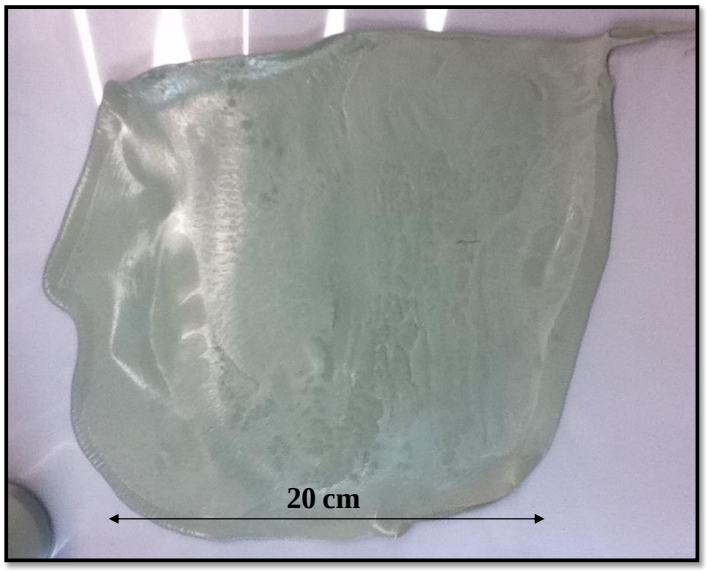

Figure III-37: Picture of a green tape BIT07 (MT1) / NiO containing 2 Wt% of jellified starch.

This experiment indicates that the introduction of starch gel requires an **additional amount of organics to disperse it**, following the conclusions of Sanson et al. [306]. Indeed, starch is composed by two polysaccharides: the linear and helical amylose (20 - 25 Wt%) and the branched amylopectin (75 - 80 Wt%). When heated in water, the granules are breaking up and the amylose and amylopectin are solubilised, giving grains with sizes around 25 nm after drying [307]. Thus, binder content had to be significantly increased to disperse and stabilise the nanometric particles.

Green tapes containing 2 and 4 Wt% of jellified starch (% relative to the weight of ceramic powders) have been successfully casted using the new formulations given in *Table III-4*. Note that in this case the solid amount refers to the amount of BIT07, NiO and starch gel.

Table III-4:
Slurry formulation for the tapes involving jellified starch as a pore forming agent.

Material	Wt% / solid amount	Vol% green tape	Wt% / solid amount	Vol% green tape	Wt% / solid amount	Vol% green tape
Starch gel	0	0	2	9.16	4	16.63
Ethyl Alcohol	13.36		13.36		15.69	
Methyl Ethyl Ketone	25.93		25.93		30.46	
Dispersant	1	2.74	1.8	4.31	1.8	
Binder	6	17.25	8.5	18.78	8.5	17.37
Plasticiser I	5.5	17.97	7	17.57	7	16.26
Plasticiser II	4.5	12.59	6	12.90	6	11.94

In the case of anode substrates containing jellified starch, shrinkages of around 19% after sintering at 1350°C for 9 hours have been obtained, a value that is slightly higher than for the substrates without pore forming agent made with the MT1 powder (17%). This higher shrinkage value may indicate that there is a reduction of the ceramic particle packing in the green tapes due to the distribution of the extra organic additives on the surface of the pore forming agent, thus going in the way of a good dispersion of the elements in the slurry.

After sintering, **fine (sizes around 1 - 2 µm) and well distributed pores** have been obtained (*Fig. III-38*).

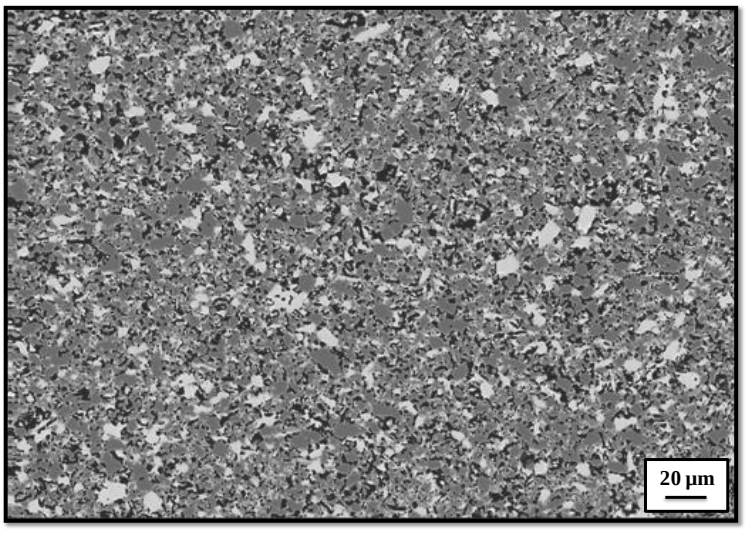

Figure III-38: BSE SEM micrograph of polished cross-section for a BIT07 (MT1) / NiO anode substrate containing 4 Wt% of jellified starch.

By SEM micrograph image treatment (average made on three micrographs taken at three different locations), the different proportion of each constituent (BIT07, NiO and pores)

could be determined. Thus, substrates without pore formers were presenting around 8% of porosity, while adding 2 Wt% and 4 Wt% of jellified starch gave porosities of around 13% and 25%, respectively. The *Fig. III-39* shows the SEM micrographs of the polished cross-sections and the corresponding treated images for the substrates with 0, 2 and 4 Wt% of starch gel. The *Table III-5* gives the details about the relative proportions of each phase (BIT07, NiO and pores). The additional obtained porosity is well correlated to the volume fraction of jellified starch present in the slurry.

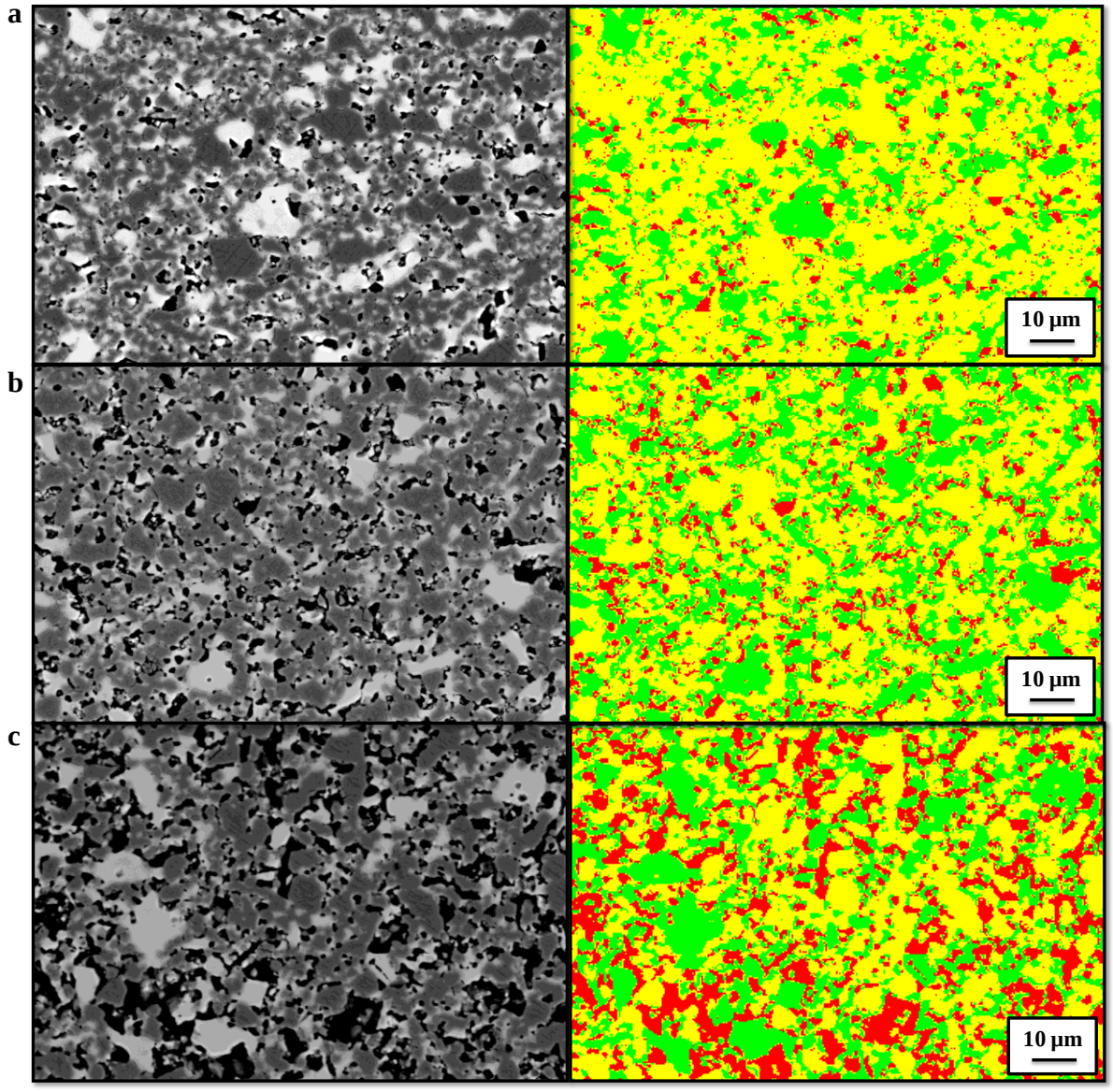

Figure III-39: BSE SEM micrographs before and after image treatment of polished cross-sections for BIT07 (MT1) / NiO anode substrates a) without pore-former, b) containing 2 Wt% of jellified starch and c) containing 4 Wt% of jellified starch, with pores in red, NiO in yellow and BIT07 in green.

Table III-5:
Proportion of each phase in sintered BIT07 (MT1) / NiO substrates containing 0, 2 and 4 Wt% of jellified starch as a pore forming agent.

Phase	0 Wt % starch gel	2 Wt % starch gel	4 Wt % starch gel
pores	8% ± 2%	13% ± 2%	25%
NiO	63% ± 3%	57% ± 7%	47% ± 4%
BIT07	28% ± 3%	30% ± 5%	27% ± 4%

The use of jellified starch gel as a pore forming agent seems thus like an effective way to produce anode substrates by tape casting with a **highly homogeneous repartition of small-sized pores**. **Adding 4 Wt% of jellified starch gave porosities around 25%** on non-reduced substrates, which is well fitting with the anode specifications. However, no complete cells have been obtained due to the swelling of some substrates during pre-sintering, probably due to the larger amount of organics to be burned, also when using slower heating rates (tests made with heating rates down to 0.2°C / min). In addition, the reduced mechanical strength linked to the increased porosity made difficult the deposit of the electrolyte layer by vacuum slip casting. In opposition, the number of cracks observed on substrates decreased compared to substrates without pore former based on MT1 powder, coming from the reduced shrinkage and thus reduced stress during pre-sintering.

The next step of this study would be to introduce starch gel in slurries using larger ceramic grain sizes; decreased sinterability induces higher porosity, giving more paths for the organic vapour motion in the substrates during debinding.

4.5. Up-scaling

As described in the first three paragraphs of this chapter, a shaping protocol has been implemented at lab scale for the elaboration of complete cells based on BIT07 EMPA powders. To further validate this protocol at a pre-industrial scale, attempts have been made to produce larger cells (targeted size 10 × 10 cm²). For this purpose, the first step concerned the increase of the size of the green tapes.

Larger volume of slurry using the standard formulation (*Table III-2*) was prepared and cast, with an obtained green tape size around 20 × 40 cm². In this case however the dried tape appeared oily with “raindrop” patterns of plasticiser on the surface. This oily surface is coming from a large excess of plasticiser, most likely type II (the lubricant) since it has a little or no chemical reaction with the other components of the system [41]. In this case, a phase separation is observed and the plasticiser does not remain homogeneously distributed in the

tape matrix, and even squeezes out of the matrix during drying shrinkage. This difference of behaviour compared to the smaller tapes might come from the slower drying rate of the larger volumes, giving more time to the polymer chains to reorganise and leading thus to higher shrinkages.

A new formulation with decreased plasticiser content to 5 Wt% and 4 Wt% (relative to solid amount) for type I and type II plasticisers, respectively, gave good quality green tapes, as shown in *Fig. III-40*. Note that this new formulation has been successfully used in smaller batches.

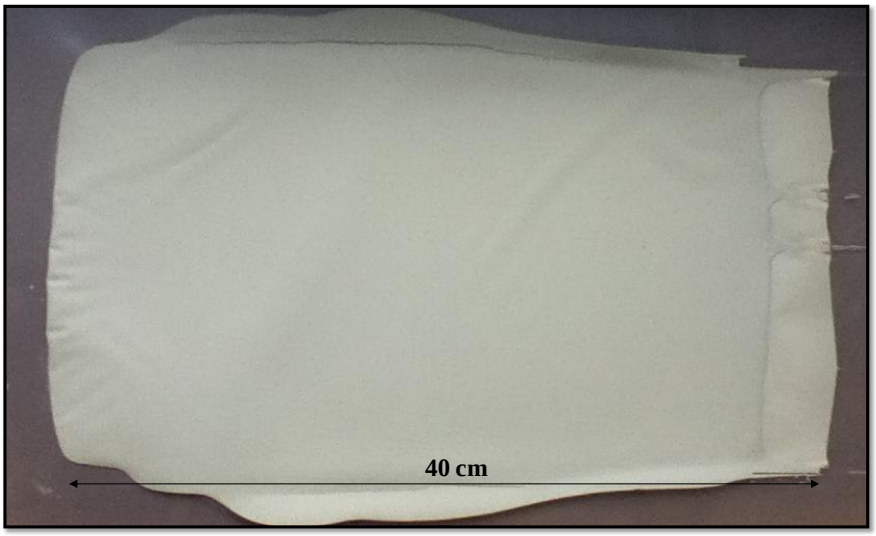

Figure III-40: Picture of a green tape BIT07 (EMPA) / NiO from larger slurry.

The green tape was then cut in 12.2 × 12.2 cm² piece(s), for a final product size of 10 × 10 cm², and pre-sintered at 1150°C for 6 hours. After pre-sintering, **crack-free substrates (size 11.4 × 11.4 cm²)** have been obtained, as shown in *Fig. III-41*.

However, these large substrates appeared slightly swelled and were thus breaking during the vacuum slip casting process, making so far impossible the production of complete cells. The first explanation to the swelling might come from inhomogeneities in the green tapes, related to eventual inhomogeneities in the slurries themselves, less critical in the smaller batches. This difference of behaviour during the pre-sintering step might also be linked to the increased size of the substrates: we observed in smaller substrates that at around 300°C the substrates are bending upwards, recovering their flatness at increased temperatures. This bending allows organics removal from both sides of the substrates. However, in the case of larger cells, it might be assumed that since the weight to move upwards is greater, more surface

remains in contact with the sintering plate, organic vapours going downwards causing the swelling. Also, temperature gradients in the furnace's chamber may cause differential thermal behaviour within the substrate.

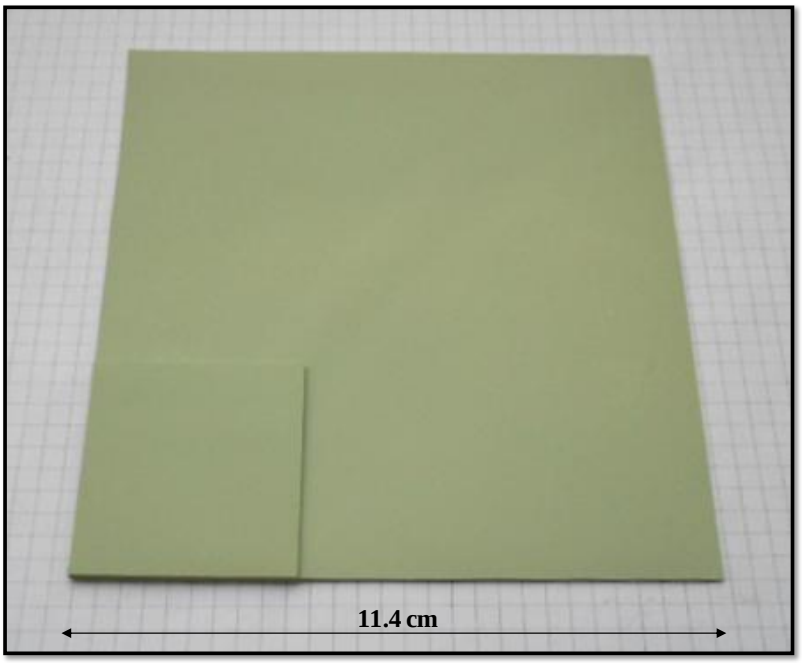

Figure III-41: Substrates BIT07 (MT1) / NiO after pre-sintering at 1150°C for 6 hours.

SEM analyses on cross-section of sintered substrates from larger tapes would give more information about the repartition of matter through the thickness of the tapes. Sintering on nickel foam to allow binder burnout from both up and down sides could also help to keep the flatness of the tapes.

Moreover, depositing the electrolyte layer on green tapes instead of pre-sintered substrates would avoid the problem of breaking of the substrates, as shown in the work of Rieu et al. where high quality half-cells of 10 × 10 cm² size were obtained by screen printing BIT07 on YSZ / NiO green tapes [308]. In our case, promising results have been obtained on 4 × 4 cm² green substrates using this protocol, both on BIT07 (EMPA) / NiO and BIT07 (MT1) / NiO, with BIT07 batch MT1 as an electrolyte. Note that in this case, the electrolyte sintering time could be decreased down to 5 hours.

5. Conclusion

In this chapter, the development of a protocol for the elaboration of anode-supported complete cells has been detailed.

The first part was devoted to the tape casting process for the elaboration of the anode substrates. The scientific pathway for the determination of a **slurry formulation** for BIT07 (EMPA) / NiO (J.T. Baker®) 40 : 60 Wt% using **environmental friendly additives** has been described. Efforts have been made in differentiating the influence of parameters such as drying speed or binder content on the drying behaviour of the tapes. A suitable recipe giving **high quality tapes** in a reproducible way could be proposed. The optimum pre-sintering program for the substrates has been set to **1150°C for 6 hours**.

Afterwards, deposit of the BIT07 (EMPA) electrolyte by vacuum slip casting followed by at sintering step at 1350°C for 9 hours has been achieved. **Good quality sintered anode substrates** with a homogeneous repartition of the BIT07 and NiO grains were obtained, though with a porosity slightly too low for optimum diffusion of gaseous species through the thickness of the anode substrate. The electrolytes appeared **thin** (around 10 µm thickness) and **dense**.

The cathode deposition was the object of the third part. The three cathode materials involved in this study have been successfully deposited by screen printing and sintered using the temperatures and dwelling optimised in the INNOSOFC project. The **best cathode / electrolyte** interface in terms of adherence has been obtained with $\mathbf{Nd_{1.97}NiO_{4+\delta}}$. The adhesion of $Pr_{1.97}NiO_{4+\delta}$ on BIT07 appeared poor, with in addition cracks in the cathode layer explained by the small particle size of the cathode powder.

Finally, the work described led to the successful determination of a shaping protocol for a first generation of cells.

However, some issues and possible improvement ways have been pointed out:

i) On the cathode side, significant improvement of the cathode / electrolyte interfaces has been obtained by adding a **functional layer of GDC**, although work remains to be done mainly to increase the density of this GDC layer. An optimisation of the sintering program of the cathodes on GDC remains also to be done.

ii) Concerning the half-cells, further tests have been performed for the microstructural optimisation of the anode substrates:

- First, the slurry formulation has been successfully transferred to BIT07 powders supplied by Marion Technologies. Although good quality green tapes have been obtained, problems of cracking during pre-sintering still subsist.

- Second, thin **anode functional layers** BIT07 (MT2) / NiO (J.T. Baker®) and BLITiMn (EMPA) / NiO (J.T. Baker®) were also introduced, with an obtained BIT07 / NiO layer presenting a high density and for BLITiMn a poor interface with the electrolyte layer.

- Then, the introduction of **jellified starch as a pore forming agent** has been assessed in order to optimise the anode substrate microstructure; a slurry formulation has been developed and successful tape casting of green tapes has been done. The limiting step however remained the pre-sintering, making so far difficult the elaboration of complete cells.

Finally, **larger size green tapes (11.4 × 11.4 cm^2)** have been casted and crack-free substrates could be obtained, for a final product size of 10 × 10 cm^2. These substrates were however breaking during the vacuum slip casting process. An optimisation of the pre-sintering step and an increase in the thickness of the substrates could be proposed as possible solutions to improve their mechanical strength.

Chapter IV

Electrochemical characterisation of cells

This chapter presents several electrochemical results on performance and reliability of BIT07 / nickelates couple-based cells made using our procedure.

As described in *Chapter I*, a working cell exhibits kinetic losses (overpotentials, polarisations or voltage losses), increasing with the current density. A direct measure of the voltage vs. current, so called I-V curve (or I-P characteristics for power density vs. current), allows the identification of the overall losses of a cell and the direct determination of its performance. The testing of the cells has been performed using the setup described in *Chapter II*, under air at the cathode side and dry hydrogen at the anode side, with a testing protocol as follows:

- injection of the air on the cathode side (4 L / hour),
- injection of the nitrogen on the anode side (4 L / hour),
- heating up until 700°C with a rate of 60°C / hour,
- reduction of the anode by replacing N_2 with H_2 step by step (12% of the total flow per 5 minutes, target 4 L / hour). The gas-switching speed depends on the response of the cell voltage.
- optimisation of electrical contacts under current,
- stabilisation of the Open Circuit Voltage (OCV) at 700°C (typically 24 hours),
- I-V curve (V_{limit} = 0.6 V, scanning speed 5 mA s^{-1}) and impedance measurements.

The first section of this chapter relates the main results about the first generation of cells associating BIT07 electrolyte with the LnN cathode materials. The performance will be compared in a second part with those of the second generation of cells involving the addition of a GDC barrier layer in between the cathode and the electrolyte. Finally, preliminary results on optimisations at the half-cell level will be presented.

1. Influence of the cathode material

1.1. I -V and power density characteristics

1.1.1 *Experimental results*

This series of tests concerns the first generation of planar anode-supported BIT07 / NiO | BIT07 | LnN (with Ln = La, Nd and Pr) cells, prepared using the protocol described in the previous chapter.

The I-V characteristics of BIT07-based cells using three different types of cathodes are shown in *Fig. IV-1*. The values of OCV, total Area Specific Resistance ($ASR_{(I-V)}$), power density at 0.7 V and maximal power density at 700°C for each cell are presented in *Table IV-1*. The given ASR values are determined by taking the slope of the I-V curve around the operating point 0.7 V and correspond to the total resistance of the cells, including both ohmic and polarisation losses (activation and concentration), given per surface unit (in our case the active surface of the cells is 2 cm^2). The given maximal power densities P_{max} are extrapolated values assuming the linearity of the I-V curves.

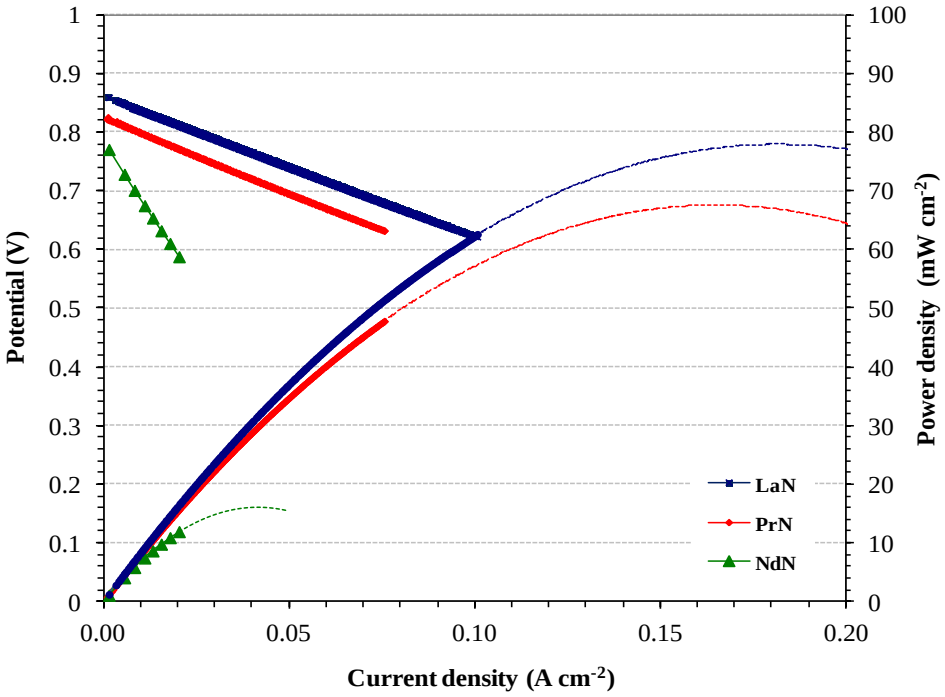

Figure IV-1: I-V curves and power densities under dry hydrogen at 700°C for the cells BIT07 / Ni | BIT07 | LnN with Ln = La, Nd and Pr.

Table IV-1:
OCV, total ASR and power densities ($P_{(0.7V)}$ and P_{max}) for the cells BIT07 / Ni | BIT07 | LnN (Ln = La, Nd, Pr).

cathode	OCV (V)	$ASR_{(I-V)}$ (Ω cm^2)	$P_{(0.7V)}$ (mW cm^{-2})	P_{max} (mW cm^{-2})
LaN	0.86	2.28	47	78
NdN	0.78	9.88	6	16
PrN	0.83	2.41	34	67

The cell with **NdN** cathode exhibited by far the **lowest performance** of this series of measurements, with a high total ASR value of 9.7 Ω cm² at 700°C. In comparison, power densities above 500 mW cm^{-2} have been reported at 700°C and 0.7 V by Lalanne et al. with $Nd_{1.95}NiO_{4+\delta}$ cathode on YSZ electrolyte (commercial HT-Ceramix half-cells) [255]; another study from Letilly et al. showed ASR values for $Nd_2NiO_{4+\delta}$ on BIT07 around 3 Ω cm² at 700°C (symmetrical cell) [254]. Also, as the half-cells are considered as identical for the three cells tested here, such low performance has been attributed to the cathode side and in particular to the quality of the cathode powder, with for example a batch presenting a low value of conductivity. Electrical measurements are thus needed on this powder to validate this hypothesis.

The highest performance, corresponding to a maximal power density of **78 mW cm^{-2}** and a total ASR of **2.4 Ω cm²**, has been obtained with the cell **BIT07 / Ni | BIT07 | LaN**, although PrN is usually shown as being the most performing cathode among this family of nickelates [259]. The first reason of this various performance is the higher OCV value of the cell using LaN as cathode, as the total ASR for the two cells are quite similar. These results are however in accordance with the microstructures of the complete cells presented in *Chapter III*, the cathode / electrolyte interface being better for the couple BIT07 / LaN than for BIT07 / PrN (*Fig. III-23*).

1.1.2 *Discussion about the OCV values*

For the three tested cells, **OCV values are low (< 0.85 V at 700°C)** compared to the expected theoretical value (above 1.2 V) under equivalent conditions (i.e. using dry hydrogen inlet), considering experimental results obtained at stack level using standard materials.

NB: the theoretical value of the OCV could not be here calculated due to the lack of information regarding the water content (and thus p_{H_2O}) in the hydrogen inlet of our test rig, since the measurements have been performed without humidification of the gas.

The first explanation of such low OCVs could be the presence of leakages caused by macroscopic defects in the electrolyte layer. For instance, defects as (a few) microscopic cracks have been observed after the electrolyte sintering step, as the one shown in *Fig. IV-2*. The presence of such defects induces gas leakages in the cells and may lead to a decrease of the OCV values.

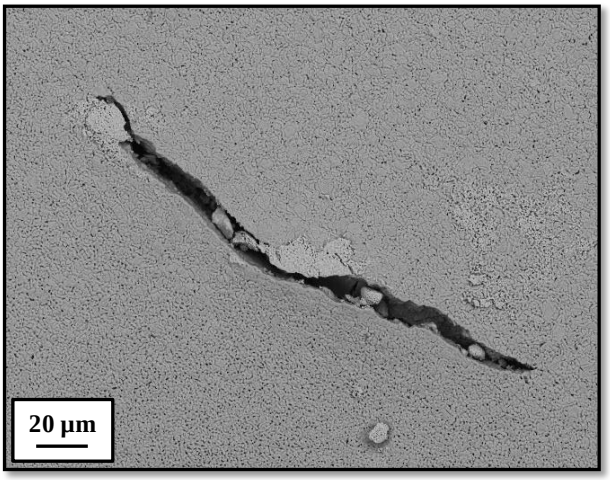

Figure IV-2: BSE SEM micrograph (top view) of a crack observed in a half-cell BIT07 / NiO | BIT07.

Also, it is typical for doped perovskites to be pure oxygen-ion (or n-type) conductors at low oxygen partial pressures but to become mixed conductors at high oxygen partial pressures, acquiring p-type electronic conductivity [309]. For instance, acceptor-doped $BaTiO_{3-\delta}$ with trivalent cations as Al^{3+}, Ho^{3+}, Dy^{3+}, Y^{3+}, Er^{3+} has been shown in the literature as being p-type conductor with a transition p-to-n at lower oxygen partial pressures [310-312].

Thus, an electronic contribution to the conductivity of an electrolyte can result in a deleterious leakage of current during operation, which can significantly degrade the efficiency and performance of a cell [313-316].

All OCV values of previous BIT07-based tested cells are reported in *Table IV-2*. These values come from IMN data and were obtained with small-sized cells (∅10 mm). Although the size of the tested cells can explain the difference between the obtained OCV values and the theoretical Nernst potential as the small-sized cells need a very careful sealing in order to minimise gas leakage, a small electronic contribution to the conductivity of BIT07 can however be here envisaged.

Table IV-2:
OCV values reported at different temperatures and atmospheres for cells based on BIT07. Air was always used in the cathode side. Theoretical OCV values are calculated assuming a water content of 3%.

cathode	temperature	atmosphere	electrolyte thickness (µm)	Theoretical OCV	OCV (V)	Ratio OCV / theoretical value	Reference
LSM	810°C	dry H_2	550	/	1.046	/	[252, 317]
	810°C	wet H_2		1.110	0.976	88%	[317]
	810°C	wet Ar / 5% H_2		0.960	~ 0.9	94%	[317]
	690°C	dry H_2	100	/	0.92	/	[252, 317]
LSCF	700°C	wet H_2	23	1.119	0.97	87%	[249]
	700°C	wet H_2	11		1	89%	[249]
	650°C	wet H_2	15	1.128	0.72	64%	[318]
	700°C	wet H_2	15	1.119	0.75	67%	[318]
	600°C	wet H_2	16	1.137	0.89	78%	[303]
	650°C	wet H_2		1.128	0.88	78%	[303]
	700°C	wet H_2		1.119	0.92	82%	[303]
	750°C	wet H_2		1.110	0.97	87%	[303]
BIT07 / LSCF	600°C	wet H_2	18	1.137	1.06	93%	[303]
	650°C	wet H_2		1.128	1.06	94%	[303]
	700°C	wet H_2		1.119	1.05	94%	[303]
	750°C	wet H_2		1.110	1.05	95%	[303]
$Nd_2NiO_{4+\delta}$	600°C	wet H_2	20	1.137	0.843	74%	[318]
	650°C	wet H_2		1.128	0.809	72%	[318]
	700°C	wet H_2		1.119	0.807	72%	[318]
	750°C	wet H_2		1.110	0.807	73%	[318]
$Pr_2NiO_{4+\delta}$	600°C	wet H_2	/	1.137	0.875	77%	[318]
	650°C	wet H_2	/	1.128	0.843	75%	[318]
	700°C	wet H_2	/	1.119	0.914	82%	[318]
	750°C	wet H_2	/	1.110	0.9	81%	[318]
GDC | $Pr_2NiO_{4+\delta}$	600°C	wet H_2	3 | 10	1.137	1.11	98%	[318]
	650°C	wet H_2		1.128	1.11	98%	[318]
	700°C	wet H_2		1.119	1.07	96%	[318]
	750°C	wet H_2		1.110	1.07	96%	[318]

Conductivity measurements have been thus performed by EIS at ICMCB on dense BIT07 pellets (density > 95% of the theoretical density, diameter ∅6 mm and thickness around 2 mm) using platinum electrodes on both sides. For obtaining dense pellets, a decrease of the initial particle size has been necessary, done by planetary-milling the powder during 60 hours at 540 rpm using agate balls and ethanol as a solvent. This grinding step induced an exsolution of the barium with the formation of $BaCO_3$ (*Fig. IV-3*), as observed in smaller

magnitude for the powder after 100 hours of ball-milling used for the elaboration of our electrolytes (*Fig. III-18*). The barium carbonate however disappeared after sintering at 1400°C for 10 hours, and the formation of In_2O_3 was observed. Diffraction peaks of BIT07 appeared shifted to higher angles, which indicates a diminution of the lattice parameter. The same behaviour was observed for the BIT07 powder from the MT1 batch after planetary mill. The shift to higher angles is also observed for the BIT07 electrolyte layer of our cells.

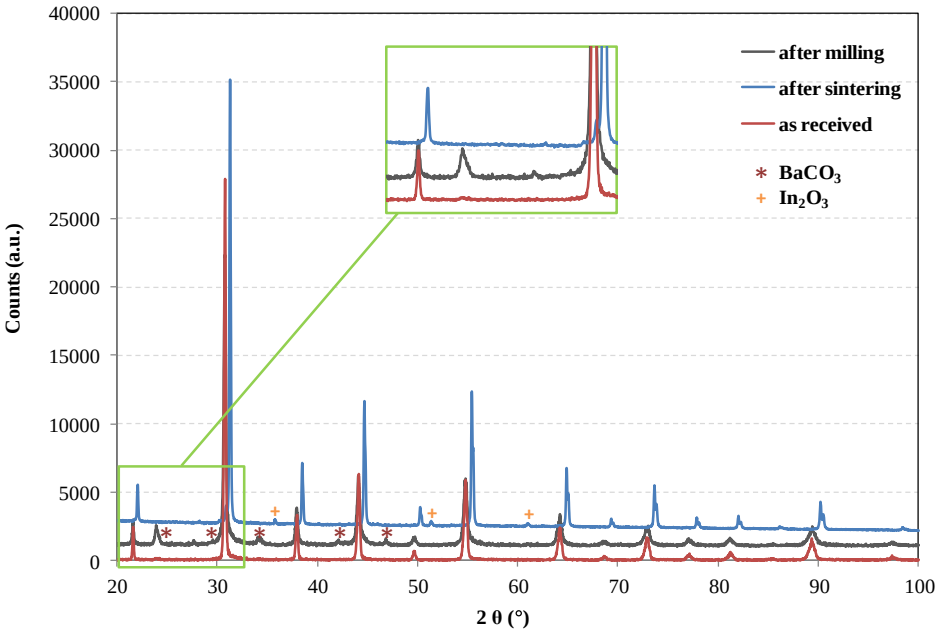

Figure IV-3: X-Rays Powder Diffraction pattern for the BIT07 powder supplied by EMPA after planetary milling and subsequent sintering at 1400°C for 10 hours.

Impedance spectra have been recorded at various temperatures between 500°C and 800°C in air and H_2 atmospheres. Conductivities have been calculated from the value of the series resistance R_s, corresponding to the intersection of the impedance spectra with the real axis at high frequencies, using the following formula:

$$\sigma = \frac{1}{R_s}\frac{L}{S} \qquad \textbf{(13)}$$

where L is the thickness of the electrolyte and S its surface. The Arrhenius plot of the corresponding conductivity values in air and dry H_2 is shown in *Fig. IV-4*.

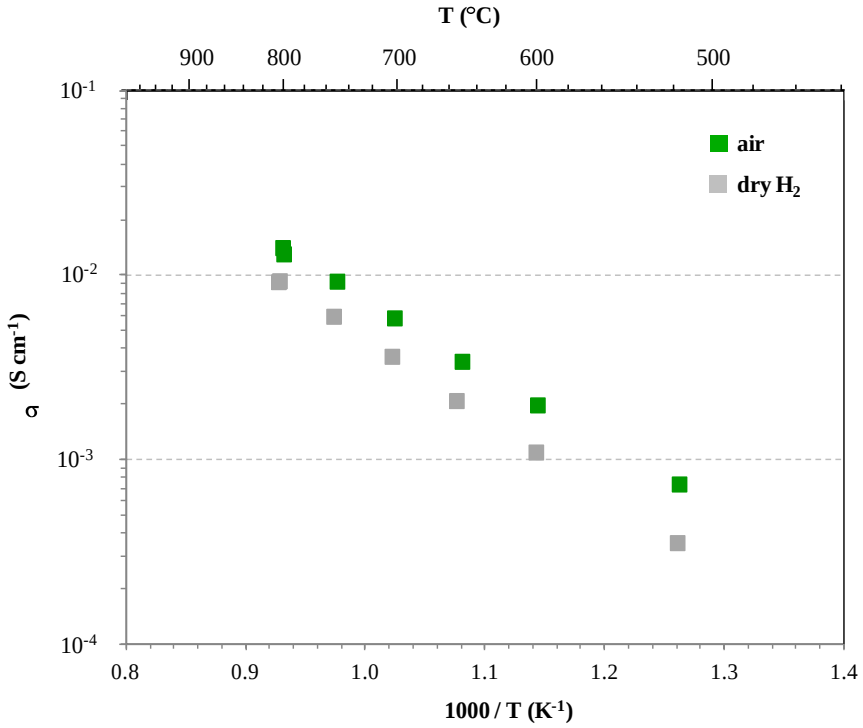

Figure IV-4: Arrhenius plot of the conductivity of BIT07 in air and dry H_2 atmospheres.

The measured conductivity of BIT07 in air reaches 5.9×10^{-3} S cm^{-1} at 700°C, value slightly below the targeted 10^{-2} S cm^{-1} obtained on powders produced by solid state reaction at lab scale (IMN process [120]). In addition, a decrease of this value down to 3.6×10^{-3} S cm^{-1} in hydrogen atmosphere is observed.

For the MT1 powder, impedance spectra have been recorded at 700°C under air, Ar, Ar / H_2 (95% / 5%), wet and dry H_2 atmospheres, respectively; corresponding conductivities are shown in *Table IV-3.*

Table IV-3:
Conductivities of different BIT07 powders at 700°C under different atmospheres, measured at ICMCB and at IMN. The mention (shift) refers to powders where a shift of the XRD pattern to the high angles was observed.

Batch		EMPA (shift)	EMPA	MT1 (shift)	MT_{IMN}
Setup		**ICMCB**	**IMN**	**ICMCB**	**IMN**
Atmosphere	Air	5.9×10^{-3}	6.8×10^{-3}	5.82×10^{-3}	8.4×10^{-3}
	Ar	/	/	3.07×10^{-3}	/
	Ar / 5% H_2 wet	/	5.4×10^{-3}	/	6.3×10^{-3}
	Ar / 5% H_2 dry	/	/	2.57×10^{-3}	/
	H_2 wet	3.55×10^{-3}	/	2.91×10^{-3}	/
	H_2 dry	3.63×10^{-3}	/	2.95×10^{-3}	/

As a general trend, the conductivity values decreased with decreasing the p_{O_2}. These measurements have been compared to the results obtained at IMN (measurements performed in air and wet Ar / H_2 95% / 5% on ∅8 mm and 1.5 mm thick pellets, using gold paste electrodes, theoretical densities > 95%) on non-grinded EMPA powder and another batch of BIT07 supplied by Marion Technologies to the IMN, labelled MT_{IMN}. Note that the EMPA pellet prepared at the IMN did not need any grinding of the powder to obtain adequate densification due to the use of a binder (Rhodoviol®); the MT_{IMN} powder was planetary milled for 15 hours in absolute ethanol, with no formation of barium carbonate detected after the grinding step due to the use of anhydrous solvent. Values at 700°C are also shown in *Table IV-3*.

A slightly higher conductivity value has been found for the EMPA and MT_{IMN} powders, prepared and measured at the IMN, which can be correlated to the negative influence of the grinding step on the properties of BIT07. The diminution of the conductivity observed in all the cases in reducing atmosphere suggests a **small p-type conductivity of BIT07 in oxidising atmosphere**, although the phenomenon is less pronounced for the non-grinded powders. Note that this can also be attributed to the milling treatments of the powders, leading to a **partial decomposition of the BIT07** phase and the formation of insulating layers at grain boundaries [319].

For a p-type conductor, oxygen-ion vacancies react with oxygen at high temperatures to produce electron holes (positive electronic defects), as shown in Eq. 14 using the Kröger-Vink notation [309].

$$½O_2 + \ddot{V_o} = O_o^x + 2\dot{h} \qquad \textbf{(14)}$$

An equivalent circuit for a cell involving a MIEC electrolyte under open circuit conditions is represented in *Fig. IV-5*, assuming similar behaviours between n-type and p-type materials [320]. Here E_{th} represents the electromotive force or theoretical Nernst potential, σ_{ion}, σ_{el}, R_{ion} and R_{el} the partial oxygen ion and electronic conductivities and resistances of the electrolyte, respectively; R_p is the polarisation resistance of the electrodes and E_{obs} the measured OCV.

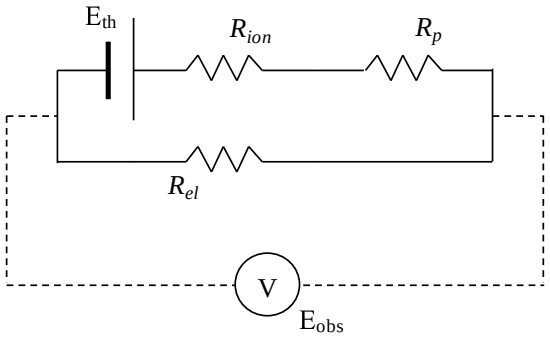

Figure IV-5: Equivalent dc circuit describing a mixed conductor placed under an oxygen chemical potential gradient under open-circuit conditions [320].

One can define the oxygen-ion transference number t_{ion} as:

$$t_{ion} = \frac{\sigma_{ion}}{\sigma_{ion} + \sigma_{el}} = \frac{R_{el}}{R_{el} + R_{ion}} \quad \textbf{(15)}$$

and the OCV or E_{obs} as:

$$\frac{E_{obs}}{E_{th}} = t_{ion} \left(1 + \frac{R_p}{R_{ion} + R_{el}}\right)^{-1} \quad \textbf{(16)}$$

As can be seen in Eq. 16, the OCV across a MIEC is strongly influenced by the electronic contribution to the total conductivity of the electrolyte, but is also related to the overpotentials R_p developed at the interfaces of the cell [321-324].

This situation correlates well with the p_{O_2} dependency measured for BIT07 in our study; the electronic contribution and its influence on the obtained OCVs might be therefore significant, and thus non-negligible in our case, especially considering the low thicknesses of our electrolyte layers (8 µm) [313, 325] and as can be seen from Eq. 16.

These results are however not in agreement with those obtained by Delahaye et al. [126] or Letilly et al. [303], observing no variation in the conductivity of BIT07 against p_{O_2} down to 5×10^{-5} atm between 250 and 750°C. Also, OCV values close to the theoretical ones have been reported in the literature for cells involving BIT07 electrolyte, indicating a **difference of behaviour between powder batches** (here lab-scale produced powders vs. pre-industrial batches in our case) and / or a strong **influence of the powder processing** steps.

1.2. EIS measurements

For a better comparison, the BIT07-based cells using LaN and PrN cathodes, respectively, have been characterised by EIS at 700°C around the operating point 0.7 V. Typical Nyquist plots for these cells are reported in *Fig. IV-6*. From these measurements, the ohmic (R_s) and the polarisation (R_p) contributions to the total resistance of the cells have been quantified. The values of R_s, R_p and R_{tot} are shown in *Table IV-4* and compared to the total ASR calculated from the IV curves ($ASR_{(I-V)}$).

Table IV-4:
R_s, R_p and R_{tot} values for each cathode, obtained from the impedance spectra at 700°C and 0.7 V compared with the total ASR calculated from the I-V curves.

Cathode	R_s (Ω cm^2)	R_p (Ω cm^2)	R_{tot} (Ω cm^2)	$ASR_{(I-V)}$ (Ω cm^2)
LaN	1.3	1.11	2.41	2.39
PrN	1.45	1.16	2.61	2.56

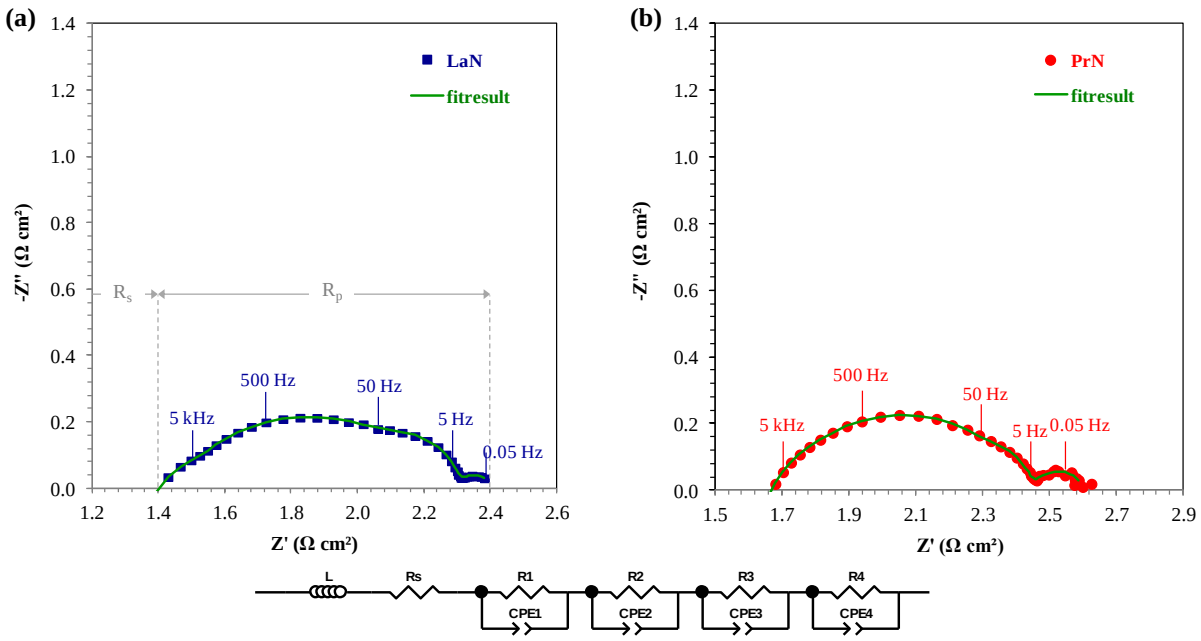

Figure IV-6: Impedance spectra measured at 700°C and 0.7 V under air and dry H_2 and fit result with the corresponding equivalent circuits for the cells involving a) LaN and b) PrN cathodes.

In both cases, a good agreement between $ASR_{(I-V)}$ and R_{tot} has been found. Also, it can be observed that the **main contribution to the total ASR of the cells comes from the series resistance R_s**.

If we assume the series resistances as stemming only from the ohmic contribution of the electrolyte, R_s values around 0.17 Ω cm^2 and 0.27 Ω cm^2 should be obtained if one consider the conductivity values of BIT07 measured under air and dry H_2 atmospheres, respectively. The R_s values are thus here almost one order of magnitude higher than expected. The first explanation for such large difference could arise from the internal resistance of the test setup itself, with a series resistance determined *ab initio* to be around 0.35 Ω cm^2 at room temperature (measurement made with the two Pt current collection grids directly in contact). Also, contamination of the Pt grid on the anode side has been evidenced by EDX analysis, with a non-negligible proportion of Ba, In and Ti found (*Fig. IV-7*). which could significantly decrease the effectiveness of the current collecting.

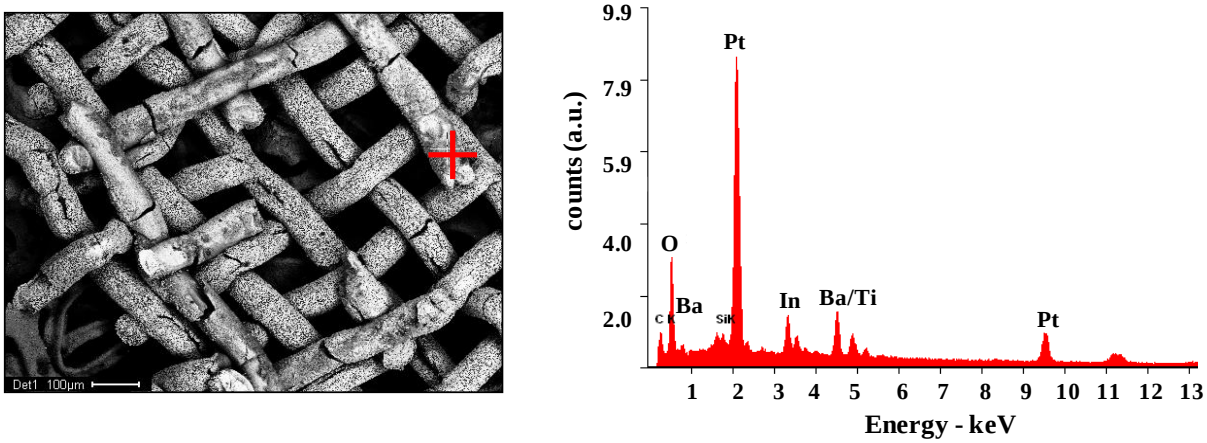

Figure IV-7: EDX point analysis on the current collecting Pt mesh.

A second explanation could be related to a bad current collection, which can be first linked to an eventual non-perfect flatness of the cells. Also, an issue could be related to the relatively high electronic resistivity of the nickelates, which might not serve well as current collectors. For instance, Laberty et al. showed a diminution by a factor 6 of the series resistance at 800°C by replacing $La_2NiO_{4+\delta}$ by LSC as a current collection layer, on standard YSZ / Ni | YSZ half-cells and composites $La_2NiO_{4+\delta}$ / SDC cathodes [326]. This effect has however to be confirmed, as series resistance and subsequently total conductivity of BIT07 in agreement with the expected properties of this material have been measured by Brüll et al. on symmetrical cells involving PrN cathode, without the addition of current collection layers [327].

Finally, the quality of the cathode / electrolyte interface can also play a role in the R_s values, which could be in agreement with the relatively lower R_s value of the cell involving LaN considering its better interface with BIT07 compared to PrN (*Fig. III-23a*). If the bonding between the cathode and the electrolyte is not effective, the active cell area is decreased since no current is flowing through the delaminated areas. Besides a sharp increase of the activation loss of the cathode, the passing current from the anode to the cathode does not thus extend into the whole electrolyte area considering its low thickness, therefore increasing ohmic losses [328]. Even if reactivity tests did not show any chemical reaction between the nickelates and BIT07 at the sintering temperature of the cathodes, the presence of highly resistant interfacial phases cannot be excluded.

A slightly **lower polarisation resistance was found in the case of PrN compared to LaN**, as can be observed in *Fig. IV-8* (here the series resistance contributions have been removed from the impedance spectra for a better visibility).

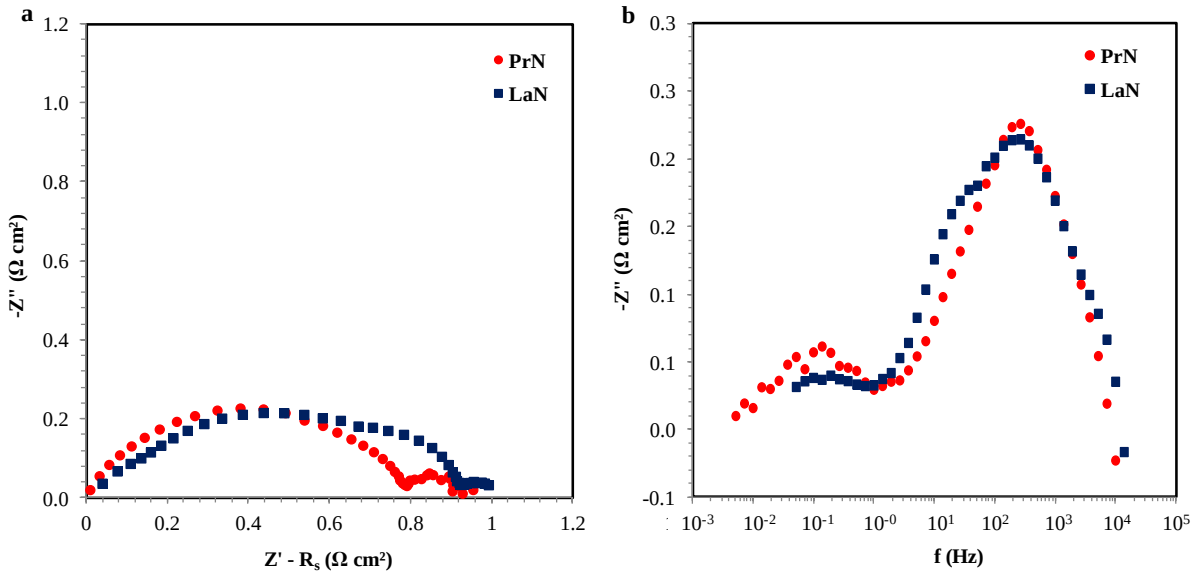

Figure IV-8: For the cells with LaN and PrN cathodes a) impedance spectra measured at 700°C and 0.7 V in air and dry H_2 atmospheres with the R_s contribution removed and b) corresponding Bode plots.

Besides, on the impedance spectra of the cell with LaN, four contributions to the polarisation resistance can be distinguished. From the Bode plot of the imaginary part (-*Z*") as a function of the frequency, shown in *Fig. IV-8b*, the four approximate relaxation frequencies associated to each arc could be identified as being around 8300, 220, 13 and 0.2 Hz, respectively. The presence of an arc in the middle frequency range (around 10 Hz) has also

been assumed in the case of PrN, even if less visible, considering the similitude in the two cell architectures and the similar positioning in frequency of the peaks observed in the Bode plots.

Each arc of the impedance spectra can be modelled by an equivalent circuit constituted by resistance - constant phase elements in parallel (R//CPE). Each resistance or CPE can be assigned to the resistance and capacitance associated with a specific rate-limiting electrochemical process.

The data were fitted using the following equivalent circuits: L + R_s + (R_1//CPE_1) + (R_2//CPE_2) + (R_3//CPE_3) + (R_4//CPE_4) (used equivalent circuits and fit results are shown in *Fig. IV-6*). The notation 1 to 4 is assigned to the respective processes by increasing time constant. For each arc, the values of the fitted resistance R, the admittance Y_0 and the frequency power n can be used to calculate the relaxation or summit frequency f_{summit} with Eq. 17 and the capacitance given at any frequency according to Eq. 18 [329].

$$f_{summit} = \frac{1}{2\pi} \left(RY_0 \right)^{-1} {}^{n} \quad \textbf{(17)}$$

$$C\ f\ = Y_0 (2\pi f)^{n-1} \sin \frac{n\pi}{2} \quad \textbf{(18)}$$

The equivalent capacity or C_{eq} corresponds to the capacity at the relaxation frequency or f_{summit}. *Table IV-5* presents the results of the fits obtained from the impedance spectra of the two cells, with in both cases the value of R_s, R_p, f_{summit} and C_{eq} obtained for each arc.

The inductance, not reported in the *Table IV-5*, was found to be around 2×10^{-6} H cm^{-2} for each fit, corresponding to the "blank" value of the test setup.

Considering now the deconvolution of the polarisation resistance of both electrodes, low value capacitances in the range 10^{-6} - 10^{-4} F cm^{-2} are typical of a double layer capacitance whereas larger capacitances (in the range 10^{-3} - 10^{-1} F cm^{-2}) are usually linked to surface processes (oxygen adsorption, charge transfer, diffusion etc.) [330-331]. The arc at the highest frequencies, corresponding to process 1, is thus attributed to the ionic transfer at the electrode / electrolyte interface for both cells, following the results obtained in other studies concerning nickelate cathodes [332-334].

Table IV-5:
f_{summit}, C_{eq} and R obtained for each contribution obtained by fitting the impedance spectra recorded at 700°C and 0.7 V, for the two cells BIT07 / Ni | BIT07 | LaN and BIT07 / Ni | BIT07 | PrN.

	LaN			PrN		
	f_{summit} (Hz)	C_{eq} (F cm^{-2})	R (Ω cm^2)	f_{summit} (Hz)	C_{eq} (F cm^{-2})	R (Ω cm^2)
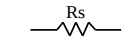	/	/	1.3	/	/	1.45
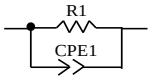	11152	9×10^{-5}	0.15	8714	3×10^{-5}	0.39
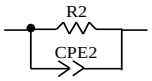	260	7×10^{-4}	0.76	228	1×10^{-3}	0.56
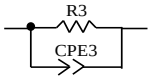	16	8×10^{-2}	0.12	21	1×10^{-1}	0.06
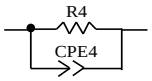	0.12	17	0.08	0.10	10	0.15

While for the cell with LaN the second process seems still to be related to the transfer of ions at the electrodes / electrolyte interface, in the case of PrN the capacity value would indicate more a contribution from electrode surface processes. In the literature, comparable capacitances values have been assigned either to a charge transfer reaction at the gas / electrode interface, as suggested by Mauvy et al. [332] or more generally to charge transfer processes [335], i.e. the dissociative adsorption of molecules at the electrode surface [332, 334-336], the transport of oxygen species at the TPB [335] or gas diffusion [334-335].

No strict conclusion can nonetheless be made regarding the processes 2 and 3 without any complementary experiments. Study of the two electrodes separately on symmetrical cells or variations of parameters such as temperature, water vapour pressure in the anode side or p_{O_2} in the cathode side would help to deconvolute the spectra [335, 337], but have not been performed in the frame of this work.

The capacitance observed for the lowest frequency process (process 4) is larger than 1. A capacitance of this magnitude is not ascribable to interfacial capacitance or adsorption on surfaces but rather to an electrode bulk process [329, 338]. So far, only two bulk processes have been reported to give such high capacitances values [336]. The first one is called a "chemical capacitance" and is related to the change of the chemical composition of the electrode material when the electrode potential is varied, as for instance a modification in the oxygen non-stoichiometry [339]. The second process that could originate high capacity values is the gas conversion, observed when experiments are performed in a test setup where the

working and reference electrodes are located in different atmospheres [338]. This comes from a change of the gas composition in the vicinity of the electrode when the current is changed, leading to a variation of the Nernst potential. As our measurements have been performed under polarisation, the current modulation around the operating point 0.7 V, leading to a modulation of the gas composition, could originate this arc.

1.3. Post-test analyses

After the electrochemical test, both LaN and NdN cathode layers kept their adherence to the half-cell while PrN was partly delaminated, some parts of the cathode remaining attached to the current collection grid.

Observations on the polished cross-sections by SEM (*Fig. IV-9)* revealed a generally **good quality of the half-cells**, with thin and dense electrolyte layers of thicknesses around 8 µm, further assessing the reproducibility of the half-cell elaboration process.

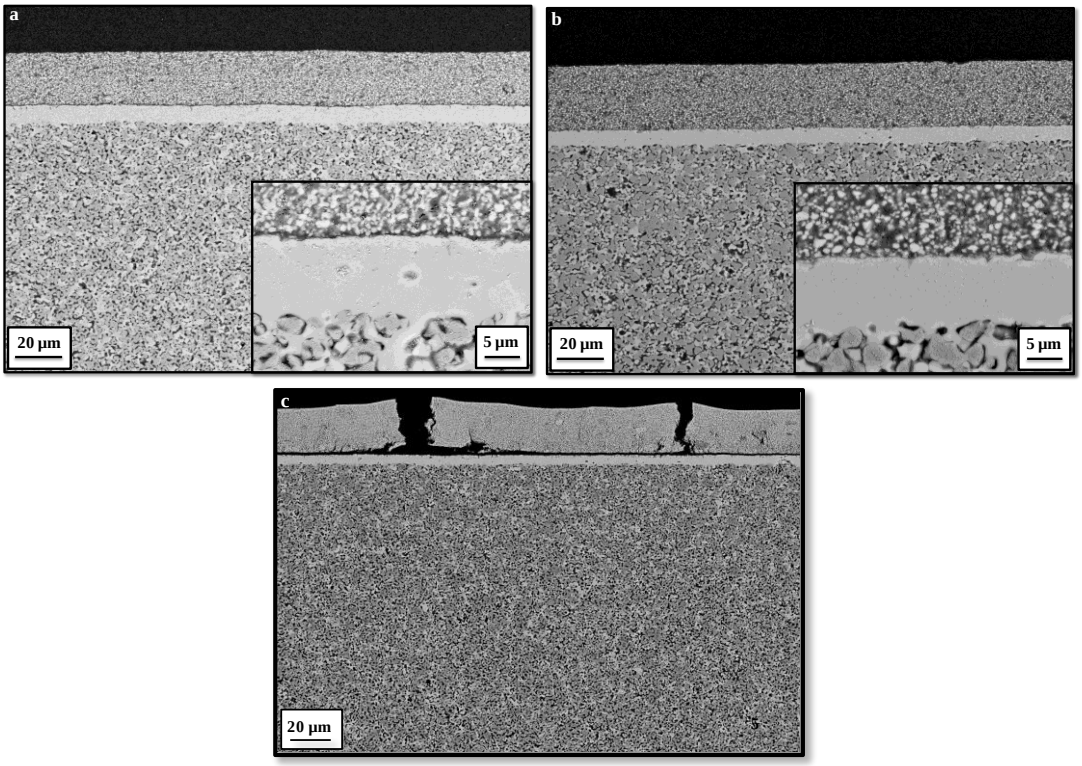

Figure IV-9: BSE SEM micrographs of polished cross-sections for the cells a) BIT07 / Ni | BIT07 | LaN, b) BIT07 / Ni | BIT07 | NdN and c) BIT07 / Ni | BIT07 | PrN after test.

Both **LaN and NdN cathodes showed satisfying microstructures**, with sufficient porosities and thicknesses (25 - 30 µm). The very low performance obtained with NdN appears thus not linked to the quality of the cell microstructure, further going in the direction

of a problem with the batch of powder used. Note that in this case the interface BIT07 / LaN seems to have deteriorated during testing or cell demounting (*Fig. IV-9a)*.

Concerning **PrN**, the **cathode appeared cracked and delaminated after test**, as can be seen in *Fig. IV-9c*. A bad bonding with BIT07 electrolyte was already observed on as-prepared cells, linking this high deterioration of the layer to the stress and constraints applied by the current collection system. In terms of microstructure, the **best cathode / electrolyte couple is NdN / BIT07**. EDX analyses by mean of linescan, point analyses and element mapping have been performed for the three cathodes on cells before and after testing. In the three cases, **no diffusion of elements** could be observed. As an example, results of the mapping concerning the cathode lanthanide element are shown in *Fig. IV-10*.

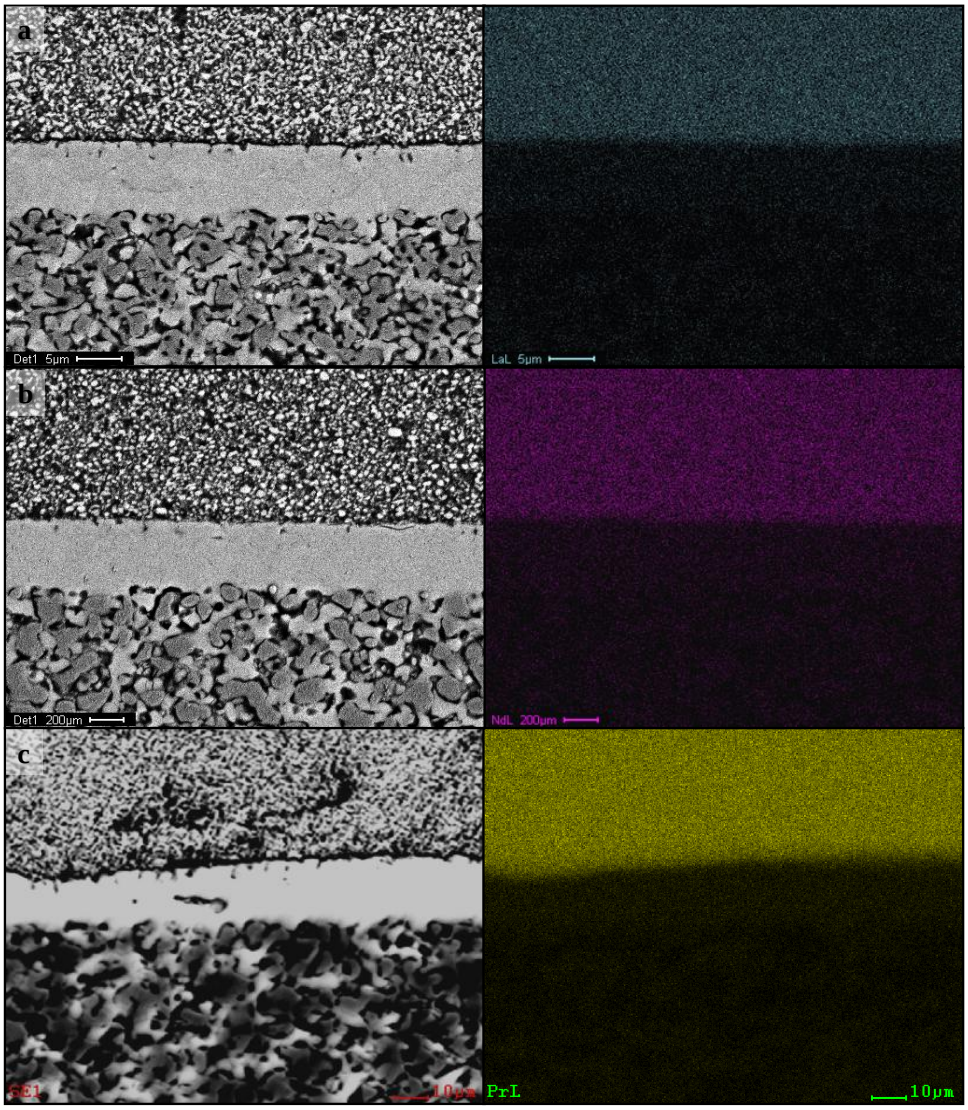

Figure IV-10: Results of the element mapping (here lanthanide element shown) for the cells after testing involving a) LaN, b) NdN and c) PrN cathodes.

1.4. Comparative studies of BIT07 / Nickelates with reference couples

The BIT07 / LSCF couple appeared in the literature as promising for IT-SOFC applications [249-250, 253-254]. In order to estimate the feasibility of the BIT07 / nickelates association in comparison to more standard cathode materials and to better compare our results with the available data, a complete cell BIT07 / NiO | BIT07 | LSCF has been prepared and tested. The cathode layer has been sintered at 1050°C for 6 hours following the optimised conditions of process proposed by Letilly et al. on LSCF │ BIT07 │ LSCF symmetrical cells [250]. The performance of the produced cell has been compared to the results obtained for the best cell of this series of tests, i.e. the cell using LaN as cathode. I-V and power density characteristics for these two cells are shown in *Fig. IV-11*. In addition, *Fig. IV-12* compares the impedance spectra of the two cells recorded at 700°C and 0.7 V, with the corresponding Bode plots.

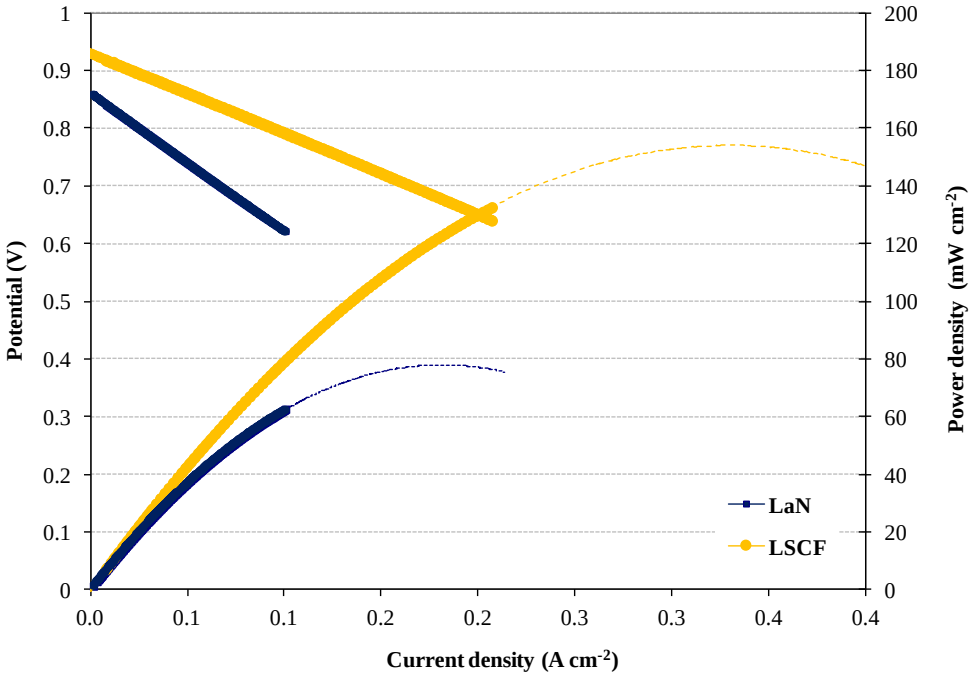

Figure IV-11: I-V curves and power densities under dry H_2 at 700°C for the cells BIT07 / Ni | BIT07 | LaN and BIT07 / Ni | BIT07 | LSCF.

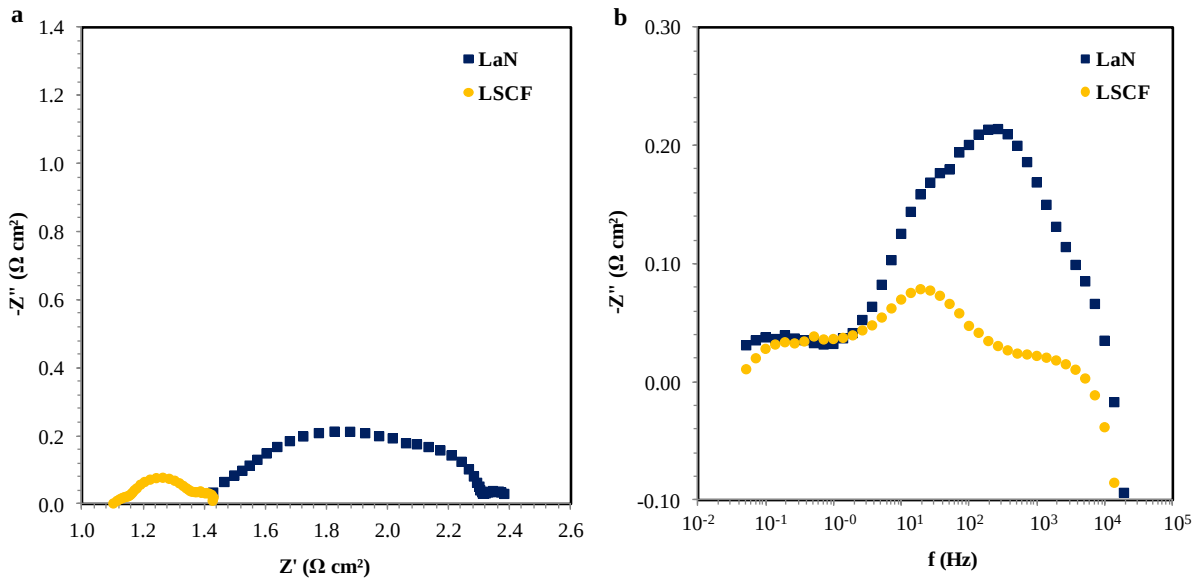

Figure IV-12: For the cells with LaN and LSCF cathodes a) impedance spectra measured at 700°C and 0.7 V under air and dry H_2 and b) corresponding Bode plots.

Electrochemical results obtained on cells with LaN or LSCF cathodes in terms of OCV, power densities, R_{tot}, R_s and R_p can be found in *Table IV-6*. These results are compared to a reference button cell BIT07 / Ni (50 : 50 Wt%) | BIT07 | LSCF (effective cell area 0.2 cm^2, electrolyte thickness 11 µm, cathode thickness around 10 µm) reported by Letilly et al. [249].

Table IV-6:
OCV, power density values, total ASR determined from the I-V curves and from EIS measurements ($ASR_{(I-V)}$ and R_{tot} respectively), R_s and R_p for the cells with LaN and LSCF cathodes compared with literature data.

Cellule	OCV (V)	$P_{(0.7V)}$ (mW cm^{-2})	P_{max} (mW cm^{-2})	$ASR_{(I-V)}$ (Ω cm^2)	R_{tot} (Ω cm^2)	R_s (Ω cm^2)	R_p (Ω cm^2)
LaN	0.86	47	78	2.39	2.41	1.3	1.11
LSCF	0.93	116	154	1.4	1.44	1.09	0.35
from ref. [249]	1	336	398	0.63	0.68	0.3	0.38

The cell using LSCF as a cathode exhibits higher performance than the cells involving the nickelates, with a **power density at 0.7 V of 116 mW cm^{-2}** (vs. 47 mW cm^{-2} for the cell with LaN) and a total ASR of 1.44 Ω cm^2 (1.09 Ω cm^2 from the series resistance and 0.35 Ω cm^2 from the polarisation resistance) vs. 2.4 Ω cm^2 (1.3 Ω cm^2 from the series resistance and 1.11 Ω cm^2 from the polarisation resistance).

It can be seen that the **polarisation resistance value for the cell using LSCF cathode is 2.2 times lower** than for the cell with LaN, and an improvement of R_s was observed,

probably due to the improved interface of LSCF with BIT07 due to the formation of a conductive perovskite-structured solid solution as a reactivity product between these two phases [132].

Beside, a relative **higher OCV** has been obtained with the cell using LSCF as a cathode than values obtained with BIT07 / LnN-based cells. This can be related to the better activity of LSCF in association with BIT07 (lower R_p), leading to higher OCVs as described earlier (Eq. 15).

The obtained performance appears however lower than those reported by Letilly et al. in [249] (336 mW cm^{-2} at 700°C and 0.7 V). This difference is nonetheless coming from the **contribution of the series resistance**, as similar R_p have been found.

Powders produced at lab-scale using the same technique as in [249] and supplied by the IMN have been used for the shaping of the electrolyte layer in our cells, giving comparable series resistance values. The high R_s in our case seems thus neither related to the properties of the raw BIT07 powder, nor to the cathode / electrolyte interface, considering the low polarisation resistances obtained. High R_s might be thus coming mainly from current collection issues, further enhanced by a too low thickness of the cathode layer (around 10 µm) (*Fig. IV-13)*. This is also confirmed by the similarities in the R_s values obtained for all our cells, regardless of the cathode used.

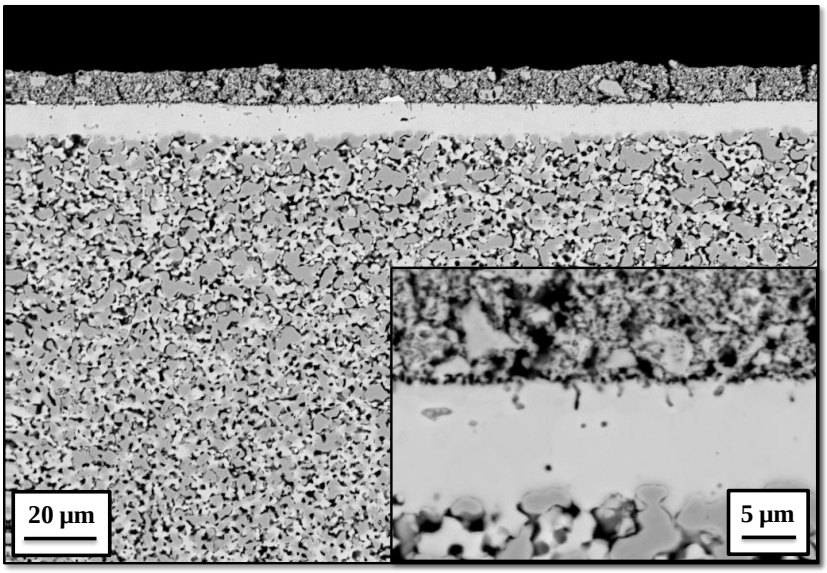

Figure IV-13: BSE SEM micrograph on polished cross-section for the cell BIT07 / Ni | BIT07 | LSCF after test.

A substantial decrease of the ohmic losses could be achieved by the addition of a current collection layer, for example made of nickel on the anode side and LSM or LSC on the cathode side. For example, in the study from Letilly et al., gold grids attached with gold paste have been used as current collection layers [249], while LSC has been used by Lalanne et al. [255] or Laberty et al. [326] on the cathode side for cells involving nickelate cathodes.

As a primary experimental feedback, **BIT07 / nickelates-based cells are not enough performing for IT-SOFC applications**, and LSCF seems to be a better cathode candidate to be directly associated with BIT07 electrolyte. Major improvements have thus to be done on the cathode side concerning the nickelates, especially regarding the quality of the interface with BIT07.

2. Influence of the GDC barrier layer

2.1. Case of PrN

As seen in *Chapter III*, the addition of a $Ce_{0.9}Gd_{0.1}O_{2-\delta}$ (GDC) barrier layer in between the electrolyte and the cathode layers substantially improved the quality of the interface BIT07 / nickelates.

The influence of this GDC layer on the electrochemical performance of the assemblies involving the three cathodes has been studied. The first part of this discussion will concern only the assemblies involving PrN.

The I-V characteristics for the cells with PrN and GDC | PrN at the cathode side are compared in *Fig. IV-14*. The values of OCV, total Area Specific Resistance ($ASR_{(I-V)}$), power density at 0.7 V and maximal power density for both cells are summarised in *Table IV-7*.

Table IV-7:
OCV, total ASR and power density values for the cells BIT07 / Ni | BIT07 | PrN and BIT07 / Ni | BIT07 | GDC | PrN.

cathode	OCV (V)	$ASR_{(I-V)}$ (Ω cm^2)	$P_{(0.7V)}$ (mW cm^{-2})	P_{max} (mW cm^{-2})
PrN	0.83	2.56	34	67
GDC | PrN	1.03	1.34	174	200

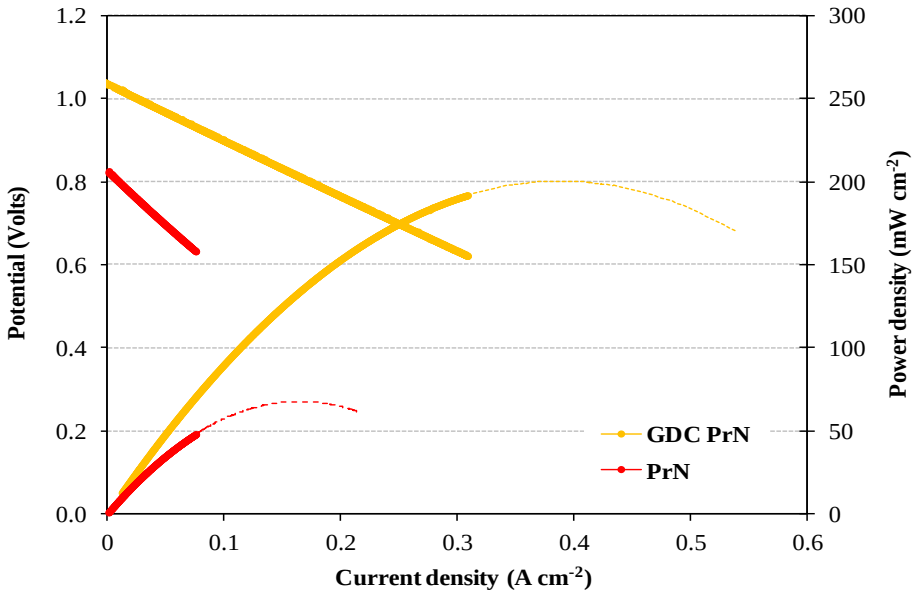

Figure IV-14: I-V curves and power densities under dry hydrogen at 700°C for the cells BIT07 / Ni | BIT07 | PrN and BIT07 / Ni | BIT07 | GDC | PrN.

The first observation concerns the **higher value of the OCVs** (here 1.03 V) compared to BIT07-based cells without the GDC interlayer. This effect is matching with the two hypotheses previously made to explain the low OCVs obtained for the first generation of cells.

Namely:

1) GDC could act as a pure ionic electrolyte layer by blocking the electron holes in the case of a small p-type contribution in the conductivity of BIT07 in oxidising atmospheres, as commonly observed for bi-layered electrolytes [340-341]. The electron-blocking effect in the bilayer electrolytes is however not clear, as the electronic conductivity is determined by the spatial distribution of oxygen activity across the bilayer electrolyte. For instance, Kwon et al. suggested the reduced electronic conductivity of a YSZ / GDC bilayer as either coming from a larger supporting of the oxygen potential gradient by the YSZ layer or an enhanced blocking of electrons at the YSZ / GDC interface, leading to an appreciable drop in the oxygen activity and thus an extended electrolytic domain [340]. The figure case of an association between p-type and n-type (in reducing atmospheres) conductor has to our best knowledge not been described in the literature.

2) at the same time, the GDC layer could fill the eventual pin holes as it is deposited after the electrolyte sintering step (see *Chapter III*).

This OCV value remains however relatively below the theoretical one, in opposition to the results reported by IMN with an equivalent button cell [318], which can be related to a non-complete filling of the pin holes or a maintained electronic path if areas of the cathode remain in direct contact with BIT07 via the porosities of the GDC layer. The electron-blocking effect of GDC on a p-type conducting electrolyte is also still to be elucidated.

The higher OCV value combined with a division of the ASR by a factor 2 lead to a **power density at 700°C and 0.7 V of 174 mW cm^{-2} and a maximal power density of 200 mW cm^{-2}**. This cell has been characterised by EIS; the comparison of the Nyquist plots for the cells with and without the GDC layer is shown in *Fig. IV-15a*. The R_s contribution has been here removed for a better visibility. Values of R_s, R_p and total ASR R_{tot} are reported in *Table IV-8*. A good agreement between R_{tot} and $ASR_{(I-V)}$ has been found.

Table IV-8:
R_s, R_p and R_{tot} values for each cathode, obtained from the impedance spectra at 700°C and 0.7 V and compared with the total ASR calculated from the I-V curves.

Cathode	R_s (Ω cm^2)	R_p (Ω cm^2)	R_{tot} (Ω cm^2)	$ASR_{(I-V)}$ (Ω cm^2)
PrN	1.45	1.16	2.61	2.56
GDC | PrN	1.1	0.29	1.39	1.34

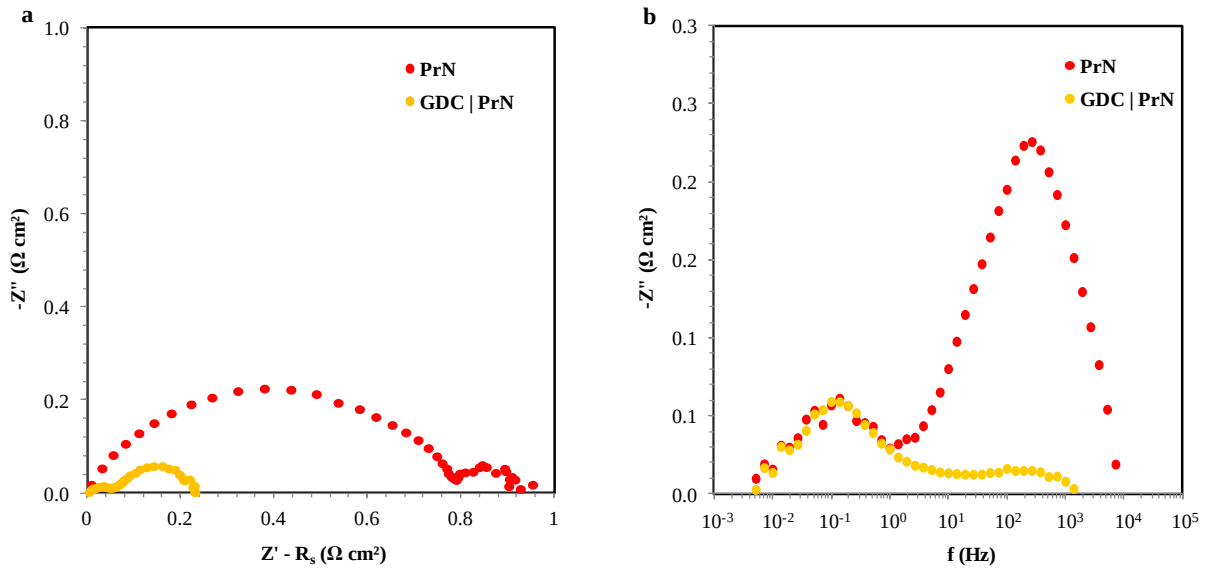

Figure IV-15: For the cells with PrN and GDC | PrN at the cathode side a) impedance spectra measured at 700°C and 0.7 V under air and dry H_2 with R_s contribution removed and b) corresponding Bode plots.

A decrease of the series resistance of about 30% has been here observed, explained by an improved bonding between the cathode and the electrolyte when adding a GDC barrier layer. The major improvement concerns however the polarisation resistance.

In the case of GDC | PrN used in the cathode side, only two (R // CPE) circuits were necessary to obtain a satisfactory fit (the fit with three or four arcs giving unacceptably high error percentages). As can be seen in the Bode plot (*Fig. IV-15b*), the low frequency arc previously assigned to a chemical capacitance or a conversion polarisation remained of unchanged shape and summit frequencies and comparable capacitances values for the cells with and without the GDC layer have been obtained. The fit concerning the first arc gave a summit frequency around 2700 Hz for a capacitance value around 10^{-4} F cm^{-2} (fit results given in *Table IV-11*), corresponding thus to a double layer capacitance. The second and third processes observed in the cell without GDC with equivalent capacitances around 10^{-3} F cm^{-2} and 10^{-1} F cm^{-2}, respectively, *were not observed in this case*. This might come from an overlapping of processes considering the increased difficulty to deconvolute impedance spectra with decreased polarisation resistances. The corresponding resistance for this first arc was found to be 0.14 Ω cm^2 compared to 1.01 Ω cm^2 (sum of processes 1-3) without GDC, which corresponds to a **reduction of the total polarisation resistance by a factor 4**.

However, this performance appeared lower than the one reported by Ferchaud et al. [260] with a cell YSZ / Ni | YSZ | GDC | $Pr_2NiO_{4+\delta}$, the GDC and $Pr_2NiO_{4+\delta}$ layers being prepared under similar conditions (apart from a lower sintering temperature of the GDC layer), without additional current collection layer (maximal power density of 300 mW cm^{-2} at 600°C). R_s and R_p values around 0.5 and 0.4 Ω cm^2, respectively, have been reported at 600°C for this "equivalent" cell using YSZ electrolyte [260]. While the polarisation resistance obtained in the present work can be considered as comparable with the value reported in ref. [260], despite the difference in temperature, we observe again that the **main limitation of the performance of our cells stems from the ohmic losses**.

Here can thus be highlighted the benefit of the use of a GDC barrier layer in between BIT07 and PrN cathode.

2.2. Comparison between the three nickelates

I-V and power density characteristics for the three cathodes when associated with a GDC barrier layer are plotted in *Fig. IV-16*. As for the previous cells, the values of OCV, total Area Specific Resistance ($ASR_{(I-V)}$), power density at 0.7 V ($P_{(0.7V)}$) and maximal power density are reported for each cathode in *Table IV-9.*

Table IV-9:
OCV, total ASR and power density values for the cells BIT07 / Ni | BIT07 | GDC | LnN (Ln = La, Nd, Pr).

cathode	OCV (V)	$ASR_{(I-V)}$ (Ω cm^2)	$P_{(0.7V)}$ (mW cm^{-2})	P_{max} (mW cm^{-2})
GDC | LaN	1.08	1.9	123	141
GDC | NdN	1.07	3.99	59	68
GDC | PrN	1.03	1.34	174	200

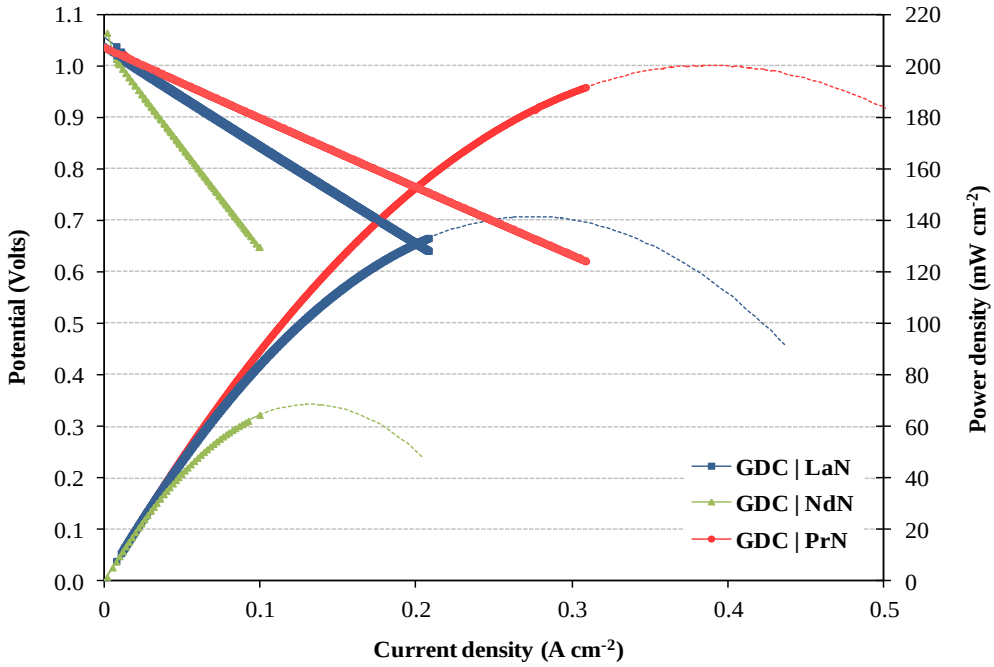

Figure IV-16: I-V curves and power densities under dry H_2 at 700°C for the cells BIT07 / Ni | BIT07 | GDC | LnN with Ln = La, Nd and Pr.

In this series of measurements, the best performance has been obtained with GDC | PrN. As for the previous series of tests, the performance of the cell involving NdN was significantly lower, and although no previous electrochemical data have been found in the literature on the association of NdN with GDC, these results are still assumed to be related to the quality of the batch of powder. The total ASR values decreased by around 20, 60 and 50% for La, Nd and PrN, respectively, when adding the GDC barrier layer. In all cases, the GDC layer has been seen as having a beneficial effect on the value of the OCV.

The values of R_s and R_p obtained from EIS measurements at 700°C and 0.7 V for the three GDC | LnN cells are given in *Table IV-10*. The obtained R_{tot} were in the three cases in good agreement with the $ASR_{(I-V)}$ values. The recorded impedance spectra are shown in *Fig. IV-17*.

Table IV-10:
R_s, R_p and R_{tot} (ASR_{EIS})values for each cathode obtained from the impedance spectra at 700°C and 0.7V and compared with the total ASR calculated from the I-V curves.

Cathode	R_s (Ω cm^2)	R_p (Ω cm^2)	R_{tot} (Ω cm^2)	$ASR_{(I-V)}$ (Ω cm^2)
GDC | LaN	1.44	0.54	2	1.9
LaN	1.3	1.11	2.41	2.39
GDC | NdN	2.7	0.96	3.66	3.99
NdN	/	/	/	13.4
GDC | PrN	1.1	0.29	1.39	1.34
PrN	1.45	1.16	2.61	2.56

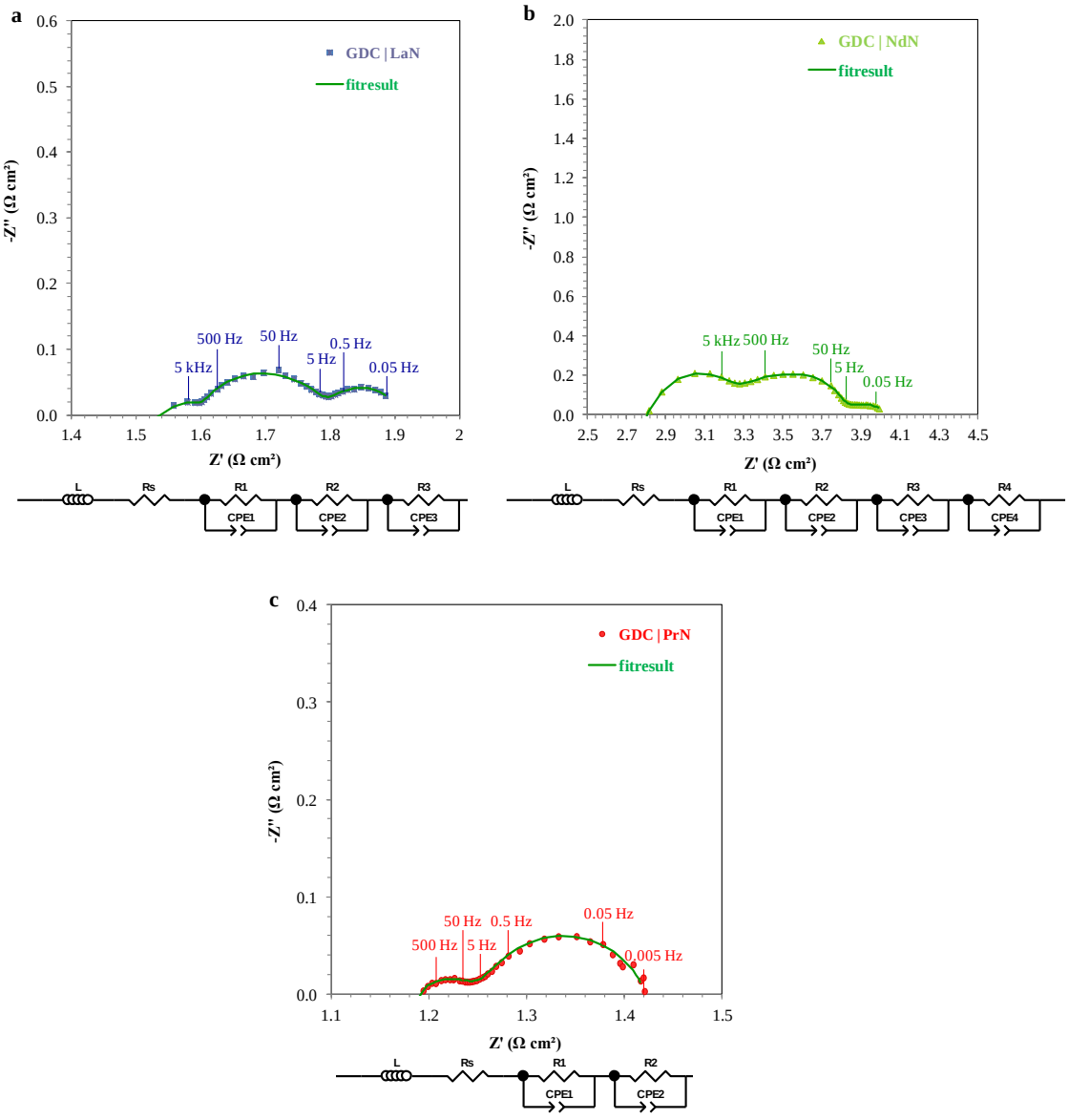

Figure IV-17: Impedance spectra measured at 700°C and at 0.7 V and equivalent circuits for the cells BIT07 / Ni | BIT07 | LnN with Ln = a) LaN, b) NdN and c) PrN.

The fit results in terms of summit frequency, equivalent capacitance and polarisation resistance corresponding to each process and for each GDC | LnN couple can be found in *Table IV-11*. The values for the corresponding cells without the GDC layer are given for comparison.

Table IV-11:
Summit frequencies, equivalent capacities and resistances obtained for each contribution after fitting of the impedance spectra recorded at 700°C and 0.7 V for the three cells BIT07 / Ni | BIT07 | GDC | LaN, BIT07 / Ni | BIT07 | GDC | NdN and BIT07 / Ni | BIT07 | GDC | PrN, compared with the fit results of the cells BIT07 / Ni | BIT07 | LaN and BIT07 / Ni | BIT07 | PrN.

		R_s	R_1 // CPE_1	R_2 // CPE_2	R_3 // CPE_3	R_4 // CPE_4
GDC | LaN	f_{summit} (Hz)	/	11434	79.51	0.17	/
	C_{eq} (F cm^{-2})	/	8×10^{-5}	9×10^{-3}	7	/
	R (Ω cm^2)	1.44	0.17	0.20	0.17	/
LaN	f_{summit} (Hz)	/	11152	260	16	0.12
	C_{eq} (F cm^{-2})	/	9×10^{-5}	7×10^{-4}	8×10^{-2}	17
	R (Ω cm^2)	1.3	0.15	0.76	0.12	0.08
GDC | NdN	f_{summit} (Hz)	/	12777	262	84	0.38
	C_{eq} (F cm^{-2})	/	2×10^{-5}	1×10^{-3}	4×10^{-2}	1.49
	R (Ω cm^2)	2.7	0.53	0.55	0.04	0.21
GDC | PrN	f_{summit} (Hz)	/	2694	0.13	/	/
	C_{eq} (F cm^{-2})	/	2×10^{-4}	8	/	/
	R (Ω cm^2)	1.1	0.14	0.15	/	/
PrN	f_{summit} (Hz)	/	8714	228	21	0.10
	C_{eq} (F cm^{-2})	/	3×10^{-5}	1×10^{-3}	1×10^{-1}	10.3
	R (Ω cm^2)	1.45	0.39	0.56	0.06	0.15

For the cells involving LaN, a slightly higher R_s value is observed when adding the GDC layer; this may indicate that either LaN is better bonded with BIT07 than with GDC or confirms that the high series resistance is more related to problems of current collection (insufficient electronic conductivity of the material, test setup, flatness of the cells…). As for the cell with GDC | PrN, a substantial decrease of the polarisation resistance has been observed. The impedance spectrum was here fitted with three R // CPE circuits. In this case, the highest frequency contribution is maintained compared to the cell with GDC, with comparable polarisation resistance, as for the lowest frequency one. The second and third processes observed for LaN alone seem now to overlap. An intermediate equivalent capacitance value of 10^{-3} F cm^{-2} indicates a contribution from surface processes in this case. The resistance of this arc was found to be around **0.2 Ω cm² for GDC | LaN, compared to 0.88 Ω cm²** for the sum of processes 2 and 3 in the case of LaN alone. This improvement

cannot however be unambiguously attributed to an improvement of the quality of the electrolyte / cathode interface (a better bonding).

Finally, concerning GDC | NdN, a fairly high series resistance of **2.7 Ω cm²** indicates an important problem of current collection, if one considers as comparable the different half-cells of this series of tests and the apparently good quality of the GDC | NdN interface (see *Chapter III, Fig. III-25b*). Around 39% of the contribution to the polarisation resistance is assigned to the ionic transfer at the electrode / electrolyte interface and 44% to electrode surface processes (four contributions found in this case). The low frequency arc was also observed here, with capacitance and polarisation resistances values in the same order of magnitude as for all the other cells tested.

2.3. Post-test analyses

After testing, no cracks or cathode delamination were observed for the cells BIT07 / NiO | BIT07 | GDC | LaN and BIT07 /NiO | BIT07 | GDC | NdN after removal from the test setup. Observations on SEM micrographs of polished cross-sections for these cells, shown in *Fig. IV-18*, do not evidence any major modification in the microstructure of the cells apart from the higher porosity due to the reduction of the anode.

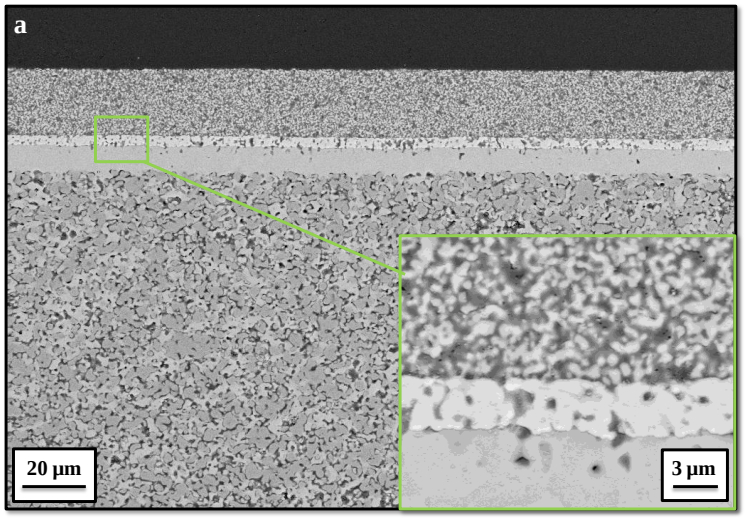

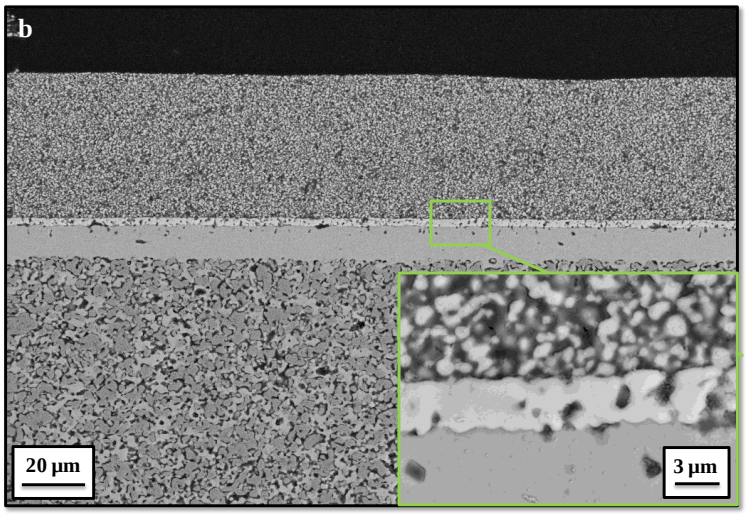

Figure IV-18: BSE SEM micrographs of polished cross-sections for the cells a) BIT07 / Ni | BIT07 | GDC | LaN and b) BIT07 / Ni | BIT07 | GDC | NdN after test.

Moreover, **no diffusion of elements** could be observed by EDX, as can be seen in *Fig. IV-19*. The small diffusion of Nd in GDC seen in *Fig. IV-18b* has been related to the non-homogeneity of the GDC layer, e.g. surface porosities, confirmed by point analyses and element mapping. Post-test analyses for the cell involving PrN will be detailed in the next section.

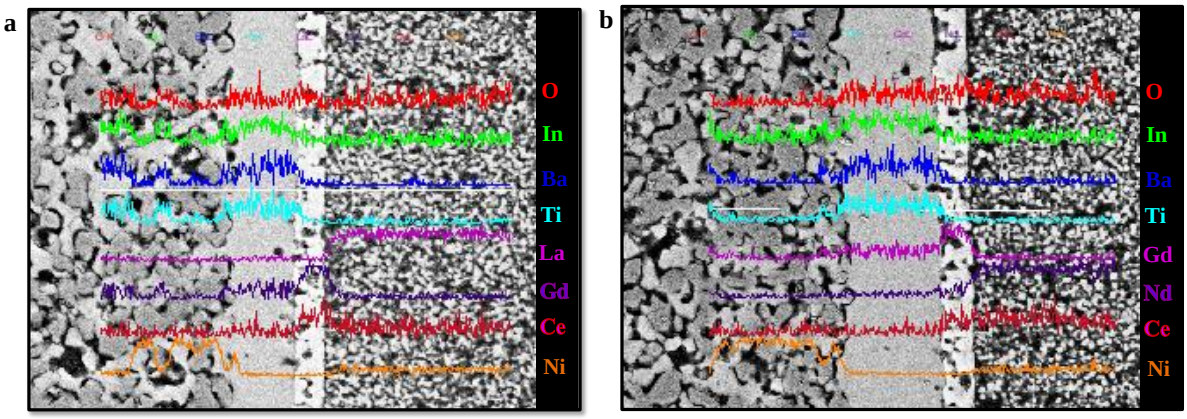

Figure IV-19: Results of the EDX measurement by linescan for the cells a) BIT07 / Ni | BIT07 | GDC | LaN and b) BIT07 / Ni | BIT07 | GDC | NdN after testing.

3. Endurance test

Besides costs and performance, long-term stability is an important requirement for the commercial application of the SOFC technology.

Tests presented in the previous part outlined temporarily GDC | PrN as the best cathode assembly to be associated to BIT07 in this study. An ageing test has thus been performed on this cell in galvanostatic mode at 700°C with a current density of 248 mA cm^{-2} (initial voltage 0.7 V). The measurement has been run **beyond 500 hours**; the evolution of the cell voltage with the time is presented in *Fig.IV-20.* The voltage loss over the measurement time was around **95.5 mV**, corresponding to an average extrapolated electrical degradation rate of **27% / kh**.

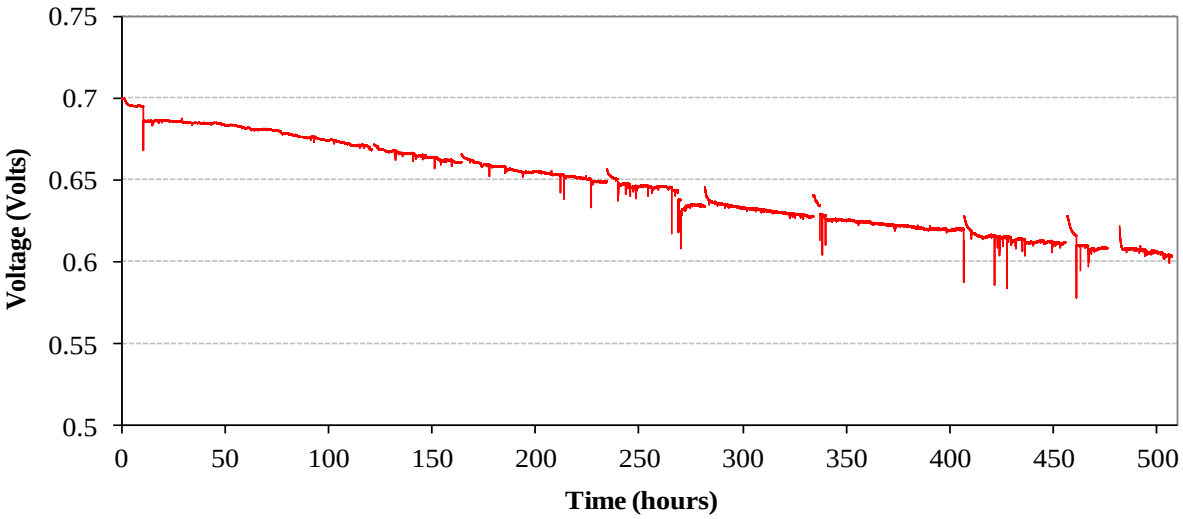

Figure IV-20: Voltage as a function of time at 700°C, 248 mA cm^{-2} for the cell BIT07 / Ni | BIT07 | GDC | PrN.

I-V characteristics as well as impedance spectra at I = 248 mA cm^{-2} have been recorded at different ageing times and are plotted in *Fig. IV-21* and *IV-22*, respectively. Note that in the case of the I-V characteristics only three curves for three different ageing times are shown for a better visibility.

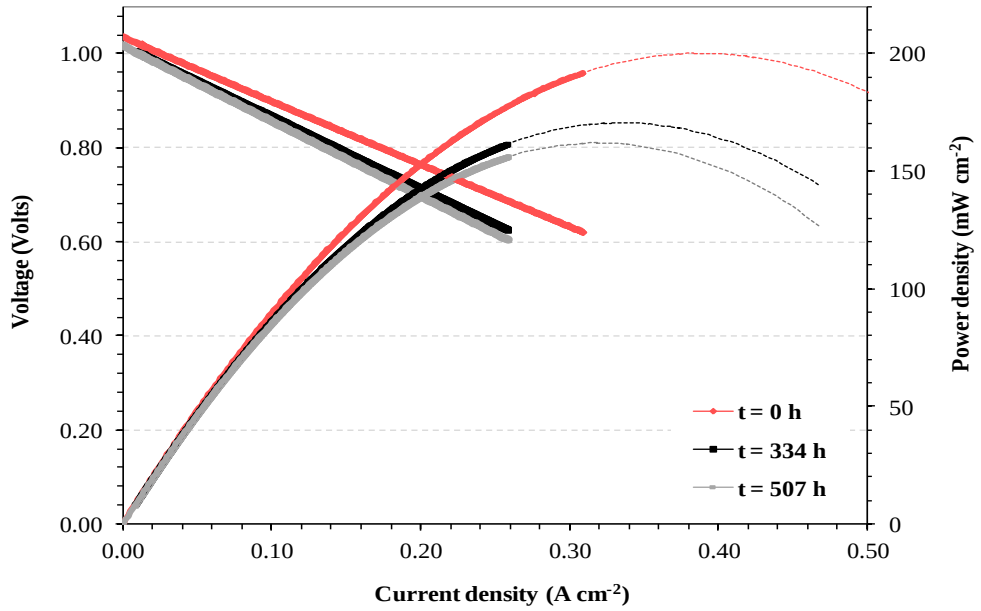

Figure IV-21: I-V curves and power densities under dry H_2 at 700°C for the cell BIT07 / Ni | BIT07 | GDC | PrN at t = 0 h (red), t = 334 h (black) and t = 507 h (grey).

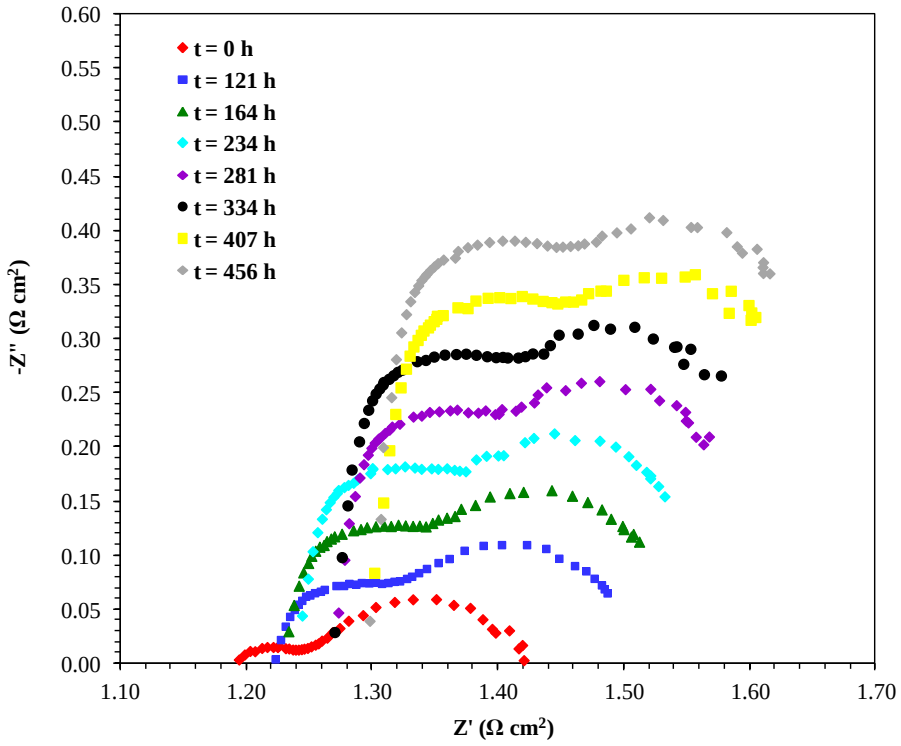

Figure IV-22: Impedance spectra measured at 700°C and 248 mA cm^2 for the cell BIT07 / Ni | BIT07 | GDC | PrN at different ageing times.

Finally, the *Table IV-12* assesses the evolution of the OCV, R_s, R_p and power densities of the cell as a function of time.

Table IV-12:
Evolution of the OCV, R_s, R_p, $P_{(0.7V)}$ and P_{max} with time for the cell BIT07 / Ni | BIT07 | GDC | PrN.

Ageing time	OCV (V)	R_s (Ω cm^2)	R_p (Ω cm^2)	$P_{(0.7V)}$ (mW cm^{-2})	P_{max} (mW cm^{-2})
t = 0 h	1.032	1.1	0.31	174	200
t = 121 h	1.023	1.17	0.32	/	/
t = 164 h	1.023	1.21	0.31	/	/
t = 234 h	1.019	1.21	0.32	/	/
t = 281 h	1.017	1.24	0.32	/	/
t = 334 h	1.016	1.25	0.33	147	170
t = 405 h	1.013	1.27	0.35	142	165
t = 456 h	1.013	1.27	0.34	142	165
t = 507 h	1.009	/	/	139	162

Impedance spectra fitting compared for three ageing times indicates that alongside the R_s increase, the R_p increase can be attributed mainly to the middle frequency contribution. Indeed, the polarisation resistance, summit frequency and capacity range of the low frequency arc, ascribed to bulk processes in *section 1.2*, remains fairly constant with ageing time, whilst the middle frequency contribution becomes more important. From 121 hours of ageing on, the middle frequency arc is accurately modeled by the deconvolution in two R // CPE contributions. Low and middle capacity value (~ 10^{-5} F cm^{-2} and 10^{-2} F cm^{-2}, respectively) contributions, assigned to ionic transfer at the electrode / electrolyte interface(s) and electrode surface processes, respectively, were found.

The values obtained by fitting the impedance spectra are reported in *Table IV-13*. Inductance values around 2 × 10^{-6} H cm^{-2}, corresponding to the "blank" of the test bench, have been obtained for each fit.

Table IV-13:
Summit frequencies, equivalent capacities and resistances obtained for each contribution after fitting of the impedance spectra recorded at 700°C and 248 mA cm^{-2} for the cell BIT07 / Ni | BIT07 | GDC | PrN at ageing times t = 0 hours, t = 121 hours and t = 457 hours.

	T= 0 h			T = 121 h			T = 457 h		
	f_{summit} (Hz)	C_{eq} (F cm^{-2})	R (Ω cm^2)	f_{summit} (Hz)	C_{eq} (F cm^{-2})	R (Ω cm^2)	f_{summit} (Hz)	C_{eq} (F cm^{-2})	R (Ω cm^2)
Rs	/	/	1.1	/	/	1.16	/	/	1.22
R1 CPE1	2694	1.77 10^{-4}	0.16	22657	7.34 10^{-5}	0.075	26932	5.23 10^{-5}	0.09
R2 CPE2	0.13	8.09	0.15	21.2	4.92 10^{-2}	0.11	17.9	6.36 10^{-2}	0.12
R3 CPE3	/	/	/	0.12	8.89	0.15	0.12	8.56	0.15

After test, the cell appeared broken and important cracking was observed, both effects being located at the periphery of the cell (*fig. IV-23*).

Figure IV-23: Picture of the cell BIT07 / Ni | BIT07 | GDC | PrN after ageing for 500 h at 700°C, 248 mA cm^{-2} (anode side).

This effect is probably related to the test configuration, as the surface of the cell is larger than the diameter of the alumina tubes. A part of the cell remains outside of the ceramic tube, and thus outside of the gas chambers. This creates stresses between the reduced part of the substrate and the part not in contact with gases. Propagation of the cracks to the centre of the cell might lead to leakages and therefore decreased OCV values. The anode in the region close to the interface (thickness ca. 50 µm) appeared dense, as shown in post-test SEM micrograph on polished cross-section shown in *Fig. IV-24*. This leads to a decrease of the TPBs, which are the chemically active areas of fuel gas oxidation, and could thus limit the performance of the cell.

Agglomeration and particle coarsening of the metallic Ni is well established as being a predominant source of degradation of the SOFC performance [7, 342-345]. This phenomenon comes from the poor adhesion of Ni to the ceramic material and is mainly driven by the affinity of nickel to reduce its free surface energy under SOFC operating conditions [343]. The decrease of the specific surface area of Ni leads to a decrease of the number of catalytic active sites and therefore the increase of the polarisation resistance. The agglomeration of Ni leads also to a loss of the Ni-Ni contact and therefore a decrease in the conductivity of the cermet [343]. Since in general an increase of R_s correlates with the conductivity of the cells components [346], interfacial reactions and the contacting resistance [347-348], the increase

of the ohmic losses observed in our study could be partially related to a potential problem of nickel coarsening, although further tests are needed to confirm this assumption.

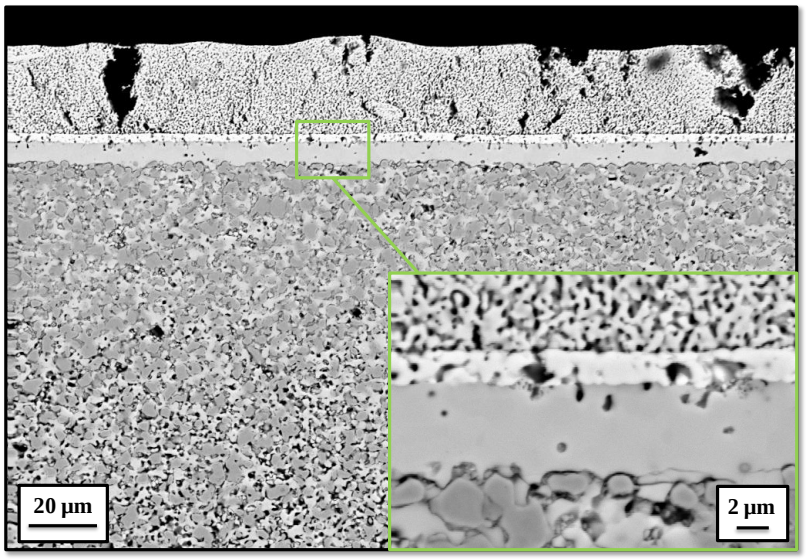

Figure IV-24: BSE SEM micrograph of polished cross-section for the cell BIT07 / Ni | BIT07 | GDC | PrN after test.

Other possible sources of anode ageing are the poor match of thermal expansion coefficients between BIT07 (12.5×10^{-6} K^{-1}) [126] and metallic Ni (16×10^{-6} K^{-1}) [349] as well as thermo-mechanical mechanisms arising from residual stresses created during cell elaboration [350-351].

The interface anode / electrolyte seems also to have degraded, which would lead to an increase of the current path, the blockage of the charge conduction and the elimination of reaction sites. The first consequence is a sharp increase of the activation polarisation due to the current concentration at the contacted areas of the anode, thus potentially related to the observed change in the double layer capacitance [328, 352], but also similarly an increase of the ohmic losses, as discussed in *Section 1.2* [328].

To our best knowledge, no data are available in the literature regarding the chemical stability of BIT07 with time under operation, even if no structural modification has been evidenced on BIT07 by Letilly et al. after two weeks at 700°C under wet (3% H_2O) Ar / H_2 95% / 5% atmosphere [251].

Concerning the cathode side, the electrode remained here attached to the electrolyte (GDC layer) after testing, in opposition to the cell without GDC. The important cracking of the layer is mainly attributed to the stress applied when contacting the current collection (Pt)

grids, as similar microstructures have been observed for equivalent cells measured without ageing. Coarsening of the microstructure of the cathode due to sintering, a common cathode degradation mechanism, might have also contributed to the formation of the cracks [343], however impossible to confirm without further experiments. A slight modification of the interface with GDC (delamination) could also play a role in the degradation of the performance of the cell (low capacitance and R_s contributions as discussed earlier).

As concerns the chemical stability of the cathode material, no evidence for an intrinsic degradation related to the use of nickelates has been found in the literature. Lalanne et al. reported a voltage degradation rate of 5% / kh over 800 hours of operation on YSZ-based standard half-cells, probably not due to cathode-related degradation effects [353]. To our best knowledge, no more data are available on long term experiments involving cells with this family of nickelates.

EDX measurements on the polished cross-section of the cell after test also did not evidence any diffusion of elements, suggesting the absence of chemical reaction with GDC that could form insulating phases at the GDC / PrN interface. The result of an element mapping, here presenting Pr as an example, is given in *Fig. IV-25*.

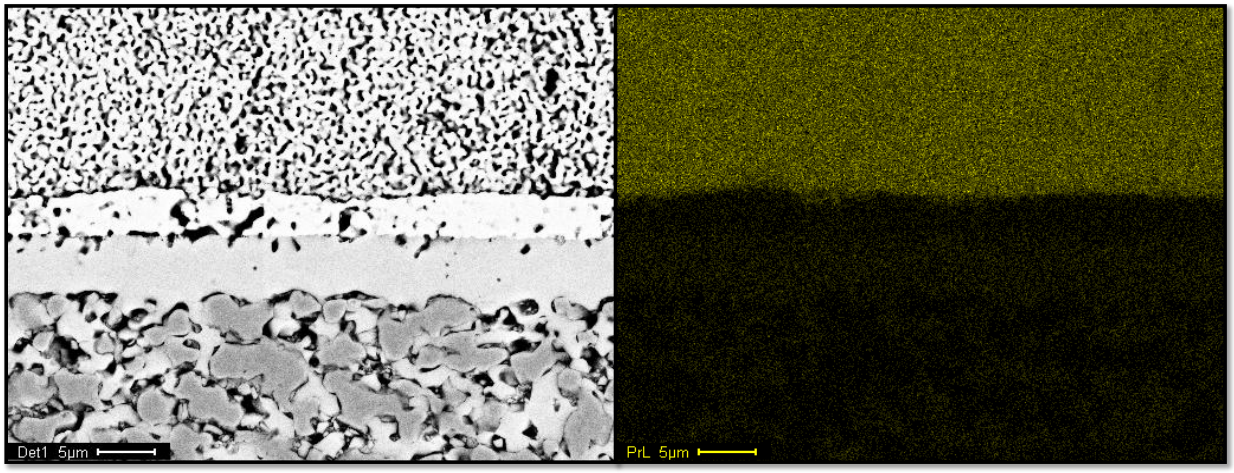

Figure IV-25: BSE SEM micrograph of polished cross-sections for the cell BIT07 / Ni | BIT07 | GDC | PrN after test and mapping result for the Pr element.

4. Towards the optimised BIT07-based half-cell

4.1. Transfer to electrolyte powders supplied by MT

As mentioned previously, no complete cells based on BIT07 powders from Marion Technologies could be obtained. The results presented here will concern cells using standard EMPA-based substrates on which an electrolyte layer of MT1 has been deposited.

Fig. IV-26 compares the I-V characteristics of the cells BIT07 (EMPA) / Ni | BIT07 (EMPA) | GDC (MT) | PrN (MT) and BIT07 (EMPA) / Ni | BIT07 (MT1) | GDC (MT) | PrN (MT). *Table IV-14* summarises the corresponding values of OCV, total $ASR_{(I-V)}$ and power densities.

Table IV-14:
OCV, total ASR and power density values for the cells BIT07 (EMPA) / Ni | BIT07 (EMPA) | GDC (MT) | PrN (MT) and BIT07 (EMPA) / Ni | BIT07 (MT1) | GDC (MT) | PrN (MT).

Powder	OCV (V)	$ASR_{(I-V)}$ (Ω cm^2)	$P_{(0.7V)}$ (mW cm^{-2})	P_{max} (mW cm^{-2})
BIT07 EMPA	1.035	1.34	174	200
BIT07 MT1	1.024	1.32	170	198

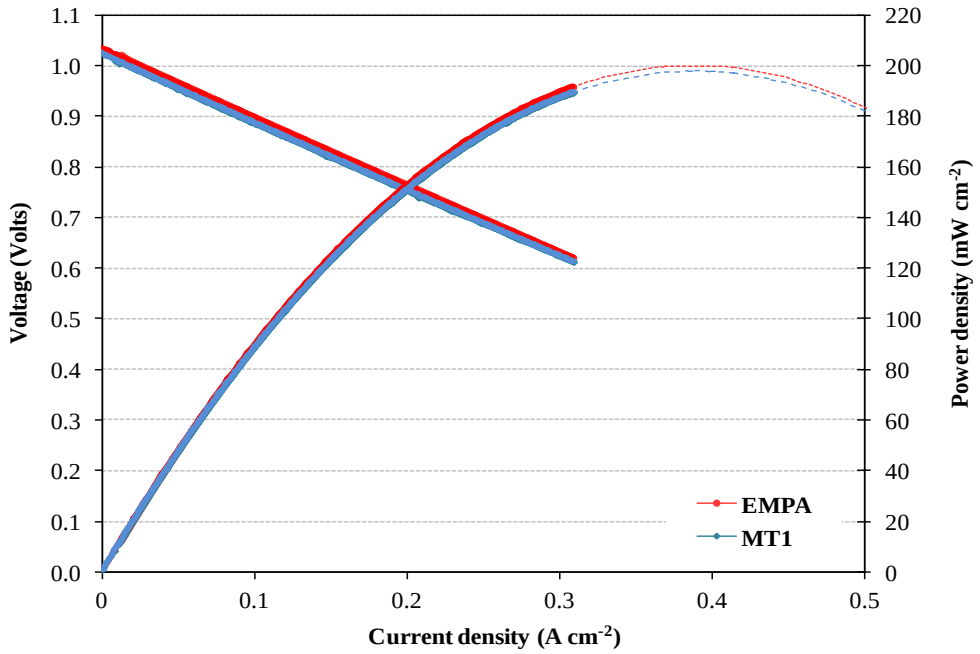

Figure IV-26: I-V curves and power densities under dry H_2 at 700°C for the cells BIT07 (EMPA) / Ni | BIT07 (EMPA) | GDC | PrN (red) and BIT07 (EMPA) / Ni | BIT07 (MT1) | GDC | PrN.

Equivalent performance has been found for these two cells. Impedance spectra have been recorded for the two cells at 700°C and 0.7 V (corresponding to current densities of 248 and 242 mA cm^{-2} for the cells with EMPA and MT1 electrolytes, respectively) and are shown in *Fig. IV-27*.

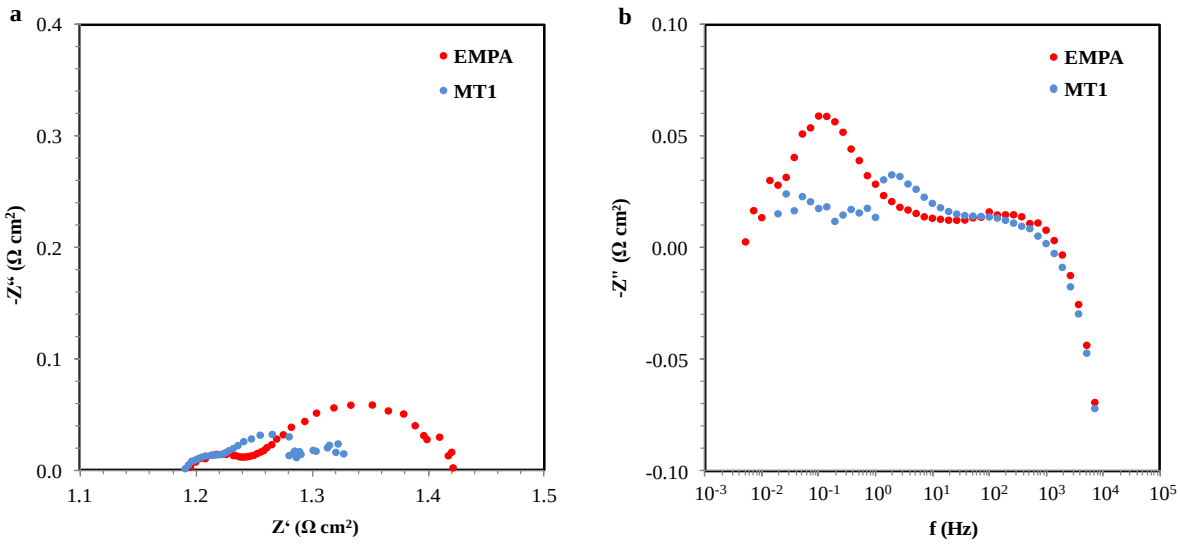

Figure IV-27: Impedance spectra measured at 700°C and at 0.7 V for the cells with electrolyte layer made of EMPA powder (red) and MT1 powder (blue).

Unfortunately, the quality of the spectra for the cell with MT1 electrolyte did not allow any fit of the results. This has been explained by the presence of water in the cathode chamber, observed at the air exit, most likely coming from the direct combustion of hydrogen in air within the cathode chamber due to the presence of a crack in the middle of the cell, which probably appeared when closing the chamber.

Similar R_s values have been observed for the two cells. Concerning the cell with MT1 powder, the apparent diminishing of the low frequency contribution has been attributed to the improved gas diffusion due to the changing of the (Pt) current collection grid on the cathode side. Please note that this also applies for the results that will be presented in the next part. Concerning the first arc, its diminishing might be due to the use of a new screen printing ink for the elaboration of the cathode layer, leading to a better quality of this layer, as can been observed on the SEM micrograph of the cell after testing, shown in *Fig. IV-28*.

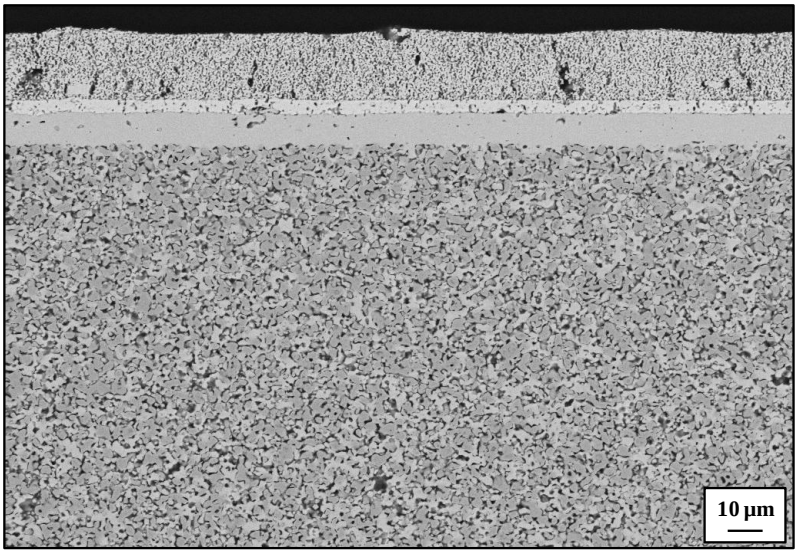

Figure IV-28: BSE SEM micrograph of polished cross-section for the cell BIT07 / Ni | BIT07 (MT1) | GDC | PrN after test.

4.2. Introduction of an anode functional layer: preliminary results

As discussed in the previous chapter, both BIT07 (MT2) and BLITiMn (EMPA) have been combined with NiO and used as anode functional layers with MT1 as an electrolyte.

The electrical characteristics of BLITiMn have been determined at IMN by EIS measurements performed on dense pellets (∅8 mm, thickness ca. 2 mm, density around 100% of the theoretical density) using gold paste electrodes under air and wet Ar / H_2 95% / 5%, the corresponding measured conductivity values being shown in *Fig. IV-29*.

As for BIT07, **BLITiMn** presents also the characteristics of a MIEC with p-type conductivity in oxidising atmospheres. A conductivity of around **2×10^{-2} S cm^{-1}** has been determined for BLITiMn under reducing atmosphere, compared to 2.95×10^{-3} S cm^{-1} for MT1.

The two cells have been prepared and measured; the results are compared to the ones obtained for the cell BIT07 (EMPA) / Ni | BIT07 (MT1) | GDC (MT) | PrN (MT). I-V curves and power densities for the three cells are plotted in *Fig. IV-30*.

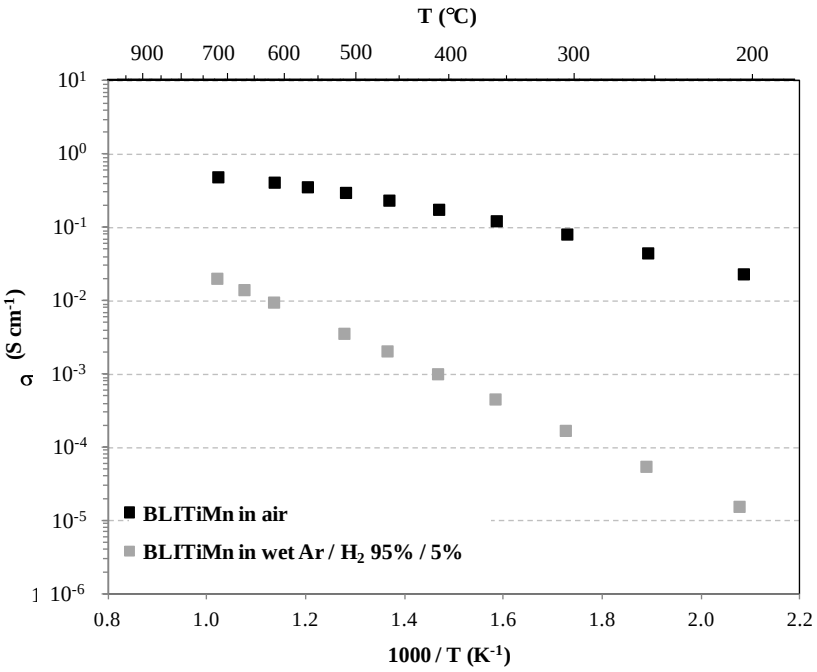

Figure IV-29: Arrhenius plots of the total conductivity of BLITiMn in air (black) and wet Ar / H_2 95% / 5% (grey) determined by EIS.

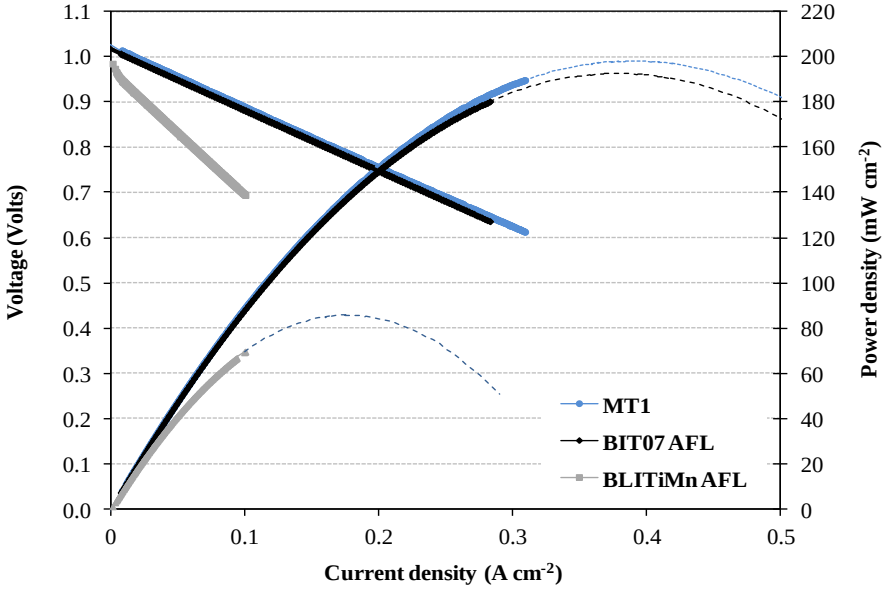

Figure IV-30: I-V curves and power densities under dry H_2 at 700°C for the cells involving BIT07 (MT2) / Ni and BLITiMn (EMPA) / Ni AFL, compared with the standard cell.

Fig. IV-31 shows the impedance spectra for the three cells, recorded at 700°C and 0.7 V, with the ohmic contribution to the total resistance removed for a better comparison.

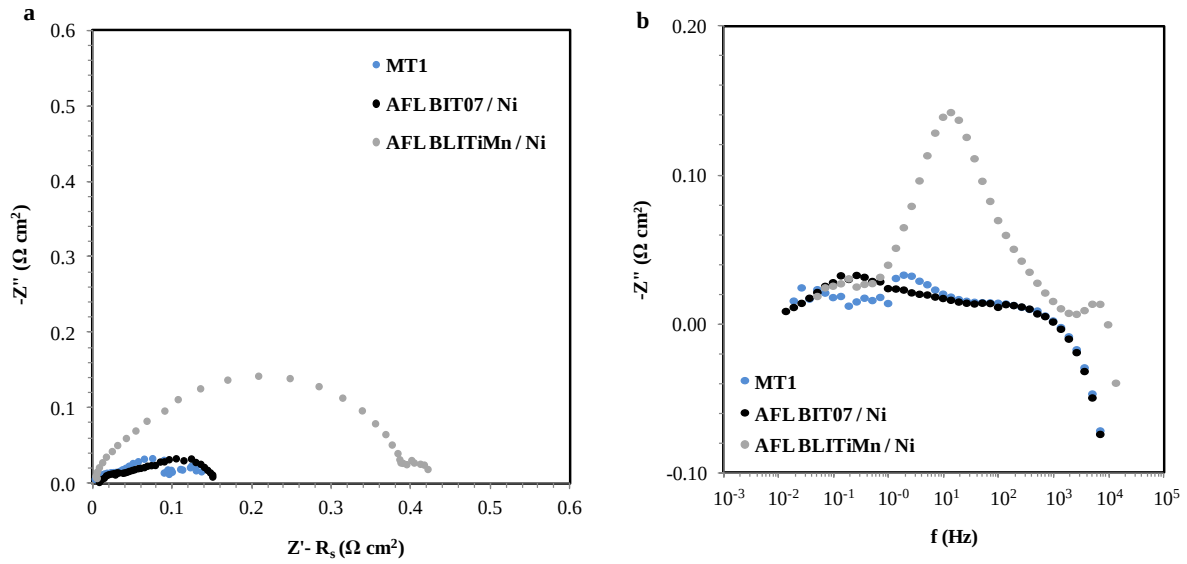

Figure IV-31: a) Impedance spectra measured at 700°C and at 0.7 V for the cells involving BIT07 (MT2) / Ni and BLITiMn (EMPA) / Ni AFLs, compared with the standard cell BIT07 (EMPA) / NiO | BIT07 (EMPA) | GDC | PrN and b) corresponding Bode plots.

Table IV-15 summarises the values of OCV, R_s and R_p determined by impedance, $ASR_{(I-V)}$ and power densities obtained for the three cells. In this case, the R_s and R_p values correspond to a direct reading of the impedance spectra due to the difficulty in obtaining a correct fit for the cell using BIT07 / Ni AFL.

Table IV-15:
OCV, R_s, R_p, total ASR and power density values for the cells without AFL, with BIT07 / Ni AFL and BLITiMn / Ni AFL.

cell	OCV (V)	R_s (Ω cm^2)	R_p (Ω cm^2)	$ASR_{(I-V)}$ (Ω cm^2)	$P_{(0.7V)}$ (mW cm^{-2})	P_{max} (mW cm^{-2})
MT1	1.024	1.19	/	1.32	170	198
BIT07 AFL	1.016	1.31	0.15	1.35	165	192
BLITiMn AFL	0.959	1.89	0.52	2.33	72	86

A first remark concerns the slightly lower OCV value measured for the cell involving BLITiMn in the AFL, which might come either from holes in the electrolyte or from the bad interface of the AFL with the BIT07 electrolyte layer (see *Chapter III*, *Fig. III-36b*). Higher series resistances have been measured for both cells involving an AFL. In the case of BIT07, it could be related to a too low porosity of the AFL leading to difficulties or delays in the reduction of NiO (see *Chapter III*, *Fig. III*-36a). Concerning the BLITiMn material, an issue could be the **bad bonding** between the AFL and the electrolyte layer, linked with the high series resistance (also correlated to a high polarisation resistance). SEM post-test analyses on

polished cross-section (*Fig. IV-32*) are in good agreement with this assumption. In addition, the functional layer itself appeared fairly porous (porosity around 47% after testing, determined by images analyses), with BLITiMn grains apparently not percolating. This might come from the low sinterability of the phase, as similar densification problems have been encountered with this material by Moser et al. [181].

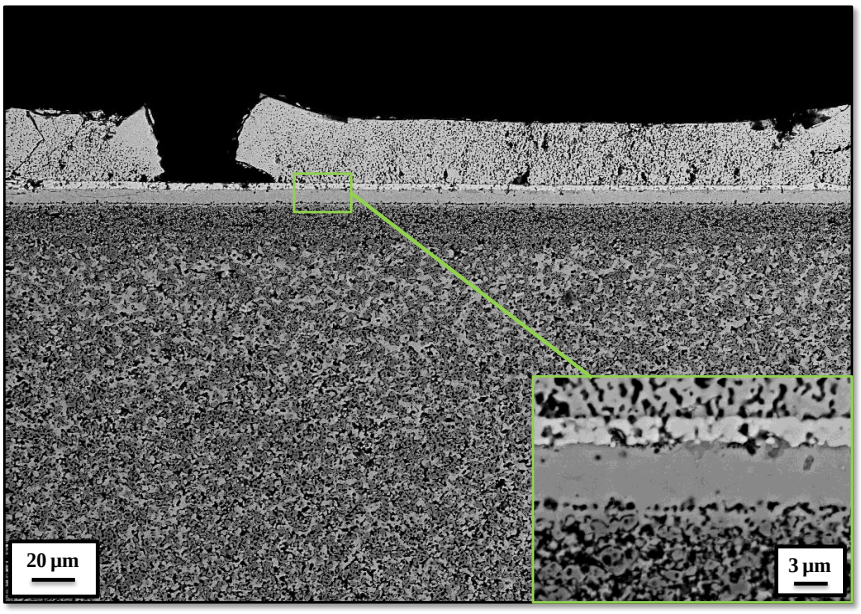

Figure IV-32: BSE SEM micrograph of polished cross-section for the cell BIT07 (EMPA) / NiO | BLITiMn (EMPA) / NiO | BIT07 (MT2) | GDC (MT) | PrN (MT) after test.

A comment regarding BLITiMn concerns the difficulty to measure its conductivity under pure hydrogen. Several attempts have been made at ICMCB to characterise the electrical conductivity of the phase using the four probes method both on dense pellets and cermets, leading in both cases to the bursting of the sample during heating up. The only explanation found to date is a problem of high volumetric changes of the phase during heating at low oxygen partial pressures.

The last comment concerning this cell relates to the cathode side, showing important cracking and high densification. An ageing of the screen printing paste (for instance sedimentation) is assumed, as the cathode of this cell has been printed using the "old" paste, but has still to be confirmed.

Comparable polarisation resistances have been obtained for the cells with and without BIT07-based anode functional layer. Even if the obtained R_s appeared slightly higher when

adding an AFL, comparable performance was obtained despite the improvements expected in the use of smaller size of the particles in the AFL (increased TPB length). The lower magnitude of the first arc of the impedance spectra using MT1 electrolyte and the new cathode screen printing paste was still observed. However, the cell with the BIT07 / Ni AFL exhibited a quite fast degradation, even if the total resistance of the cell actually decreased. As can be seen in *Fig. IV-33a*, impedance spectra at 700°C and 0.7 V recorded 20 hours later showed an important modification of both R_s and R_p. Indeed, R_s decreased down to 1.13 Ω cm^2, which might be explained by a delayed reduction of NiO in the AFL due to the high density of the layer, while R_p rose to around 0.25 Ω cm^2, corresponding to an increase of more than 60%. More visible in the Bode plots of the impedance for the two measurement times (*Fig. IV-33b*), the main cause of degradation stem from the middle frequency arc(s). As no satisfying fits were obtained, the determination of the origins of this fast ageing remained quite difficult.

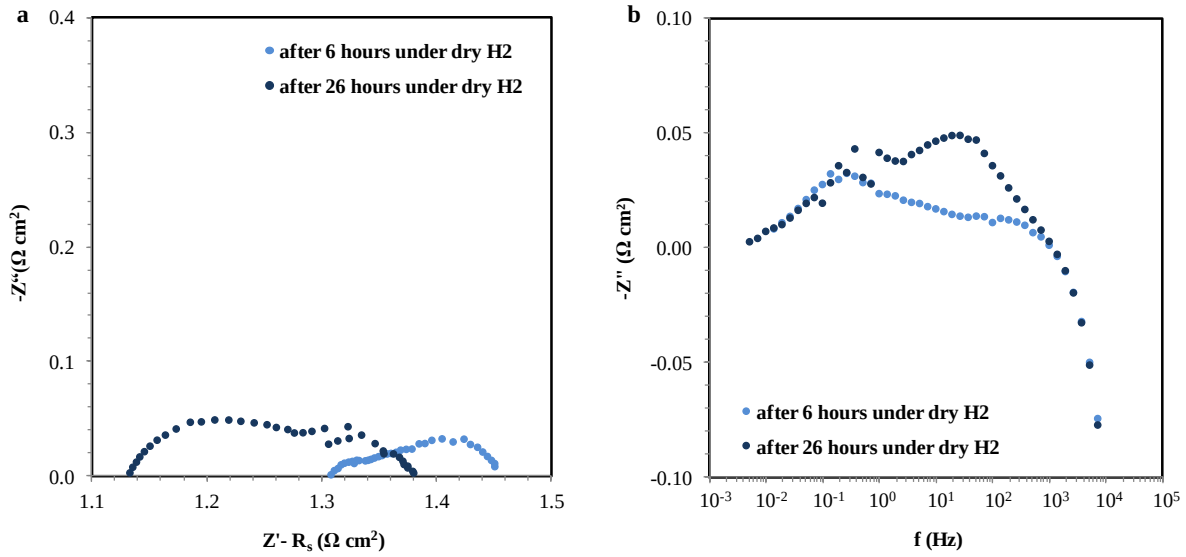

Figure IV-33: EIS measurements on the cell involving BIT07 / Ni AFL after 6 hours and 26 hours at 700 °C under air and dry H_2 a) impedance spectra recorded at 0.7 V and b) corresponding Bode plots.

Post-test analyses by SEM did not allow the identification of the source of the degradation, as the cell appeared of good quality after testing (*Fig. IV-34*) and no element diffusion has been found by EDX.

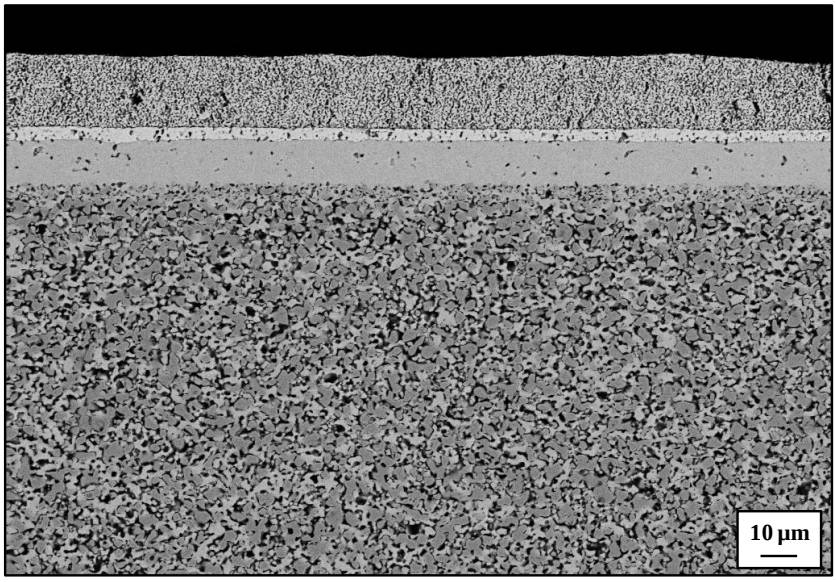

Figure IV-34: BSE SEM micrograph of polished cross-section for the cell BIT07 (EMPA) / NiO | BIT07 (MT2) / NiO | BIT07 (MT1) | GDC (MT) | PrN (MT) after test.

5. Conclusions

The subject of this chapter was the electrochemical characterisation of the BIT07 / nickelates-based cells produced as described in the *Chapter III*.

A first series of tests concerning cells BIT07 (EMPA) / NiO | BIT07 (EMPA) | LnN (MT) with Ln = La, Nd, Pr have been performed, and characteristics as OCV, I-V curves, power densities, total ASR, R_s and R_p have been determined for each cell. The first issue was the **low OCV values** (below 0.9 V compared to values expected above 1.2 V), which could be attributed either to a small **p-type mixed conductivity of BIT07 depending on the processing conditions (microstructure) of the powder**, defects such as **microscopic cracks** in the electrolyte layer or a bad cathode / electrolyte bonding. The best performance has been obtained for the cell involving LaN as a cathode, with a maximum power density of 78 mW cm^{-2} at 700°C. Besides the low OCVs, both **R_s and R_p** were determined as **too high** for an efficient operation for IT-SOFC, leading to the design of a second generation of cells.

The second generation involved the addition of a thin (2 - 3 µm) GDC barrier layer, giving when associated with PrN a **maximal power density of 200 mW cm^{-2}** at 700°C. The improvement came first from higher OCV values, which might be due to the blocking of the electrons and / or the filling of the porosities of the electrolyte by the GDC layer, and / or the improvement of the cathode / electrolyte bonding. Also, a decrease of the total ASR was

observed. A **R_p value as low as 0.29 Ω cm^2** has been obtained, the main limitation of the performance stemming from the high series resistance (above 1 Ω cm^2). Such low polarisation resistance may indicate the problem of high R_s as coming from a bad current collection and the internal resistance of the test setup (contamination of the current collection grids). The cell has been operated at 700°C and 248 mA cm^{-2} under galvanostatic mode **beyond 500 hours** with a fairly high extrapolated degradation rate of **27% / kh**.

Besides, changing the electrolyte layer from EMPA to MT1 did not induce major changes in the performance, with series resistance remaining constant independently of the powder used in the electrolyte layer, indicating the reproducibility of our results. A small decrease of the polarisation resistance in the middle frequency range has been obtained, potentially coming from an improvement of the quality of the cathode layer (new ink).

Finally, preliminary results were obtained on the influence of the addition of anode functional layers based on BIT07 (MT2) and the MIEC BLITiMn. None of them did improve the performance of the cells. Indeed, for the BLITiMn / Ni AFL, a significant increase of both R_s and R_p was attributed to the bad AFL / electrolyte interface, and for the BIT07 / AFL a fast degradation of the cell was observed.

Chapter V

General conclusion and prospects

Nowadays, main hurdles to the industrial deployment of the SOFC technology remain problems of costs and ageing. A decrease of the operating temperature is considered as a relevant approach to slow down certain thermally-activated degradation processes such as corrosion of metallic interconnects so that the lifetime of SOFC systems can be extended.

However, the performance of the fuel cells based on classical ceramic materials (i.e. yttria stabilized zirconia (YSZ) as electrolyte, its corresponding cermet (Ni / YSZ) as anode and $La_{1-x}Sr_xMnO_3$ (LSM) as cathode) is sharply lowered at intermediate temperatures. The last decade saw thus the emerging of alternative materials, and particularly mixed ionic electronic conducting cathodes such as $La_{1-x}Sr_xCo_{1-y}Sr_yO_{3-\delta}$ (LSCF). However, problems of thermomechanical constraints and chemical reactivity between LSCF and YSZ are encountered.

This thesis proposed to study a new cathode / electrolyte assembly for IT-SOFC application, namely the perovskite phase **$BaIn_{0.3}Ti_{0.7}O_{2.85}$** (**BIT07**) as an electrolyte and the oxygen over-stoichiometric nickelates **$Ln_{2-x}NiO_{4+\delta}$ (LnN, with Ln = La, Nd, Pr)** as cathodes. Indeed, a good compatibility between the two phases is awaited as both phases are perovskite-structured (or derivating) and have compatible thermal expansion coefficients.

The aim of this work was to associate these two innovative oxide materials in a **planar anode-supported SOFC** for an efficient operation in the intermediate temperature range, involving low cost shaping techniques. Moreover, industrial powders have been used in this project.

Among the existing techniques, tape casting has been selected for the elaboration of the BIT07 (EMPA) / NiO (J.T. Baker®) (40 : 60 Wt%) anode substrate, as it is a low cost and industrially well-established process. The main stake of this process lies in the slurry formulation and requires a careful selection and an accurate control on the processing additives. In our case, the well-known MEK / Ethanol solvent mixture associated with a

standard PVB (Butvar® B-98, Aldrich) binder system has been used. Environmental friendly plasticiser additives, type I Solusolv® S-2075 (Solutia) and type II PEG400, were selected, and the Nuosperse® FX-4086 used as a dispersing agent.

In a first series of formulations, the influence of the drying conditions and the binder content on the cracking behaviour of the tapes has been studied using the binder : plasticisers ratio 2 : 1. The optimum binder content has been settled to **6 Wt%**. However problems of reproducibility have been encountered. Tests with increased type I and type II plasticisers content to promote plastic deformation and stored stress in the binder polymer matrix, respectively, led to the determination of a recipe for anode substrates with **increased plasticisers content up to a ratio binder : plasticiser of almost 1 to 1**. This recipe has been validated with BIT07 powders from different suppliers.

The pre-sintering conditions for the anode substrates have been optimised to be **1150°C for 6 hours**, heating and cooling rates 1°C / min. The BIT07 electrolyte layer has been deposited by vacuum slip casting (VSC) and co-sintered at **1350°C for 9 hours** (heating and cooling rates 1°C / min), giving **thin (8 - 10 µm), dense and homogeneous electrolyte layers** in a reproducible way.

Three cathode materials, $La_{1.95}NiO_{4+\delta}$ (LaN), $Nd_{1.97}NiO_{4+\delta}$ (NdN) and $Pr_{1.97}NiO_{4+\delta}$ (PrN) have been deposited by screen printing on the produced half-cells. **Good adherence between BIT07 and both LaN and NdN has been found, while PrN was easily delaminating**.

The first generation of BIT07 / NiO | BIT07 | LnN (with Ln = La, Nd, Pr) cells have been electrochemically tested, under dry hydrogen and air atmospheres. The best performance has been obtained for the cell involving **LaN** as a cathode, with a maximum power density of about **80 mW cm^{-2} at 700°C**, nonetheless far below performance reported in the literature by Letilly et al. on button cell for the couple BIT07 / $La_{0.58}Sr_{0.4}Co_{0.2}Fe_{0.8}O_{3-\delta}$ (LSCF) (P_{max} = 336 mW cm^{-2}) or by Lalanne et al. for the couple YSZ / NdN (P_{max} > 500 mW cm^{-2}) at the same temperature. Unacceptability high series resistance (R_s) values (> 1 Ω cm^2) as well as too high polarisation resistances (R_p) have been measured. Note that the series resistance R_s corresponds to the ohmic losses, usually mainly originating from the electrolyte, and the polarisation resistance R_p corresponds to the resistance associated to the electrochemical processes at the electrodes and electrodes / electrolyte interfaces.

Beside, systematic **low OCV values** (< 0.9 V for a theoretical value above 1.2 V) at 700°C have been obtained. Two main hypotheses explaining this issue have been formulated, namely potential microscopic defects in the electrolyte layers such as **cracks** or an electronic contribution to the total conductivity of BIT07. Measurements on dense BIT07 pellets performed by EIS for three different batches of powder showed a systematic slight diminishing of the conductivity of the phase with the p_{O_2}. Although the results seem strongly dependent on the processing conditions of the powder, they seem to indicate **a small p-type conductivity** of BIT07. This conclusion is consistent with the results obtained in this study regarding different assemblies involving BIT07, although the influence of leakages caused by defects (microscopic cracks) in the electrolyte layers is believed to also play a role. The results obtained for this series of tests highlighted an insufficient performing of the BIT07 / LnN assemblies at intermediate temperatures, leading to the design of a second generation with improved architecture.

To improve the quality of the cathode / electrolyte interface, the addition of a thin (2 - 3 µm) $Ce_{0.9}Gd_{0.1}O_{2-\delta}$ (GDC for Gadolinia Doped Ceria) buffer layer in between BIT07 and the three nickelates has been studied. The layer has been deposited on sintered half-cells by screen printing and sintered at 1350°C for 2 hours. The cathodes were subsequently screen-printed and sintered at the optimised sintering temperature of 1170°C for 1 hour.

For the three cathodes, a significant improvement of the performance has been observed with the addition of a GDC barrier layer. Higher OCV values were obtained, explained both by a filling (at least partial) of the cracks in the electrolyte layer or an electrons-blocking effect by / of the layer. The best performance has been obtained for the cell BIT07 / Ni | BIT07 | GDC | PrN, with a maximal power density of **200 mW cm^{-2} at 700°C**. A competitive **polarisation resistance (0.29 Ω cm^2)** has been obtained for this cell, which corresponds to an improvement of a factor 4 compared to the cell without barrier layer, thus promising if compared to a cell involving the LSCF cathode (R_p = 0.35 Ω cm^2). It proves thus that a GDC buffer layer is still needed irrespective of the initial expectation that a buffer layer might be avoided due to analogous crystalline structures between the BIT07 electrolyte and perovskite cathodes. Nevertheless, the advantage of releasing some thermomechanical constraints thanks to the thermal expansion coefficient matching between the three layers remains.

This second generation of BIT07 based-cell has been tested under galvanostatic mode at 0.7 V (I = 248 mA cm^{-2}) beyond **500 hours**, with a fairly high average **degradation rate of**

27% / kh. Although several assumptions have been made to explain this degradation, further experiments are still needed for a better understanding of the ageing phenomena.

Additional improvements of the cells architecture were attempted on the anode side by adding BIT07 (MT2) / NiO or BLITiMn (EMPA) / NiO 44 : 66 Wt% anode functional layers (AFL), casted by vacuum slip casting. Concerning the **BIT07 / NiO AFL**, **thin (6 µm) and dense layers** were obtained, with finer grains expected to increase the TPB length. Preliminary results showed however no improvement of the cell performance, due to a **higher R_s** associated to a **fast degradation** of the cell. Post-test analyses on this cell did not revealed any failure explaining this phenomena, and the reproducibility of the results has still to be assessed before giving any conclusion. **BLITiMn / NiO AFL** appeared thicker (18 µm), fairly porous (porosity above 45% after reduction), and the interface between the anode and the electrolyte layers appeared deteriorated. **Performance was sharply reduced** by adding this AFL, with an important increase of both R_s and R_p.

From these results, further improvement of the performance could be obtained involving a better densification of the GDC layer, for instance by adding a sintering aid in the form of a cobalt nitrate salt. Promising results have been obtained by depositing the GDC layer by vacuum slip casting, but optimisations are still needed to decrease the cracking of both electrolyte and buffer layers during sintering. Optimisation of the sintering program of the three cathodes on GDC layer could also help further reducing the polarisation resistances, although the obtained R_p values are already quite low.

A general issue concerning the electrochemical results for all the cells in this study has been the **high values of the series resistances** (above 1 Ω cm^2 for all the cells), significantly detrimental for the cells performance. These values, not explainable by the ohmic contribution of the electrolyte only, are related to the internal resistance of the setup and current collection issues. Adding current collection layers seems thus here mandatory, as the low electrical conductivity of the nickelates cathodes may here limits the current collection, and modifications of the test rig are also foreseen.

Besides, increasing the porosity of the anode substrates to improve the gas diffusion by using a pore-forming agent has been attempted. Jellified starch has been selected and used in the slurries formulations. **Crack-free tapes containing 2 Wt% and 4 Wt% of jellified starch** were obtained with BIT07 (batch MT1) powders by modifying the recipe (higher binder content). The porosity of the substrates increased from **8% to 25%** (before reduction) when adding 4 Wt%. However, **no complete cells** were obtained with substrates containing pore

forming agent due to the swelling of the anode substrates during pre-sintering. Optimisations of the slurry formulation, including the size of the raw powders here, remain thus to be done.

Finally, the cell elaboration process has been successfully up-scaled at the anode substrate level, with increased slurry volume, and **pre-sintered 11.4 × 11.4 cm^2 substrates** obtained. Here, a decrease of the plasticisers content was needed to obtain workable green tapes, indicating possibilities of further optimisations of the slurry formulations. The substrates were however breaking during the vacuum clip casting step, due to their non-perfect flatness and also to a too low mechanical strength. Preliminary promising results were obtained for small (4 × 4 cm^2) BIT07 / NiO | BIT07 (MT1) half-cells produced by screen printing the electrolyte layer directly on green substrates, avoiding thus the problem of pre-sintered substrates breaking during the electrolyte coating step.

References

1. BP. *Statistical review of world energy 2012*. 2012; Available from: www.bp.com.
2. Ghoniem, A.F., *Needs, resources and climate change: Clean and efficient conversion technologies.* Progress in Energy and Combustion Science, 2011. **37**(1): p. 15-51.
3. International Energy Agency (IEA). *Key World Energy STATISTICS*. 2011; Available from: http://www.iea.org/publications/freepublications/publication/key_world_energy_stats.pdf.
4. Zhang, X., et al., *A review of integration strategies for solid oxide fuel cells.* Journal of Power Sources, 2010. **195**(3): p. 685-702.
5. CO_2 now. *Earth's CO_2 Home Page*. 2013; Available from: http://co2now.org/.
6. Stevens, P., et al., *Piles à combustible.* Techniques de l'ingénieur, traité Génie électrique, 2000. **D3340**.
7. Minh, N.Q., *Ceramic Fuel Cells.* Journal of the American Ceramic Society, 1993. **76**(3): p. 563-588.
8. Kirubakaran, A., S. Jain, and R.K. Nema, *A review on fuel cell technologies and power electronic interface.* Renewable and Sustainable Energy Reviews, 2009. **13**(9): p. 2430-2440.
9. EG&G Technical Services, Inc., *Fuel Cell Handbook (Seventh Edition)*. 2004, U.S. Department of Energy, Office of Fossil Energy.
10. Mekhilef, S., R. Saidur, and A. Safari, *Comparative study of different fuel cell technologies.* Renewable and Sustainable Energy Reviews, 2012. **16**(1): p. 981-989.
11. FuelCellToday. *The Industry Review 2011*. 2011; Available from: http://www.fuelcelltoday.com/analysis/industry-review.
12. US Fuel cell council. *Fuel cells for power generation*. 2008; Available from: http://www.fchea.org/core/import/PDFs/Fuel-Cells-for-Power-Generation-2008.pdf.
13. U.S. department of Energy. *Comparison of fuel cells technologies*. 2011; Available from: http://www1.eere.energy.gov/hydrogenandfuelcells/fuelcells/fc_types.html.
14. Larminie, J. and A. Dicks, *Fuel Cell Systems Explained*. 2 ed, ed. J.W.S. Ltd. 2003.
15. Upreti, G., et al., *Fuel cells for non-automotive uses: Status and prospects.* International Journal of Hydrogen Energy, 2012. **37**(8): p. 6339-6348.
16. UTC power. *PureCell® Model 400*. Available from: http://www.utcpower.com/products/purecell400.
17. UTC power. *Proven Fuel Cell Products*. Available from: http://www.utcpower.com/products.
18. Ballard. *Fuel Cells Products*. 2012 ; Available from: http://www.ballard.com/fuel-cell-products/.
19. *CHIC - Clean Hydrogen In European Cities*. 2010; Available from: http://chic-project.eu/.
20. New Energy World IG. *Hydrogen & Fuel Cells*. 2011; Available from: http://www.new-ig.eu/hydrogen-fuel-cells.
21. Toshiba. *Toshiba launches direct methanol fuel cell in japan as external power for mobile electronic devices*. 2009; Available from: http://www.toshiba.com/taec/news/press_releases/2009/dmfc_09_580.jsp.

22. FuelCell Energy. *Ultra-Clean, Efficient, Reliable Power*. 2012; Available from: http://www.fuelcellenergy.com.
23. Sammes, N. and J.-S. Chung. *High Temperature Fuel Cell Activities in Korea*. in *Proceedings of the 10th European SOFC Forum*. 2012. Luzern, Switzerland.
24. Bloom Energy. *Website*. Available from: http://www.bloomenergy.com/fuel-cell/solid-oxide/.
25. Nanjou, A. *Commercialization of SOFC micro-CHP in the Japanese market*. in *Proceedings of the 10th European SOFC Forum*. 2012. Luzern, Switzerland.
26. CALLUX. *Callux, Practical tests for Fuel Cells in a Domestic Setting*. 2008; Available from: http://www.callux.net/home.English.html.
27. Mai, A., Denzler, R. et al. *Progress in the Development of the Hexis' SOFC Stack and the Galileo 1000 N Micro-CHP System*. in *Proceedings of the 10th European SOFC Forum*. 2012. Luzern, Switzerland.
28. Hexis. *Galileo fuel cell system: Compelling advantages*. Available from: http://www.hexis.com/en.
29. *Callux residential demonstrations reach 1 billion hours of operation.* Fuel Cells Bulletin, 2012. **2012**(6): p. 5-6.
30. FuelCellWorks. *Callux Fuel Cell Total Installations Reaches 300 Units as it Moves Forward to Commercialization*. 2013; Available from: http://fuelcellsworks.com/news/2012/12/20/callux-fuel-cell-total-installations-reaches-300-units-as-it-moves-forward-to-commercialization/.
31. Delphi. *Delphi Solid Oxide Fuel Cell Auxiliary Power Unit*. Available from: http://ppd.delphi.com/pdf/ppd/cv/energy/solid-oxide-fuel-cell-auxiliary-power-unit.pdf.
32. Ceramic Fuel Cells Limited (CFCL) Website. *BlueGEN*. 2012; Available from: http://www.bluegen.info.
33. Föger, K., *BlueGen for Europe – Commercialisation of Ceramic Fuel Cells' residential SOFC Product*, in *Proceedings of the 10th European SOFC Forum*. 2012. Luzern, Switzerland.
34. Ivers-Tiffée, E. and A.V. Virkar, *Chapter 9 - Electrode Polarisations*, in *High Temperature and Solid Oxide Fuel Cells*, S.C. Singhal and K. Kendall, Editors. 2003, Elsevier Science: Amsterdam. p. 229-260.
35. Kendall, K., N.Q. Minh, and S.C. Singhal, *Chapter 8 - Cell and Stack Designs*, in *High Temperature and Solid Oxide Fuel Cells*, S.C. Singhal and K. Kendall, Editors. 2003, Elsevier Science: Amsterdam. p. 197-228.
36. Explow. *Solid Oxide Fuel Cells Images*. 2011; Available from: http://explow.com/Solid_oxide_fuel_cell.
37. Singhal, S.C., *Solid oxide fuel cells for stationary, mobile, and military applications.* Solid State Ionics, 2002. **152-153**(0): p. 405-410.
38. Holtappels, P. and U. Stimming, *Handbook of fuel cells: fundamentals, technology and applications*, ed. W. Vielstich, A. Lamm, and H.A. Gasteiger. Vol. chapter 20: Solid Oxide Fuel Cells (SOFC). 2003: John Wiley & sons Ltd.
39. Howe, K.S., et al. *New Methods of Electrode Preparation for Micro-Tubular Solid Oxide Fuel Cells*. in *Proceedings of the 10th European SOFC Forum*. 2012. Luzern, Switzerland.
40. Pham, Q. *Solid Oxide Fuel Cells Stack Up to Efficient, Clean Power*. 2002; Available from: https://www.llnl.gov/str/September02/Pham.html.
41. Mistler, R.E. and E.R. Twiname, *Tape casting: Theory and Practice*. 2000, Westerville, USA: The American Ceramic Society.
42. Multilayer. *Tape development*; Available from: http://multilayer.4m-association.org/node/37.

43. Menzler, N. H., et al., *Materials and manufacturing technologies for solid oxide fuel cells.* Journal of Materials Science, 2010. **45**(12): p. 3109-3135.
44. Rahaman, M.N., *Ceramic processing*, ed. L. Taylor & Francis Group. 2007: CRC Press. 473.
45. Menzler, N. H., W.S., Hans Peter Buchkremer, *Influence of Processing Parameters on the Manufacturing of Anode-Supported Solid Oxide Fuel Cells by Different Wet Chemical Routes.* Materials Science Forum, 2010. **638 - 642**: p. 1098-1105.
46. Technische Universität Dortmund, I.o.m. *A thermomechanical material model for aluminum alloys during extrusion*. 2011; Available from: http://www.im.mb.tu-dortmund.de/typo3/en/research/research_topics/metal_plasticity/a_thermomechanical_material_model_for_aluminum_alloys_during_extrusion/.
47. Jardiel, T., et al., *Fabrication of 8-YSZ thin-wall tubes by powder extrusion moulding for SOFC electrolytes.* Ceramics International, 2009. **35**(6): p. 2329-2335.
48. Alston, T., et al., *A 1000-cell SOFC reactor for domestic cogeneration.* Journal of Power Sources, 1998. **71**(1-2): p. 271-274.
49. Will, J., et al., *Fabrication of thin electrolytes for second-generation solid oxide fuel cells.* Solid State Ionics, 2000. **131**(1-2): p. 79-96.
50. Minh, N.Q., *Solid oxide fuel cell technology - features and applications.* Solid State Ionics, 2004. **174**(1-4): p. 271-277.
51. Bacher, R.-J., *Screen Printing*, in *Encyclopedia of Materials: Science and Technology (Second Edition)*, Buschow, K.H.J., Cahn R.W. et al., Editors. 2001, Elsevier: Oxford. p. 8281-8283.
52. Tarr, M., University of Bolton. *Online postgraduate courses for the electronics industry - screen and stencil printing*. 2012; Available from: http://www.ami.ac.uk/courses/topics/0222_print/index.html.
53. Li, H.-P. and E. Pfender, *Three Dimensional Modeling of the Plasma Spray Process.* Journal of Thermal Spray Technology, 2007. **16**(2): p. 245-260.
54. Kleijn, C.R., et al., *Multi-scale modeling of chemical vapor deposition processes for thin film technology.* Journal of Crystal Growth, 2007. **303**(1): p. 362-380.
55. Pal, U.B. and S.C. Singhal, *Electrochemical vapor deposition of yttria-stabilized zirconia films.* Journal of The Electrochemical Society, 1990. **137**(9): p. 2937-2941.
56. Fergus, J.W., *Electrolytes for solid oxide fuel cells.* Journal of Power Sources, 2006. **162**(1): p. 30-40.
57. Goodenough, J.B., *Oxide-ion electrolytes.* Annual Review of Materials Research, 2003. **33**(1): p. 91-128.
58. Skinner, S.J. and J.A. Kilner, *Oxygen ion conductors.* Materials Today, 2003. **6**(3): p. 30-37.
59. Ishihara, T., N.M. Sammes, and O. Yamamoto, *Chapter 4 - Electrolytes*, in *High Temperature and Solid Oxide Fuel Cells*, S.C. Singhal and K. Kendall, Editors. 2003, Elsevier Science: Amsterdam. p. 83-117.
60. Ralph, J.M., A.C. Schoeler, and M. Krumpelt, *Materials for lower temperature solid oxide fuel cells.* Journal of Materials Science, 2001. **36**(5): p. 1161-1172.
61. Goodenough, J.B., *Ceramic solid electrolytes.* Solid State Ionics, 1997. **94**(1-4): p. 17-25.
62. Fergus, J., *Materials challenges for solid-oxide fuel cells.* Journal of the Minerals, Metals and Materials Society, 2007. **59**(12): p. 56-62.
63. Kostogloudis, G.C., G. Tsiniarakis, and C. Ftikos, *Chemical reactivity of perovskite oxide SOFC cathodes and yttria stabilized zirconia.* Solid State Ionics, 2000. **135**(1-4): p. 529-535.
64. Yamamoto, O., *Solid oxide fuel cells: fundamental aspects and prospects.* Electrochimica Acta, 2000. **45**(15-16): p. 2423-2435.

65. Kharton, V.V., F.M.B. Marques, and A. Atkinson, *Transport properties of solid oxide electrolyte ceramics: a brief review.* Solid State Ionics, 2004. **174**(1-4): p. 135-149.
66. Arachi, Y., et al., *Electrical conductivity of the ZrO_2-Ln_2O_3 (Ln=lanthanides) system.* Solid State Ionics, 1999. **121**(1-4): p. 133-139.
67. Badwal, S.P.S., F.T. Ciacchi, and D. Milosevic, *Scandia-zirconia electrolytes for intermediate temperature solid oxide fuel cell operation.* Solid State Ionics, 2000. **136-137**: p. 91-99.
68. Etsell, T.H. and S.N. Flengas, *Electrical properties of solid oxide electrolytes.* Chemical Reviews, 1970. **70**(3): p. 339-376.
69. Yamamoto, O., et al., *Electrical conductivity of stabilized zirconia with ytterbia and scandia.* Solid State Ionics, 1995. **79**: p. 137-142.
70. Weber, A. and E. Ivers-Tiffée, *Materials and concepts for solid oxide fuel cells (SOFCs) in stationary and mobile applications.* Journal of Power Sources, 2004. **127**(1-2): p. 273-283.
71. Kerafol (Keramische Folien GmbH). *Electrolyte substrates*. 2009; Available from: http://www.kerafol.com/en/sofc/products-solutions/electrolyte-substrates.html.
72. Inaba, H. and H. Tagawa, *Ceria-based solid electrolytes.* Solid State Ionics, 1996. **83**(1-2): p. 1-16.
73. Mogensen, M., N.M. Sammes, and G.A. Tompsett, *Physical, chemical and electrochemical properties of pure and doped ceria.* Solid State Ionics, 2000. **129**(1-4): p. 63-94.
74. Ivers-Tiffée, E., A. Weber, and D. Herbstritt, *Materials and technologies for SOFC-components.* Journal of the European Ceramic Society, 2001. **21**(10-11): p. 1805-1811.
75. Sha, X., et al., *Preparation and properties of rare earth co-doped $Ce_{0.8}Sm_{0.2-x}Y_xO_{1.9}$ electrolyte materials for SOFC.* Journal of Alloys and Compounds, 2006. **424**(1-2): p. 315-321.
76. Ishihara, T., et al., *Oxide ion conductivity in $La_{0.8}Sr_{0.2}Ga_{0.8}Mg_{0.2-x}Ni_xO_3$ perovskite oxide and application for the electrolyte of solid oxide fuel cells.* Journal of Materials Science, 2001. **36**(5): p. 1125-1131.
77. Lybye, D., F.W. Poulsen, and M. Mogensen, *Conductivity of A- and B-site doped $LaAlO_3$, $LaGaO_3$, $LaScO_3$ and $LaInO_3$ perovskites.* Solid State Ionics, 2000. **128**(1-4): p. 91-103.
78. Nomura, K. and S. Tanase, *Electrical conduction behavior in $(La_{0.9}Sr_{0.1})M^{III}O_{3-\delta}$ (M^{III}=Al, Ga, Sc, In, and Lu) perovskites.* Solid State Ionics, 1997. **98**(3-4): p. 229-236.
79. Takahashi, T. and H. Iwahara, *Ionic conduction in perovskite-type oxide solid solution and its application to the solid electrolyte fuel cell.* Energy Conversion, 1971. **11**(3): p. 105-111.
80. Mizusaki, J., et al., *Electrical Conductivity, Defect Equilibrium and Oxygen Vacancy Diffusion Coefficient of $La_{1-x}Ca_xAlO_{3-\delta}$ Single Crystals.* Journal of The Electrochemical Society, 1993. **140**(2): p. 467-471.
81. Chen, T.-Y. and K.-Z. Fung, *A and B-site substitution of the solid electrolyte $LaGaO_3$ and $LaAlO_3$ with the alkaline-earth oxides MgO and SrO.* Journal of Alloys and Compounds, 2004. **368**(1-2): p. 106-115.
82. Georges, S. and M. Salaün, *Redox cycling and metastability of $La_2Mo_2O_9$-based ceramics.* Solid State Ionics, 2008. **178**(37-38): p. 1898-1906.
83. Goutenoire, et al., *Structural and transport characteristics of the LAMOX family of fast oxide-ion conductors, based on lanthanum molybdenum oxide $La_2Mo_2O_9$.* Journal of materials chemistry, 2001. **11**: p. 119-124.
84. Evans, I.R., J.A.K. Howard, and J.S.O. Evans, *The Crystal Structure of α-$La_2Mo_2O_9$ and the Structural Origin of the Oxide Ion Migration Pathway.* Chemistry of Materials, 2005. **17**(16): p. 4074-4077.

85. Khadasheva, Z.S., et al., *Synthesis and Properties of $La_2(Mo_{1-x}M_x)_2O_9$ (M = Nb, Ta) Ionic Conductors.* Inorganic Materials, 2002. **38**(11): p. 1168-1171.
86. Collado, J.A., et al., *Synthesis, Structures, and Thermal Expansion of the $La_2W_{2-x}Mo_xO_9$ Series.* Journal of Solid State Chemistry, 2002. **167**(1): p. 80-85.
87. Georges, S., et al., *Thermal, structural and transport properties of the fast oxide-ion conductors $La_{2-x}R_xMo_2O_9$ (R=Nd, Gd, Y).* Solid State Ionics, 2003. **161**(3-4): p. 231-241.
88. Arulraj, A., et al., *Synthesis and Characterization of the Anionic Conductor System $La_2Mo_2O_{9-0.5x}F_x$ (x = 0.02-0.30).* Chemistry of Materials, 2002. **14**(6): p. 2492-2498.
89. Higuchi, et al., *Oxide ionic conductivities of apatite-type lanthanum silicates and germanates and their possibilities as an electrolyte of lower temperature operating SOFC*. Ceramics international, 2010. **36**: p. 955-959.
90. Nakayama, S., H. Aono, and Y. Sadaoka, *Ionic Conductivity of $Ln_{10}(SiO_4)_6O_3$ (Ln = La, Nd, Sm, Gd, and Dy.* Journal of Materials Chemistry, 1995. **26**(45): p. 1801-1805.
91. Nakayama, S., et al., *Ionic conductivity of lanthanoid silicates, $Ln_{10}(SiO_4)_6O_3$(Ln = La, Nd, Sm, Gd, Dy, Y, Ho, Er and Yb).* Journal of Materials Chemistry, 1995. **5**(11): p. 1801-1805.
92. Nakayama, S. and M. Sakamoto, *Electrical properties of new type high oxide ionic conductor $RE_{10}Si_6O_{27}$ (RE = La, Pr, Nd, Sm, Gd, Dy).* Journal of the European Ceramic Society, 1998. **18**(10): p. 1413-1418.
93. Yuan, W., Y. Gu, and L. Li, *Synthesis and Ionic Conduction of Cation-deficient Apatite $La_{9.332x/3}M_xSi_6O_{26}$ Doped with Mg, Ca, Sr.* Chinese Journal of Chemical Engineering, 2008. **16**(3): p. 488-491.
94. Shaula, A.L., et al., *Transport properties and Mössbauer spectra of Fe-substituted $La_{10-x}(Si,Al)_6O_{26}$ apatites.* Materials Research Bulletin, 2004. **39**(6): p. 763-773.
95. Kakinuma, K., et al., *Oxide-ion conductivity of $(Ba_{1-x}La_x)_2In_2O_{5+x}$ system based on brownmillerite structure.* Solid State Ionics, 2001. **140**(3-4): p. 301-306.
96. Shaula, A.L., et al., *Oxygen ionic and electronic transport in apatite ceramics.* Journal of the European Ceramic Society, 2005. **25**(12): p. 2583-2586.
97. Battle, P.D., et al., *The structural properties of the oxygen conducting δ phase of Bi_2O_3.* Journal of Physics C: Solid State Physics, 1983. **16**(17): p. L561.
98. Kant, R., K. Singh, and O.P. Pandey, *Synthesis and characterization of bismuth vanadate electrolyte material with aluminium doping for SOFC application.* International Journal of Hydrogen Energy, 2008. **33**(1): p. 455-462.
99. Beg, S., N.A.S. Al-Areqi, and S. Haneef, *Study of phase transition and ionic conductivity changes of Cd-substituted $Bi_4V_2O_{11-\delta}$.* Solid State Ionics, 2008. **179**(39): p. 2260-2264.
100. Kant, R., K. Singh, and O.P. Pandey, *Structural and ionic conductive properties of $Bi_4V_{2-x}Ti_xO_{11-\delta}$ ($0 \leq x \leq 0.4$) compound.* Materials Science and Engineering: B, 2009. **158**(1-3): p. 63-68.
101. Vannier, R.N., et al., *Oxygen transfer in BIMEVOX materials.* Solid State Ionics, 2003. **160**(1-2): p. 85-92.
102. Vannier, R.N., et al., *Double substitutions in $Bi_4V_2O_{11}$.* Solid State Ionics. **70-71**(Part 1): p. 248-252.
103. Abraham, F., et al., *The bimevox series: A new family of high performances oxide ion conductors.* Solid State Ionics, 1990. **40-41**(Part 2): p. 934-937.
104. Mori, M., et al., *Compatibility of $Gd_xTi_2O_7$ pyrochlores ($1.72 \leq x \leq 2.0$) as electrolytes in high-temperature solid oxide fuel cells.* Solid State Ionics, 2003. **158**(1-2): p. 79-90.
105. Daidouh, A., et al., *Structural and electrical behaviour of the pyrochlores: $Sm_{2-x}M_xTi_2O_{7-x/2}$ (M=Mg, Co, Ni).* Solid State Sciences, 2004. **6**(1): p. 71-76.

106. Colville, A.A. and S. Geller, *The crystal structure of brownmillerite, Ca_2FeAlO_5.* Acta Crystallographica Section B, 1971. **27**(12): p. 2311-2315.
107. Goodenough, J.B., J.E. Ruiz-Diaz, and Y.S. Zhen, *Oxide-ion conduction in $Ba_2In_2O_5$ and $Ba_3In_2MO_8$ (M=Ce, Hf, or Zr).* Solid State Ionics, 1990. **44**(1-2): p. 21-31.
108. Zhang, G.B. and D.M. Smyth, *Defects and transport of the brownmillerite oxides with high oxygen ion conductivity - $Ba_2In_2O_5$.* Solid State Ionics, 1995. **82**(3-4): p. 161-172.
109. Schober, T. and J. Friedrich, *The oxygen and proton conductor $Ba_2In_2O_5$: Thermogravimetry of proton uptake.* Solid State Ionics, 1998. **113-115**: p. 369-375.
110. Yoshinaga, M., et al., *The electrical conductivity and structural phase transitions of cation-substituted $Ba_2In_2O_5$.* Solid State Ionics, 2004. **169**(1-4): p. 9-13.
111. Ta, T.Q., T. Tsuji, and Y. Yamamura, *Thermal and electrical properties of $Ba_2In_2O_5$ substituted for In-site by rare earth elements.* Journal of Alloys and Compounds, 2006. **408-412**: p. 253-256.
112. Kendall, K.R., et al., *Recent developments in perovskite-based oxide ion conductors.* Solid State Ionics, 1995. **82**(3-4): p. 215-223.
113. Shimura, T. and T. Yogo, *Electrical properties of the tungsten-doped $Ba_2In_2O_5$.* Solid State Ionics, 2004. **175**(1-4): p. 345-348.
114. Niwa, J., et al., *Structure and electrical characteristics of Ce^{4+}-doped $Ba_2In_2O_5$.* Journal of Materials Science, 2003. **38**(18): p. 3791-3795.
115. Gregory, D.H. and M.T. Weller, *Phases in the System $Ba_2M_{2-x}Cu_xO_{4+\delta}$, M = In, Sc: Structure and Oxygen Stoichiometry.* Journal of Solid State Chemistry, 1993. **107**(1): p. 134-148.
116. Yamamura, H., et al., *Order–disorder transition of oxygen vacancy in the brownmillerite system.* Solid State Ionics, 1998. **108**(1-4): p. 377-381.
117. Yao, T., et al., *Crystal structure of Ga-doped $Ba_2In_2O_5$ and its oxide ion conductivity.* Solid State Ionics, 2000. **132**(3-4): p. 189-198.
118. Rolle, A., G. Fafilek, and R.N. Vannier, *Redox stability of $Ba_2In_2O_5$-doped compounds.* Solid State Ionics, 2008. **179**(1-6): p. 113-119.
119. Jayaraman, V., et al., *Characterization of perovskite systems derived from $Ba_2In_2O_5\square$: Part I: the oxygen-deficient $Ba_2In_{2(1-x)}Ti_{2x}O_{5+x}\square_{1-x}$ ($0 \le x \le 1$) compounds.* Solid State Ionics, 2004. **170**(1-2): p. 17-24.
120. Delahaye, T., et al., *Synthesis and characterization of a Ni/$Ba_2In_{0.6}Ti_{1.4}O_{5.7}\square_{0.3}$ cermet for SOFC application.* Solid State Ionics, 2006. **177**(33-34): p. 2945-2950.
121. Manthiram, A., J.F. Kuo, and J.B. Goodenough, *Characterization of oxygen-deficient perovskites as oxide-ion electrolytes.* Solid State Ionics, 1993. **62**(3-4): p. 225-234.
122. Hashimoto, T., et al., *Characterization of phase transition of $Ba_{2x}Sr_xIn_2O_5$ by thermal analysis and high temperature X-ray diffraction.* Journal of Thermal Analysis and Calorimetry, 2002. **69**(3): p. 909-917.
123. Kakinuma, K., et al., *Oxide-ion conductivity of the perovskite-type solid-solution system, $(Ba_{1-x-y}Sr_xLa_y)_2In_2O_{5+y}$.* Solid State Ionics, 2002. **154-155**(0): p. 571-576.
124. Kakinuma, K., et al., *Solid oxide fuel cell using $(Ba_{0.3}Sr_{0.2}La_{0.5})InO_{2.75}$ electrolyte.* Solid State Ionics, 2004. **175**(1-4): p. 139-143.
125. Magrez, A. et al., *Nouveaux oxydes électrolytes solides : relation entre microstructure et conductivité ionique.* 2002, PhD thesis. Université de Nantes. Supervisor: O. Joubert.
126. Delahaye, T. at al., *Réalisation et optimisation d'électrolytes et d'anodes pour piles à combustible à oxide solide fonctionnant à température intermédiaire*. 2006, PhD thesis. Université de Nantes. Supervisor: O. Joubert.
127. Quarez, E., et al., *Water incorporation and proton conductivity in titanium substituted barium indate.* Journal of Power Sources, 2010. **195**(4): p. 1136-1141.
128. Lay, E., L. Dessemond, and G. Gauthier, *Ba-substituted LSCM anodes for solid oxide fuel cells.* Journal of Power Sources, 2013. **221**(0): p. 149-156.

129. La Rosa, D., et al., *Mitigation of carbon deposits formation in intermediate temperature solid oxide fuel cells fed with dry methane by anode doping with barium.* Journal of Power Sources, 2009. **193**(1): p. 160-164.
130. Mawdsley, J.R. and T.R. Krause, *Rare earth-first-row transition metal perovskites as catalysts for the autothermal reforming of hydrocarbon fuels to generate hydrogen.* Applied Catalysis A: General, 2008. **334**(1-2): p. 311-320.
131. Yang, L., et al., *Promotion of water-mediated carbon removal by nanostructured barium oxide/nickel interfaces in solid oxide fuel cells.* Nat Commun, 2011. **2**: p. 357.
132. Letilly, M., et al., *Synthesis, structural analysis and electrochemical performances of BLSITCFx as new cathode materials for solid oxide fuel cells (SOFC) based on BIT07 electrolyte.* Journal of Power Sources, 2010. **195**(15): p. 4779-4784.
133. Jiang, S.P. and S.H. Chan, *A review of anode materials development in solid oxide fuel cells.* Journal of Materials Science, 2004. **39**(14): p. 4405-4439.
134. Setoguchi, T., et al., *Effects of Anode Material and Fuel on Anodic Reaction of Solid Oxide Fuel Cells.* Journal of The Electrochemical Society, 1992. **139**(10): p. 2875-2880.
135. de Boer, B., et al., *The effect of the presence of fine YSZ particles on the performance of porous nickel electrodes.* Solid State Ionics, 2000. **127**(3-4): p. 269-276.
136. Tsipis, E. and V. Kharton, *Electrode materials and reaction mechanisms in solid oxide fuel cells: a brief review.* Journal of Solid State Electrochemistry, 2008. **12**(11): p. 1367-1391.
137. Park, S., J.M. Vohs, and R.J. Gorte, *Direct oxidation of hydrocarbons in a solid-oxide fuel cell.* Nature, 2000. **404**(6775): p. 265-267.
138. Rösch, B., et al. *Electrochemical behaviour of Ni-$Ce_{0,9}Gd_{0,1}O_{2-\delta}$ SOFC anodes in methane*. in *SOFC VIII, Proceedings of the 8th International Symposium*. 2003: The electrochemical society.
139. Joerger, M.B. and L.J. Gauckler. *Catalytically active anodes for SOFC*. in *SOFC IV. Proceedings of the 4th International Symposium.* 2000: The electrochemical society.
140. Zhu, W.Z. and S.C. Deevi, *A review on the status of anode materials for solid oxide fuel cells.* Materials Science and Engineering: A, 2003. **362**(1-2): p. 228-239.
141. Marina, O.A. and M. Mogensen, *High-temperature conversion of methane on a composite gadolinia-doped ceria-gold electrode*. Applied Catalysis A: General, 1999. **189**(1): p. 117-126.
142. Fergus, J.W., *Oxide anode materials for solid oxide fuel cells.* Solid State Ionics, 2006. **177**(17-18): p. 1529-1541.
143. Wen, C.J., T. Masuyama, and T. Yoshikawa. *The effect of electrolytes in the nickel cermet on the anodic overpotential of SOFC*. in *SOFC IV, Proceedings of the 4th International Symposium*. 2000: The electrochemical society.
144. Hibino, T., et al., *High performance anodes for SOFCs operating in methane-air mixture at reduced temperatures*. Journal of the Electrochemical Society, 2002. **149**(2): p. A133-A136.
145. Hibino, T., et al., *An Intermediate-Temperature Solid Oxide Fuel Cell Providing Higher Performance with Hydrocarbons than with Hydrogen.* Electrochemical and Solid-State Letters, 2002. **5**(11): p. A242-A244.
146. Primdahl, S. and Y.L. Liu, *Ni Catalyst for Hydrogen Conversion in Gadolinia-Doped Ceria Anodes for Solid Oxide Fuel Cells.* Journal of The Electrochemical Society, 2002. **149**(11): p. A1466-A1472.
147. Primdahl, S. and M. Mogensen, *Mixed conductor anodes: Ni as electrocatalyst for hydrogen conversion.* Solid State Ionics, 2002. **152-153**: p. 597-608.
148. Metcalfe, I.S., et al., *Hydrocarbon activation in solid state electrochemical cells.* Solid State Ionics, 1992. **57**(3-4): p. 259-264.

149. Savaniu, C.D. and J.T.S. Irvine, *La-doped $SrTiO_3$ as anode material for IT-SOFC.* Solid State Ionics, 2011. **192**(1): p. 491-493.
150. Hui, S. and A. Petric, *Electrical conductivity of yttrium-doped $SrTiO_3$: influence of transition metal additives.* Materials Research Bulletin, 2002. **37**(7): p. 1215-1231.
151. Noll, F., et al., *$SrTiO_3$ as a prototype of a mixed conductor Conductivities, oxygen diffusion and boundary effects.* Solid State Ionics, 1996. **86-88, Part 2**(0): p. 711-717.
152. Lepe, F.J., et al., *Synthesis and electrical properties of new rare-earth titanium perovskites for SOFC anode applications.* Journal of Power Sources, 2005. **151**: p. 74-78.
153. Holt, A., E. Ahlgrend, and F.W. Poulsen. *Synthesis, electrical properties and defect chemistry of Ti-doped $NdCrO_3$*. in *SOFC III, Proceedings of the 3rd International Symposium*. 1998: The electrochemical society.
154. Sutija, D.P.a.T.N. *AC van der Paw Measurements of the Electrical Conductivity of Iron-doped Calcium Titanate.* in *SOFC III, Proceedings of the 3rd International Symposium*. 1998: The electrochemical society.
155. Mantzouris, X., et al., *Mixed conducting oxides $Y_xZr_{1-x-y}Ti_yO_{2-x/2}$ (YZT) and corresponding Ni/YZT cermets as anode materials in an SOFC.* Journal of Materials Science, 2007. **42**(24): p. 10152-10159.
156. Stoukides, M., M. Othoneos, and N. Kiratzis. *Modelling of the synthesis of hydrogen cyanide in an Yttria-stabilized Zirconia Cell*. in *SOFC II, Proceedings of the 2nd International Symposium*. 1991. Athen, Greece: Commission of the European Communities.
157. Tao, S. and J.T.S. Irvine, *Optimization of Mixed Conducting Properties of Y_2O_3-ZrO_2-TiO_2 and Sc_2O_3-Y_2O_3-ZrO_2-TiO_2 Solid Solutions as Potential SOFC Anode Materials.* Journal of Solid State Chemistry, 2002. **165**(1): p. 12-18.
158. Middleton, P.H., H.J. Steiner, and G.M. Christie. *Evaluation of novel oxide anodes for methane conversion in SOFC systems*. in *SOFC III, Proceedings of the 3rd International Symposium*. 1998: The electrochemical society.
159. Fagg, D.P., S.M. Fray, and J.T.S. Irvine, *Reduced magnesium titanate electrodes for solid oxide fuel cells.* Solid State Ionics, 1994. **72**(Part 2): p. 235-239.
160. Vulliet, J., et al. *First results on a (La, Sr)CrO_3 anode fed with methane*. in *SOFC VIII, Proceedings of the 8th International Symposium*. 2003: The electrochemical society.
161. Sfeir, J., J. van herle, and A.J. McEvoy, *Stability of calcium substituted lanthanum chromites used as SOFC anodes for methane oxidation.* Journal of the European Ceramic Society, 1999. **19**(6-7): p. 897-902.
162. Tao, S. and J.T.S. Irvine, *Discovery and characterization of novel oxide anodes for solid oxide fuel cells.* The Chemical Record, 2004. **4**(2): p. 83-95.
163. Sfeir, J., *$LaCrO_3$-based anodes: stability considerations.* Journal of Power Sources, 2003. **118**(1-2): p. 276-285.
164. Primdahl, S., et al., *Sr-doped $LaCrO_3$ anode for solid oxide fuel cells*. Journal of the Electrochemical Society, 2001. **148**(1): p. A74-A81.
165. Goodenough, J.B. and Y.-H. Huang, *Alternative anode materials for solid oxide fuel cells.* Journal of Power Sources, 2007. **173**(1): p. 1-10.
166. Vernoux, P., J. Guindet, and M. Kleitz, *Gradual Internal Methane Reforming in Intermediate-Temperature Solid-Oxide Fuel Cells.* Journal of The Electrochemical Society, 1998. **145**(10): p. 3487-3492.
167. Jardiel, T., et al., *New SOFC electrode materials: The Ni-substituted LSCM-based compounds $(La_{0.75}Sr_{0.25})(Cr_{0.5}Mn_{0.5-x}Ni_x)O_{3-\delta}$ and $(La_{0.75}Sr_{0.25})(Cr_{0.5-x}Ni_xMn_{0.5})O_{3-\delta}$.* Solid State Ionics, 2010. **181**(19-20): p. 894-901.
168. Vernoux, P., et al., *Alternative anode material for gradual methane reforming in solid oxide fuel cells.* Solid State Ionics, 2000. **135**(1-4): p. 425-431.

169. Aguilar, L. et al., *Sulfur-tolerant materials for the hydrogen sulfide SOFC*. Electrochemical and Solid-State Letters, 2004. **7**(10): p. A324-A326.
170. Cheng, Z., et al., *Chemical, electrical, and thermal properties of strontium doped lanthanum vanadate.* Solid State Ionics, 2005. **176**(23-24): p. 1921-1928.
171. Hui, S. and A. Petric, *Conductivity and stability of $SrVO_3$ and mixed perovskites at low oxygen partial pressures.* Solid State Ionics, 2001. **143**(3-4): p. 275-283.
172. Hartley, A., et al., *$La_{0.6}Sr_{0.4}Co_{0.2}Fe_{0.8}O_3$ as the anode and cathode for intermediate temperature solid oxide fuel cells.* Catalysis Today, 2000. **55**(1-2): p. 197-204.
173. McColm, T.D. and J.T.S. Irvine, *Structural and property investigations of Strontium Galloniobate.* Solid State Ionics, 2002. **152-153**(0): p. 615-623.
174. Tao, S. and J.T.S. Irvine, *Structure and properties of nonstoichiometric mixed perovskites $A_3B'_{1+x}B''_{2-x}O_{9-\delta}$.* Solid State Ionics, 2002. **154-155**(0): p. 659-667.
175. Tomita, A., T. Hibino, and M. Sano, *Surface Modification of a Doped $BaCeO_3$ to Function as an Electrolyte and as an Anode for SOFCs.* Electrochemical and Solid-State Letters, 2005. **8**(7): p. A333-A336.
176. Hirabayashi, D., et al., *Solid oxide fuel cells operating without using an anode material.* Solid State Ionics, 2004. **168**(1-2): p. 23-29.
177. Slater, P.R. and J.T.S. Irvine, *Synthesis and electrical characterisation of the tetragonal tungsten bronze type phases, $(Ba/Sr/Ca/La)_{0.6}M_xNb_{1-x}O_{3-\delta}$ (M=Mg, Ni, Mn, Cr, Fe, In, Sn): evaluation as potential anode materials for solid oxide fuel cells.* Solid State Ionics, 1999. **124**(1-2): p. 61-72.
178. Holtappels, P., F.W. Poulsen, and M. Mogensen, *Electrical conductivities and chemical stabilities of mixed conducting pyrochlores for SOFC applications.* Solid State Ionics, 2000. **135**(1-4): p. 675-679.
179. Sprague, J.J. and H.L. Tuller, *Mixed ionic and electronic conduction in Mn/Mo doped gadolinium titanate.* Journal of the European Ceramic Society, 1999. **19**(6-7): p. 803-806.
180. Hirabayashi, D. et al., *Bi-based oxide anodes for direct hydrocarbon SOFCs at intermediate temperatures.* Electrochemical and Solid-State Letters, 2004. **7**(5).
181. Moser, F., *Développement de nouveaux matériaux d'anode pour pile à combustible à oxyde solide SOFC fonctionnant sous gaz naturel.* PhD thesis, 2009. (Université de Nantes). Supervisor: O. Joubert.
182. Hamakawa, S., et al., *Design of one-component ceramic membrane-reactor for natural gas conversion.* Catalysis Today, 2006. **117**(1-3): p. 297-303.
183. Sun, C., R. Hui, and J. Roller, *Cathode materials for solid oxide fuel cells: a review.* Journal of Solid State Electrochemistry, 2010. **14**(7): p. 1125-1144.
184. Ishihara, T., et al., *Doped Perovskite Oxide, $PrMnO_3$, as a New Cathode for Solid-Oxide Fuel Cells that Decreases the Operating Temperature.* Journal of the American Ceramic Society, 1994. **77**(6): p. 1682-1684.
185. Kostogloudis, G.C., N. Vasilakos, and C. Ftikos, *Preparation and characterization of $Pr_{1-x}Sr_xMnO_{3\pm\delta}$ (x = 0, 0.15, 0.3, 0.4, 0.5) as a potential SOFC cathode material operating at intermediate temperatures (500-700°C).* Journal of the European Ceramic Society, 1997. **17**(12): p. 1513-1521.
186. Rim, H.-R., et al., *Characteristics of $Pr_{1-x}M_xMnO_3$ (M = Ca, Sr) as cathode material in solid oxide fuel cells.* Materials Chemistry and Physics, 1998. **52**(1): p. 54-59.
187. Lalanne, C., *Synthèse et mise en forme de nouveaux matériaux de cathode pour piles ITSOFC: réalisation et tests de cellules.* PhD thesis, 2005. **n° 3046** (Université Bordeaux 1). Supervisor : J.-M. Bassat. Available from: *tel.archives-ouvertes.fr/docs/00/09/26/66/PDF/T0508.pdf*

188. Gu, H., et al., *Effect of Co doping on the properties of $Sr_{0.8}Ce_{0.2}MnO_{3-\delta}$ cathode for intermediate-temperature solid-oxide fuel cells.* International Journal of Hydrogen Energy, 2008. **33**(17): p. 4681-4688.
189. Ishihara, T., et al., *Doped $PrMnO_3$ Perovskite Oxide as a New Cathode of Solid Oxide Fuel Cells for Low Temperature Operation.* Journal of The Electrochemical Society, 1995. **142**(5): p. 1519-1524.
190. Anderson, M.D., J.W. Stevenson, and S.P. Simner, *Reactivity of lanthanide ferrite SOFC cathodes with YSZ electrolyte.* Journal of Power Sources, 2004. **129**(2): p. 188-192.
191. Ralph, J.M., C. Rossignol, and R. Kumar, *Cathode Materials for Reduced-Temperature SOFCs.* Journal of The Electrochemical Society, 2003. **150**(11): p. A1518-A1522.
192. Coffey, G., et al., *Copper doped lanthanum strontium ferrite for reduced temperature solid oxide fuel cells.* Solid State Ionics, 2004. **175**(1-4): p. 73-78.
193. Yokokawa, H. and T. Horita, *Chapter 5 - Cathodes*, in *High Temperature and Solid Oxide Fuel Cells*, S.C. Singhal and K. Kendall, Editors. 2003, Elsevier Science: Amsterdam. p. 119-147.
194. Mai, A., et al. *A-site defficient Lanthanum Ferrites as cathode materials for SOFCs*. in *SOFC IX, Proceedings of the 9th International Symposium*. 2005. Pennington, USA: The electrochemical society.
195. Meng, X., et al., *Characterization of $Pr_{1-x}Sr_xCo_{0.8}Fe_{0.2}O_{3-\delta}$ ($0.2 \leq x \leq 0.6$) cathode materials for intermediate-temperature solid oxide fuel cells.* Journal of Power Sources, 2008. **183**(2): p. 581-585.
196. Shao, Z. and S.M. Haile, *A high-performance cathode for the next generation of solid-oxide fuel cells.* Nature, 2004. **431**(7005): p. 170-173.
197. Li, S., et al., *Thermal, electrical, and electrochemical properties of Nd-doped $Ba_{0.5}Sr_{0.5}Co_{0.8}Fe_{0.2}O_{3-\delta}$ as a cathode material for SOFC.* Solid State Ionics, 2008. **178**(35-36): p. 1853-1858.
198. Li, S., et al., *A study of* $(Ba_{0.5}Sr_{0.5})_{1-x}Sm_xCo_{0.8}Fe_{0.2}O_{3-\delta}$ *as a cathode material for IT-SOFCs.* Journal of Alloys and Compounds, 2006. **426**(1-2): p. 408-414.
199. Li, S., et al., *Electrical and thermal properties of $(Ba_{0.5}Sr_{0.5})_{1-x}Sm_xCo_{0.8}Fe_{0.2}O_{3-\delta}$ perovskite oxides.* Solid State Ionics, 2007. **178**(5-6): p. 417-422.
200. Yan, A., et al., *Investigation of a $Ba_{0.5}Sr_{0.5}Co_{0.8}Fe_{0.2}O_{3-\delta}$ based cathode SOFC: II. The effect of CO_2 on the chemical stability.* Applied Catalysis B: Environmental, 2007. **76**(3-4): p. 320-327.
201. Kharton, V.V., et al., *Ionic transport in oxygen-hyperstoichiometric phases with K_2NiF_4-type structure.* Solid State Ionics, 2001. **143**(3-4): p. 337-353.
202. Aguadero, A., et al., *Evaluation of the $La_2Ni_{1-x}Cu_xO_{4+\delta}$ system as SOFC cathode material with 8YSZ and LSGM as electrolytes.* Solid State Ionics, 2008. **179**(11-12): p. 393-400.
203. Boehm, E., et al., *Oxygen diffusion and transport properties in non-stoichiometric $Ln_{2-x}NiO_{4+\delta}$ oxides.* Solid State Ionics, 2005. **176**(37-38): p. 2717-2725.
204. Skinner, S.J. and J.A. Kilner, *Oxygen diffusion and surface exchange in $La_{2-x}Sr_xNiO_{4+\delta}$.* Solid State Ionics, 2000. **135**(1-4): p. 709-712.
205. Tarancon, A., et al., *Advances in layered oxide cathodes for intermediate temperature solid oxide fuel cells.* Journal of Materials Chemistry, 2010. **20**: p. 3799-3813.
206. Al Daroukh, M., et al., *Oxides of the AMO_3 and A_2MO_4-type: structural stability, electrical conductivity and thermal expansion.* Solid State Ionics, 2003. **158**(1-2): p. 141-150.

207. Mauvy, F., et al., *Chemical oxygen diffusion coefficient measurement by conductivity relaxation - correlation between tacer diffusion coefficient and chemical diffusion coefficient.* Journal of the European Ceramic Society, 2004. **24**(6): p. 1265-1269.
208. Munnings, C.N., et al., *Structure, stability and electrical properties of the $La_{(2-x)}Sr_xMnO_{4\pm\delta}$ solid solution series.* Solid State Ionics, 2006. **177**(19-25): p. 1849-1853.
209. Mauvy, F., et al., *Oxygen electrode reaction on $Nd_2NiO_{4+\delta}$ cathode materials: impedance spectroscopy study.* Solid State Ionics, 2003. **158**(1-2): p. 17-28.
210. Cao, Y., et al., *Preparation and characterization of $Nd_{2-x}Sr_xCoO_{4+\delta}$ cathodes for intermediate-temperature solid oxide fuel cell.* International Journal of Hydrogen Energy, 2010. **35**(11): p. 5594-5600.
211. Nie, H.W., et al., *Preparation, thermal expansion, chemical compatibility, electrical conductivity and polarization of $A_{2-\alpha}A'_{\alpha}MO_4$ (A = Pr, Sm; A' = Sr; M = Mn, Ni; α = 0.3, 0.6) as a new cathode for SOFC.* Solid State Ionics, 2006. **177**(19-25): p. 1929-1932.
212. Kovalevsky, A., et al., *Oxygen permeability, stability and electrochemical behavior of $Pr_2NiO_{4+\delta}$-based materials.* Journal of Electroceramics, 2007. **18**(3): p. 205-218.
213. Liu, Y., et al., *Microstructures and electric characteristics of $SrNdCoO_4$ ceramics with K_2NiF_4 structure.* Journal of Electroceramics, 2008. **21**(1): p. 706-710.
214. Hernández, A.M., L. Mogni, and A. Caneiro, *$La_2NiO_{4+\delta}$ as cathode for SOFC: Reactivity study with YSZ and CGO electrolytes.* International Journal of Hydrogen Energy, 2010. **35**(11): p. 6031-6036.
215. Egger, A., et al., *Oxygen Exchange Kinetics and Chemical Stability of the IT-SOFC Cathode Material $Nd_2NiO_{4+\delta}$.* ECS Transactions, 2009. **25**(2): p. 2547-2556.
216. Chauveau, F., et al., *A new anode material for solid oxide electrolyser: The neodymium nickelate $Nd_2NiO_{4+\delta}$.* Journal of Power Sources, 2010. **195**(3): p. 744-749.
217. Zhu, W.Z. and S.C. Deevi, *Development of interconnect materials for solid oxide fuel cells.* Materials Science and Engineering: A, 2003. **348**(1-2): p. 227-243.
218. Anderson, H.U. and F. Tietz, *Chapter 7 - Interconnects*, in *High Temperature and Solid Oxide Fuel Cells*, S.C. Singhal and K. Kendall, Editors. 2003, Elsevier Science: Amsterdam. p. 173-195.
219. Quadakkers, W.J., et al., *Metallic interconnectors for solid oxide fuel cells - a review.* Materials at High Temperatures, 2003. **20**(2): p. 115-127.
220. Fergus, J.W., *Lanthanum chromite-based materials for solid oxide fuel cell interconnects.* Solid State Ionics, 2004. **171**(1-2): p. 1-15.
221. Zuev, A., L. Singheiser, and K. Hilpert, *Defect structure and isothermal expansion of A-site and B-site substituted lanthanum chromites.* Solid State Ionics, 2002. **147**(1-2): p. 1-11.
222. Chen, Y., et al., *Microwave assisted synthesis, sinterability and properties of Ca-Zn co-doped $LaCrO_3$ as interconnect material for IT-SOFCs.* Journal of Rare Earths, 2010. **28**(1): p. 153-157.
223. Sakai, N., et al., *Sinterability and electrical conductivity of calcium-doped lanthanum chromites.* Journal of Materials Science, 1990. **25**(10): p. 4531-4534.
224. Fu, Y.-P. and H.-C. Wang, *Preparation and characterization of ceramic interconnect $La_{0.8}Ca_{0.2}Cr_{0.9}M_{0.1}O_{3-\delta}$ (M = Al, Co, Cu, Fe) for IT-SOFCs.* International Journal of Hydrogen Energy, 2011. **36**(1): p. 747-754.
225. Ding, X., et al., *Effects of cation substitution on thermal expansion and electrical properties of lanthanum chromites.* Journal of Alloys and Compounds, 2006. **425**(1-2): p. 318-322.
226. Deng, F., et al., *Characterization of A-site excessive perovskite $La_{0.7-x}Sm_{x+0.02}Ca_{0.3}CrO_{3-\delta}$.* Journal of Rare Earths, 2009. **27**(2): p. 227-230.

227. Mori, M., *Enhancing Effect on Densification and Thermal Expansion Compatibility for $La_{0.8}Sr_{0.2}Cr_{0.9}Ti_{0.1}O_3$-Based SOFC Interconnect with B-Site Doping.* Journal of The Electrochemical Society, 2002. **149**(7): p. A797-A803.
228. Park, B.-K., et al., *La-doped $SrTiO_3$ interconnect materials for anode-supported flat-tubular solid oxide fuel cells.* International Journal of Hydrogen Energy, 2012. **37**(5): p. 4319-4327.
229. Mori, M. and N.M. Sammes, *Sintering and thermal expansion characterization of Al-doped and Co-doped lanthanum strontium chromites synthesized by the Pechini method.* Solid State Ionics, 2002. **146**(3-4): p. 301-312.
230. Zhu, X., et al., *Effect of Ca^{2+} and Zn^{2+} cations substitution on the properties of $La_{0.85}Sr_{0.15}CrO_3$ as SOFC interconnect.* Journal of Alloys and Compounds, 2009. **480**(2): p. 958-961.
231. Liu, M., et al., *High sintering ability and electrical conductivity of Zn doped La(Ca)CrO_3 based interconnect ceramics for SOFCs.* Journal of Power Sources, 2008. **177**(2): p. 451-456.
232. Devi, P.S. and M.S. Rao, *Preparation, structure and electrical properties of the system $LaCr_{1-x}Ti_xO_3$.* Journal of Materials Science Letters, 1992. **11**(4): p. 226-228.
233. Badwal, S.P.S., *Stability of solid oxide fuel cell components.* Solid State Ionics, 2001. **143**(1): p. 39-46.
234. Anderson, H.U. and F. Tietz, *Chapter 7 - Interconnects*, in *High Temperature and Solid Oxide Fuel Cells*, S.C. Singhal and K. Kendall, Editors. 2003, Elsevier Science: Amsterdam. p. 173-195.
235. Simner, S.P., J.S. Hardy, and J.W. Stevenson, *Sintering and Properties of Mixed Lanthanide Chromites.* Journal of The Electrochemical Society, 2001. **148**(4): p. A351-A360.
236. Yu, C.J., H.U. Anderson, and D.M. Sparlin, *High-temperature defect structure of Nb-doped $LaCrO_3$.* Journal of Solid State Chemistry, 1989. **78**(2): p. 242-249.
237. Yoon, K.J., et al., *Advanced ceramic interconnect material for solid oxide fuel cells: Electrical and thermal properties of calcium- and nickel-doped yttrium chromites.* Journal of Power Sources, 2010. **195**(22): p. 7587-7593.
238. Wu, J. and X. Liu, *Recent Development of SOFC Metallic Interconnect.* Journal of Materials Science & Technology, 2010. **26**(4): p. 293-305.
239. Antepara, I., et al., *Evaluation of ferritic steels for use as interconnects and porous metal supports in IT-SOFCs.* Journal of Power Sources, 2005. **151**(0): p. 103-107.
240. Jian, L., et al., *Heat resistant alloys as interconnect materials of reduced temperature SOFCs.* Journal of Power Sources, 2006. **157**(1): p. 368-376.
241. Jeffrey W, F., *Metallic interconnects for solid oxide fuel cells.* Materials Science and Engineering: A, 2005. **397**(1-2): p. 271-283.
242. Hui, S., et al., *A brief review of the ionic conductivity enhancement for selected oxide electrolytes.* Journal of Power Sources, 2007. **172**(2): p. 493-502.
243. Maldonado, L., et al., *Characterization of polymer electrolyte Nafion membranes: Influence of temperature, heat treatment and drying protocol on sorption and transport properties.* Journal of Membrane Science, 2012. **389**(0): p. 43-56.
244. Liu, M. and J. Winnick, *Fundamental issues in modeling of mixed ionic-electronic conductors (MIECs).* Solid State Ionics, 1999. **118**(1-2): p. 11-21.
245. Matsuzaki, Y. and I. Yasuda, *The poisoning effect of sulfur-containing impurity gas on a SOFC anode: Part I. Dependence on temperature, time, and impurity concentration.* Solid State Ionics, 2000. **132**(3-4): p. 261-269.
246. Singh, D., et al., *Carbon deposition in an SOFC fueled by tar-laden biomass gas: a thermodynamic analysis.* Journal of Power Sources, 2005. **142**(1-2): p. 194-199.

247. Mori, M., et al., *Thermal Expansion of Nickel-Zirconia Anodes in Solid Oxide Fuel Cells during Fabrication and Operation.* Journal of The Electrochemical Society, 1998. **145**(4): p. 1374-1381.
248. Ullmann, H., et al., *Correlation between thermal expansion and oxide ion transport in mixed conducting perovskite-type oxides for SOFC cathodes.* Solid State Ionics, 2000. **138**(1-2): p. 79-90.
249. Letilly, M., O. Joubert, and A.L.G.L. Salle, *Characteristics and Performance Improvement of Anode Supported Solid Oxide Fuel Cells based on $BaIn_{0.3}Ti_{0.7}O_{2.85}$ (BIT07) as Electrolyte, BIT07-Ni as Anode and $La_{0.58}Sr_{0.4}Co_{0.2}Fe_{0.8}O_{3-\delta}$ (LSCF) as Cathode.* Journal of Power Sources, 2012. **206**(0): p 210-214.
250. Letilly, M., A.L.G. La Salle, and O. Joubert, *Electrochemical Optimization of LSCF/BIT07 as an Alternative Cathode/electrolyte Couple for SOFC.* ECS Transactions, 2009. **25**(2): p. 2837-2844.
251. Letilly, M., et al., *Tape casting fabrication, co-sintering and optimisation of anode/electrolyte assemblies for SOFC based on BIT07-Ni/BIT07.* International Journal of Hydrogen Energy, 2012. **37**(5): p. 4346-4355.
252. Prakash, D., et al., *Design and Evaluation of SOFC Based on $BaIn_{0.3}Ti_{0.7}O_{2.85}$ Electrolyte and Ni/$BaIn_{0.3}Ti_{0.7}O_{2.85}$ Cermet Anode.* ECS Transactions, 2007. **7**(1): p. 2343-2350.
253. Le Gal La Salle, A., et al., *Electrochemical impedance measurements for evaluation of the different components of a complete solid oxide fuel cell associating $La_{0.58}Sr_{0.4}Co_{0.2}Fe_{0.8}O_{3-\delta}$ as cathode, $BaIn_{0.3}Ti_{0.7}O_{2.85}$ as electrolyte and $BaIn_{0.3}Ti_{0.7}O_{2.85}$-Ni cermet as anode.* Journal of Power Sources, 2011. **196**(24): p. 10576-10583.
254. Letilly, M., et al., *Validation of $BaIn_{0.3}Ti_{0.7}O_{2.85}$ as SOFC Electrolyte with Nd_2NiO_4, LSM and LSCF as Cathodes.* Fuel Cells, 2009. **9**(5): p. 622-629.
255. Lalanne, C., et al., *Neodymium-deficient nickelate oxide $Nd_{1.95}NiO_{4+\delta}$ as cathode material for anode-supported intermediate temperature solid oxide fuel cells.* Journal of Power Sources, 2008. **185**(2): p. 1218-1224.
256. Lalanne, C., et al., *Intermediate temperature SOFC single cell test using $Nd_{1.95}NiO_{4+\delta}$ as cathode.* Journal of the European Ceramic Society, 2007. **27**(13-15): p. 4195-4198.
257. Grenier, J.C., et al., *$A_2MO_{4+\delta}$ Oxides: Flexible Electrode Materials for Solid Oxide Cells.* ECS Transactions, 2009. **25**(2): p. 2537-2546.
258. Mauvy, F., et al., *Electrochemical study of the $Nd_{1.95}NiO_{4+\delta}$/oxide electrolyte interface.* Solid State Ionics, 2009. **180**(20-22): p. 1183-1189.
259. Mauvy, F., et al., *Oxygen reduction on porous $Ln_2NiO_{4+\delta}$ electrodes.* Journal of the European Ceramic Society, 2005. **25**(12): p. 2669-2672.
260. Ferchaud, C., et al., *High performance praseodymium nickelate oxide cathode for low temperature solid oxide fuel cell.* Journal of Power Sources, 2011. **196**(4): p. 1872-1879.
261. Dimarcello, F.V., K. P.L., and J.C. Williams, *Preferred Organisation in Alumina Substrates.* American Society Bulletin, 1972. **10**: p. 309-314.
262. Moreno, R., *The role of slip additives in tape casting technology. I: Solvents and dispersants.* American Ceramic Society bulletin, 1992. **71**(10).
263. Moreno, R., *The role of slip additives in tape casting technology. II: Binders and plasticizers.* American Ceramic Society bulletin, 1992. **71**(11).
264. Immergut Edmund, H. and F. Mark Herman, *Principles of Plasticization,* in *Plasticization and Plasticizer Processes*. 1965, Amercian Chemical Society. p. 1-26.
265. Schafbauer, W., *Entwicklung und Herstellung von foliengegossenen, anodengestützten Festoxidbrennstoffzellen*. 2009: PhD thesis, Forschungszentrum Jülich GmbH.

266. Ceylan, A., E. Suvaci, and H. Mandal, *Role of organic additives on non-aqueous tape casting of SiAlON ceramics.* Journal of the European Ceramic Society. **31**(1-2): p. 167-173.
267. Jean, J.-H. and H.-R. Wang, *Organic Distributions in Dried Alumina Green Tape.* Journal of the American Ceramic Society, 2001. **84**(2): p. 267-72.
268. Scherer, G.W., *Theory of Drying.* Journal of the American Ceramic Society, 1990. **73**(1): p. 3-14.
269. Chiu, R.C., T.J. Garino, and M.J. Cima, *Drying of Granular Ceramic Films: I, Effect of Processing Variables on Cracking Behavior.* Journal of the American Ceramic Society, 1993. **76**(9): p. 2257-2264.
270. Chiu, R.C. and M.J. Cima, *Drying of Granular Ceramic Films: II, Drying Stress and Saturation Uniformity.* Journal of the American Ceramic Society, 1993. **76**(11): p. 2769-2777.
271. Holmes, D.M., F. Tegeler, and W.J. Clegg, *Stresses and strains in colloidal films during lateral drying.* Journal of the European Ceramic Society, 2008. **28**(7): p. 1381-1387.
272. Basu, R.N., et al., *Simplified processing of anode-supported thin film planar solid oxide fuel cells.* Journal of the European Ceramic Society, 2005. **25**(4): p. 463-471.
273. White, G., et al., *A model for the screen-printing of Newtonian fluids.* Journal of Engineering Mathematics, 2006. **54**(1): p. 49-70.
274. Schmidt, R., et al., *An investigation into the surface topology and thickness profile of functional ceramic spinel manganate sputtered, evaporated and screen-printed layers.* Applied Surface Science, 2006. **252**(24): p. 8760-8767.
275. Von Dollen, P. and S. Barnett, *A Study of Screen Printed Yttria-Stabilized Zirconia Layers for Solid Oxide Fuel Cells.* Journal of the American Ceramic Society, 2005. **88**(12): p. 3361-3368.
276. Dullaert, K. and J. Mewis, *A structural kinetics model for thixotropy.* Journal of Non-Newtonian Fluid Mechanics, 2006. **139**(1-2): p. 21-30.
277. Burnat, D., et al., *The Rheology of Stabilised Lanthanum Strontium Cobaltite Ferrite Nanopowders in Organic Medium Applicable as Screen Printed SOFC Cathode Layers.* Fuel Cells, 2010. **10**(1): p. 156-165.
278. Lin, H.-W., et al., *The rheological behaviors of screen-printing pastes.* Journal of Materials Processing Technology, 2008. **197**(1-3): p. 284-291.
279. Nair, A. and R.L. White, *Effects of inorganic oxides on polymer binder burnout. I. Poly(vinyl butyral).* Journal of Applied Polymer Science, 1996. **60**(11): p. 1901-1909.
280. Masia, S., et al., *Effect of oxides on binder burnout during ceramics processing.* Journal of Materials Science, 1989. **24**(6): p. 1907-1912.
281. Cullity, B.D., *Elements of X-ray diffraction*. Adison - Wesley publishing company, Inc. ed. 1956.
282. Kippax, P. *Measuring particle size using modern laser diffraction techniques*. 2012; Available from: http://www.chemeurope.com/en/whitepapers/61205/measuring-particle-size-using-modern-laser-diffraction-techniques.html.
283. Rawle, A., Malvern Instruments Ltd, *Basic principle of particle size analysis.* Technical paper. Available from: http://www.atascientific.com.au/publications/wp-content/uploads/2012/07/Basic_principles_of_particle_size_analysis_MRK034-low_res.pdf
284. Malvern Instruments Ltd, *Laser Diffraction Particle Sizing*. 2013; Available from: http://www.malvern.com/labeng/technology/laser_diffraction/particle_sizing.htm.
285. Hatakeyama, T. and F.X. Quinn, *Thermal Analysis: Fundamentals and Applications to Polymer Science*. 1999: John Wiley & Sons Ltd.

286. Brown, M.E., *Introduction to Thermal Analysis: Techniques and Applications (Hot Topics in Thermal Analysis and Calorimetry)*. 2001: Kluwer Academic Publishers. ISBN-13: **978-1402002113.**
287. Ohnsorge, J. and R. Holm, *Scanning Electron Microscopy: An Introduction to Physicians and Biologists*. 1978: Goerg Thieme Publishers Stuttgart.
288. Joy, D.C., *The theory and practice of high-resolution scanning electron microscopy.* Ultramicroscopy, 1991. **37**(1-4): p. 216-233.
289. Werner, W. *Surface & Plasma Technology - Research Group of the Institut für Allgemeine Physik: Interaction of electron beams with matter*. 2012; Available from: http://eaps4.iap.tuwien.ac.at/~werner/qes_tut_interact.html.
290. Carter, H.W., *Backscattered electron imaging: Theory and applications.* Micron (1969), 1980. **11**(3-4): p. 259-260.
291. Wittke, J. H. Northern Arizona University. *Electron microprobe laboratory - Instrumentation*. 2008; Available from: http://www4.nau.edu/microanalysis/microprobe-sem/instrumentation.html.
292. Leonide, A., A. Weber, and E. Ivers-Tiffée. *Electrochemical Impedance Spectroscopy: A Key Tool for SOFC Development*. in *10th European SOFC Forum*. 2012. Lucerne, Switzerland.
293. Ivers-Tiffée, E. and A.V. Virkar, *Electrodes polarisations*, in *High Temperature Solid Oxide Fuel Cells: Fundamentals, Design and Applications*, S.C. Singhal and K. Kendall, Editors. 2003, Elsevier Ltd. p. Chapter 9.
294. Huang, Q.-A., et al., *A review of AC impedance modeling and validation in SOFC diagnosis.* Electrochimica Acta, 2007. **52**(28): p. 8144-8164.
295. Tietz, F., et al., *Evaluation of commercial nickel oxide powders for components in solid oxide fuel cells.* Journal of the European Ceramic Society, 2000. **20**(8): p. 1023-1034.
296. Schafbauer, W., N.H. Menzler, and H.P. Buchkremer, *Influence of Thermal Treatment During Cell Manufacturing on the Performance of Tape Cast Solid Oxide Fuel Cells.* ECS Transactions, 2009. **25**(2): p. 649-654.
297. Solutia, *Butvar Ceramic Binder Applications Technical Bulletin*.
298. Kim, D.-H., et al., *Effects of chemical structure and molecular weight of plasticizer on physical properties of green tape in $BaTiO_3$/PVB system.* Journal of the European Ceramic Society, 2004. **24**(5): p. 733-738.
299. *Tables of Azeotropes and Nonazeotropes*, in *Azeotropic Data III*. 1973, The American Chemical Society. p. 1-613.
300. Mistler, R.E., et al., *Evaluation of an Environmentally Friendly Plasticizer for Polyvinyl Butyral for Use in Tape Casting*, in *Advanced Processing and Manufacturing Technologies for Structural and Multifunctional Materials: Ceramic Engineering and Science Proceedings, Volume 28, Issue 7*. 2009, John Wiley & Sons, Inc. p. 27-34.
301. Lim, K.Y., et al., *Effect of the molecular weight of poly(ethylene glycol) on the plasticization of green sheets composed of ultrafine $BaTiO_3$ particles and poly(vinyl butyral).* Materials Research Bulletin, 2003. **38**(6): p. 1021-1032.
302. Available from: http://www.inkline.gr/inkjet/newtech/tech/dispersion/#fattyacid.
303. Letilly, M., *Mise en forme et évalutaion des performances de cellules de piles à combustible SOFC à base de $BaIn_{0,3}Ti_{0,7}O_{2,85}$ (BIT07).* PhD thesis. 2010. Université de Nantes, 2010. Supervisor : O. Joubert. Available from: http://archive.bu.univ-nantes.fr/pollux/show.action?id=0c8ac704-2b08-4b84-afe5-b8e80d6debf6.
304. Taillades, G., et al., *Engineering of porosity, microstructure and electrical properties of $Ni–BaCe_{0.9}Y_{0.1}O_{2.95}$ cermet fuel cell electrodes by gelled starch porogen processing.* Microporous and Mesoporous Materials, 2011. **145**(1-3): p. 26-31.

305. Corbin, S.F. and P.S. Apte, *Engineered Porosity via Tape Casting, Lamination and the Percolation of Pyrolysable Particulates.* J. Am. Ceram. Soc., 1999. **83**(7): p. 1693-1701.
306. Sanson, A., P. Pinasco, and E. Roncari, *Influence of pore formers on slurry composition and microstructure of tape cast supporting anodes for SOFCs.* Journal of the European Ceramic Society, 2008. **28**(6): p. 1221-1226.
307. Batocchi, P., *Pile à combustible à céramique conductrice protonique : développement, optimisation des matériaux, réalisaiton de cellules élémentaires PCFC opérant dans le domaine de température 400-600°C*. 2012, PhD thesis, Université Montpellier II. Supervisors: J. Roziere and G. Taillades.
308. Rieu, M., et al., *Fabrication and Characterization of Anode-Supported $BaIn_{0.3}Ti_{0.7}O_{2.85}$ Thin Electrolyte for Solid Oxide Fuel Cell.* International Journal of Applied Ceramic Technology, 2012. **9**(6): p. 1049-1057.
309. Minh, N.Q. and T. Takahashi, *Chapter 4 - Electrolyte*, in *Science and Technology of Ceramic Fuel Cells*. 1995, Elsevier Science Ltd: Oxford. p. 69-116.
310. Song, C.-R. and H.-I. Yoo, *Chemical Diffusivity of $BaTiO_{3-\delta}$: IV, Acceptor-Doped Case.* Journal of the American Ceramic Society, 2000. **83**(4): p. 773-779.
311. Chan, N.H., R.K. Sharma, and D.M. Smyth, *Nonstoichiometry in Acceptor-Doped $BaTiO_3$.* Journal of the American Ceramic Society, 1982. **65**(3): p. 167-170.
312. Jeong, J., E.J. Lee, and Y.H. Han, *Effects of Ho_2O_3 addition on defects of $BaTiO_3$.* Materials Chemistry and Physics, 2006. **100**(2-3): p. 434-437.
313. Duncan, K.L. and E.D. Wachsman, *Continuum-Level Analytical Model for Solid Oxide Fuel Cells with Mixed Conducting Electrolytes.* Journal of The Electrochemical Society, 2009. **156**(9): p. B1030-B1038.
314. Riess, I., *Theoretical Treatment of the Transport Equations for Electrons and Ions in a Mixed Conductor.* Journal of The Electrochemical Society, 1981. **128**(10): p. 2077-2081.
315. Steele, B.C.H., *Material science and engineering: The enabling technology for the commercialisation of fuel cell systems.* Journal of Materials Science, 2001. **36**(5): p. 1053-1068.
316. Tannhauser, D.S., *The Theoretical Energy Conversion Efficiency of a High Temperature Fuel Cell Based on a Mixed Conductor.* Journal of The Electrochemical Society, 1978. **125**(8): p. 1277-1282.
317. Prakash, D., et al., *Intermediate temperature solid oxide fuel cell based on $BaIn_{0.3}Ti_{0.7}O_{2.85}$ electrolyte.* Journal of Power Sources, 2007. **167**(1): p. 111-117.
318. Benamira, M., et al., *Mise en forme d'une cellule complète à base de l'électrolyte BIT07 et de Pr_2NiO_4: Influence de la présence d'une couche aux interfaces anode/électrolyte et cathode/électrolyte*, in *GDR PACS*. June 2012: Belfort, France.
319. Kharton, V.V., et al., *Electron-hole transport in $(La_{0.9}Sr_{0.1})_{0.98}Ga_{0.8}Mg_{0.2}O_{3-\delta}$ electrolyte: effects of ceramic microstructure.* Electrochimica Acta, 2003. **48**(13): p. 1817-1828.
320. Kharton, V.V. and F.M.B. Marques, *Interfacial effects in electrochemical cells for oxygen ionic conduction measurements: I. The e.m.f. method.* Solid State Ionics, 2001. **140**(3-4): p. 381-394.
321. Lai, W. and S.M. Haile, *Electrochemical impedance spectroscopy of mixed conductors under a chemical potential gradient: a case study of Pt|SDC|BSCF.* Physical Chemistry Chemical Physics, 2008. **10**(6): p. 865-883.
322. Liu, M. and H. Hu, *Effect of Interfacial Resistance on Determination of Transport Properties of Mixed-Conducting Electrolytes.* Journal of The Electrochemical Society, 1996. **143**(6): p. L109-L112.

323. Hu, H. and M. Liu, *Interfacial studies of solid-state cells based on electrolytes of mixed ionic–electronic conductors.* Solid State Ionics, 1998. **109**(3-4): p. 259-272.
324. Virkar, A.V., *Theoretical analysis of the role of interfaces in transport through oxygen ion and electron conducting membranes.* Journal of Power Sources, 2005. **147**(1-2): p. 8-31.
325. Duncan, K.L., K.-T. Lee, and E.D. Wachsman, *Dependence of open-circuit potential and power density on electrolyte thickness in solid oxide fuel cells with mixed conducting electrolytes.* Journal of Power Sources, 2011. **196**(5): p. 2445-2451.
326. Laberty, C., et al., *High-Performance Solid Oxide Fuel Cell Cathodes with Lanthanum-Nickelate-Based Composites.* Electrochemical and Solid-State Letters, 2007. **10**(10): p. B170-B174.
327. Brüll, A., et al., *Etude de l'assemblage BIT07/CGO/$Ln_2NiO_{4+\delta}$ (Ln = Lanthanide) en vue d'une utilisation comme cathode SOFC à 700°C*, in *GDR PACS*. June 2012: Belfort, France.
328. Park, K., et al., *Fast performance degradation of SOFC caused by cathode delamination in long-term testing.* International Journal of Hydrogen Energy, 2010. **35**(16): p. 8670-8677.
329. Primdahl, S. and M. Mogensen, *Oxidation of Hydrogen on Ni/Yttria-Stabilized Zirconia Cermet Anodes.* Journal of The Electrochemical Society, 1997. **144**(10): p. 3409-3419.
330. Ringuedé, A. and J. Fouletier, *Oxygen reaction on strontium-doped lanthanum cobaltite dense electrodes at intermediate temperatures.* Solid State Ionics, 2001. **139**(3-4): p. 167-177.
331. Dusastre, V. and J.A. Kilner, *Optimisation of composite cathodes for intermediate temperature SOFC applications.* Solid State Ionics, 1999. **126**(1-2): p. 163-174.
332. Mauvy, F., et al., *Electrode properties of $Ln_2NiO_{4+\delta}$ $(Ln = La, Nd, Pr)$: AC Impedance and DC Polarization Studies.* Journal of The Electrochemical Society, 2006. **153**(8): p. A1547-A1553.
333. Zhao, H., et al., *New cathode materials for ITSOFC: Phase stability, oxygen exchange and cathode properties of $La_{2-x}NiO_{4+\delta}$.* Solid State Ionics, 2008. **179**(35-36): p. 2000-2005.
334. Montenegro-Hernández, A., L. Mogni, and A. Caneiro, *Microstructure and reactivity effects on the performance of $Nd_2NiO_{4+\delta}$ oxygen electrode on Ce0.9Gd0.1O1.95 electrolyte.* International Journal of Hydrogen Energy, 2012. **37**(23): p. 18290-18301.
335. Ramos, T., J. Hjelm, and M. Mogensen, *Towards Quantification of Relations Between Electrode Polarisation and Microstructure.* Journal of The Electrochemical Society, 2011. **158**(7): p. B814-B824.
336. Fu, Q.X., F. Tietz, and D. Stöver, *$La_{0.4}Sr_{0.6}Ti_{1-x}Mn_xO_{3-\delta}$ Perovskites as Anode Materials for Solid Oxide Fuel Cells.* Journal of The Electrochemical Society, 2006. **153**(4): p. D74-D83.
337. Leng, Y.J., et al., *Performance evaluation of anode-supported solid oxide fuel cells with thin film YSZ electrolyte.* International Journal of Hydrogen Energy, 2004. **29**(10): p. 1025-1033.
338. Primdahl, S. and M. Mogensen, *Gas Conversion Impedance: A Test Geometry Effect in Characterization of Solid Oxide Fuel Cell Anodes.* Journal of The Electrochemical Society, 1998. **145**(7): p. 2431-2438.
339. Jamnik, J. and J. Maier, *Treatment of the Impedance of Mixed Conductors Equivalent Circuit Model and Explicit Approximate Solutions.* Journal of The Electrochemical Society, 1999. **146**(11): p. 4183-4188.
340. Kwon, T.-H., T. Lee, and H.-I. Yoo, *Partial electronic conductivity and electrolytic domain of bilayer electrolyte $Zr_{0.84}Y_{0.16}O_{1.92}/Ce_{0.9}Gd_{0.1}O_{1.95}$.* Solid State Ionics, 2011. **195**(1): p. 25-35.

341. Myung, D.-H., et al., *The effect of an ultra-thin zirconia blocking layer on the performance of a 1-μm-thick gadolinia-doped ceria electrolyte solid-oxide fuel cell.* Journal of Power Sources, 2012. **206**(0): p. 91-96.
342. Simwonis, D., F. Tietz, and D. Stöver, *Nickel coarsening in annealed Ni/8YSZ anode substrates for solid oxide fuel cells.* Solid State Ionics, 2000. **132**(3-4): p. 241-251.
343. Yokokawa, H., et al., *Fundamental mechanisms limiting solid oxide fuel cell durability.* Journal of Power Sources, 2008. **182**(2): p. 400-412.
344. Lanzini, A., P. Leone, and P. Asinari, *Microstructural characterization of solid oxide fuel cell electrodes by image analysis technique.* Journal of Power Sources, 2009. **194**(1): p. 408-422.
345. Faes, A., et al., *Nickel–Zirconia Anode Degradation and Triple Phase Boundary Quantification from Microstructural Analysis.* Fuel Cells, 2009. **9**(6): p. 841-851.
346. Dees, D.W., et al., *Conductivity of Porous Ni / ZrO_2 - Y_2O_3 Cermets.* Journal of The Electrochemical Society, 1987. **134**(9): p. 2141-2146.
347. Guillodo, M., P. Vernoux, and J. Fouletier, *Electrochemical properties of Ni–YSZ cermet in solid oxide fuel cells: Effect of current collecting.* Solid State Ionics, 2000. **127**(1-2): p. 99-107.
348. Jiang, S.P., J.G. Love, and L. Apateanu, *Effect of contact between electrode and current collector on the performance of solid oxide fuel cells.* Solid State Ionics, 2003. **160**(1-2): p. 15-26.
349. Sung, P.K. and D.R. Poirier, *Estimation of densities and coefficients of thermal expansion of solid Ni-base superalloys.* Materials Science and Engineering: A, 1998. **245**(1): p. 135-141.
350. Fischer, W., et al., *Residual stresses in planar solid oxide fuel cells.* Journal of Power Sources, 2005. **150**(0): p. 73-77.
351. Malzbender, J., W. Fischer, and R.W. Steinbrech, *Studies of residual stresses in planar solid oxide fuel cells.* Journal of Power Sources, 2008. **182**(2): p. 594-598.
352. Hsiao, Y.C. and J.R. Selman, *The degradation of SOFC electrodes.* Solid State Ionics, 1997. **98**(1-2): p. 33-38.
353. Lalanne, C., et al. *Suitability of Nickelate Compounds for SOFC Cathode Applications*. in *Proceedings of the 7th European SOFC Forum*. 2006. Oberrohrdorf, Switzerland.